Ab-initio Calculations of the Relaxor Ferroelectric $Na_{1/2}Bi_{1/2}TiO_3$ and its Solid Solutions

Vom Fachbereich
Materialwissenschaft
der Technischen Universität Darmstadt
zur Erlangung der Würde eines Doktor-Ingenieurs (Dr.-Ing.)
genehmigte Dissertation

von

Dipl.-Ing. Melanie Gröting

aus Frankfurt am Main

Referent:	Prof. Dr. Karsten Albe
Korreferent:	Prof. Dr. Wolfgang Donner
Tag der Einreichung:	5. März 2013
Tag der mündlichen Prüfung:	3. Mai 2013

Darmstadt, 2013

D 17

Acknowledgments - Danksagung

An dieser Stelle möchte ich mich bei all denen bedanken, die zum Gelingen dieser Arbeit beigetragen und die die Jahre meiner Promotion zu einem unvergesslichen Lebensabschnitt gemacht haben.

Als allererstes möchte ich mich bei meinem Diplomvater Peter Schmidt bedanken, denn ohne ihn wäre ich nicht, wo ich heute bin. Er hat wesentlich dazu beigetragen, dass ich 2008 wieder Boden unter die Füße bekommen habe und an die TU Darmstadt zurückgekehrt bin. Herzlichsten Dank für Deine bedingungslose Unterstützung in allen Lebenslagen!

Ich danke Wolfgang Donner für die Begutachtung meiner Arbeit, und auch den übrigen Mitgliedern meiner Prüfungskomission, Jürgen Rödel und Jens Kreisel, für die Wertschätzung, die sie meiner Arbeit, und das Vertrauen, das sie mir, in den vergangenen Jahren zuteil haben lassen.

Ich möchte mich herzlich bei meinem Doktorvater Karsten Albe für seine Geduld, die große Freiheit in der Themenwahl und das mir entgegengebrachte Vertrauen bedanken.

Je remercie Brahim Dkhil et tout le Laboratoire SPMS de l'École Centrale Paris pour mon séjour à l'étranger tres chouette chez eux. Merci á Brahim pour le tutorat global, notamment pour m'avoir emmenée au synchrotron à Grenoble et familiarisée avec la communauté des ferroélectriques à Gaithersburg. Tu m'as montré l'importance des pauses café créatives et que la science peut être un plaisir. En fait, l'idée du calcul de pression chimique est né dans cette salle de café.

I want to thank Igor Kornev for the illuminative stay abroad at École Centrale Paris. He gave me a lot of new ideas, especially how to complete my work by using group theoretical tools for the characterization of my hundreds of optimized crystal structures. Thank you very much for all our discussions during my stay and since then.

Ich danke Renate Hernichel für die durchschwätzten Nächte in unserer gemeinsamen Suite in Edesheim und für alles andere, was wir freiwilllig und unfreiwillig geteilt haben.

Ich danke allen MMs für die kollegiale Zusammenarbeit in den letzten Jahren. Besonders bei Yvonne für ihr offenes Ohr und die guten Buchempfehlungen, bei Jonathan für seinen herrlich bissigen Humor, und bei Peter für seine Hilfsbereitschaft, ohne seine Skript-Sammlung wäre ich wahrscheinlich niemals fertig geworden.

Schließlich möchte ich mich bei den SFB- und AdRIA-Mitgliedern dafür bedanken, dass sie mich so herzlich in ihrer Mitte aufgenommen haben, vor allem bei den bleifreien NAWs, die mich quasi-adoptiert haben, und bei Jens Kling und Marton Major für die wissenschaftliche Kooperation und die Einblicke in das komplexe Geschäft der Strukturaufklärung. Außerdem bei Hanna Hahn, mit der mich nicht nur ein gemeinsames Schicksal in der Materialwissenschaft verbunden hat, sondern schon ein ganzes Chemiestudium, sowie die Widrigkeiten einer Industriepromotion und vieles mehr.

Ein Dank geht auch an die Odenwaldbahn-Mitfahrer (besonders an Gerrit Günther und Felix Holzinger). Mit Euch waren die Heimfahrten nochmal so schön.

Un grand bisous à mon doudou. Je te remercie pour ton soutien aimant et ta patience avec moi en particulier l'an dernier, et que tu m'aimes le plus quand je ne le peux pas seule.

Schließlich will ich mich bei denen bedanken, die mich gefühlt "schon immer" begleitet und unterstützt haben, den Mitgliedern meiner erweiterten Familie: Margot Gröting und Roman Hensel, sowie Katharina Herbert, Martin Deutsch, und Claus und Gudrun Gröting. Ihr seid die Besten!

Die vorliegende Arbeit wurde vom LOEWE-Zentrum AdRIA finanziert. Während meines Forschungsaufenthaltes an der École Centrale Paris wurde ich zudem im Rahmen eines Kurzzeit-Stipendiums vom Deutschen Akademischen Austausch Dienst (DAAD) unterstützt.
Ein Großteil der Rechnungen wurde auf dem Hessischen Hochleistungsrechner (HHLR) in Darmstadt durchgeführt.

Contents

Symbols and Abbreviations

Crystallographic Items

$(\mathbf{a}, \mathbf{b}, \mathbf{c})$	Basis vectors of the unit cell
a, b, c	Lengths of the basis vectors
α, β, γ	Lattice angles
V	Unit cell volume
$\mathbf{x}$	Position vector of an atom
x, y, z	Atomic coordinates
$(\boldsymbol{P}, \boldsymbol{p})$	Transformation of the coordinate system
$(\boldsymbol{Q}, \boldsymbol{q})$	Inverse transformation of $(\boldsymbol{P}, \boldsymbol{p})$
$\mathcal{G}$	Space group
$\mathcal{H}$	Subgroup
$\mathcal{P}$	Point group
$[i]$	Index i of a group-subgroup transformation
Z	Number of formula units
$\mathbf{u}$	Atomic displacement

Symmetry Elements

m	Reflection plane
a, b, c	Axial glide plane
n	Diagonal glide plane
$2, 3, 4$	n-fold rotation axis
1	Identity
$\bar{1}$	Inversion centre
$2_1, 4_2$	n-fold screw axis

Physical Properties

q	Ionic charge
E	Energy (eV/f.u.)
E_0	Equilibrium energy (eV/f.u.)
V_0	Equilibrium volume (Å^3/f.u.)
F	Free energy (eV/f.u.)
H	Enthalpy (eV/f.u.)
S	Entropy (eV/(f.u.·K)
T	Temperature (K)
p	Hydrostatic pressure (GPa)
B_0	Bulk modulus (GPa)
B_0'	Pressure derivative
η	Elastic strain
σ	Elastic stress
D	Dielectric displacement
P	Polarization
E_k	Electric field
ϕ	In-phase tilt
θ	Anti-phase tilt
Q	Any order parameter

Physical Constants

$\hbar$	Reduced Planck constant ($1.05457 \cdot 10^{-34}$ Js)
N_A	Avogadro constant ($6.022 \cdot 10^{23}$ mol^{-1})
e	Elementary electric charge ($1.602 \cdot 10^{-19}$ C)
$4\pi\epsilon_0$	Permittivity of vacuum ($1.113 \cdot 10^{-10}$ C^2/Jm)
k_B	Boltzmann constant ($8.617343 \cdot 10^{-5}$ eV/K)
F	Faraday constant (96485 J/mol)

Acronyms and Abbreviations

BT	$BaTiO_3$
BZT	$BaZr_xTi_{(1-x)}O_3$
KNN	$K_xNa_{1-x}NbO_3$
NBT	$Na_{1/2}Bi_{1/2}TiO_3$
PMN	$PbMg_{1/3}Nb_{2/3}O_3$
PSN	$PbSc_{1/2}Nb_{1/2}O_3$
PST	$PbSc_{1/2}Ta_{1/2}O_3$
PZN	$PbZn_{1/3}Nb_{2/3}O_3$
PZT	$PbZr_xTi_{(1-x)}O_3$
SBN	$Sr_xBa_{1-x}Nb_2O_6$

APB	Antiphase boundary
CNR	Chemically ordered nanoregion
DW	Domain wall
MPB	Morphotropic phase boundary
PNR	Polar nanoregion

IUPAC	International Union of Pure and Applied Chemistry
MAK	Maximale Arbeitsplatz-Konzentration (occupational exposure limit)

ESR	Electron spin resonance
NMR	Nuclear magnetic resonance
PDF	Pair distribution function
TEM	Transmission electron microscopy
XAFS	X-ray absorption spectroscopy
XRD	X-ray diffraction
XRDS	X-ray diffuse scattering

BZ	Brillouin zone
DFT	Density functional theory
GGA	Generalized gradient approximation
HF	Hartree-Fock
LDA	Local density approximation
PAW	Projector augmented waves

f.u.	Formula unit
irrep	Irreducible representation
DOS	Density of states

Abstract

The necessity of substituting $PbZr_xTi_{(1-x)}O_3$ by lead-free piezoelectric materials in numerous applications, such as sensors, actuators and ultrasonic transducers, has lead to a large number of research activities on perovskite solid solutions based on $Na_{1/2}Bi_{1/2}TiO_3$ in recent years.

The present dissertation deals with the characterization of the relaxor ferroelectric $Na_{1/2}Bi_{1/2}TiO_3$ in terms of structure and ferroelectric properties as a function of various parameters such as chemical order/disorder, hydrostatic pressure and alloying with other lead-free perovskites by computational methods. For this analysis it is necessary to combine *ab-initio* calculations with Landau theory and group theoretical tools.

Part I begins in Ch. 1 with the motivation of this work. In Ch. 2, a brief overview of the regulatory framework, which triggered research activities in the field of lead-free piezoelectrics, is given and an example how lead can be substituted by other elements with similar properties. Afterwards the development concepts for these materials are introduced in Ch. 3. They are borrowed from the lead-containing perovskite solid solution $PbZr_xTi_{(1-x)}O_3$, i.e. the presence of stereochemically active cations and solid solution formation with a morphotropic phase boundary. In Ch. 4, first relaxor ferroelectrics are introduced and the importance of chemical order/disorder discussed. Finally, the crystal structures of pure $Na_{1/2}Bi_{1/2}TiO_3$ and four selected lead-free solid solutions are presented. The introduction closes in Ch. 5 with a listing of 13 specific questions this work aims to answer.

In Part II the methods employed in this work are introduced. We start our investigations on the atomistic level using quantum mechanics. The atomistic simulations are performed in the Density Functional Theory (DFT) framework, which will be introduced on a very basic level, in Ch. 6. Some important remarks on the technique of structure optimization and mechanical boundary conditions will be given and a new nomenclature characterizing local structures of low symmetry will be presented, which is very similar to the well-known Glazer notation.
Phase transitions are well described within the phenomenological Landau theory outlined in Ch 7. Landau theory allows to expand the free energy of a system in terms of its so-called order parameters. The application of Landau theory on the order parameters and displacive phase transitions relevant in $Na_{1/2}Bi_{1/2}TiO_3$ requires also knowledge of some group theoretical tools, which will be introduced in Ch. 8. These tools are not only necessary for the Landau treatment, they are also enormously useful in the analysis of calculated crystal structures in an ultimately systematic way in terms of symmetry-adapted distortion modes. The amplitudes of these (frozen-in) distortion modes can be directly used as order parameters in the Landau potentials. As Landau theory and group theory both are absolutely concrete but not demonstrative at all, both chapters contain numerous examples, which are all relevant for the understanding of this work.

After introduction of the methods, the results will be discussed in Part III. The results are divided into five chapters. In Ch. 9 first the problem of chemical order will be treated in the cubic perovskite structure, accompanied by the question, whether it is possible to change the ordering

tendency by application of hydrostatic pressure or chemical substitution. Afterwards the complexity of the structures is enhanced by including lattice distortions like polar displacements and octahedral tilts in Ch. 10. Here also the question of phase stabilities under hydrostatic pressure is addressed, together with the investigation of possible phase coexistence and formation of chemically ordered nanoregions.
Afterwards the experimentally relevant phases $R3c$, *Pbnm* and $P4bm$ will be compared in two representative chemical configurations, in order to investigate the effects of chemical order and hydrostatic pressure on the presence of different lattice distortions by using the group theoretical analysis in Ch. 11. This analysis helps us to identify the dominating distortion modes active in these phases. Landau theory then gives insights into the coupling interactions between these modes. In Ch. 12 Landau potentials are derived and energies obtained from DFT calculations, under systematic variation of atomic displacements induced by the separate distortion modes, allow the determination of the coefficients of the Landau potential.
Ch. 13 finally treats the question of the possibility of morphotropic phase boundary predictions in NBT-based solid solutions. The method of determining pressure-induced phase transitions in pure NBT from Ch. 10 is extended to solid solutions in order to predict composition-induced phase transitions.

Part IV starts by answering the initially posed 13 questions based on the findings of this work and finalises with a concluding discussion of the results and abilities of atomistic simulations and an outlook on possible future works.

Part I

Introduction

1 Motivation

Natural resources are limited. Therefore their use and waste have to be limited to a minimum in order for our grand children to still find good living conditions on this planet. As this task cannot mean a reduction of our standards of living, we have to find new ways to satisfy our personal needs and especially those of the people living in the less developed countries of this world. The idea of global sustainable development was born in 1987,[1] but after 25 years humanity is still far from having created a world of ecological, economical and social sustainability.
What has materials science, especially computational materials science, to do with that? More knowledge about the properties of existing materials and the development of new materials, that are considered harmless for humans and ecosystems and that help to reduce the consumption of materials and energy resources, are the basis of the technological solution of the multidimensional sustainable development challenge.

One possible highly sophisticated ansatz to reduce the consumption of materials and energy is the employment of adaptronic or smart systems, which are able to adapt autonomously to varying environmental and operating conditions. The aim of the LOEWE-Center "Adaptronik - Research, Innovation, Application (AdRIA)" in Darmstadt is to establish a leading competence center of adaptronics focused on structural applications, such as adaptive vibration control, noise reduction and structure health monitoring.[2] Adaptronics is an interdisciplinary field at the cross-section between material development, mathematics, and electrical, automatic control and mechanical engineering. Adaptronic systems are characterized by adaptability and multifunctionality. A maximum of application specific functionalities is combined in a minimum of elements.[3] The simplest adaptronic system consists of a sensor and an actuator, which are regulated by integrated automatic control. In more complex systems a network of several sensors and actuators has to be regulated across wide distances e.g. in order to monitor and control the integrity of bridges or cars, then wireless connections and local energy supply have to be integrated. As it can have severe consequences if such complex systems destined for safety control fail, their development has to be accompanied by diligent life cycle engineering and reliability testing. All these disciplines are covered by different groups collaborating in AdRIA. The development of new functional materials based on piezoelectrics for actuator and sensor applications by both experimental and simulation techniques is the objective of the materials scientists involved in the centre.

Other applications of piezoelectrics besides actuators and sensors are ultrasonic transducers and energy harvesting. According to a market report on piezoelectric ceramic devices from 2008, the overall world market of piezoelectrics in 2007 had a volume of 10.6 billion US-$ and was expected to reach 19.5 billion US-$ by 2012.[4] In Fig. 1.1 the nine markets are shown, in which piezoelectrics are utilized. Piezoelectrics can be found almost everywhere. In computers they are used as actuators for disk drives. Fine positioning devices are needed in highly automatized industries like semiconductor manufacturing. Sonars are found mainly in military application, but ultrasonic transducers are also used in medical devices. In cars piezoelectrics find application as fuel injectors, igniters and in numerous sensors. It is a mature but still broadening market, as

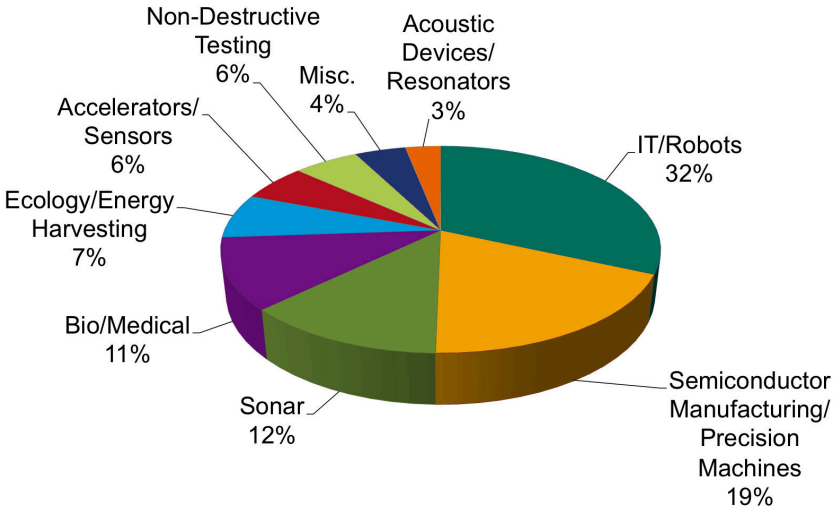

Figure 1.1: Market of piezoelectric ceramic devices in 2007.[4]

continuously new applications are explored and novel devices are brought to market. One of the sectors with the highest growth expectations is energy harvesting.[4]
The workhorse of the piezoelectric industry are ceramics and thin films based on lead zirconate titanate $Pb(Zr_{0.52}Ti_{0.48})O_3$ (PZT).[5] This ferroelectric material has the advantages of a high value of piezoelectric constant d_{33}, which is more or less temperature independent between -40 and 150°C. Moreover, it is very robust and versatile. After about 50 years of mass production the degree of manufacturing and processing expertise is enormously high. Both ceramics and thin films are available, only single crystals are problematic. The electromechanical properties can be varied easily and in a predictable way by doping with acceptors or donors to make the material softer or harder, as different applications require different material profiles.[5]
Though, there arose external conditions in recent years, that require a mind and technology shift. Since PZT contains 64wt% lead, a chemical element becoming banned worldwide due to its health and environmental issues, new materials with similar abilities and reliabilities as PZT have to be developed.[6]

Nowadays, two different approaches in the design of compounds and materials, be it drugs, catalysts or functional materials, can be distinguished. The first one is the rather empirical high-throughput experimentation with a high degree of parallelization, which helps to reduce costs and time, with the aim of hitting the target as fast as possible.[7] The second approach is the ancient rational one-by-one experiment design with the aim to understand the underlying physics and chemistry in order to choose the best set of parameters based on knowledge and experience. The first approach is very often found in industrial research, while the luxury of the second becomes more and more reserved to academical research. Atomistic computer simulations as used in the present work can be adapted to both approaches[8–10] but their strength is the latter one. Especially *ab-initio* calculations are ideal to investigate phase stabilities and structure-property relationships in ferroelectric materials on a very fundamental and accurate level.[11,12]

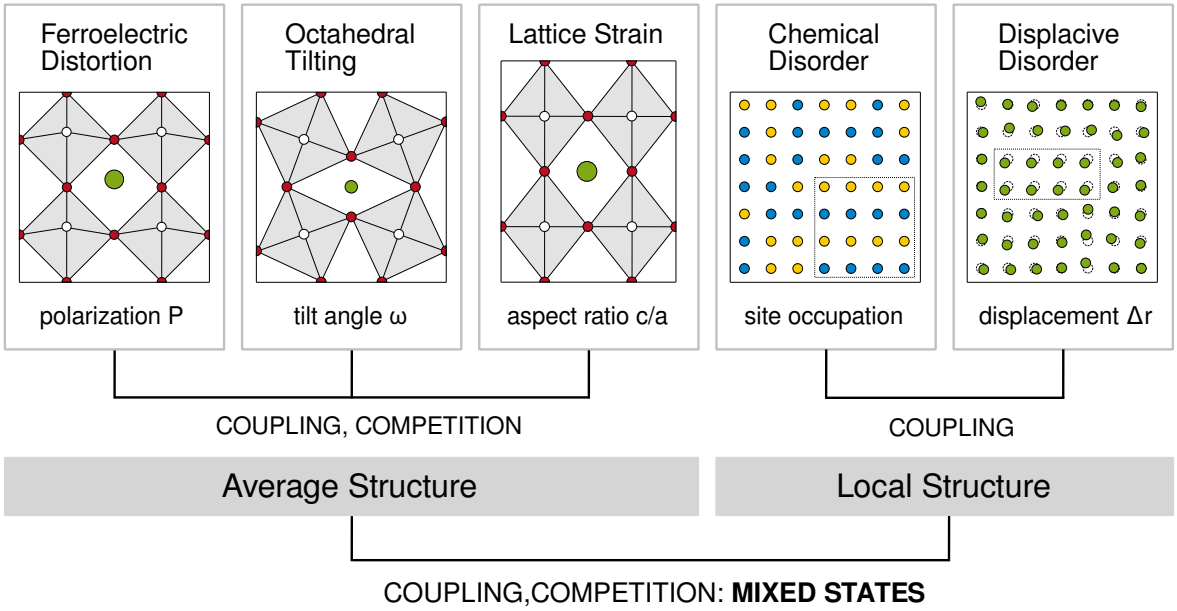

Figure 1.2: Order parameters present in $Na_{1/2}Bi_{1/2}TiO_3$ (NBT). Ferroelectric distortions, octahedral tilting and spontaneous lattice strain characterize the average crystal structure of the material, while chemical order/disorder and accompanying displacive order/disorder determine the local structure. Different order parameters can be cooperatively or competitively coupled. If different chemical configurations favour different average structures, even competition between different phases arises, which can lead to mixed phase ground states.

A class of materials exhibiting giant piezoelectric coefficients are relaxors. The understanding of structure-property relationships in relaxors is not comprehensive yet, but chemical order/disorder plays probably a key role. The material investigated in this work, $Na_{1/2}Bi_{1/2}TiO_3$ (NBT), is considered as a model relaxor ferroelectric with a complex perovskite structure having two different cations (Na^+ and Bi^{3+}) on the A-site. The material exhibits a complex temperature phase sequence in addition to the relaxor features (nano-scale local structure and frequency-dependent dielectric dispersion).[13–16] However, the pronounced nano-scale local structure is difficult to access by most of the experimental techniques. Therefore, atomistic simulation methods can help to gain deeper understanding of the relationships between chemical order, structure and ferroic properties.

Ab-initio calculations offer the valuable opportunity to investigate the structural variations arising from chemical order/disorder on different levels of complexity. The structural instabilities present in NBT are shown schematically in Fig. 1.2. In this material, ferroelectric distortions, octahedral tilts and spontaneous lattice strains coexist, which characterize the average crystal structure and can be coupled in a cooperative or competitive way. In this cation mixed system they are accompanied by additional displacive order/disorder resulting from chemical order/disorder, both determining the local structure. The high complexity renders NBT a challenging problem, but also a perfect model system to study interactions between these five degrees of freedom by *ab-initio* calculations combined with Landau theory in a systematic way. The aim of this work is to deepen the understanding of the local and average crystal structure present in this material and of the arising ferroic properties (polarization and octahedral tilting).

The ultimate dream of theoreticians is the prediction of new materials. In the field of perovskite ferroelectrics, especially a technique to predict morphotropic phase boundaries in solid solutions is still sought for. We developed a method that is capable to determine the chemical substitution-induced phase transitions in NBT-based solid solutions, which should be transferable to other perovskite materials.

There are also some drawbacks of this kind of simulations, these are the limited system size up to several hundred atoms and the restriction to athermal conditions, which prevents us from the direct investigation of polar nanoregions, which are believed to be the origin of relaxor behaviour, and their nucleation, growth and interactions at elevated temperatures. For that purpose other simulation methods such as Monte-Carlo or Molecular Dynamics simulations based on effective Hamiltonians have to be employed. However, for building such an effective Hamiltonian fundamental understanding of all underlying interactions are necessary, which for such a mixed perovskite can only be provided by *ab-initio* calculations. Thus, this study can be understood as the first stair to climb in order to resolve the relaxor enigma in NBT by means of atomistic simulations.

2 Demand for Lead-Free Piezoelectrics

2.1 Environmental Legislation

The European Union passed January 2003 two directives with the aim to prevent, reuse and recycle waste from electrical and electronic equipment, thereby contributing to sustainable development. In the last two years both directives were recast. The goal of the "Directive on Waste Electrical and Electronic Equipment 2012/19/EU (WEEE)"[17] is the prevention of waste, moreover it sets targets for collection, recycling and recovery for all types of electrical and electronic equipment, while the "Directive on the restriction of the use of certain hazardous substances in electrical and electronic equipment 2011/65/EU (RoHS)"[18] limits the use of the heavy metals Cd, Pb, Hg, of hexavalent chromium Cr(VI), and of the flame retardants polybrominated biphenyls (PBB) and polybrominated diphenyl ethers (PBDE) in electrical and electronic equipment used in households and industries. These elements/compounds have to be replaced by less harmful substitutes. Exemptions from the substitution requirement are only permitted if substitution is not possible from the scientific and technical point of view. By now, PZT in piezoelectric ceramics devices is still allowed, as no suitable lead-free substitutes have been found yet.

2.2 Bismuth as an Alternative to Lead

2.2.1 Lone-Pair Effect

Lead is special. Lead-based ferroelectrics and relaxor materials such as PZT or $PbMg_{1/3}Nb_{2/3}O_3$ (PMN) show superior response properties as compared to most lead-free materials. This is attributed to the stereochemical activity of the so-called inert electron pair of Pb^{2+} with electron configuration $6s^2\ 6p^0$. Though there are strong indications that this lone-pair, as it is also very often called, is by no means inert, but interacts quite strongly with its ligands. According to Walsh *et al.* the stereochemical activity of the lone-pair originates from interactions between the cation s and p orbitals with the anion p orbitals.[19] In PbO_2 for example the O $2p$ states mediate the intraatomic $6sp$ hybridization in Pb, which leads to anti-bonding states with a considerable Pb $6s$ character at the top of the valence band. These features were observed in *ab-initio* calculations of bismuth oxides and sulphides as well.[20–22] The hybridization is expected to be stronger the closer the cation s states are to the anion p states. In Fig. 2.1 the relative positions of the metal $5d$, $6s$ and $6p$ states and the valence band dominated by O $2p$ states is shown, as they can be calculated in the perovskite compounds $PbTiO_3$ and $Tl_{1/2}Bi_{1/2}TiO_3$. The $6s$ states of thallium are right in the valence band, which leads to a very strong Tl $6s-$O $2p$ interaction. The $6s$ orbitals of the heavier elements lie at deeper energies, reducing the $6s$ contributions to the valence band. Still, the $6s$ states of Pb and Bi contribute to the top of the valence band.

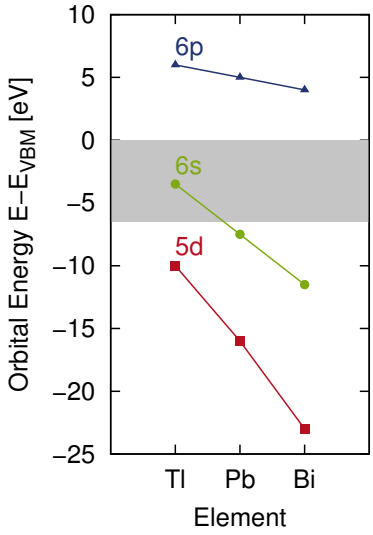

Figure 2.1: Energies of the valence states (gravity centres are given!) of Tl, Pb and Bi relative to the O $2p$ states (grey area) in the perovskites $PbTiO_3$ and $Tl_{1/2}Bi_{1/2}TiO_3$. Although the majority of the $6s$ states in Pb and Bi lie well below the valence band, they contribute also to the valence band maximum.

2.2.2 Toxicology of Thallium, Lead and Bismuth

Thallium and lead are both easily absorbed through the gastrointestinal and respiratory tracts and can also be taken up through the skin. Thallium and its compounds are extremely toxic (MAK 0.1 mg/m^3). The lethal dose in adults is 10-15 mg/kg.[23] The acute toxicity of thallium is characterized by hair loss (alopecia), abdominal pain and vomiting, damage of the central and peripheral nervous system, coma and death within 10-12 days. In sublethal poisonings, recovery often requires months and neurological and mental disturbances or blindness can remain. Inorganic lead compounds are classified as probably carcinogenic to humans (Group 2A),[24] moreover is lead considered as teratogene and mutagene (Group 3A), as a consequence there exists no MAK.[25] Chronic low-dose lead exposure leads to neuropsychiatric, reproductive and kidney problems. The primary symptoms of acute lead poisoning are similar to those of thallium. Depression, coma and death occur within 1 to 2 days.[23]

Bismuth is regarded as the only non-toxic heavy metal. So far, there is no evidence for carcinogenicity, teratogenicity or mutagenicity of bismuth compounds. The low solubility of metallic bismuth and its salts in fat and water results in poor resorption by the human body. Some bismuth salts even are used in medical practice e.g. in the treatment of gastrointestinal problems, but also in cosmetics. Acute poisoning with bismuth may cause kidney damage, encephalopathy and peripheral neuropathy. Neurotoxicity may also occur after chronic treatment with bismuth salts, but is reversible if bismuth intake is stopped.[23] Soluble bismuth compounds especially organic compounds like $BiMe_3$, however, can cause severe damages and death. Still, bismuth is the least toxic heavy metal and accidental poisoning more often results from bismuth medical therapy than from exposure at the workplace.[26]

3 Perovskite Solid Solutions

The perovskite structure is adopted by numerous compounds with the composition ABX_3. Nearly 90% of the metallic elements of the periodic table can be incorporated in the perovskite structure as A or B. X is in most cases O, but also other elements like N, F or Cl are possible.[27] This compositional flexibility of the perovskite structure stems from its ability to develop several types of lattice distortions like polar cation displacements, tilt or Jahn-Teller distortions of the BO_6 octahedral backbone, spontaneous lattice strain, as well as small systematic displacements induced by chemical disorder. Atomic displacements associated with these types of lattice distortions are in the range of few tenth of an Å. Displacive phase transitions are an important feature of perovskite materials.[28,29]
The occurrence of ferroelectricity in ABX_3 perovskites results from a delicate balance between long-range Coulomb ionic interaction favouring ferroelectric distortions and short-range electronic effects preferring the undistorted paraelectric cubic structure. This balance can be tipped towards ferroelectricity by covalent effects that weaken the short range repulsion (like e.g. hybridization between Ti $3d$-orbitals or Pb $6sp$-orbitals and O $2p$-states) as demonstrated by Cohen.[30] Furthermore it was shown that Pb-O hybridization in $PbTiO_3$ enhances electromechanical coupling leading to higher c/a-strain in $PbTiO_3$ (6%) as compared to $BaTiO_3$ (1%).

In the following, we report the structural and physical properties of ordinary ferroelectrics and relaxor ferroelectrics, which finally leads us to our study of the promising lead-free model relaxor ferroelectric $Na_{1/2}Bi_{1/2}TiO_3$.

3.1 $PbZr_xTi_{(1-x)}O_3$

The most prominent perovskite solid solution is the already mentioned $PbZr_xTi_{(1-x)}O_3$ (PZT), which exhibits enhanced piezoelectric, dielectric and elastic properties at $x = 0.52$.[5] For $x < 0.52$ a rhombohedral *R*3*c* (or *R*3*m* depending on temperature) crystal structure is found, while for $x > 0.52$ it is tetragonal *P*4*mm*. The region at $x = 0.52$ is called morphotropic phase boundary (MPB); it appears to be almost independent of temperature.
Various opinions exist how the crystal structure evolves in the MPB-region. They range from the existence of a bridging monoclinic *Cc* phase (or *Cm* at higher temperatures),[31] a continuous phase change across the MPB-region[32] to a *P*4*mm*/*R*3*m* nanodomain coexistence region.[33]
It was also pointed out, that the occurrence of a line boundary in the composition-T phase diagram separating rhombohedral and tetragonal phases contradicts Gibbs phase rule, which requires a two-phase region.[34] The experimental phase diagram thus should more precisely be called "diffusion-less" (non-equilibrium) phase diagram as it does not describe the thermodynamic equilibrium state.

3.2 The Concept of the Morphotropic Phase Boundary

The MPB is a key concept in the understanding of the property changes observed in perovskite solid solutions with variation of composition. IUPAC defines the morphotropic phase transition as "An abrupt change in the structure of a solid solution with variation in composition".[35] The MPB is represented as a nearly temperature-independent boundary in the concentration-temperature phase diagram. The MPB in ferroelectric solid solutions thus indicates the material composition at which the transition from one ferroelectric structure to another one is facilitated. This fact is believed to be the origin of the enhanced electromechanical response of materials, that exhibit morphotropic phase boundaries, and explains why researchers are searching in complex solid solutions for new piezoelectrics, that are able to outperform the PZT all-round talent.

3.2.1 Flat Energy Surfaces

The enhanced electromechanical response can be understood within the concept of flat energy surfaces. It was introduced by Fu and Cohen, in order to explain the enhancement of piezoelectric response at electric field-induced phase transitions in single crystals.[36] Using *ab initio* calculations they showed how large piezoelectric response in $BaTiO_3$ can be driven by polarization rotation induced by an external electric field. The electric field can induce a phase transition from rhombohedral *R*3*m* to tetragonal *P*4*mm*, which is accompanied by a large change of strain.[36] Budimir *et al.*[37] applied Landau-Ginzburg-Devonshire theory to several perovskite materials and demonstrated the universal applicability of this idea.
The free energy surface can be flattened by temperature or composition variation, but also by application of hydrostatic pressure or electric field bias. Under these conditions piezoelectric properties can be enhanced.[37,38] Rossetti applied Landau theory to PZT and found a ferroelectric glass state at the MPB-composition, in which the anisotropy of polarization vanishes and a so-called adaptive nanodomain state results.[39,40] Electric or stress fields induce a reconfiguration of these adaptive nanodomains which results in a softening of piezoelectric, dielectric and elastic properties near the MPB.
Damjanovic demonstrated that polarization rotation is not the only mechanism that leads to large enhancement of the piezoelectric response, a second mechanism is polarization contraction and extension.[41]

Researchers have been looking for design rules for ferroelectric MPB materials since a long time. The first guide lines originated from empirical models and were applicable to $PbTiO_3$-based solid solutions only. Relationships between the tolerance factor t of the non-$PbTiO_3$ end member and the Curie temperature T_C of the solid solution at the MPB-composition[42] or the mole fraction of $PbTiO_3$ at the MPB[43] were established. Grinberg *et al.* complemented the empirical models with data from *ab-initio* calculations in order to predict Curie temperatures and MPB-compositions in $PbTiO_3$-based solid solutions more accurately.[44]
More general insights beyond the tolerance factor into phase stabilities and how they originate from A-O interaction and preferred cation displacements were given by Woodword.[45]

The flat energy surface concept was applied also to *ab-initio* calculations of solid solutions. Ghita *et al.* found that $Pb(Zr_{0.50}Ti_{0.50})O_3$ exhibits an energy degeneracy of tetragonal and rhombohedral distorted structures.[46] The authors suggested in addition that morphotropic phase boundaries can be found between A-site and B-site driven ferroelectrics.
Indeed, in a recent *ab-initio* study members of our group demonstrated that the morphotropic phase boundary in the lead-free $(Na_{1/2}Bi_{1/2}TiO_3)_{(1-x)}$-$(BaTiO_3)_x$ solid solution coincides with the composition region where both A- and B-cations are equally active.[47] Pure $Na_{1/2}Bi_{1/2}TiO_3$ is mainly A-site active (with small contributions from the B-site through inter-sublattice cooperation), while pure $BaTiO_3$ is solely B-active.

3.2.2 Effect of Hydrostatic Pressure

Samara demonstrated in 1975 that hydrostatic pressure reduces, and even annihilates ferroelectricity for high enough values in fluoride $A^{+I}B^{+II}F_3$ and oxide $A^{+II}B^{+IV}O_3$ perovskites.[48] This can be understood by a simple theory based on the assumption that short-range repulsion increase more rapidly than long-range attraction as pressure increases, leading to the reduction of ferroelectricity. The effect of pressure on antiferrodistortive instabilities like oxygen octahedral tilting is contrary. Antiferrodistortion is dominated by short-range forces and increases with increasing pressure. *Ab initio* calculations on $BaTiO_3$, $PbTiO_3$ and $PbZrO_3$ confirmed this model.[49] The increase of pressure leads to octahedral tilting and reduction of ferroelectric distortions.
This general rule was revised only few years ago as perovskites with A- and B-cations both having a charge of +3 showed phase transitions to cubic phases accompanied by loss of octahedral tilting under pressure.[50] The decisive parameter is the ratio of the compressibilities of the two types of polyhedra present in the perovskite structure, the cuboctahedron AO_{12} and the octahedron BO_6. In $LaAlO_3$, for example, it is easier to compress the octahedron (by reducing B–O bond length) than to reduce the size of the cuboctahedron (by tilting). Thus, under pressure tilting vanishes, while the B–O bond lengths are reduced considerably. In case of perovskites with the A-cations having a lower charge than the B-cations and in halogenides, the opposite is the case and the cuboctahedron AO_{12} is easier to compress leading to tilted high-pressure phases as observed by Samara before.[48]

3.2.3 The Idea of Chemical Pressure

From *ab-initio* calculations of pure $PbTiO_3$ a pressure-induced sequence of phase transitions $P4mm \rightleftharpoons Cm \rightleftharpoons R3m \rightleftharpoons Pm\bar{3}m$ with enhancement of piezoelectricity was first proposed by Wu and Cohen[51] and later modified by including tilted phases $R3c$ and $R\bar{3}c$ at high pressures by other authors[52,53]. High pressure experiments at 10 K confirmed, that hydrostatic pressure can induce a morphotropic-like phase sequence $P4mm \rightleftharpoons M_C \rightleftharpoons M_C \rightleftharpoons R\bar{3}c$ in pure $PbTiO_3$.[54] The authors proposed that alloying $PbTiO_3$ with other perovskites simply shifts the intrinsic transitions of pure $PbTiO_3$ to ambient pressure, and thus suggested that morphotropic phase boundaries can be understood from the idea of chemical pressure. The idea of chemical pressure can also be found

in Ref. 55 based on the observation that in the perovskite $(Na_{1/2}Bi_{1/2}TiO_3)_{0.89}$-$(BaTiO_3)_{0.11}$ the pressure-induced phase transitions occurring in the pure perovskite compound $Na_{1/2}Bi_{1/2}TiO_3$, are shifted to higher pressures, corresponding to a negative (tensile) pressure induced by Ba^{2+}. The authors proposed that the introduction of 11 mole% $BaTiO_3$ leads to a "chemical pressure" of $\Delta P = -2.5$ GPa.[55]

4 Relaxor Ferroelectrics

4.1 Properties of Relaxors

Relaxor-based materials possess giant piezoelectric constants, which make them technologically interesting for actuator and ultrasonic transducer applications.[56,57] Moreover, they show a strong frequency-dependent dielectric susceptibility, which exhibits a broad dielectric maximum around T_m, these features are generally referred to as "relaxor behaviour".[58–60] At the temperature of dielectric maximum T_m no macroscopic phase transition can be observed. Relaxors are generally described as two component systems, for example as consisting of a glassy matrix and polar nanoregions, which form below the Burns temperature T_B. Relaxor behaviour is only observed in mixed perovskites and is suppressed by chemical order.[61] It is assumed that chemical disorder induces local random fields which are responsible for the existence of polar nanoregions (PNRs). The presence of these polar nanoregions and correlations among them are believed to be the origin of relaxor behaviour

The giant responses to relatively weak excitations are attributed to proximity effects, which are also responsible for colossal magnetoresistance and high-temperature superconductivity.[62,63] An important similarity of all these materials is the competition between several ordered states on the nanoscale resulting from the presence of compositional disorder, which gives rise to random fields. In relaxors, the relative stability of those ordered states can be easily shifted by weak disturbances such as mechanical stress or electric field leading to the observed strong responses.[36,56,64]

Various materials can be assigned relaxors. There is a smaller group of uniaxial relaxors reported with tetragonal tungsten bronze structures like $Sr_xBa_{1-x}Nb_2O_6$ (SBN),[65] while most relaxors belong to the big family of mixed perovskites. Prominent examples are the lead-containing relaxors $PbMg_{1/3}Nb_{2/3}O_3$ (PMN), $PbZn_{1/3}Nb_{2/3}O_3$ (PZN) or $PbSc_{1/2}Nb_{1/2}O_3$ (PSN). In contrast to PZT, these materials are all compounds with a fixed stoichiometry, not solid solutions with arbitrary compositions. In recent years also numerous lead-free relaxors have been discovered,[66] examples are $Na_{1/2}Bi_{1/2}TiO_3$[13,14,67] (NBT) or $BaZr_xTi_{(1-x)}O_3$[68–72] (BZT). The latter material demonstrates, that by no means charge disorder on the perovskite B-site is necessary for relaxor behaviour to develop, as Zr^{4+} and Ti^{4+} in $BaZr_xTi_{(1-x)}O_3$ have identical charges, but differ significantly in size and bonding properties, only.

Two classes of relaxors are distinguished.[59] Depending on whether they develop at low temperatures a long-range ferroelectric phase or not, they are named canonical relaxors or relaxor ferroelectrics, respectively. Moreover, there exist two different types of relaxor states at elevated temperatures, these are the ergodic and the nonergodic relaxor state. At high temperatures all relaxor materials adopt a paraelectric prototypic structure. Then below a critical temperature named Burns temperature the ergodic state develops. At lower temperatures canonical relaxors enter a nonergodic state below the so-called freezing temperature, while in relaxor ferroelectrics a fer-

roelectric state occurs below the Curie temperature. In the following, the transition temperatures will be introduced in more detail.

4.1.1 Characteristic Temperatures in Relaxors

Burns Temperature T_B

If a relaxor material is cooled down from the paraelectric state, at the Burns temperature nucleation of polar nanoregions can be observed. Burns himself referred to this characteristic temperature as depolarization temperature T_d.[73] The nucleation process is not accompanied by a macroscopic phase transformation. The average crystal structure stays unchanged below T_B, modifications occur only on the nanoscale. Polar nanoregions can be understood as large dipoles resulting from cooperative off-centring of cations in neighbouring unit cells. They are very mobile and can vary in size and orientation. This state of dynamic, spatially and temporally fluctuating polar nanoregions characterizes the ergodic relaxor state. Ergodicity means, that the state of a system is independent of its history. Even after application of an electric field or other perturbations, the system finds a path back to its ground state.
T_B can be determined from anomalies in the temperature dependence of the refractive index,[73] deviations of the dielectric constant from Curie-Weiss law[74] or deviations from the linear temperature dependence of the lattice parameter[58] or of the thermal expansion,[75] or from anomalies in the specific heat.[76] Other indicators are arising diffuse scattering[77,78] or acoustic emissions.[79] It exists even the possibility of a direct observation of PNRs by transmission electron microscopy (TEM).[80]

Intermediate Temperature T^*

The intermediate temperature T^* was introduced first as a local Curie temperature in PMN by Viehland,[74] later it was reinvestigated by Toulouse and Dkhil in more lead-based relaxors.[81,82] Dkhil *et al.* could demonstrate that T^* equals 500 ± 30 K in all investigated lead-based relaxor materials independent of the B-cations. This observation leads to the conclusion that T^* is related to the polar shifts of Pb^{2+}, which become correlated (or static) along $\langle 001 \rangle$-directions if $T < T^*$, while they are uncorrelated (or dynamic) with a spherical off-centre distribution above T^*, which was in agreement with results from effective Hamiltonian Monte-Carlo simulations of $PbSc_{1/2}Nb_{1/2}O_3$.[82] T^* can be measured by acoustic emission or can be identified from characteristic kinks in the temperature dependence of the lattice parameter.[79,82]

Temperature of Maximum Permittivity T_m

One of the features of relaxor materials is their broad temperature and frequency dependent maximum of dielectric permittivity $\varepsilon(T, f)$. The temperatures of the maxima are called $T_\mathrm{m}(f)$. At these temperatures no macroscopic phase transitions can be observed. The broad frequency distribution

of dielectric response is related to a broad distribution of activation energies below T^*. The characteristic relaxation times are found to obey the Vogel-Fulcher law, which generally describes the slowing down of relaxation processes associated with glasses[83]

$$\tau = \tau_0 \exp\left[\frac{U}{k_B(T - T_f)}\right] \tag{4.1}$$

with the inverse attempt frequency τ_0, the activation energy U and the freezing temperature T_f, at which τ diverges. However, the structure of relaxors is more complex than the one of ordinary glasses and the polarization mechanisms behind the broad peak in $\varepsilon(T, f)$ have not been identified yet.[59]

Below $T_\mathrm{m}(f)$ the relaxation becomes extremely slow. This can be understood as follows. With decreasing temperature the PNRs will grow in size and correlations between them will be enhanced. At some point, they will start to merge leading to larger polarization clusters and finally a percolating network will develop. The larger the clusters become, the slower becomes their ability to vary their polarization directions. As soon as the percolation limit is reached, the reorientation will be suppressed completely.[84]

Freezing Temperature T_f and Curie Temperature T_C

The Vogel-Fulcher freezing temperature T_VF or simply freezing temperature T_f in canonical relaxors shares some analogies with the Curie temperature T_C in ordinary and relaxor ferroelectrics. As the name implies, at the freezing temperature the dynamics of the PNRs freeze in, the PNRs become static. The ergodic relaxor state transforms into a nonergodic relaxor state. A macroscopic phase transition is still missing, the average structure is still identical to the one of the paraelectric prototypic phase. Upon cooling in large enough electric fields, however, a transformation into a ferroelectric state can be induced, which is irreversible due to the nonergodicity of the system below T_f. It was found that some PNR still persist even in the induced ferroelectric state.[85] The nonergodic relaxor state can only be reached again by heating above T_B.[60]

Relaxor ferroelectrics in contrast show more or less diffuse relaxor-to-ferroelectric phase transitions at T_C spontaneously, without application of an electric field. In these materials a macroscopic phase transformation into a polar structure occurs. Many relaxor ferroelectrics, though, show strong structural disorder below T_C.[59]

4.1.2 Effect of Hydrostatic Pressure

Pressure can suppress the formation of the ferroelectric phase upon field cooling in canonical relaxors or below T_C in relaxor ferroelectrics.[60,86] As pressure in general reduces the stability of polar distortion modes,[48] under pressure the local random fields become dominating and favour the relaxor state. This view was confirmed by molecular dynamics simulations using first-principles Hamiltonians of $PbSc_{1/2}Nb_{1/2}O_3$.[87]

4.1.3 Role of Chemically Ordered Nanoregions

It is still a matter of debate, whether chemically ordered and polar nanoregions are correlated or not. As a source of characteristic local electric fields chemically ordered nanoregions (CNRs) have to be considered as one of the influencing factors in the nucleation and growth of polar nanoregions, but it is not clear how important their role is. On the other hand it is for sure that long-range chemical order suppresses relaxor properties, as thermally annealed ordered $PbSc_{1/2}Ta_{1/2}O_3$ (PST) behaves like a normal ferroelectric, while disordered $PbSc_{1/2}Ta_{1/2}O_3$ is a canonical relaxor.[61] For Sc-doped $PbMg_{1/3}Nb_{2/3}O_3$ with enhanced cation order it was shown by in situ TEM that chemically ordered regions are rather spectators than actors in the field-induced relaxor-to-ferroelectric transition. Inhomogeneous stress effects seem to play a more important role in this material, as the phase transformations started in the grain boundaries.[88] Somewhat contrary conclusions were drawn from molecular dynamics simulations based on a first-principles Hamiltonian of $PbSc_{1/2}Nb_{1/2}O_3$ in a $40 \times 40 \times 40$ supercell by Burton *et al.*[89] The authors reported on enhanced polarization and susceptibilities in chemically ordered regions in contrast to the chemically disordered matrix. Moreover, strongest correlation is found for the interactions between chemically ordered regions. Their results imply "that the characteristic length scale for polar nanoregions is the same as for chemical short-range order."[89] The simulations, however, suffer from the relatively small size of the simulation box, which has hardly the length of six times the diameter of a typical PNR.

4.1.4 Models and Theory

Although it is quite commonly accepted that polar nanoregions exist and that their existence is related to compositional disorder, it is neither clear how they look like nor why they form.[59,90]
Two contradicting views exist on the nanoscale structure of the ergodic relaxor state. The first concept is the random field scenario, which is in favour of a state of low-symmetry nanodomains separated by domain walls.[91] The second one is the spherical dipolar glass model, which explains the relaxor state arising from the existence of ellipsoid shaped polar nanoregions, which are embedded into a cubic nonpolar matrix.[92]
The random field scenario can be theoretically described by the random field Ising model (RFIM) of Westphal, Kleemann and Glinchuk,[91] which is based on the work of Imry and Ma.[93] If a system possesses an order parameter of continuous symmetry, a macroscopic disorder-order transition can be destroyed by quenched random local fields in favour of a nanodomain state. This model is quite successful to describe the properties of uniaxial relaxors like SBN.[94]
The dipolar glass scenario can be described by the spherical random-bond-random field model (SRBRF) of Pirc and Blinc.[92] This model predicts two phases in zero field, a dipolar glass state and a long-range ferroelectric state, depending on the strength of the random fields. The dipolar glass state can, however, be transformed into the long-range ferroelectric state by applying a sufficiently strong electric field. Experimental results for perovskites seem to be more in favour of the latter model, like a recent high-resolution calorimetric study of $PbMg_{1/3}Nb_{2/3}O_3$.[92,95]

4.2 Chemical Ordering in Perovskites

As chemical order/disorder is regarded as one of the key factors for the development of relaxor properties in mixed perovskites, we want to give a brief overview about chemical ordering in perovskites.
For B-site mixed perovskites chemical ordering is generally understood.[96] Order, commonly rock-salt (111)-order, occurs when the charge difference between the cation species occupying the same crystallographic site is $\Delta q > 2$, while for charge differences $\Delta q < 2$ disorder is found. For $\Delta q = 2$ disordered, partially ordered and fully ordered examples can be found depending on size and/or bonding preferences of the different cations. In contrast, A-site ordering is much less common. There exist only a few examples where A-site order was experimentally found. Knapp and Woodward reported on (001)-order for $(Na_{1/2}La_{1/2})(Mg_{1/2}W_{1/2})O_3$ driven by cooperative effects of both A-site and B-site ordering.[97] More examples can be found in a review recently published by King and Woodward.[98] They show that A-site order commonly occurs in $\{001\}$-layers, but that charge differences between the cations of $\Delta q = 2$ are not sufficient to cause ordering. Systematic oxygen vacancies, vacancies in the A-sublattice or B-site ordering are necessary to stabilize chemical A-site order in mixed perovskites.

4.3 Model-Relaxor Ferroelectric $Na_{1/2}Bi_{1/2}TiO_3$

$Na_{1/2}Bi_{1/2}TiO_3$ (NBT) is a model relaxor ferroelectric with two different cations (Na^+ and Bi^{3+}) on the A-site of the perovskite structure. The usual lead-containing relaxors $PbMg_{1/3}Nb_{2/3}O_3$ (PMN), $PbZn_{1/3}Nb_{2/3}O_3$ (PZN) or $PbSc_{1/2}Nb_{1/2}O_3$ (PSN), in contrast, are mixed on the B-site. Similarly to $PbMg_{1/3}Nb_{2/3}O_3$ (PMN), $PbZn_{1/3}Nb_{2/3}O_3$ (PZN) or $PbSc_{1/2}Nb_{1/2}O_3$ (PSN), both relaxor ingredients i.e. off-centreing (Bi^{3+} in NBT and Pb^{2+} in lead-based relaxors) and random cation distribution on the mixed site, are present in $Na_{1/2}Bi_{1/2}TiO_3$.
NBT-based materials exhibit extraordinarily high strains and are amongst the most promising candidates for substituting the toxic PZT in piezoelectric applications. Especially, recent results on $(Na_{1/2}Bi_{1/2}TiO_3)_{(1-x-y)}$-$(BaTiO_3)_x$-$(K_{0.5}Na_{0.5}NbO_3)_y$ (NBT-BT-KNN) solid solutions revealed promising piezoelectric properties.[6,99,100]

NBT displays a complex phase sequence depending on temperature, it shows typical relaxor features (nanoscale local structure and dielectric dispersion) between 200°C and 320°C and is ferroelectric at lower temperatures.[13–16]

Pure NBT is known since a long time, it was discovered by Smolenskii in 1956,[101,102] but understanding of this material is still not conclusive, especially when it comes to the discrepancies between local and average structure and the related relaxor properties. Moreover, average and local crystal structures, as well as physical properties crucially depend on the thermal, mechanical and poling history of the samples.[103–107]

4.3.1 Average Crystal Structure

XRD diffraction studies demonstrated that above 540°C NBT is in its cubic perovskite parent phase (space group $Pm\overline{3}m$).[13] On cooling two reversible phase transformations are observed. Between 500 and 540°C a tetragonal structure with space group symmetry $P4bm$ is formed with in-phase $a^\circ a^\circ c^+$ octahedral tilting (in Glazer notation[108]) and anti-parallel displacements of A- and B-cations along [001]. The tetragonal distortion is rather small (0.14%).[14,67] Other authors refined the tetragonal phase above 400°C in the centrosymmetric space group $P4/mbm$ based on electron diffraction experiments.[109,110]
Between 250 and 400°C the second transformation into a rhombohedral $R3c$ structure takes place, which is characterized by anti-phase $a^-a^-a^-$ octahedral tilting and polar cation displacements along the [111]-direction of the pseudo-cubic cell with $\alpha = 89.83°$.[14] Recently, a peculiarity of this phase transformation was reported. At about 300°C optical birefringence microscopy revealed an isotropization point, which corresponds structurally to an "untilted cubic structure" as a high-resolution X-ray powder diffraction study indicated.[107,111] Tetragonality is maximum at about 400°C and reduces to zero on both cooling and heating.
Regarding the low temperature rhombohedral phase, data from high-resolution single-crystal X-ray diffraction revealed monoclinic-like deviations from $R3c$ symmetry.[112] Similar local deviations from the average structure were already found in an earlier work of Thomas *et al.*[113] In the meantime also for ceramics a monoclinic phase with Cc symmetry was reported.[114] An ex-situ diffraction study showed that poled samples rather have $R3c$ symmetry, while unpoled samples are better described in monoclinic Cc.[104] The idea of average Cc symmetry becomes more and more accepted, though it probably rather reflects the importance of local deviations from the average $R3c$ symmetry than a "real" monoclinic phase.

4.3.2 Local Structure

In order to obtain information about the local structure in perovskites a wide variety of local probe techniques was applied successfully on different ferroelectrics, namely total scattering experiments (pair distribution function analysis (PDF)[115] or diffuse scattering[116]) and x-ray absorption spectroscopy (XAFS), electron spin resonance and nuclear magnetic resonance (ESR/NMR) or optical and Raman spectroscopy.[117] NMR and Raman spectroscopy are reliable fingerprint methods, which can be used to identify phase transformations, but they cannot provide conclusive information about the local structure of NBT.[118–122] ESR is only applicable to doped NBT, as it requires ions with unpaired electrons. Thus, in doped systems ESR provides information about the local environment of the point defects induced upon doping, but not about the local structure in general.[105,123,124] Optical spectroscopy suffers from a similar problem, since transition metals with high sensitivity of their optical transitions to the crystal field environment are not present in NBT.
Diffuse scattering of electrons,[103,109,110,125] X-rays,[106,126,127] PDF analysis[128] and XAFS[129] were successfully applied to pure NBT or its solid solutions $(NBT)_{(1-x)}$-$(BaTiO_3)_x$ (NBT-xBT) or $(NBT)_{(1-x)}$-$(K_{1/2}Bi_{1/2}TiO_3)_x$ (NBT-xKBT).

One of the puzzling findings for NBT is a diffuse phase transition observed in dielectric measurements at temperatures between 200 and 320°C,[16,99,130] which does not correlate with any macroscopic structural phase transition - a typical feature of a relaxor transition.
TEM and diffuse electron diffraction scattering revealed at temperatures between 280 and 320°C an additional intermediate orthorhombic phase with *Pbnm* symmetry and $a^-a^-c^+$ octahedral tilting bridging the rhombohedral and tetragonal phase.[109,110] Already at 200°C *Pbnm*-modulation of the *R*3*c* phase starts, which can be understood as formation of tilt twin-planes (stacking faults) with *Pbnm* symmetry within the *R*3*c*-host. The phase transition from *Pbnm* to *P*4*/mbm* then occurs between 320 and 370°C.[109,110] Guo *et al.* reported similar findings for the solid solution $(NBT)_{(1-x)}$-$(BaTiO_3)_x$ in the composition range $0.04 < x < 0.08$.[131] They found the same disorder of octahedral tilt twinning along $\langle 001 \rangle$-directions, which could be increased and even observed at room temperature by adding $BaTiO_3$. These twin boundaries lead to a different environment for the A-cations and to local off-centre displacements distinct from the rhombohedral matrix, which gives rise to a local antiferroelectric-like behaviour. Guo *et al.* regard compositional modulation as the origin of the tilt disorder as it can be increased by Bi-excess and/or Na-deficiency.[125] Moreover, X-ray diffuse scattering in single crystals with composition $(NBT)_{0.96}$-$(BaTiO_3)_{0.04}$ indicated tilt disorder present in this NBT-based solid solution. In the *R*3*c* phase streaking of the superstructure reflections characteristic of the anti-phase tilts is observed, which is indicative of planar defects in the stacking of tilts as it would result from accidental in-phase tilting. These streaks disappear after application of an electric field of 4.3 kV/mm, but reappear if the sample is heated above 400°C.[106]
Similar conclusions were drawn from earlier X-ray diffuse scattering experiments. Kreisel *et al.*[126] suggested that zones with chemical short-range order lead to segregation planes with correlated cation displacements along $\langle 001 \rangle$ (comparable to Guinier-Preston-Zones in metal alloys) resulting in sharp L-shape asymmetric streak patterns in the diffuse scattering, while a second much broader streak pattern was assigned to chemical short-range order. In addition to these streaks, Thomas *et al.*[127] could identify satellite reflections in reciprocal space maps which are thought to have their origin in a modulated domain structure with modulation length of about 40 Å (about ten unit cells).
Structural polar disorder of the Bi-sites is assumed by Shuvaeva *et al.* for explaining XAFS results,[129] where statistically disordered Bi-displacements off the [111]-direction lead to few short Bi–O bonds of 2.22 Å. However, this short bond length never appeared in average crystal structures deduced from diffraction methods implying that strong local disorder exists in NBT due to the mixed A-site.
Reverse Monte Carlo simulations of PDFs obtained at different temperatures showed the evolution of separate off-centre displacements of Bi and Na, which revealed the coexistence of two very different Bi displacements already at room temperature.[132] All A-cation displacements lie in the monoclinic plane between [111] and [001]. Only at very low temperatures (-263°C) displacements of both Na and Bi are ordered and directed towards [111] direction, as well as in the tetragonal phase at 493°C, where ordering occurs along [001].

A TEM study just published few months ago investigated the local structure of NBT, taking several types of order/disorder on different length scales into consideration.[103] The authors conclude

that there exists significant disorder of the octahedral rotations and cation displacements, manifested in rods and sheets of diffuse electron scattering, respectively. They propose a single-phase "continuous tilting" model with mesoscale antiphase domains and nanoscale twin domains, which exhibit $a^-a^-c^+$ tilts with a very short coherence length of few unit cells. On average the crystal structure is supposed to look as if it had $a^-a^-c^-$ tilts, which is consistent with space group *Cc*.

4.3.3 Evidence for Chemical Order

Many authors reported on chemical order in NBT. Park suggested a low degree of Bi/Na-order in NBT with a face-centred structure (space group $Fm\bar{3}m$) for the high-temperature cubic phase based on single-crystal XRD measurements.[133] Dorcet and Trolliard proposed the same type of order based on TEM images and electron diffraction. According to them ordering occurs in nanometre sized domains embedded in a disordered matrix.[110] Rock-salt type order was also deduced from Raman spectra, which indicated an additional strong lattice disorder.[134] Chemical short range order emerging as segregation planes with correlated cation displacements along $\langle 001 \rangle$ (comparable to Guinier-Preston-Zones in metal alloys) leading to asymmetric streak patterns in diffuse scattering were suggested by Kreisel *et al.*[126] Despite these few reports on chemical order in NBT,[110,133,134] it is generally assumed to be disordered on the mixed A-site.[14,113,114] The TEM study of Levin and Reaney showed no indications for chemical order, as the typical $1/2\{eeo\}$ superstructure reflections were missing and high angle annular dark field (HAADF) scanning transmission electron microscopy (STEM) images revealed "no obvious nanoscale Bi/Na order".[103] An earlier *ab-initio* study by Burton *et al.* treating effects of chemical order in NBT by a cluster expansion method reported on a monoclinic Pm phase within a 40-atom supercell with criss-cross rows of Bi and Na perpendicular to [001] and octahedral tilting $a^-a^-c^+$.[135]

4.3.4 High-Pressure Phases

The high-pressure phases of NBT have also been investigated by several methods, like neutron and synchrotron X-ray powder diffraction,[113] X-ray diffuse scattering (XRDS)[126] and Raman spectroscopy.[55,122,136] It was found that the rhombohedral phase (*R*3*c*) present at ambient pressure transforms into a lower-symmetry structure which can be described by space group *Pbnm*. This phase shows $a^-a^-c^+$ octahedral tilts and anti-parallel displacements of the A-cations along pseudo-cubic $\langle 001 \rangle$-directions, which is assumed to lead to antiferroelectric behaviour. Since space group *Pbnm* is not a subgroup of *R*3*c*, there should either exist one or more intermediate phases or a pressure range of coexistence. The latter was reported by Thomas *et al.* between 2.0 and 3.3 GPa.[113] Kreisel *et al.* suggested a two step mechanism for the phase transition based on their Raman study, where the phase transition occurred between 2.7 GPa and 5.0 GPa.[122] At the lower critical pressure A-cation displacements reorient from parallel along [111] to anti-parallel along [100]/[$\bar{1}$00]-directions and B-cations return from displacing along the [111]-direction back to their ideal positions, whereas at the higher critical pressure the octahedral tilts change from pure anti-phase $a^-a^-a^-$ to mixed in- and anti-phase $a^-a^-c^+$. Both states are described as antiferro-

electric although no dielectric measurements under pressure have been performed to date. Kreisel *et al.* also studied the local structure of NBT by X-ray diffuse scattering at high-pressure.[126] The phase transition rhombohedral-orthorhombic of the average structure in this case occurred between 1.6 GPa and 2.0 GPa. In their study a second phase transition to a tetragonal phase was found between 9.9 and 11.1 GPa. In the diffuse scattering the two features described above respond differently to pressure. The characteristic sharp L-shape diffuse streaks lose intensity at 2.8 GPa and vanish at 3.7 GPa, while the broad pattern indicative for chemical short-range order is not affected by pressure at all. The loss of the XRDS L-shape fingerprint is consistent with a model where the planar defects and the matrix adopt the same local structure at high-pressure.

4.4 $Na_{1/2}Bi_{1/2}TiO_3$-Based Solid Solutions

4.4.1 $(Na_{1/2}Bi_{1/2}TiO_3)_{(1-x)}$-$(CaTiO_3)_x$

The crystal structures within the solid solution system $(Na_{1/2}Bi_{1/2}TiO_3)_{(1-x)}$-$(CaTiO_3)_x$ were investigated by Ranjan *et al.*[137,138] The authors reported on phase coexistence for $0.05 < x < 0.15$ of rhombohedral *R*3*c* and orthorhombic *Pbnm* structures, the latter is identical with the crystal structure of pure $CaTiO_3$[139] and the high-pressure phase of pure NBT.[126] Watanabe *et al.*[140] analysed electrical properties and phase transition temperatures of these materials for $x \leq 0.08$. On increasing $CaTiO_3$-content the piezoelectric constant has a small maximum at $x = 0.02$ ($d_{33} = 75$ pC/N).

4.4.2 $(Na_{1/2}Bi_{1/2}TiO_3)_{(1-x)}$-$(BaTiO_3)_x$

The $(Na_{1/2}Bi_{1/2}TiO_3)_{(1-x)}$-$(BaTiO_3)_x$ solid solution ceramics are among the most promising candidates for substituting PZT in actuator applications as they show extraordinarily high strains.[6] The phase diagram shows an MPB-region at $0.06 \leq x \leq 0.11$ between rhombohedral *R*3*c* and tetragonal *P*4*mm* structures. The crystal structure within this MPB-region, however, is still a matter of debate.[141–143] Electric fields can easily induce phase transformations[130,143,144] and even shift or "create" morphotropic phase boundaries.[145] Within the MPB-region piezoelectric coefficients are enhanced up to $d_{33} = 170$ pC/N at $x = 0.07$.[143]

4.4.3 $(Na_{1/2}Bi_{1/2}TiO_3)_{(1-x)}$-$(Li_{1/2}Bi_{1/2}TiO_3)_x$

The pure end member $Li_{1/2}Bi_{1/2}TiO_3$ is not stable at atmospheric pressure but the solid solution $(Na_{1/2}Bi_{1/2}TiO_3)_{(1-x)}$-$(Li_{1/2}Bi_{1/2}TiO_3)_x$ can be synthesized up to $Li_{1/2}Bi_{1/2}TiO_3$-contents of $x \leq 0.24$. The substitution of Na^+ by the much smaller Li^+ leads to a maximum in the piezoelectric constant of $d_{33} = 108$ pC/N at $x = 0.16$. No change of the crystal structure was found, all solid solution materials remained in the rhombohedral space group *R*3*c*, as it is found for pure NBT.[146]

4.4.4 $(Na_{1/2}Bi_{1/2}TiO_3)_{(1-x)}$-$(K_{1/2}Bi_{1/2}TiO_3)_x$

Also $(Na_{1/2}Bi_{1/2}TiO_3)_{(1-x)}$-$(K_{1/2}Bi_{1/2}TiO_3)_x$ solid solutions are very promising candidates for PZT substitution.[6] Moreover, the debate on structure evolution in the solid solution bears some similarities with $(Na_{1/2}Bi_{1/2}TiO_3)_{(1-x)}$-$(BaTiO_3)_x$.
The crystal structures of single crystals within the $(Na_{1/2}Bi_{1/2}TiO_3)_{(1-x)}$-$(K_{1/2}Bi_{1/2}TiO_3)_x$ solid solution were investigated intensively by neutron powder diffraction by Jones *et al.*[147] The authors proposed a phase sequence *R*3*c*⇌*R*3*m*⇌*P*4*mm*. The first phase transition *R*3*c*⇌*R*3*m* (loss of tilts) takes place at $0.4 \leq x \leq 0.5$ and the second phase transition *R*3*cm*⇌*P*4*mm* takes place at $0.6 \leq x \leq 0.8$ (both transitions at room temperature). Similarly, an intermediate phase located at $0.5 \leq x \leq 0.8$ was proposed by Kreisel *et al.* based on Raman spectroscopy and X-ray diffraction experiments of single crystals.[121] Polycrystalline materials behave a bit different, they exhibit, in contrast, an MPB-region at much lower $K_{1/2}Bi_{1/2}TiO_3$-contents of $0.16 \leq x \leq 0.20$ between the rhombohedral *R*3*c* and tetragonal *P*4*mm* structure.[128,148] The piezoelectric constant has a maximum value of $d_{33} = 168$ pC/N at $x = 0.20$.[149] As in the $(NBT)_{(1-x)}$-$(BaTiO_3)_x$ solid solution, within the MPB-region at $x = 0.20$ electric field-induced phase transitions from *R*3*c* to *P*4*mm* were reported.[150]

5 13 Specific Questions to be Answered in this Work

Here is a collection of 13 basic questions, which we will try to answer in this work. The questions and their answers will be found at the beginning of Part IV.

1. Is there any type of chemical order preferred in $Na_{1/2}Bi_{1/2}TiO_3$?
2. What are the driving forces for ordering?
3. Can ordering occur under synthesis conditions?
4. Is it possible to enhance chemical ordering at elevated temperatures?
5. How does chemical order affect the average and local crystal structure?
6. Which phases are stable under hydrostatic pressure?
7. Can in-phase tilts be stable in an anti-phase tilted matrix?
8. How do chemical order and pressure affect the different lattice instabilities polarization, octahedral tilting and chemically induced distortions?
9. How strongly are the different lattice instabilities coupled to each other?
10. What are the ferroic properties of the phases *R*3*c*, *Pbnm* and *P*4*bm*?
11. Is it possible to predict morphotropic phase boundaries in $Na_{1/2}Bi_{1/2}TiO_3$-based solid solutions based on determination of pressure-induced phase transformations?
12. What are the limitations of such a technique?
13. Can alloying be understood as an analogue to hydrostatic pressure, is chemical pressure something real and quantifiable?

Part II

Methods

6 *Ab-initio* Calculations

Ab-initio calculations are based on quantum mechanics and allow to investigate the electronic state of many-body systems such as atoms, molecules or condensed matter without using any parameters from experiments. In chemistry both Hartree-Fock (HF) and Density Functional Theory (DFT) calculations are used equally often, while in physics and materials science Density Functional Theory is the more common technique. Nowadays, new methods like GW quasiparticle theory[151] or Time-Dependent Density Functional Theory (TDDFT)[152] allow even the investigation of excited states. In the last twenty years the availability of parallel computing on large clusters pushed the development of algorithms for the prediction of the energy and electronic structure of systems including up to several hundreds or thousands of atoms. Moreover, the increase of computing capacity allows to study complex solid state configurations including defects, thin films and nanostructures.
In this chapter a brief introduction into the basics of Density Functional Theory is given. DFT calculations allow the determination of phase stabilities by comparing total energies of different phases, structure optimizations and the investigation of charge densities, electronic band structures or densities of states.

6.1 Density Functional Theory

Density Functional Theory (DFT) is used to solve the time-independent Schrödinger equation for a many-body system containing electrons and nuclei[153]

$$E\Psi = \hat{H}\Psi \tag{6.1}$$

with the Hamilton operator

$$\begin{aligned}\hat{H} &= -\frac{\hbar^2}{2m_e}\sum_i \nabla_i^2 + \frac{1}{2}\sum_{i\neq j}\frac{e^2}{|\mathbf{r}_i-\mathbf{r}_j|} \\ &- \sum_I \frac{\hbar^2}{2M_I}\nabla_I^2 + \frac{1}{2}\sum_{I\neq J}\frac{Z_I Z_J e^2}{|\mathbf{R}_I-\mathbf{R}_J|} \\ &- \sum_{i,I}\frac{Z_I e^2}{|\mathbf{r}_i-\mathbf{R}_I|},\end{aligned} \tag{6.2}$$

where m_e is the electron mass and $\mathbf{r}_i$ the position of the ith electron, M_I, Z_i and $\mathbf{R}_I$ are the mass, charge and position of the Ith nucleus and $\hbar$ is the reduced Planck constant. The first and second terms give the kinetic energy of the electron system and the energy resulting from the interactions between different electrons, respectively, the third and fourth terms specify the kinetic energy of the nucleus system and the interaction energies between different nuclei. The last term specifies

the energy resulting from the interactions between electrons and nuclei. This differential equation is practically unsolvable due the dependence of the total wave function $\Psi(\mathbf{r_1}, \mathbf{r_2}, ..., \mathbf{R_1}, \mathbf{R_2}, ...)$ on $3N$ spatial variables ($N = i_{\text{tot}} + I_{\text{tot}}$). Therefore several approximations were made to reduce the complexity of the problem.
The most fundamental one is the Born Oppenheimer approximation.[154] It states that the movements of the electrons is decoupled from the nuclei. Thus the problem can be split into two. With the nuclei frozen in fixed positions, the second line of Eq. 6.3 can be skipped and the electron-nuclei interactions are reduced to the movement of mobile electrons in a static external potential. The nuclei movements can be solved separately then.
Two self consistent calculation cycles can be distinguished: The (inner) electronic cycle, where the charge density is calculated, and the (outer) ionic cycle, where the nuclei are displaced.

6.1.1 Hohenberg-Kohn Theorems

Hohenberg and Kohn[155] formulated DFT as an exact theory of multiple objects (here the electrons) in an external potential (here the Coulomb potential of the nuclei), with Eq. 6.3 written in the reduced form

$$\hat{H} = -\frac{\hbar^2}{2m_e}\sum_i \nabla_i^2 + \sum_i V_{\text{ext}}(\mathbf{r}_i) + \frac{1}{2}\sum_{i\neq j}\frac{e^2}{|\mathbf{r}_i - \mathbf{r}_j|} \tag{6.3}$$

The first theorem of Hohenberg-Kohn states that for any system of interacting particles in an external potential $V_{\text{ext}}(\mathbf{r})$, the potential $V_{\text{ext}}(\mathbf{r})$ is determined uniquely, except for a constant, by the ground state charge density $n_0(\mathbf{r})$. Therefore the ground state charge density $n_0(\mathbf{r})$ provides all information about the system in a unique way.

The second theorem constitutes that for any given external potential $V_{\text{ext}}(\mathbf{r})$, the total energy of the system can be written as a functional of the charge density $E[n(\mathbf{r})]$ and that the minimum (ground state) energy E_0 is uniquely associated with the ground state charge density $n_0(\mathbf{r})$. The exact solution of a system with i_{tot} interacting electrons is therefore transferred to the determination of the functional $E[n(\mathbf{r})]$. It seems convenient to have reduced the number of variables from $3N$ to 3, but essentially the problem was shifted only, since the correct functional $E[n(\mathbf{r})]$ is unknown.

6.1.2 Kohn-Sham Equations

Following the theorems of Hohenberg and Kohn, Kohn and Sham[156] reformulated Eq. 6.3 in terms of functionals of the charge density $n(\mathbf{r})$

$$E[n] = T_{\text{s}}[n] + \int d\mathbf{r} V_{\text{ext}}(\mathbf{r}) n(\mathbf{r}) + E_{\text{Hartree}}[n] + E_{\text{xc}}[n] \tag{6.4}$$

with

$$E_{\text{Hartree}}[n] \;=\; \frac{1}{2}\int d\mathbf{r}\, d\mathbf{r}' \frac{n(\mathbf{r})n(\mathbf{r}')}{|\mathbf{r} - \mathbf{r}'|} \tag{6.5}$$

where the Hartree energy $E_{\text{Hartree}}[n]$ specifies the self interaction of the charge density. T_{s} is the kinetic energy of these Kohn-Sham orbitals. V_{ext} contains the Coulomb potential of the nuclei and possibly from external fields. E_{xc} is the exchange and correlation energy. Kohn and Sham introduced orbitals (wave functions) $\psi_{\text{KS},i}$ of the electronic states i, which are given by the self-consistent solution of the Kohn-Sham equations

$$\left[-\frac{\hbar^2}{2m_e}\nabla^2 + V_{\text{ext}}(\mathbf{r}) + V_{\text{Hartree}}(\mathbf{r}) + V_{\text{xc}}(\mathbf{r})\right]\psi_{\text{KS},i}(\mathbf{r}) = \varepsilon_i\psi_{\text{KS},i}(\mathbf{r}) \tag{6.6}$$

providing also the Kohn-Sham eigenvalues ε_i. The Kohn-Sham orbitals are related to the charge density in the form

$$n(\mathbf{r}) = \sum_i |\psi_{\text{KS},i}(\mathbf{r})|^2 \tag{6.7}$$

Thus, the problem of correctly describing a complex system of interacting particles is elegantly replaced by the problem of finding an auxiliary system of independent particles that generates the same charge density as the interacting system and putting the missing parts into the exchange correlation functional. The only blemish of this approach is that exchange correlation energies to date can not be calculated exactly. Fortunately, their contribution to the total energy in most systems is small.

The energy eigenvalues of the Kohn-Sham orbitals ε_i have little physical meaning, though they are often treated like real energies of the electron eigenstates and compared with electronic structures obtained from experiments. This is only justified for the occupied states in a qualitative manner. Strictly speaking, only the eigenvalue of the highest occupied state has a real physical meaning. It is nearly the unrelaxed ionization energy.[157]

6.1.3 Exchange and Correlation Functionals

Numerous exchange and correlation functionals were proposed since the formulation of the Kohn-Sham equation. The most widely used are the Local Density Approximation (LDA) and the Generalized Gradient Approximation (GGA), which will be described in the following in more detail. Both functionals suffer, however, from the fact that they underestimate bandgaps in semiconductors and insulators since they do not provide information on the excited states. Today more sophisticated functionals are available which improve the description of highly correlated electron subsystems of d and f-elements, van-der-Waals interactions and electronic structures of small bandgap semiconductors. These are for example hybrid functionals like HSE[158,159] or B3LYP,[160,161] which include some exact exchange energy from Hartree-Fock theory taking into account the full Slater determinant, while normal exchange and correlation functionals consider only the occupied states.

Local Density Approximation

LDA is the most commonly used functional, because for many solids the homogeneous electron gas, on which it is based, is a good approximation. This formulation is particularly convenient as it is local, which means that it only depends on the position $\mathbf{r}$. The exchange and correlation energy is in that case the integral of the exchange and correlation energy density over the full space as if it was the energy of a perfect homogeneous electron gas of density $n(\mathbf{r}_0)$.
This approximation is particularly efficient for non-strongly interacting systems like non-magnetic materials and systems, where the charge density does not vary fast (the gradient of the density should be close to zero). In the program package VASP used in this work the implementation of Ceperley and Alder is used.[162] LDA underestimates typically the cell volume caused by overestimation of bonding interactions.

Generalized Gradient Approximation

The GGA functional was developed to include the effects of gradients in the charge density. For $3d$ elements magnetic properties are very sensitive to the occupation of states around the Fermi level. Near the Fermi level, the charge density gradient can be quite large. Several formulations of GGA can be found like PBE[163] or PW91.[164] GGA both under- and overestimates unit cell volumes in an unpredictable way.

6.1.4 Basis Sets

Differences between several DFT codes arise from the choice of the single electron basis functions ϕ_i. These can be atomic orbital-based functions, like Gaussians or Hankel-Bessel functions, or plane waves in combination with pseudopotentials, like the Ultrasoft Pseudopotentials of Vanderbilt (US-PP)[165] or Projector Augmented Plane Waves (PAW).[166,167] Also hybrid techniques exist, that treat core electrons in an atomic orbital-basis and valence electrons by plane waves, like Full Potential Linearised Augmented Plane Waves (FLAPW).[168,169] Chemists traditionally use atomic orbital bases, as implemented in GAUSSIAN,[170] or SIESTA,[171,172] which are best suited for the simulation of molecular systems, while for crystals plane wave bases are the best adapted method, as implemented in VASP,[173–176] ABINIT[177–179] or QUANTUM ESPRESSO.[180] The most accurate, but also computationally most demanding, technique, however, is FLAPW as implemented in FLEUR.[181]

6.2 Application to Crystals

For periodic structures like in crystals the quantum number i in Eq. 6.7 can be replaced by the band index n_a and the allowed *k*-vector of the reciprocal lattice and it is convenient to expand the Kohn-Sham orbitals of the valence states in linear combinations of plane waves.

6.2.1 Description of the Brillouin Zone

The most accurate description of the electronic structure of a crystal would be obtained from a continuous integration over all allowed *k*-points in the Brillouin zone (BZ). Fortunately, in most cases it is completely sufficient to include a small selection of high symmetry *k*-points within the BZ only. A large number of *k*-points is required to determine correctly the occupation near the Fermi level, when occupancy of a state depends on its eigenvalue like in metallic systems. Moreover, several quantities such as the total energy require an integration over the BZ. A commonly used simple type of *k*-point mesh was proposed by Monkhorst and Pack.[182] VASP automatically generates Monkhorst-Pack meshes. One can choose between meshes including or excluding the Γ-point. The choice depends on the crystal symmetry, as the *k*-point mesh may not break the symmetry.

6.2.2 Core and Valence States

The charge density in a crystal exhibits fast oscillations near the nuclei, which are difficult to capture by linear combinations of plane waves. For an accurate description of such charge densities an enormous number of plane waves would be required or in other words huge cutoff energies. In order to avoid these fast oscillations several techniques can be used: core states can be decomposed into local muffin tin orbitals, and valence states into plane waves to create norm conserving pseudopotentials or the Projector Augmented Waves (PAW). The first two techniques have the advantage of conserving the real charge density but are resulting in very slow execution times and are generally not transferable. In PAW on the other hand, the real charge density is replaced by an effective charge density. Yet up to now, this is the most efficient basis set. Another advantage of this method is the transferability of the potentials, which allows the user to work with the same pseudopotential at low and high pressures.

6.2.3 Determination of Forces

Forces acting on the nuclei can be determined via the Hellmann-Feynman theorem.[183] They are determined as the derivatives of the energy with respect to the atomic positions $\mathbf{R}$.

$$\mathbf{F}_{\mathbf{R}} = -\frac{\partial E}{\partial \mathbf{R}} \tag{6.8}$$

Using the Hellmann-Feynman theorem these forces can be described by the expectation value

$$\mathbf{F}_{\mathbf{R}} = \langle \psi_{\mathbf{R}} \left| \frac{\partial H}{\partial \mathbf{R}} \right| \psi_{\mathbf{R}} \rangle \tag{6.9}$$

This elegant formulation leads to the difference of the energy for two different values of $\mathbf{R}$:

$$\Delta E = \int d\mathbf{R} \langle \psi_{\mathbf{R}} \left| V_{\text{int}} \right| \psi_{\mathbf{R}} \rangle \tag{6.10}$$

As the wave function always reflects the symmetry of the system, no symmetry-breaking forces can be expected.

VASP offers different settings for the structural optimization. One can choose between relaxation of atomic positions, cell shape or the unit cell volume and any combinations of the three.

6.3 Details of the Calculations

Computational Setup

The ab-initio calculations presented in this study were performed using the Vienna Ab-initio Simulation Package (VASP).[173–176] Prior to the calculations convergence tests for the *k*-point meshes and the energy cutoff of the plane waves were performed, which can be found in App. A.
The Projector Augmented Wave method was applied with the LDA exchange correlation functional. The energy cutoff of the plane waves was chosen at 600 eV. Both Γ-centred and ordinary 8×8×8 Monkhorst-Pack k-point meshes for the primitive cell (one formula unit ABX_3) were used for the Brillouin zone integration, resulting in an overall numerical error of less than 1 meV/atom for energy differences. Forces were optimized to less than 0.01 eV/Å. The valence electron configurations of the PAW datasets are given in Tab. 6.1.
The crystal structures were visualized using the program VESTA.[184]

Table 6.1: PAW datasets used in this work.

Element	Valence Electrons
Li	$1s^2 2s^1$
O	$2s^2 2p^4$
Na	$2p^6 3s^1$
K	$3s^2 3p^6 4s^1$
Ca	$3s^2 3p^6 4s^2 3d^{0.01}$
Ti	$3s^2 3p^6 4s^2 3d^2$
Rb	$4s^2 4p^6 5s^1$
Ag	$5s^1 4d^{10}$
Cs	$5s^2 5p^6 6s^1$
Ba	$5s^2 5p^6 6s^2$
Tl	$5d^{10} 6s^2 6p^1$
Pb	$5d^{10} 6s^2 6p^2$
Bi	$5d^{10} 6s^2 6p^3$

Ground State Structures and Energies

The determination of ground state structures and energies are standard DFT procedures. These calculations can be performed under static conditions (without relaxation) or including relaxations of atomic positions and/or the unit cell shape. In order to investigate the driving forces for the stabilization of different chemical orders in cation mixed perovskites, we perform successive calculations: first without relaxation, and then relaxation of atomic positions and afterwards of

atomic positions and cell shape. The energy contributions of the different relaxation processes can be obtained by subtraction afterwards. [1]

In principle it is also possible to optimize the unit cell volume within VASP, but it is more accurate to do that externally, by calculating energies at different volumes (variation from the equilibrium volume of about 10% is recommended) and to fit the $E(V)$-data to the 3rd order Birch-Murnaghan Equation of State[185]

$$E(V) = E_0 + \frac{9V_0B_0}{16}\left\{\left[\left(\frac{V}{V_0}\right)^{\frac{2}{3}} - 1\right]^3 B_0' + \left[\left(\frac{V}{V_0}\right)^{\frac{2}{3}} - 1\right]^2\left[6 - 4\left(\frac{V}{V_0}\right)^{\frac{2}{3}}\right]\right\} \tag{6.11}$$

with the bulk modulus

$$B_0 = -V\left(\frac{\partial P}{\partial V}\right)_T \tag{6.12}$$

and its pressure derivative

$$B_0' = \left(\frac{\partial B}{\partial P}\right)_T. \tag{6.13}$$

From these data also pressures p and enthalpies H can be calculated by

$$p(V) = \frac{3B_0}{2}\left[\left(\frac{V_0}{V}\right)^{\frac{7}{3}} - \left(\frac{V_0}{V}\right)^{\frac{5}{3}}\right]\left\{1 + \left[\frac{3B_0'}{4} - 1\right]\left[\left(\frac{V_0}{V}\right)^{\frac{2}{3}} - 1\right]\right\} \tag{6.14}$$

and

$$H(V) = E(V) + p(V) \cdot V \cdot 6.242 \cdot 10^{-3}\,\text{eV}\text{Å}^{-3}\text{GPa}^{-1}. \tag{6.15}$$

Bader Analysis

The Bader analysis is a computational method that decomposes the charge density $n(\mathbf{r})$ in so-called Bader volumes around the nuclei and allows for the calculation of Bader charges inside these volumes. In chemistry, the concept of separate atoms is very common, while in a crystal it is less obvious, which parts of the crystal belong to which atom. Fortunately, the charge density between atoms reaches generally a minimum providing natural borders for the separation of atoms from each other. The algorithm of Henkelman *et al.* was used in this work.[186–188]
The Bader volumes and Bader charges depend strongly on the grid (FFT-mesh) of the charge density, which is set by the variables `NGXF`, `NGYF`, `NGZF`. In App. A the convergence tests for the Bader charges with respect to the FFT-mesh can be found. A mesh of $300 \times 300 \times 300$ was finally chosen, which limits the accuracy of the Bader charges to $0.005e$. Despite the recommendation to include the density of the core charges in the analysis, we used the valence charge density alone, because the core charge densities exhibited pronounced artefacts along the unit cell axes, that caused strong oscillations and prevented the convergence of the Bader charges.

[1] We noticed though, that in more complex structures especially in the presence of polarization, it is better to relax atomic positions and cell shape simultaneously instead of successively, this is due to the strong coupling between polarization and strain.

Phase Stabilities under Pressure

We compare the relative stabilities of a representative selection of high-symmetry varieties of the perovskite structure in $2 \times 2 \times 2$ supercells, which result from chemical order and well-known lattice instabilities like in-phase and anti-phase octahedral tilts or polar and antipolar cation displacements at different pressures. The chemical order varieties are called *chemical configurations*. The varieties arising from combinations of lattice instabilities are denoted as *structure types*, as they are completely characterized by their tilts and A-cation displacements.

All structural optimizations are carried out under the constraint of symmetry conservation, i.e. in the starting configurations certain structure types are imposed together with chemical configurations, yielding certain space groups, which do not change during the atomic relaxation. Although these space groups can have considerably lower symmetry than their chemically indifferent counterparts in the same structure type, which would have for example full *R*3*c* symmetry, we call them "*R*3*c*-like", because the main structural features, in this case anti-phase tilts and polarization components along all three pseudo-cubic axes directions, are still present after relaxation. Macroscopically, a chemically disordered sample would show *R*3*c* symmetry on average, but is only *R*3*c*-like on the local scale. The local structure results from the fact that chemical order breaks the higher (average) symmetry of the polar distorted/tilted structures (e.g. *R*3*c*). Accordingly, we find a broad variation of tilt angles and local ionic polar distortions within one structure type and even within one structure.

Nomenclature of Structure Types

In order to have an unambiguous nomenclature for all structure types, but to also to indicate the deviations from the ideal lattice distortions, we chose a simplified modified Glazer notation.[108,189] The letters x, y, z represent the directions along the pseudo-cubic axes [100], [010] and [001], respectively. Superscripts indicate the tilting, $+$ for in-phase and $-$ for anti-phase tilts. We do not give any information about the magnitude of tilts, for tilt angles are ill-defined in strongly distorted octahedra, as they emerge on the local scale. Subscripts represent the kind of A-cation displacements, $+$ for polar displacements and $-$ for anti-polar displacements. For example, $x_+^- y_+^- z_+^-$ describes a structure with anti-phase tilts around and polar displacements along the [111]-direction (*R*3*c*-like), while $x_-^- y_-^- z_o^+$ gives a structure with anti-phase tilts along [110], and in-phase tilts around [001] with anti-polar displacements of the A-cations along [110]- and $[\bar{1}\bar{1}0]$-directions in the pseudocubic setting (*Pbnm*-like).

Mechanical Boundary Conditions

For the investigation of phase stabilities we calculate enthalpies for two conditions: isotropic strain and isotropic stress. In the first case, we determine total energies at different volumes of the supercells allowing for relaxation of the atomic positions with fixed pseudo-cubic lattice parameters ($a = b = c$ and all angles 90°). In this case deviatoric stress components occur at a given volume

and the hydrostatic pressure needs to be calculated from the trace of the stress tensor.
In the second set of calculations, the cell shape as well as the atomic positions are fully relaxed at a fixed volume. In this case the relaxed structures are isotropically stressed and the $E(V)$-data can be fitted to the Birch-Murnaghan equation of state, which is more accurate than the trace of the stress tensor. The resulting bulk moduli and pressure derivatives were then employed to calculate the respective $H(P)$-data analytically.

Phase Coexistence

In order to explore the possibility of coexistence of phases with different structure types we use larger supercells of the size $(2n) \times 2 \times 2$ with $n = 1, 2, 3$, these larger supercells are constructed and relaxed like the small ones, but allowing for optimization of atomic positions at fixed lattice parameters only. The mixed structure is schematically shown in Fig. 6.1.

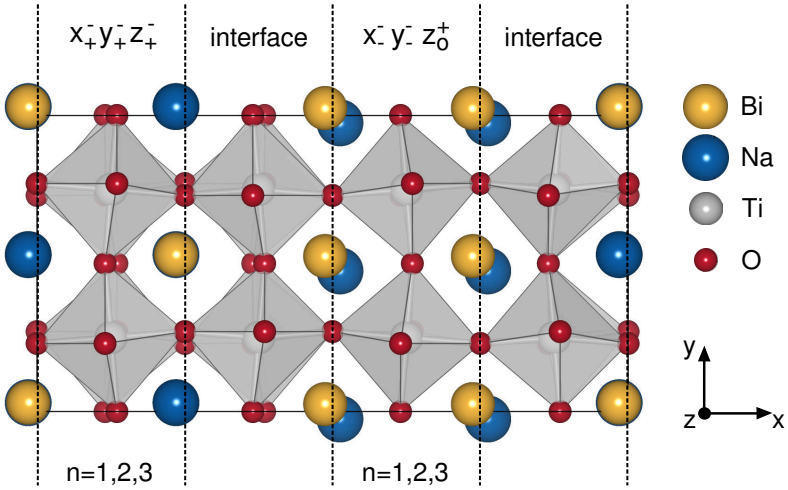

Figure 6.1: Schematic structure of the mixed state $x_+^- y_+^- z_+^- / x_-^- y_-^- z_0^+$ with interfacial regions. Displacements of Bi/Na ions are exaggerated. In the $x_+^- y_+^- z_+^-$ slab both Bi and Na ions are displaced along $[\bar{1}11]$-, while in the $x_-^- y_-^- z_0^+$ slab Bi ions are displaced along $[\bar{1}10]$- and Na ions along $[1\bar{1}0]$-direction. Half of the octahedra in the interfacial regions are distorted due to the tilt misfit. The octahedra in the planes below and above the paper plane are regular across the interfacial regions. The number of unit cells n within the slabs of the pure phases $x_+^- y_+^- z_+^-$ and $x_-^- y_-^- z_0^+$ was varied from one to three while keeping the interfacial area constant.

NBT-based Solid Solutions

Four different NBT-based solid solutions with the second end members $BaTiO_3$, $CaTiO_3$, $Li_{1/2}Bi_{1/2}TiO_3$ and $K_{1/2}Bi_{1/2}TiO_3$ are studied to investigate their phase stabilities under pressure. Based on the experience from the previous calculations with different mechanical boundary conditions we chose a mixed procedure, taking lattice strain into account only for the $P4mm$ structures and neglecting it for the $R3c$ and $Pbnm$ structures. Thus, for $P4mm$ structures the cell shape as well as the atomic positions were fully relaxed at a fixed volume. But for $R3c$ and $Pbnm$ structures total energies were determined at different volumes of the supercells allowing for relaxation of the atomic positions with fixed pseudo-cubic lattice parameters ($a = b = c$ and all angles 90°). Tests on several compositions with full relaxation including lattice strain supported this procedure. Pressures varied by less than 0.3 GPa, which is in the same order of magnitude as the variation resulting from different A-site configurations, as given in Tab. 6.2 for $(NBT)_{(0.50)}$-$(CaTiO_3)_{0.50}$ for the three different A-site configurations.

Table 6.2: Equilibrium cell volumes of $R3c$-like structures and transition pressures of the phase transformation $R3c \rightleftharpoons Pbnm$ for the three different A-site configurations in $(NBT)_{0.5}$-$(CaTiO_3)_{0.5}$ given in Fig. 13.1.

Configuration	Volume [Å^3/f.u.]	Trans. Pressure [GPa]
I	55.545	-4.7
II	55.413	-5.1
III	55.474	-5.4

7 Landau Theory of Phase Transitions

The phenomenological Landau theory is based on a group-theoretical description of phase transformations.[190] It was developed to describe the behaviour of crystalline solids in the vicinity of a second order phase transition, but it is also applicable to other types of phase transitions. The free energy of the system is expanded in a power series of the so-called order parameters. This macroscopic description requires only a small number of coefficients, which can be determined from experiments or from *ab-initio* calculations. Landau theory thus provides insights into the interactions between order parameters expressed by the coupling terms in the free energy expansion.

7.1 Order Parameter

The main reasons of the high success of Landau theory are - besides its universality - its simplicity and efficiency.
The free energy of a system undergoing a displacive phase transition can be written as a Taylor expansion of the driving order parameter Q[191–193] like

$$F(Q) = \frac{1}{2}aQ^2 + \frac{1}{4}bQ^4 + \frac{1}{6}cQ^6 \tag{7.1}$$

or

$$F(Q) = aQ^2 + bQ^4 + cQ^6. \tag{7.2}$$

Order parameters are physical quantities, which are zero in the high-symmetry (disordered) phase and change to a finite value at the transition temperature, where the ordered phase is formed. The order parameter in a ferroelectric phase transition for instance is the spontaneous polarization P, and in a ferroelastic phase transition it is the spontaneous strain η. In most cases every order parameter is associated with a single irreducible representation (irrep). In the following chapter we will learn what an irrep is.
It is generally assumed, that only the first coefficient a is temperature dependent

$$a = a_0(T - T_0), \tag{7.3}$$

and the remaining coefficients are independent of temperature. T_0 is the temperature, at which a changes sign. If $a > 0$ the distortion mode is said to be "hard", the high symmetry phase is the more stable configuration, whereas if $a < 0$ the low-symmetry structure becomes favoured. The distortion mode is said to be "soft" then. In the picture of lattice vibrations the displacive phase transition is associated with a phonon, that has an imaginary frequency in the harmonic approximation, also designated as a "soft mode".[28,29] The coefficients a_0 and c are in general both positive.[194,195]

The order parameter varies with temperature for $T < T_0$ like

$$Q \sim (T_0 - T)^{\beta}. \tag{7.4}$$

The critical exponent β depends on the order of the phase transition, which can be deduced from the form of the polynomial. Three cases can be distinguished.[194–196]

1. Second order phase transitions result, if $b > 0$ and $c \to 0$, then $\beta = \frac{1}{2}$.
2. First order phase transitions are observed, if $b < 0$ and $c > 0$, but Q possesses a discontinuity at T_0.
3. Tricritical transitions can be found, if $b = 0$ and $c > 0$, then $\beta = \frac{1}{4}$.

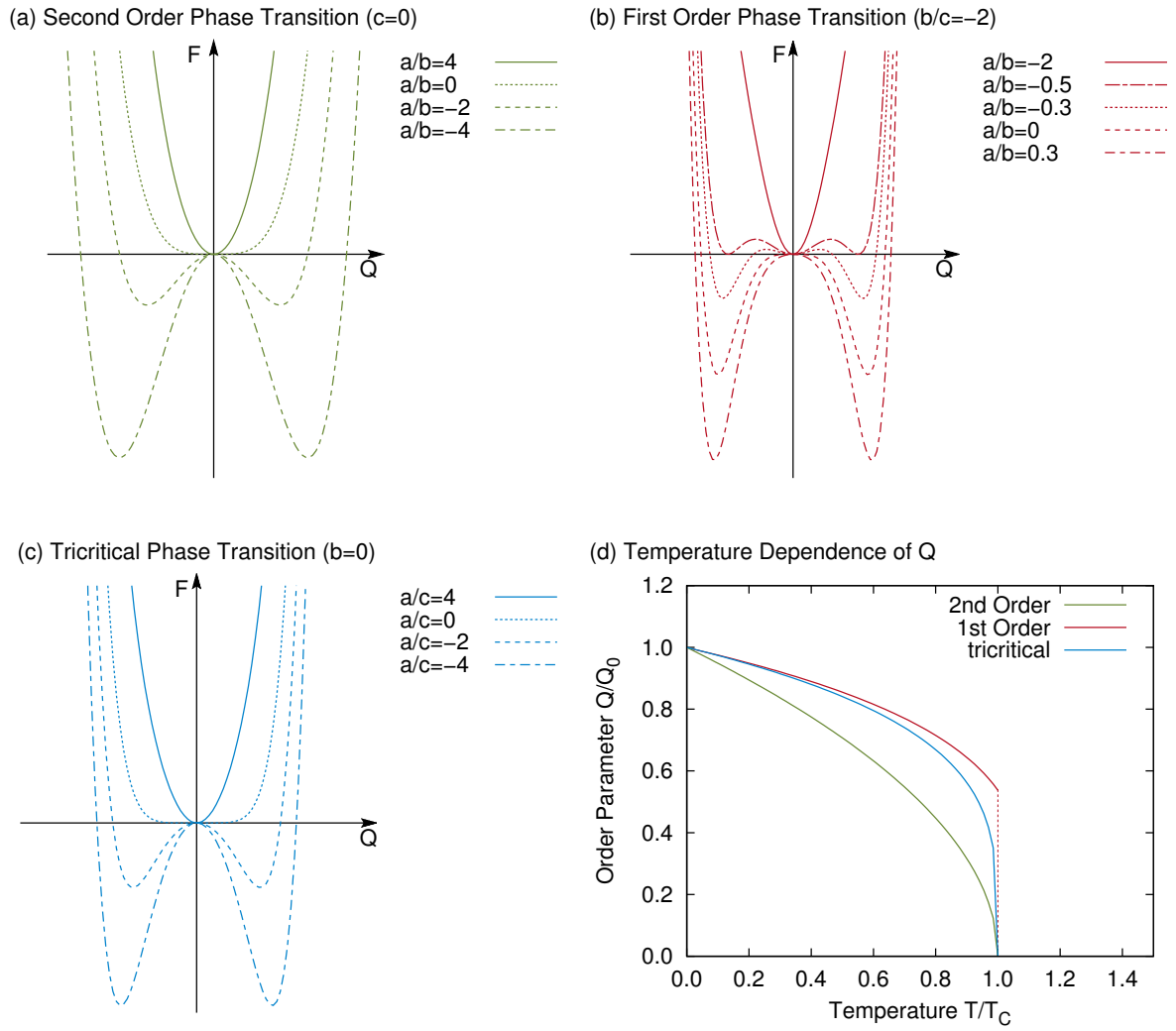

Figure 7.1: $F(Q)$ curves for second order (a), first order (b) and tricritical (c) phase transitions, depending on the temperature dependent coefficient a. In (d) the evolution of $Q(T)$ for all three cases is shown. $Q_0 = Q(T = 0)$

In Fig. 7.1 the developments of the $F(Q)$ curves with temperature for all three cases are shown along with the evolution of the order parameter with temperature.

Introduction of the sixth-order term leads to the formation of a third minimum at $Q = 0$ at temperatures above T_C in Fig. 7.1 (b). T_C marks the temperature, at which all three minima are degenerate, which leads to phase coexistence and thermal hysteresis behaviour, as they are typical for first order phase transitions. Just below T_0 the third local minimum vanishes. A phase transition becomes also first order, if there exist odd order terms in the energy expansion.[194]

Essentially, the appropriate polynomial form of the Landau potential and the existence of certain coupling terms between more than one order parameter depend solely on symmetry considerations and can be obtained from group theoretical treatment, while the values of the coupling coefficients are determined by materials chemistry and can strongly depend on volume or other state variables. The Landau potential can be obtained from the polynomial invariant of all irreps of the parent high-symmetry structure, which are responsible for the symmetry-lowering during the (hypothetical) phase transition. Polynomial invariants can be determined with the help of the software package ISOTROPY developed by Stokes, Hatch and Campbell.[197]

7.2 Coupling between Order Parameters

Anharmonic interactions between different order parameters can favour or disfavour the simultaneous occurrence of the related lattice instabilities. This can cause suppression of formerly soft modes or induce otherwise hard modes under certain conditions. Similar to the effect of an external field, coupling of order parameters can change the order of a phase transition and shift the transition temperature.[93] A new phenomenon caused by coupling between several lattice instabilities are re-entrant phase transitions.[198]
The order of the direct coupling between different order parameters is dictated by symmetry. Biquadratic coupling between two order parameters Q_1 and Q_2 of the type $b_{22}Q_1^2Q_2^2$ is always allowed. Bilinear or linear-cubic coupling terms of the type $a_{11}Q_1Q_2$, $b_{31}Q_1^3Q_2$ and $b_{13}Q_1Q_2^3$, in contrast, are only possible in the rare case, where Q_1 and Q_2 correspond to the same irrep. In the following the discussion of coupling between order parameters is divided into two categories, which is completely arbitrary and due to the limitation of this work to the first category of coupling between polarization and octahedral tilts. The second category is the coupling between polarization and strain. Different types of so-called electromechanical coupling can lead to additional indirect coupling contributions to the interaction between polarization and octahedral tilts. It is almost impossible to discern between direct and indirect coupling in an experiment.

7.2.1 Direct Coupling between Polarization and Octahedral Tilts

Different types of anharmonic coupling have been reported in literature. Depending on the lowest order coupling term in the Landau potential improper ferroelectric phase transitions (trilinear

coupling $Q_1Q_2Q_3$ or linear-quadratic coupling $Q_1Q_2^2$) and triggered ferroelectric phase transitions (negative biquadratic coupling $Q_1^2Q_2^2$) were distinguished.[199,200]

Improper Ferroelectricity

If polarization is not the primary order parameter, but just a secondary one, a phase transition is called improper or extrinsic ferroelectric.[193] In fact, improper ferroelectrics should not possess a polar soft mode, so that polarization can only be induced via coupling between polarization and other lattice instabilities.
Improper ferroelectrics were first reviewed by Levanyuk and Sannikov in 1974.[199] The early prominent examples were rare-earth molybdates like $Gd_2(MoO_4)_3$, where polarization couples to a shear strain, which is induced by a soft M-point zone boundary mode.[201–203] In recent years improper ferroelectrics were also found in perovskites. Bousquet and Ghosez reported on improper ferroelectric behaviour in artificial (Pb,Sr)TiO_3 superlattices, where in-phase and anti-phase tilts about the z-axis are coupled to polarization along the [001]-direction via a trilinear coupling term $\phi_+\theta_-P_z$.[204] The resulting space group is $P4bm$. Similarly, improper ferroelectricity was found in hexagonal manganites such as $YMnO_3$, which do not adopt the perovskite structure, but a similar structure with layers of corner-sharing MnO_5 trigonal-bipyramides separated by planes of yttrium ions. The primary distortion mode is a rotation mode which is coupled to a polar mode via the two fourth-order terms $\phi_{K_3}^3P$ and $\phi_{K_3}^2P^2$.[205] Although the lowest order coupling term is not of third order, this material fulfils the requirement that the polar mode is solely induced by coupling to the rotation mode K_3. Benedek and Fennie introduced the term hybrid improper ferroelectricity to describe the fact that polarization can be induced by the combination of two independent rotation modes resulting in a trilinear coupling term $\phi_1\phi_2P$,[206] just as in the example of Bousquet *et al.*[204] Very recently, Fukushima *et al.*[207] and Rondinelli *et al.*[208] demonstrated how in cation-ordered perovskites ferroelectricity can be induced by two octahedral rotation modes described by Glazer-notation as $a^0a^0c^+$ and $a^-a^-c^0$. The resulting space group of A-site chemically (001)-ordered perovskites with tilt system $a^-a^-c^+$ is $Pmc2_1$ (it is lowered to $P2_1$ if also the B-site is ordered as in $(Na_{1/2}La_{1/2})(Mn_{1/2}W_{1/2})O_3$[207]), which allows for polar displacements.

Improper ferroelectrics do not possess the classical double-well potential, just a single well exists, which is shifted from $P = 0$ to some non-zero values with increasing amplitude of the rotation modes. Some authors compared this shift with electric-field induced polarization, just that here polarization is induced by a "geometrical field".[205,209] The third-order coupling term $\phi_1\phi_2P$ is somewhat special, as its pure existence is sufficient to imply improper ferroelectric behaviour. Because it is an odd-order term, there always exist four combinations of ϕ_1, ϕ_2 and P, which lead to a decrease of free energy independent of the sign of the coupling coefficient.[199] Yet, technically speaking, the sole existence of the trilinear coupling term is a necessary but not sufficient condition for the existence of improper ferroelectric behaviour. Also single mode properties and the pairwise interactions between the modes ϕ_1, ϕ_2 and P play an important role.[210] In order to have polarization induced by a leading trilinear term ϕ_1, ϕ_2, P, the following conditions must be fulfilled:[210]

1. P should be a hard mode at $\phi_1 = \phi_2 = 0$. Under certain circumstances P can also be a soft mode. It should be weakly competitive with both tilt modes then, otherwise the biquadratic coupling terms $\phi^1 P^2$ and $\phi_2^2 P^2$ would dominate the polarization-tilt interactions, leaving the trilinear term only a minor contributor.

2. ϕ_1 and ϕ_2 have to be soft modes, but their single mode minima have to be saddle points in the energy surface $E(\phi_1, \phi_2)$. This means the two tilt modes must not be highly competitive allowing their coexistence at $P = 0$.

Fennie, Ghosez and Stengel just recently revisited the two supposedly improper ferroelectric materials they discovered ($YMnO_3$ and superlattice (Pb,Sr)TiO_3) and analysed the materials' electrical properties in the framework of the constrained-D *ab-initio* calculations developed by Stengel and Vanderbilt.[210,211] In this article, it was revealed, however, that superlattice (Pb,Sr)TiO_3 does not fulfil the conditions for improper ferroelectricity. First, the polar mode is a soft mode, which couples strongly with the two tilt modes in a cooperative manner. Second, the two tilt modes are both soft, but highly competitive and cannot coexist on their own. They operate only pairwise by cooperative coupling to the soft polar mode. Thus, superlattice (Pb,Sr)TiO_3 should rather be considered an ordinary ferroelectric with dominating biquadratic polarization-tilt coupling. $YMnO_3$ on the other hand shows properties as they are expected for an improper ferroelectric, i.e. existence of two single well potentials with energy minima at $P \neq 0$, between which can be switched by reversing the orientation of the K-mode.[210] Moreover, Stengel's calculations demonstrate that the polarization in $YMnO_3$ is almost constant within the limits of open- and short-circuit electrical boundary conditions, which explains the persisting polarization in free-standing ultrathin films found by earlier *ab-initio* calculations of this material.[209]

Triggered Ferroelectricity

Holakovsky[200] stated that a ferroelectric phase transition can also be triggered by another lattice instability and its order parameter Q. The necessary condition for the existence of a triggered ferroelectric phase transition is that the biquadratic coupling term Q^2P^2 is the lowest order (and dominating) interaction term in the free energy expansion leading to decreasing energies for simultaneous non-zero values of both Q and P, which means that the biquadratic coupling coefficient needs to be negative and that the terms QP, Q^2P and QP^2 have to be forbidden by symmetry. This mixed term was already discussed by Levanyuk and Sannikov and it was shown to give rise to double hysteresis loops.[199] The symmetry lowering due to triggered ferroelectricity corresponds to the intersection of symmetry changes due to the onset of Q and P and it is always greater than the lowering of symmetry connected with one parameter only. Such a triggered ferroelectric phase transition was reported for $BiFeO_3$ which has space group $R3c$ and where neither tilting leading to $R\bar{3}c$ nor polarization leading to $R3m$ are the primary order parameter, both instabilities are equally important and coexist due to a negative biquadratic coupling coefficient.[212]

Avalanche Transition

A third type of coupled phase transition was reported by Perez-Mato *et al.*[213] for the Aurivillius compound $Bi_4Ti_3O_{12}$, which the authors called *avalanche* transition. This material undergoes a single phase transition at about 675°, which can be characterized by the simultaneous condensation of three primary modes corresponding to three different irreps, followed by three additional secondary modes. A thorough analysis of the energy landscape in terms of the three primary modes exhibited that neither biquadratic nor trilinear coupling terms can explain the simultaneous condensation of the three primary modes in the ground state structure of $Bi_4Ti_3O_{12}$. The biquadratic coupling coefficients were all positive while the trilinear coupling coefficients were found to be very small. Based on this study, no explanation was found for the simultaneous condensation of the three primary modes.[213] Essentially, it stays unclear, which kind of coupling gives rise to the *avalanche* transition.
Yet, contributions from higher order coupling terms (e.g. 6th order) or indirect coupling via common strain components and other secondary modes were not taken into account, which might provide the missing link.

7.2.2 Electromechanical Coupling

Depending on the symmetry of the crystal structure and on the (electrical and mechanical) boundary conditions different types of electromechanical coupling can occur. Piezoelectricity and electrostriction assume homogeneous boundary conditions, while flexoelectricity is related to inhomogeneous boundary conditions (field gradients).

Piezoelectricity

Piezoelectricity is a property exhibited by any crystal that belongs to a non-centrosymmetric crystal class (except 432). The most widely used piezoelectric material is quartz. The term piezoelectricity literally means "electric charge induced by pressing" (from $\pi\iota\epsilon\zeta\epsilon\iota\nu$ - to press and $\eta\lambda\epsilon\kappa\tau\rho o\nu$ - amber). The direct piezoelectric effect characterizes the dielectric displacement D induced by application of a mechanical stress σ (like uniaxial compression or tension). The converse piezoelectric effect describes the strain η exhibited when submitted to an electric field E. Polarization of opposite direction is induced by tensile and compressive stresses and, in analogy, the direction of the applied electric field determines, whether the material contracts or expands. In both cases the response is proportional to the force, the proportionality constant is called piezoelectric coefficient. Depending on the boundary conditions four different piezoelectric compliances are defined, the most commonly used is the piezoelectric coefficient d defined as[5,193]

$$d_{ijk} = \left.\frac{\partial D_k}{\partial \sigma_{ij}}\right|_E = \left.\frac{\partial \eta_{ij}}{\partial E_k}\right|_\sigma \tag{7.5}$$

The piezoelectric coefficient d_{ijk} is actually a third rank tensor describing the relations between the second rank tensors η_{ij} and σ_{ij} and the first rank tensors (vectors) E_k and D_k. Crystals belonging

to the crystal class $4mm$ for example possess three different components of the piezoelectric tensor d_{33}, d_{31} and d_{15}, which relate longitudinal, transverse and shear deformations along and perpendicular to the poling direction. Quartz and ZnO are examples of non-polar piezoelectric materials. Due to the anisotropy of the piezoelectric effect it is self-evident, that we need single crystals with defined orientation in order to make optimal use of the piezoelectric effect. Moreover, non-polar piezoelectrics have rather small piezoelectric coefficients.

Electrostriction

Electrostriction is a property exhibited by any dielectric.[214] Electrostriction relates strain to the square of the electric field, or strain to the square of polarization. The latter definition is especially important in ferroelectrics, which show non-linear dielectric properties,

$$\eta_{ij} = Q_{ijkl} P_k P_l. \tag{7.6}$$

The electrostrictive coefficient Q_{ijkl} is a fourth rank tensor. Electrostrictive strain has its origin in the field induced polarization.
Interestingly, electrostrictive materials exposed to electric field bias exhibit piezoelectric behaviour. The piezoelectric coefficient is proportional to the induced polarization, therefore the strain becomes proportional to the square of induced polarization.[214,215] This is the origin of piezoelectricity in perovskite ferroelectrics. The poled ferroelectric ceramic brings so-to-say its own biasing field, the spontaneous polarization.

Flexoelectricity

Flexoelectricity, like electrostriction, exists in any dielectric. It relates an induced polarization P_l to a mechanical strain gradient $\frac{\partial \eta_{ij}}{\partial x_k}$,

$$P_l = \mu_{ijkl} \frac{\partial \eta_{ij}}{\partial x_k}, \tag{7.7}$$

There exists also the inverse flexoelectric effect, describing the coupling between stress and a polarization gradient. The flexoelectric effect becomes important in nanostructures such as thin films, but also in the vicinity of point defects and dislocations.[216] Moreover it was shown to affect ferroelectric domain walls.[217]

Indirect Coupling between Polarization and Tilt via Common Strain Components

Electromechanical coupling terms between polarization P and strain η give rise to the piezoelectric and the electrostrictive effects, which were discussed above. The free energy contributions due to the two effects are as follows

$$F(P,\eta) = d\eta P \tag{7.8}$$

$$F(P,\eta) = Q\eta P^2 \tag{7.9}$$

with the piezoelectric tensor d and the electrostrictive tensor Q. In the same manner, strain components can couple linearly or quadratically to other order parameters, such as octahedral tilts or Jahn-Teller distortions. If different modes couple to the same strain component, this can lead to an indirect coupling contribution to the overall interaction between the two modes. Salje and Devarajan studied the effect of strain-induced order parameter couplings on phase transitions investigating bilinear and linear-quadratic couplings between strain and the two order parameters.[218] They found that the strain-mediated interactions lead to new bilinear or biquadratic forms of order parameter coupling. In Ref. 219 the effects of elastic 3D clamping on ferroic phase transitions were investigated. Besides shifts of the transition temperature and change of the order of phase transition relative to the stress-free crystal, elastic clamping opens the door to new low-symmetry phases which do not exist in single crystals. The authors showed theoretically that 3D clamping for example can stabilize a rhombohedral phase in $PbTiO_3$.

7.3 Examples of Free Energy Diagrams $F(Q_1, Q_2)$

In the following some examples of energy diagrams $F(Q_1, Q_2)$ resulting from the coexistence and interaction of two order parameters Q_1 and Q_2 are discussed in order to make the reader familiar with this kind of description and to introduce the most common energy surfaces found for pairwise order parameter coupling in NBT. We start with a fourth order Landau potential describing the coexistence of two order parameters, which do not correspond to the same irrep. Thus, only a biquadratic coupling term exists. This Landau potential was already extensively investigated before,[93] here we want to focus on the shape of the energy surface $E(Q_1, Q_2)$ and how it changes with the relative softness of the two single modes associated with order parameters Q_1 and Q_2 and the strength of the biquadratic coupling b_{22}.
The Landau potential adopts then the form

$$F(Q_1, Q_2) = a_{20}Q_1^2 + b_{40}Q_1^4 + a_{02}Q_2^2 + b_{04}Q_2^4 + b_{22}Q_1^2Q_2^2 \tag{7.10}$$

The stable configurations are those, which minimize the energy. Thus, the first derivatives have to be equal to zero,

$$\frac{\partial F}{\partial Q_1} = (2a_{20} + 2b_{22}Q_2^2)Q_1 + 4b_{40}Q_1^3 = 0 \tag{7.11a}$$

$$\frac{\partial F}{\partial Q_2} = (2a_{02} + 2b_{22}Q_1^2)Q_2 + 4b_{04}Q_2^3 = 0, \tag{7.11b}$$

while the second derivatives have to be positive

$$\frac{\partial^2 F}{\partial Q_1^2} = (2a_{20} + 2b_{22}Q_2^2) + 12b_{40}Q_1^2 > 0 \tag{7.12a}$$

$$\frac{\partial^2 F}{\partial Q_2^2} = (2a_{02} + 2b_{22}Q_1^2) + 12b_{04}Q_2^2 > 0 \tag{7.12b}$$

$$\frac{\partial^2 F}{\partial Q_1 \partial Q_2} = 4b_{22}Q_1Q_2 > 0. \tag{7.12c}$$

There exist three types of solutions (Q_1, Q_2) fulfilling Eqs. (7.11):

1. The trivial solution $Q_1 = Q_2 = 0$ leads to:
   - a minimum, if both modes are hard ($a_i > 0$)
   - a saddle point, if one of the modes is hard, the other one soft
   - a maximum, if both modes are soft ($a_i < 0$)

2. There are four "real" solutions with

$$Q_1 = \pm\sqrt{\frac{-a_{02}b_{22} + 2a_{20}b_{04}}{b_{22}^2 - 4b_{40}b_{04}}},\ Q_2 = \pm\sqrt{\frac{-a_{20}b_{22} + 2a_{02}b_{40}}{b_{22}^2 - 4b_{40}b_{04}}} \tag{7.13}$$

   These solutions possess singularities, if $b_{22}^2 = 4b_{40}b_{04}$.

3. The set of "imaginary" solutions is given by,

$$Q_1 = 0,\ Q_2 = \pm i\sqrt{\frac{a_{02}}{2b_{04}}}, \tag{7.14}$$

$$Q_1 = \pm i\sqrt{\frac{a_{20}}{2b_{40}}},\ Q_2 = 0. \tag{7.15}$$

   If the radicand is negative, the imaginary solutions become real numbers. This is always the case, if Q_1 and Q_2 are associated with a soft mode.

The single modes have their minimum positions at $Q_{\text{min},i} = \pm\frac{a_i}{2b_i}$ and $F_{\text{min},i} = -\frac{a_i}{2b_i^2}$. The energy surface of such a system always has at least a two-fold symmetry. Depending on the relative softness of the two single modes and the strength of their coupling the energy surface possesses 1, 3, 5, 9 or an infinite number of extrema, as we will see now.

Let us start with the most simple case. We assume that both modes are equally soft and that their single mode energy minima are at $Q_1 = \pm 1$ and at $Q_2 = \pm 1$. This gives us the constraints

$$a_{20} = a_{02} = a_2 < 0 \tag{7.16a}$$

$$b_{40} = b_{04} = b_4 = -\frac{a_2}{2} \tag{7.16b}$$

The trivial solution now represents an energy maximum. The "real" solutions become (under exclusion of $b_{22} = \pm a_2$)

$$Q_1 = \pm\sqrt{\frac{-a_2}{b_{22} - a_2}},\ Q_2 = \pm\sqrt{\frac{-a_2}{b_{22} - a_2}} \tag{7.17}$$

and the "imaginary" solutions become

$$Q_1 = 0,\ Q_2 = \pm 1 \tag{7.18}$$

$$Q_1 = \pm 1,\ Q_2 = 0 \tag{7.19}$$

All solutions reflect the fourfold symmetry of the system.

Four different types of free energy surfaces can be distinguished, they are depicted in Fig. 7.2.

1. If $b_{22} = 0$ the real solutions describe four minima at the positions $(+1, +1)$, $(+1, -1)$, $(-1, +1)$ and $(-1, -1)$. The imaginary solutions become saddle points, they are identical to the single mode minimum positions $(\pm 1, 0)$ and $(0, \pm 1)$. The energy surface adopts a square-shape.

2. If $b_{22} = -a_2$ the imaginary solutions become positions of minimal energy, but they are not the only solutions. The real solutions possess a singularity in this case. Essentially, the energy adopts the form $F(Q_1, Q_2) = a_2(Q_1^2 + Q_2^2) + b_4(Q_1^2 + Q_2^2)^2$. This equation describes a Mexican hat in 3D. Projected on the (Q_1, Q_2)-plane it looks more like a flattened donut. The two modes compete strongly with each other.

3. If $b_{22} > -a_2$ the real solutions describe saddle points, while the imaginary solutions become minima at $(\pm 1, 0)$ and $(0, \pm 1)$. The two modes compete so strongly that they cannot coexist any more, they exclude each other. The energy surface becomes diamond-shaped.

4. If $b_{22} < 0$ the two modes cooperate and enhance each other, shifting the four minima to positions $|Q_1| = |Q_2| > 1$ and changing the energy surface from square-shaped to a four-pointed star.

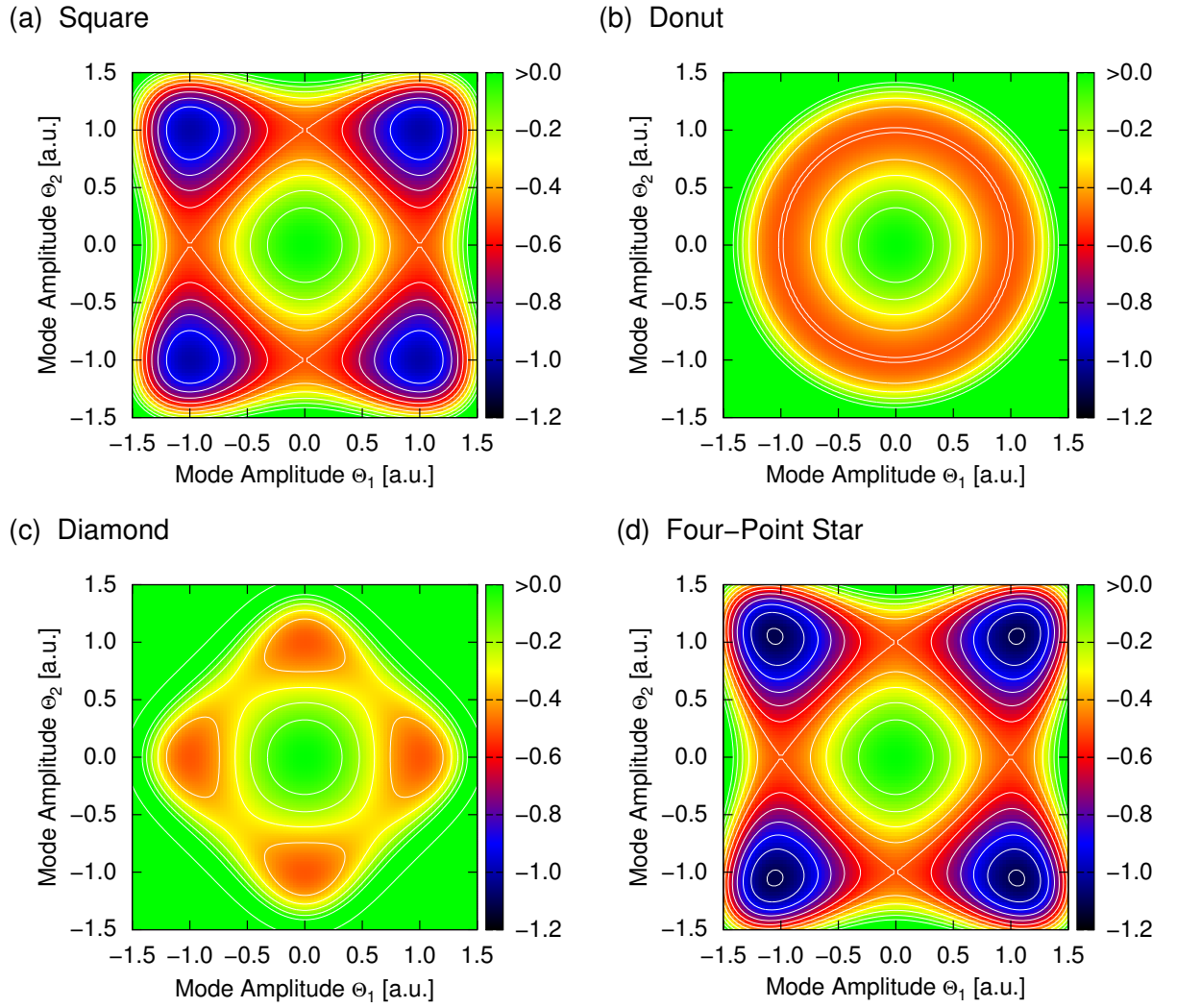

Figure 7.2: Free energy surface for coexistence of two equally strong single modes with $a_2 < 0$ and $b_4 = -\frac{a_2}{2}$. Coupling parameters are chosen as follows: (a) $b_{22} = 0$, (b) $b_{22} = -a_2$, (c) $b_{22} = -2a_2$ and (d) $b_{22} < 0$.

Now let us investigate the solutions for two modes, that are not equally soft, but their single mode minima stay at positions ± 1, which gives us the following constraints:

$$a_{20} < 0,\ a_{02} < 0, \tag{7.20a}$$

$$b_{40} = -\frac{a_{20}}{2},\ b_{04} = -\frac{a_{02}}{2}. \tag{7.20b}$$

The trivial solution $(0,0)$ still is a maximum. The four real solutions then become

$$Q_1 = \pm\sqrt{\frac{\frac{b_{22}}{a_{02}} + \frac{a_{20}}{a_{02}}}{-\left(\frac{b_{22}}{a_{02}}\right)^2 + \frac{a_{20}}{a_{02}}}},\ Q_2 = \pm\sqrt{\frac{\frac{b_{22}}{a_{20}} + \frac{a_{02}}{a_{20}}}{-\left(\frac{b_{22}}{a_{20}}\right)^2 + \frac{a_{02}}{a_{20}}}}, \tag{7.21}$$

and the four imaginary solutions become

$$Q_1 = 0,\ Q_2 = \pm 1 \tag{7.22}$$

$$Q_1 = \pm 1,\ Q_2 = 0. \tag{7.23}$$

Again, four different types of free energy surfaces can be distinguished. They are shown in Fig. 7.3.

1. In the decoupled case with $b_{22} = 0$, four minima at positions of the real solutions at $(\pm 1, \pm 1)$ develop. Depending on the ratio a_{02}/a_{20} the shape of the free energy landscape varies between éclairs, sunglasses and the square-shape already described above. At the positions of the imaginary solutions saddle points can be found.

2. If the two modes are competitively coupled, but not too strong, the energy minima are shifted to smaller amplitudes, leading to the goggles-shape.

3. If the competitive coupling is stronger than the softness of the weaker mode, the weaker mode can become completely suppressed. Two energy minima result at positions $Q_1 = \pm 1$, $Q_2 = 0$, if $a_{20}/a_{02} > 1$ and $b_{22} > -a_{02}$, or at positions $Q_1 = 0$, $Q_2 = \pm 1$, if $a_{20}/a_{02} < 1$ and $b_{22} > -a_{20}$. The energy surface becomes kidney-shaped.

4. If the two modes couple cooperatively, pointed sunglasses result (not shown).

In the last scenario, we want to assume that only one of the modes is soft, the other one hard, which gives us the following constraints:

$$a_{20} > 0,\ a_{02} < 0, \tag{7.24a}$$

$$b_{40} > 0,\ b_{04} = -\frac{a_{02}}{2}. \tag{7.24b}$$

The trivial solution $(0,0)$ now becomes a saddle point. The four real solutions become

$$Q_1 = \pm\sqrt{\frac{-a_{02}b_{22} - a_{02}a_{20}}{b_{22}^2 - 4b_{40}b_{04}}},\ Q_2 = \pm\sqrt{-\frac{a_{20}}{b_{22}}}, \tag{7.25}$$

and only two of the four imaginary solutions give real numbers,

$$Q_1 = 0,\ Q_2 = \pm 1, \tag{7.26}$$

$$Q_1 = \pm i\sqrt{\frac{a_{20}}{2b_{40}}},\ Q_2 = 0. \tag{7.27}$$

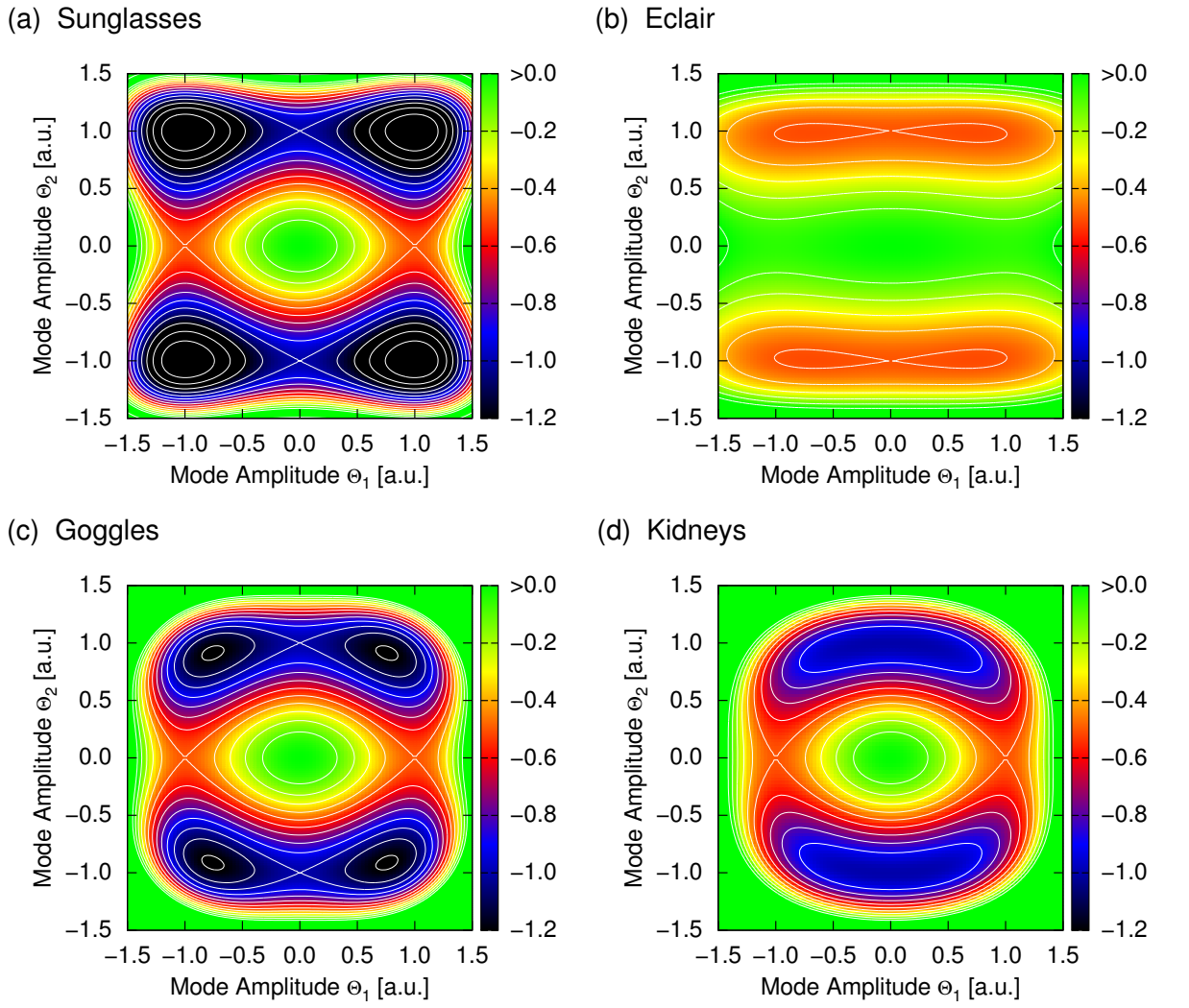

Figure 7.3: Free energy surfaces for coexistence of a strong and a weak single mode with $a_{20} = \frac{a_{02}}{2}$. Coupling parameters are chosen as follows: (a) $b_{22} = 0$, (b) (c) $b_{22} < a_{20}$ and (d) $b_{22} = a_{20}$.

Whatever value the coupling parameter adopts, it is impossible to soften the hard mode, we will always find an hourglass-shaped energy surface. The situation is presented in Fig. 7.4 (a).

In order to describe first order phase transitions or in order to improve the fit between calculated values and the Landau potential sixth order terms can be included

$$F(Q_1, Q_2) = a_{20}Q_1^2 + b_{40}Q_1^4 + c_{60}Q_1^6 + a_{02}Q_2^2 + b_{04}Q_2^4 + c_{06}Q_2^6 + b_{22}Q_1^2Q_2^2 + c_{42}Q_1^4Q_2^2 + c_{24}Q_1^2Q_2^4 \tag{7.28}$$

The sixth order coupling terms induce asymmetries at large amplitudes of both order parameters. For example a large c_{42} induces a V-shape as shown in Fig. 7.4 (b). Like the biquadratic coupling term the quadratic-quartic coupling terms can lead to suppression or enhancement of the two modes. It is also possible that both types of coupling are working against each other.

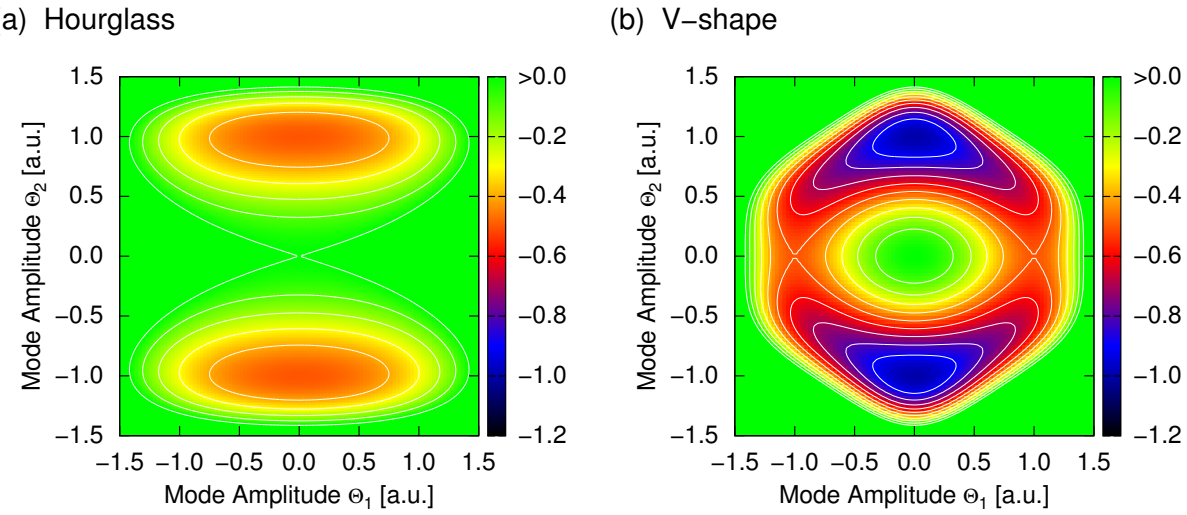

Figure 7.4: Free energy surfaces for coexistence of a strong and a weak single mode. In (a) the second mode is much weaker than the first mode: $10 \cdot a_{20} = a_{02} = -1.0$, $10 \cdot b_{40} = b_{04} = 0.5$ and $c_{60} = c_{06} = 0$, $b_{22} = b_{40} = 0.05$ and $c_{24} = c_{42} = 0$. In (b) the second mode is not a weak soft mode, but a hard mode with a very flat curvature around the origin: $-10 \cdot a_{20} = a_{02} = -1.0$, $10 \cdot b_{40} = b_{04} = 0.5$ and $c_{60} = c_{06} = 0$, $b_{22} = b_{40} = 0.05$ and $c_{24} = c_{42} = 0$.

Saddle points can be interpreted as zero-field switching barriers. These barriers are valid under the assumption that the order parameters switch direction (i.e. sign) by following a minimum free energy path in the configuration space of fixed directions of the distortion vectors.
In a real switching process also rotations of order parameters can play a major role (this process is especially assumed to be crucial in MPB-systems), these rotation paths can not be extracted from this type of free energy diagram.

8 Analysis of Displacive Phase Transitions

For the characterization of phase transitions on the basis of Landau theory it is essential to have some basic knowledge of group theory. In this chapter some new tools will be introduced, that are essential for the group theoretical description of the transformation of crystal structures upon displacive phase transitions. These phase transitions can be qualitatively and quantitatively described by symmetry-adapted distortion modes characterized by their irreducible representations, their amplitudes and resulting atomic displacements. After introducing group-subgroup relations and demonstrating, what we can learn from the description of irreducible representations, it will be explained how we can distinguish primary from secondary distortion modes. Finally, this chapter will be completed by two elaborated examples, which are relevant for this study. The first example is octahedral tilting, a phenomenon very often encountered in perovskite structures. The second example is A-site order, that originates from varying site occupation probabilities for atoms of different elements on the perovskite A-site, and which can induce atomic displacements onto the parent structure depending on the accompanied symmetry breaks.

8.1 Symmetry-Mode Description of Distorted Structures

Group-subgroup relations are the adequate tool for analysing displacive phase transitions in a condensed and comprehensive way. The symmetry-breaking static distortions underlying these phase transitions can be understood as distortion modes acting on a (real or hypothetical) structure of higher symmetry, which is referred to as *parent structure*. The resulting lower symmetry structures are called *distorted structures*. The static frozen distortions present in the distorted structure can be described by collective atomic displacements, which are identical to the modes known from thermal vibrations (i.e. dynamic distortions or phonons). Every distorted structure can be deconvoluted into displacive normal modes (i.e. eigenmodes) with symmetries given by irreducible representations of the parent space group. A thorough review on the description of distorted structures by symmetry-adapted modes was given by Perez-Mato *et al.* [220]
Besides the investigation of real phase transitions as they arise for example on changes of temperature or pressure, it can be also instructive to describe low-symmetry structures with respect to a hypothetical parent structure (also called prototypic phase), as it allows to quantify e.g. polarization and octahedral tilts and to distinguish between primary and secondary distortion modes.

8.2 Group-Subgroup Relations

Group-subgroup relations can be illustrated in so-called group-subgroup graphs or, if more detailed information about unit cell transformations and Wyckoff splittings is needed, in Bärnighausen tree diagrams.[221,222] Here only group-subgroup graphs will be used, as those are already complex enough. Details about unit cell transformations and Wyckoff splittings will be provided separately. Most important for building up diagrams of group-subgroup relations are the maximal (i.e. direct) subgroups of a given space group, which are listed in the *International Tables for Crystallography A1*.[223]

Two different types of maximal subgroups exist.[223] There are t-subgroups (*translationengleiche*) and k-subgroups (*klassengleiche*). Translationengleiche subgroups $\mathcal{H}$ of a space group $\mathcal{G}$ possess the same translation lattice, the volume of the primitive unit cell stays unchanged: $\mathcal{T}_\mathcal{H} = \mathcal{T}_\mathcal{G}$, but they belong to a crystal class of lower symmetry: $\mathcal{P}_\mathcal{H} < \mathcal{P}_\mathcal{G}$. The subgroup $\mathcal{H}$ loses rotation type operations with respect to $\mathcal{G}$. *Klassengleiche* subgroups $\mathcal{H}$ of a space group $\mathcal{G}$, on the other hand, belong to the same crystal class (point group): $\mathcal{P}_\mathcal{H} = \mathcal{P}_\mathcal{G}$, but have lost translations compared to $\mathcal{G}$, the conventional unit cell is either enlarged or lost centring translations: $\mathcal{T}_\mathcal{H} < \mathcal{T}_\mathcal{G}$. A special type of *klassengleiche* subgroups are *isomorphic* subgroups $\mathcal{H}$, which belong to the same space group as $\mathcal{G}$. Maximal t- and k-subgroups can be chained to general subgroups $\mathcal{H}$, which lost both crystal-class symmetries and translations compared to $\mathcal{G}$. However, Hermann's theorem states, that any general subgroup $\mathcal{H}$ is a *klassengleiche* subgroup of a uniquely determined *translationengleiche* subgroup $\mathcal{M}$ of the space group $\mathcal{G}$, such that $\mathcal{H} \leq \mathcal{M} \leq \mathcal{G}$.[224]

The complete group-subgroup chains of a given unit cell transformation (e.g. as a consequence of a phase transition) can be easily obtained, if one knows the parent space group $\mathcal{G}$, the subgroup $\mathcal{H}$ and the index of the transformation $[i]$, which is given by

$$i = i_k \cdot i_t = \frac{Z_\mathcal{H}}{Z_\mathcal{G}} \cdot \frac{|\mathcal{P}_\mathcal{G}|}{|\mathcal{P}_\mathcal{H}|} \tag{8.1}$$

where $Z_\mathcal{G}$, $Z_\mathcal{H}$ are the numbers of formula units per primitive unit cell of the two structures with space groups $\mathcal{G}$ and $\mathcal{H}$, and $|\mathcal{P}_\mathcal{G}|$ and $|\mathcal{P}_\mathcal{H}|$ are the orders of the corresponding point groups of the space groups. The index is the factor by which the number of symmetry elements has been reduced.

Another special subgroup type are isotropy subgroups. Isotropy subgroups can be maximal or general subgroups of the space group $\mathcal{G}$, their characteristic is that they can be reached by a displacive transformation associated with a single irrep, a term which will be explained soon. Moreover, there exists a simple rule for the possible occurrence of second order phase transitions. The symmetry of the space group of the distorted structure arising in a second order phase transition must be an isotropy subgroup of the group of the parent structure. This condition is necessary but not sufficient for a second order phase transition to occur. In the end, only the experiment can show if the transition is really of second order. On the other hand, the phase transition must be of first order, if the distorted structure is not an isotropy subgroup, but e.g. a common subgroup of isotropy subgroups or not a subgroup at all.

The fundamentals of unit cell transformations are outlined in App. E.

8.3 Domain Structure

Upon a displacive phase transition from space group $\mathcal{G}$ to subgroup $\mathcal{H} < \mathcal{G}$ a single crystal of the parent phase splits into many domains, which are homogeneous regions within the new phase and which all belong to the same space group type. They can be distinguished by their orientation and their location in space. Every domain is a single crystal. Domains are separated by domain walls, which are planar entities of reduced symmetry. The number of different domain states that can evolve upon a specific phase transition $\mathcal{G} \rightarrow \mathcal{H}$ is determined by the space groups and the unit cell transformation, because it is equal to the transformation index $[i]$ introduced in the previous section. If $\mathcal{H}$ is a *translationengleiche* subgroup ($\mathcal{M} = \mathcal{H}$), $[i_t]$ different orientational (twin) domains form. If $\mathcal{H}$ is a *klassengleiche* subgroup ($\mathcal{M} = \mathcal{G}$), $[i_k]$ different antiphase (orientational twin) domains can develop. In case of a general subgroup ($i_t \neq 0$ and $i_k \neq 0$) the crystal is split into both twin and antiphase domains. Let us have a look at some examples. The first example is the ferroelectric phase transition of $BaTiO_3$ at 403 K from the prototypic *Pm*$\bar{3}$*m* phase with lattice vectors $\mathbf{a}, \mathbf{b}, \mathbf{c}$ to the polar *P*4*mm* phase with the same lattice vectors, which is thus a translationengleiche subgroup of the parent space group. The transformation index is $[i] = [i_t] = 6$. Upon the ferroelectric phase transition six different twin domains can develop, whose polar axes are oriented along the six different $\langle 001 \rangle$-directions of the cubic parent structure. They can be distributed into three groups of domain states oriented along the x, y and z-direction, that have identical space groups but antiparallel polar axes, as indicated in Fig. 8.1 (a). In a *P*4*mm* crystal two types of domain boundaries can develop, depending on the angle between the two polarization vectors they are called 90° and 180° domain walls (DW). In a rhombohedral system, where the vector of spontaneous polarization is oriented along the [111]-direction, three different domain walls are possible, besides 180° domain walls, there exist also 71° and 109° domain walls.
The second example is an order-disorder transition from an A-site disordered perovskite structure with space group *Pm*$\bar{3}$*m* and lattice vectors $\mathbf{a}, \mathbf{b}, \mathbf{c}$ to an A-site 111-ordered perovskite structure with space group *Fm*$\bar{3}$*m* and lattice vectors $2\mathbf{a}, 2\mathbf{b}, 2\mathbf{c}$, which is a *klassengleiche* subgroup of the parent space group, because both space groups belong to the same point group. The transformation index is $[i] = [i_k] = 2$. Two different translational domain states result. The origin of the doubled unit cell of the *Fm*$\bar{3}$*m* phase can coincide with any of the origins of the smaller unit cells of the parent structure. Thus, the origins of the antiphase domains are shifted by (I) $0, 0, 0$ and (II) $\frac{1}{2}, \frac{1}{2}, \frac{1}{2}$, as shown in Fig. 8.1 (b). Both shifts lead to identical unit cells as the following shifts (I) $\frac{1}{2}, \frac{1}{2}, 0$ or $\frac{1}{2}, 0, \frac{1}{2}$, or $0, \frac{1}{2}, \frac{1}{2}$ and (II) $\frac{1}{2}, 0, 0$ or $0, \frac{1}{2}, 0$ or $0, 0\frac{1}{2}$. Shown is also an antiphase boundary (APB) formed on the (100)-plane between the two domain states.
The last example is a phase transition, that is a combination of the former two. It is from the simple disordered perovskite structure with space group *Pm*$\bar{3}$*m* and lattice vectors $\mathbf{a}, \mathbf{b}, \mathbf{c}$ to a simultaneously A-site 001-ordered and polar perovskite structure with space group *P*4*mm* and lattice vectors $\mathbf{a}, \mathbf{b}, 2\mathbf{c}$, which is a general subgroup of the parent space group. Here the transformation index is given by $[i] = [i_t] \cdot [i_k] = 6 \cdot 2 = 12$. In total 12 domain states can be distinguished. In Fig. 8.1 (c) only those examples with y-orientation are shown. Analogous domains with x and z-orientations are also possible. The domain states are characterized by their origin shift and their direction of the polarization vector as indicated in Fig. 8.1 (c). A manifold of different domain boundaries can be

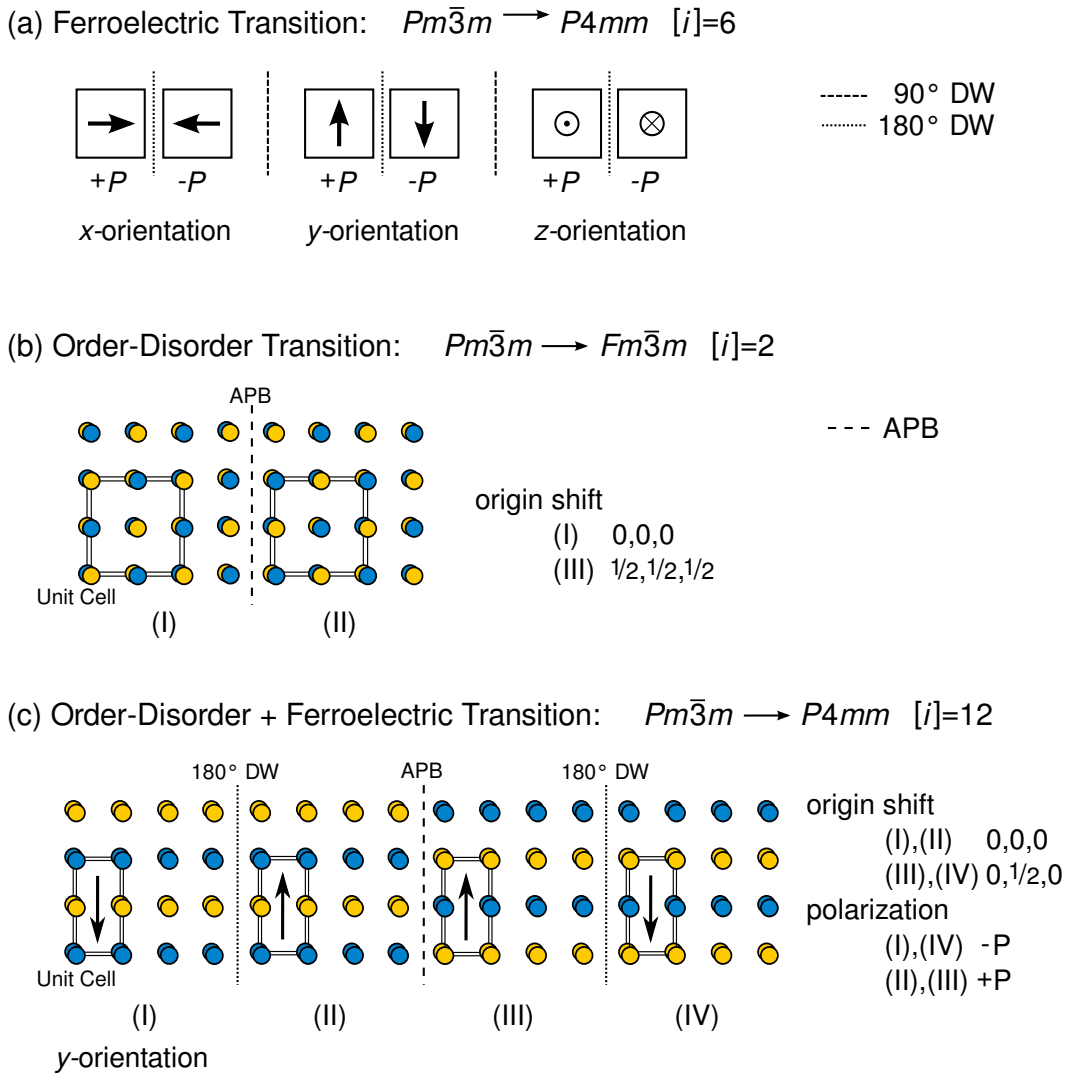

Figure 8.1: Examples for twin and antiphase domains, that form upon (a) a ferroelectric transition, (b) an order-disorder transition and (c) a phase transition that combines the former two. Schematically shown are the different domain states and some (100)-plane domain boundaries, that can develop between them.

found in such a phase, shown are only two examples, 180° domain walls and an antiphase boundary. But also 90° domain walls and the mixed boundaries 90° DW + APB and 180° DW + APB are possible.

This group-theoretical treatment is based on the assumption that the lattice parameters do not change upon the phase transition, which is referred to as the *parent-clamping approximation*.[223] Domain structures in real crystals, however, are determined by a much wider range of factors. Especially, the spontaneous strains accompanying ferroelectric-ferroelastic phase transitions complicate the situation, because the lattice parameters meeting at non-180° domain walls do not match any more. Moreover, electrostatic constraints exist, favouring antiparallel or head-to-tail orientations of the polarization vectors, in contrast to head-to-head and tail-to-tail configurations, that lead to charge accumulations within the domain walls. Other long-range forces, electrostatic

or elastic in nature, originating from charged defects and impurities severely affect the domain structure as well as higher dimensional defects such as dislocations or voids and cracks.

8.4 Wyckoff Positions

The set of symmetry equivalent sites in a space group is called Wyckoff position,[223] it is characterized by the coordinates of one representative point (x, y, z) on which the symmetry elements of the space group are applied to generate the other equivalent points within the unit cell. The coordinates of a Wyckoff position can be all fixed to special values, like $(\frac{1}{2}, \frac{1}{2}, \frac{1}{2})$, or they can contain free variables, like z in $(0, 0, z)$. In the latter case, there exists an infinity of different orbits, each having a specific value z. Wyckoff positions with the same site symmetry form a Wyckoff set.
In any periodic structure every atomic position belongs to a specific Wyckoff position of the space group $\mathcal{G}$. Upon a displacive phase transition to the subgroup $\mathcal{H}$ these Wyckoff positions can split into different Wyckoff positions of the subgroup and/or their site symmetries reduce. If atoms on a specific Wyckoff position are substituted by atoms of different elements this Wyckoff position has to split. Additionally, due to the symmetry lowering in the subgroup, distortions can act on specific atoms within the structure, displacing them from their ideal positions.

8.5 Irreducible Representations

Irreducible representations (abbreviated as irreps) express the essence of a (point or space) group. As any integral number can be factorized into multiples of prime numbers, the representation of a group can be "factorized" into irreducible representations. Irreps and character tables of the point and space groups can be used to characterize the properties of molecules and crystals in terms of symmetry. The character table is an abstract of the properties of a group in terms of symmetry operations. Due to their general character irreps are employed in a wide range of fields like crystallography, vibrational spectroscopy or quantum mechanics. The characterization of any property depending on electronic or vibrational wave functions, that reflect the inherent symmetries of a system, will at some point rely on irreps and character tables. Character tables of point groups play a central role in molecular vibrational spectroscopy in order to characterize the vibrations by their symmetry. Moreover, character tables can provide information on which transitions are forbidden and allowed by symmetry.
In this work, the irrep notation of Cracknell *et al.*[225] will be followed, which is widely used in perovskite literature, such as by ISOTROPY[189] and the tools of the *Bilbao Crystallographic Server*.[226–228] Irreps of point groups are associated with the Γ-point $k = (0, 0, 0)$, as translational symmetry operations are not contained in point groups. In space groups, however, irreps associated with high-symmetry points of the whole Brillouin zone can be found. Distortion modes associated with irreps at the Γ-point lead to *translationengleiche* isotropy subgroups, while those associated with irreps at the M $(\frac{1}{2}, 0, 0)$, X $(\frac{1}{2}, \frac{1}{2}, 0)$ or R-point $(\frac{1}{2}, \frac{1}{2}, \frac{1}{2})$ lead to general isotropy subgroups, accompanied by unit cell-multiplication or loss of centring symmetry. Spontaneous

polarization and strain are typically described by modes at the Brillouin zone-center (Γ), while octahedral tilting and antipolar displacements are described by modes at the zone-boundary (M,X or R), but in special cases they can also be represented by Γ-modes.
Furthermore, irreps provide direct information about the order parameters, which play a central role in the Landau theory of displacive phase transitions (see Ch. 12). Each irrep has a specific dimension n, that is equal to the maximal number of degrees of freedom arising with the irrep's transformation. Irreps of dimension $n > 1$ have more than one isotropy subgroup depending on the direction of the order parameter in the irrep space.
Examples of phase transitions, where only the direction of the distortion changes, but not the active irrep itself, can be found in $BaTiO_3$ and $CeAlO_3$ with the parent structure *Pm*$\bar{3}$*m*. In $BaTiO_3$ the Γ_4^- distortion with $n = 3$ is responsible for the spontaneous polarization that changes its direction upon heating from $[111]$ in the rhombohedral low-temperature phase *R*3*m* to $[110]$ in the orthorhombic *Amm*2-phase, and finally to $[001]$ in the tetragonal *P*4*mm*-phase, before spontaneous polarization vanishes completely in the cubic high-temperature phase *Pm*$\bar{3}$*m*.[5] Accordingly changes the direction of the order parameter from (a, a, a) to $(a, a, 0)$, and finally to $(0, 0, a)$, before it vanishes:

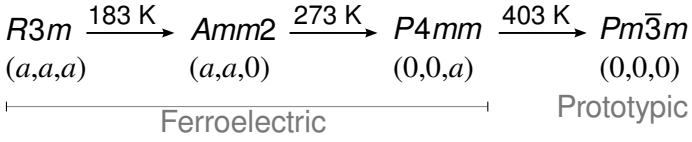

The R_5^- distortion (also $n = 3$), that is responsible for anti-phase tilts of the AlO_6 octahedra, acts very similarly in $CeAlO_3$.[229] On increasing temperature the tilt system changes from $a^o a^o a^-$ in the low-temperature tetragonal phase *I*4*/mcm* to $a^- a^- a^o$ in the orthorhombic *Imma*-phase and finally to $a^- a^- a^-$ in the rhombohedral *R*$\bar{3}$*c*-phase, before all tilts vanish in the cubic high-temperature phase *Pm*$\bar{3}$*m*:

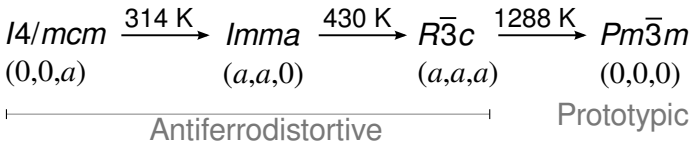

Phase transitions can not only result from a direction change of the order parameter within the same active irrep, but also from the additional condensation of a second mode transforming according to another irrep. An example is the low-temperature structure of $CaTiO_3$ with space group *Pnma*. In this structure, in-phase and anti-phase tilts are combined to the mixed tilt system $a^- a^- c^+$. Both types of tilts are described by different irreps. The in-phase tilt distortion transforms according to irrep M_2^+, while the anti-phase tilts are represented by the same irrep R_5^- as in $CeAlO_3$.

A comprehensive overview of the isotropy subgroups resulting from single or joint condensation of polar and tilt distortions in the simple perovskite structure was given by Stokes *et al.*[189] But please mind, that in most articles of this kind, the A-centred perovskite unit cell was chosen as the asymmetric unit with B-atoms on Wyckoff position 1a $(0, 0, 0)$, A-atoms on 1b $(\frac{1}{2}, \frac{1}{2}, \frac{1}{2})$ and X-atoms on 3d $(0, 0, \frac{1}{2})$; in contrast to this work, where the B-centred perovskite unit cell is used

instead with the A-atoms on 1a $(0,0,0)$, B-atoms on 1b $(\frac{1}{2},\frac{1}{2},\frac{1}{2})$ and X-atoms on 3c $(0,\frac{1}{2},\frac{1}{2})$. These differences in the asymmetric unit change the active irreps from R_4^+ for anti-phase tilts to R_5^- and M_3^+ into M_2^+ for in phase-tilts. The polar mode Γ_4^- is unchanged.

Irreps and isotropy subgroups of a certain group-subgroup transformation can be obtained with COPL, a tool of the software package ISOTROPY[197], or with SYMMODES available on the *Bilbao Crystallographic Server*.[226–228,230]

8.6 Primary and Secondary Distortion Modes

The distortion that drives a phase transformation, and whose appearance is fully sufficient to explain the symmetry break in the distorted structure, is referred to as primary mode. Besides the primary mode also other distortions with different irreps can condense upon the phase transformation. Any degree of freedom, which is compatible with the space group symmetry of the distorted structure, can have non-zero values. These induced distortions are named secondary modes. Trivial secondary distortion modes are those that maintain the symmetry of the parent structure. They transform according to the identity irrep Γ_1^+.

There are several characteristics that distinguish secondary from primary distortion modes summarized in Tab. 8.1. The irreps associated with primary modes have the same isotropy subgroup as the space group of the distorted structure $\mathcal{H}$, while secondary distortions can have isotropy subgroups which are supergroups of $\mathcal{H}$. Generally secondary modes have much smaller amplitudes than primary modes. The reason is that they appear solely due to symmetry-allowed anharmonic coupling of the order parameter Q_{sec} with order parameters Q_{prim} of the primary modes of the type $Q_{\text{prim}}^m \times Q_{\text{sec}}$, as they are intrinsically hard modes with positive stiffness coefficients. Primary modes are always soft modes with negative stiffness coefficients. Small displacements towards the direction of the soft mode are sufficient to push the system into a local energy minimum in configuration space.

A special case are symmetry breaks that violate the Landau postulate of having a single active irrep only. Although that might sound exceptional, it has been reported quite often.[212,231] In these specific cases the symmetry of the distorted structure is not an isotropy subgroup of the parent structure but a common subgroup of two or more isotropy subgroups. This type of phase transition is allowed under certain conditions (anharmonic coupling of the primary order parameters), but it will be strongly of first order.

Table 8.1: Differences between primary and secondary distortions. $\mathcal{H}$ is the space group of the distorted structure.

Property	Primary Distortion	Secondary Distortion
Isotropy subgroup	$= \mathcal{H}$	$\geq \mathcal{H}$
Amplitude of the distortion	large	small
Intrinsic stability	soft mode	hard mode
Stiffness coefficients	negative	positive

8.7 Mode Amplitudes and Atomic Displacements

A displacive distortion can be qualitatively characterized by its irrep and isotropy subgroup, but it can also be quantified by its mode amplitude and by the atomic displacements it causes in the distorted structure with respect to the parent structure. AMPLIMODES[232] is a program available on the *Bilbao Crystallographic Server*, which can perform such an analysis of the symmetry-adapted distortion modes. The only input data that have to be provided are the crystal structures of the distorted and the parent structure in their conventional settings and the unit cell transformation that relates the two. The program identifies pairs of atoms which correspond to each other in both structures and calculates the atomic displacements. In order to obtain results independent of the lattice strain, it is advisable to adapt the reference structures to the unit cell parameters of the distorted structures. In polar structures it can be necessary to eliminate a global translation, because the center of inertia can be shifted due to the arbitrary choice of origin along the polar axis. This can be done by the program, automatically. The atomic displacements are generally given in terms of a displacement vector $\mathbf{u}$ (sometimes also referred to as polar vector), whose dimension is equal to the number of Wyckoff positions experiencing displacements by the distortion mode. This displacement vector is given as the normalized displacement vector $\hat{\mathbf{u}}$ in cell relative units, specified in Eq. 8.2. The mode amplitude $|\mathbf{u}|$ of a distortion is the length of the displacement vector $\mathbf{u}$.

$$\hat{\mathbf{u}} = \frac{\mathbf{u}}{|\mathbf{u}|}. \tag{8.2}$$

The actual atomic displacements are then obtained by multiplying the normalized displacement vector $\hat{\mathbf{u}}$ with the mode amplitude $|\mathbf{u}|$ and the lattice parameter a_{lat}:

$$\mathbf{u} = |\mathbf{u}| \times \hat{\mathbf{u}} \times a_{\text{lat}}. \tag{8.3}$$

Here the example of the polar vector in the *P*4*mm* phase of $BaTiO_3$, structurally optimized at 61.86 Å^3/f.u., is given.

$$\begin{pmatrix} u_{\text{Ba}} \\ u_{\text{Ti}} \\ u_{\text{O1}} \\ u_{\text{O2}} \end{pmatrix} = |\mathbf{u}| \times \begin{pmatrix} \hat{u}_{\text{Ba}} \\ \hat{u}_{\text{Ti}} \\ \hat{u}_{\text{O1}} \\ \hat{u}_{\text{O2}} \end{pmatrix} \times c_{\text{t}} = 0.0925 \times \begin{pmatrix} -0.0655 \\ -0.1868 \\ +0.0627 \\ +0.1269 \end{pmatrix} \times 3.980\,\text{Å} =$$

$$= \begin{pmatrix} -0.0241 \\ -0.0688 \\ +0.0231 \\ +0.0467 \end{pmatrix} \text{Å}.$$

The distortion mode causing spontaneous polarization along the z-direction is associated with the irrep Γ_4^-. The barium atoms are situated on Wyckoff positions 1a, titanium atoms on 1b and oxygen atoms occupy 2c (O1) and 1b (O2). Accordingly, the displacement vector has the dimension four. Cations and anions displace in opposite directions, which is typical for a polar mode. The main contribution to spontaneous polarization originates from displacements of Ti and O2. Overall, the atomic displacements are rather small at this volume with a c/a-ratio of only 1.009.

8.8 Octahedral Tilting

Octahedral tilting is a very common distortion type in perovskites. It reduces the symmetry of the A-site cation coordination environment and results in a change of A-X bond lengths. However, there are multiple ways in which the octahedra can tilt, each leading to a different coordination environment for the A-site cation(s). These changes in the coordination environment have been studied intensively by Woodward.[45,233]

A standard notation to describe octahedral tilting distortions in perovskites has been developed already in 1972 by Glazer.[108] This notation describes a tilt system by rotations of BX_6 octahedra about the three orthogonal Cartesian axes of the perovskite structure's cubic unit cell. Both the magnitude and the phase of the octahedral rotations are specified. The letters indicate the magnitude of the rotation about a given axis, the letters a, b, and c imply unequal tilts about the x, y, and z axes. A superscript is used to denote the phase of the octahedral tilting in neighbouring layers. A positive superscript shows that the neighbouring octahedra tilt in the same sense (in-phase) and a negative superscript implies the tilts of neighbouring octahedra tilt with the opposite sense (anti-phase). A superscript of o signifies no tilting about that axis. In the extended Glazer-notation an additional subscript is used to denote the axes of spontaneous polarization. The $R3c$ structure of NBT is denoted as $a^-_+a^-_+a^-_+$ in the extended Glazer notation, as it exhibits spontaneous polarization along the $[111]$-direction of the pseudocubic unit cell and anti-phase tilts about the same axis.

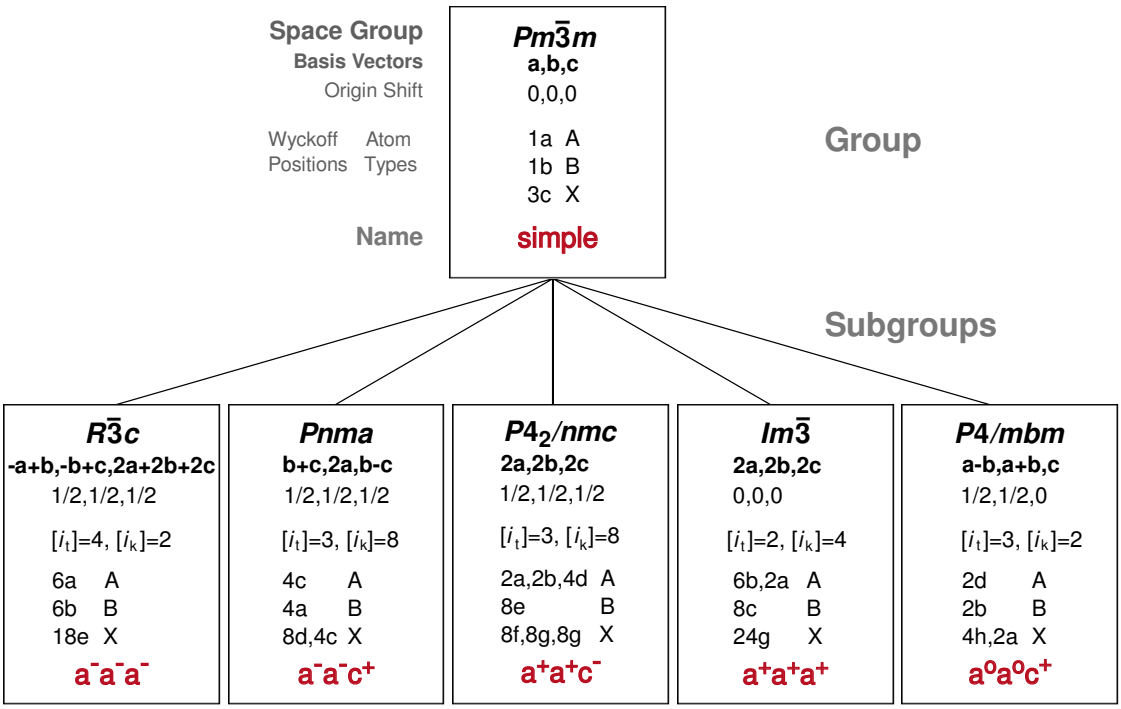

Figure 8.2: Unit cell transformations (in vector notation plus origin shift) with transformation indices and splittings of Wyckoff positions that relate tilted perovskite structures to the simple perovskite unit cell with space group $Pm\bar{3}m$.

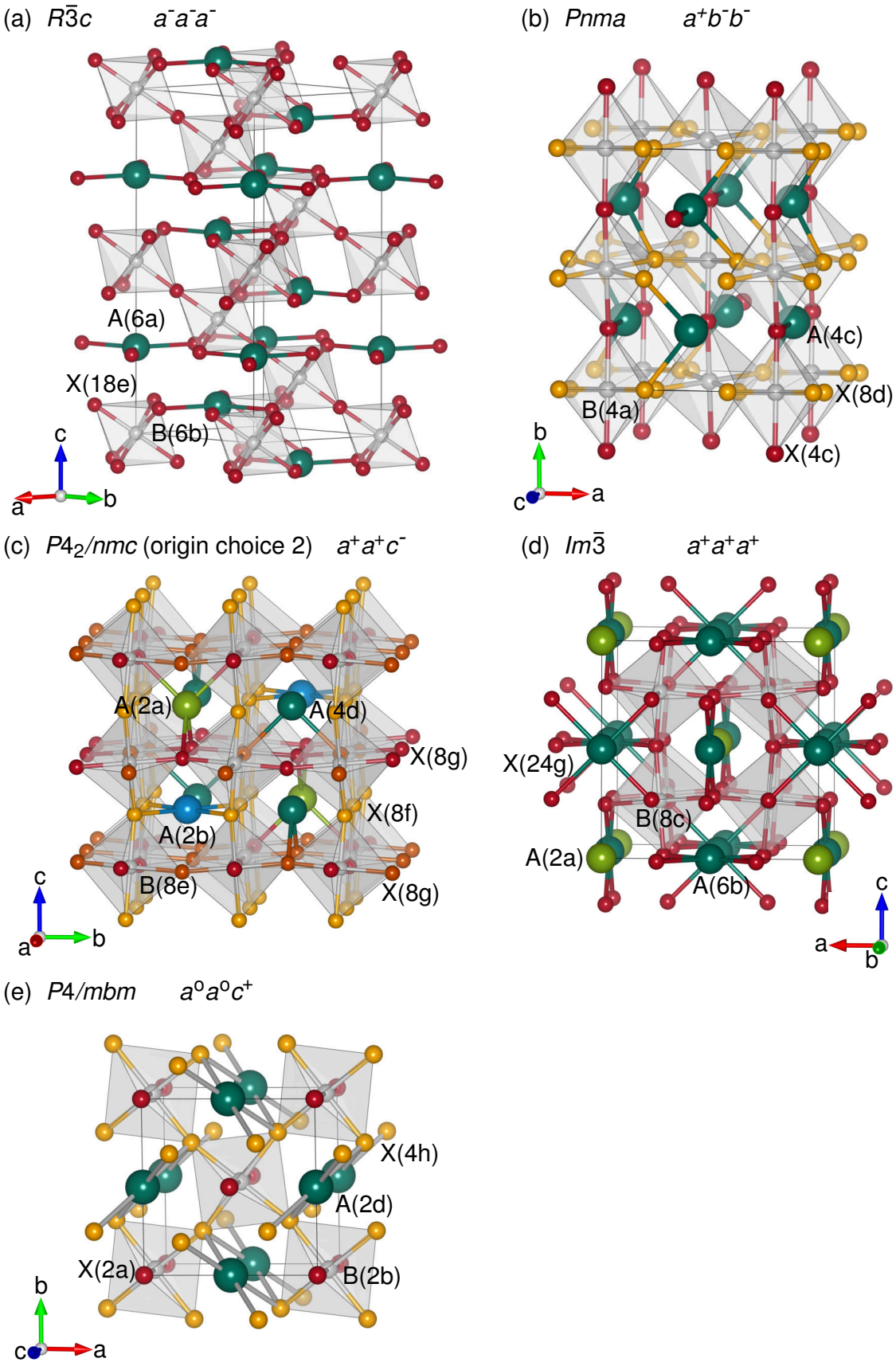

Figure 8.3: Structures of the tilted perovskites (a) rhombohedral $R\bar{3}c$, (b) orthorhombic *Pnma*, (c) tetragonal $P4_2/nmc$, (d) cubic $Im\bar{3}$ and (e) tetragonal $P4/mbm$ in their conventional settings. The different Wyckoff positions are given.

In the following, five examples will be discussed, which will be relevant in this study. They are illustrated in Fig. 8.3 in their conventional settings. The BX_6-octahedra and the next neighbour coordinations of the A-atoms are shown. Different colors indicate different Wyckoff positions. Besides the three-tilted structures *R*$\bar{3}$*c* ($a^-a^-a^-$), *Pnma* ($a^-a^-c^+$), *P*4_2*/nmc* ($a^+a^+c^-$) and *Im*$\bar{3}$ ($a^+a^+a^+$), also the one-tilted structure $a^oa^oc^+$ (*P4/mbm*) is included. Only the three-tilted structures *R*$\bar{3}$*c* and *Pnma* and the one-tilted structure *P*4*/mbm* provide symmetry equivalent positions for all A-atoms, while *P*4_2*/nmc* and *Im*$\bar{3}$ have split Wyckoff positions of different symmetries for the A-site. The B-site never splits. The X-site is split in *Pnma*, *P*4_2*/nmc* and *P*4*/mbm*.

In the rhombohedral *R*$\bar{3}$*c*-structure the X-atoms have three A-atoms as next neighbours in a trigonal-planar coordination. This structure is adopted e.g. by $LaAlO_3$.[234,235]
In the orthorhombic *Pnma*-structure the A-atoms again have three next neighbours but here in a trigonal pyramidal coordination. This structure can be found in numerous perovskite materials, the most prominent is probably the perovskite mineral $CaTiO_3$ itself[139] or $GdFeO_3$, the material, after which this structure type is named.[236]
The tetragonal structure with space group *P*4_2*/nmc* provides three different Wyckoff positions for the A-atoms, two having four next neighbours in tetrahedral (2a) and square planar (2b) coordination and one having two next neighbours in an angular coordination (4d). For this structure, up to now, only one example is reported in the literature. In $Ca_{1/2}Fe_{1/2}TiO_3$ Ca^{2+} occupies both sites with coordination number four (2a and 2b) and Fe^{2+} occupies the 4d site with two next neighbours resulting in a columnar order along the 4-four fold axis.[237]
The pure in-phase tilted cubic *Im*$\bar{3}$-structure provides two different A-sites in the ratio 1:3, the first position (2a) is a regular cuboctahedron with all oxygen ions at the same distance and the second one (6b) has four short bonds in a square planar coordination. It is adopted by compounds with large size differences between the two cations sharing the A-site, as for example by $Ca_{1/4}Cu_{3/4}TiO_3$, where the Jahn-Teller cations Cu^{2+} occupy the square planar 6b-site.[238]

In Fig. 8.2 the complete data necessary to obtain information about group-subgroup relations and distortion modes, such as unit cell transformations and transformation indices are given. It is completed by the splitting of Wyckoff positions upon the transformations. The unit cells of the structures *P*4_2*/nmc* and *Im*$\bar{3}$ are octuplicated with respect to the simple perovskite unit cell. *R*$\bar{3}$*c* is six times larger, *Pnma* is quadrupled and *P*4*/mbm* is doubled. Except for *Im*$\bar{3}$, all transformed unit cells are shifted in such a way that the B-atom is moved to the origin. The modes responsible for the octahedral tilts, but also accompanying secondary modes for all tilted structures are summarized in Tab. 8.2. The higher the index $[i_k]$ the higher is the number of active modes. In this table only modes are given, which act on the occupied Wyckoff positions in the parent structure 1a, 1b and 3c. Generally, there exist additional Γ-modes, like the trivial secondary eigenmode Γ_1^+, which does not break the symmetry of the parent space group. However, these Γ-modes act on unoccupied Wyckoff positions only and are not relevant for the distortions within the structures, that is why they are skipped here. Besides the irreps and isotropy subgroups, also the directions of the order parameter in the irrep spaces are given. All irreps in Tab. 8.2 have dimension $n = 3$ or $n = 6$.
In *Im*$\bar{3}$, *R*$\bar{3}$*c* and *P*4*/mbm*, primary distortion modes can be easily identified, they are M_2^+ and R_5^-,

Table 8.2: Symmetry-adapted distortion modes in tilted perovskite structures. Only modes acting on the occupied Wyckoff positions are given.

Tilt sytem	Space group	k-Point	Irrep	Direction	Isotropy subgroup	Wyckoff
$a^-a^-a^-$	*R*$\bar{3}$*c*	$(1/2, 1/2, 1/2)$	R_5^-	$(-a, a, -a)$	*R*$\bar{3}$*c*	3c
$a^-a^-c^+$	*Pnma*	$(0, 1/2, 0)$	X_5^-	$(0, 0, a, 0, 0, 0)$	*Cmcm*	3c, 1a
		$(1/2, 1/2, 0)$	M_2^+	$(a, 0, 0)$	*P*4*/mbm*	3c
		$(1/2, 1/2, 0)$	M_3^+	$(a, 0, 0)$	*P*4*/mbm*	3c
		$(1/2, 1/2, 1/2)$	R_4^-	$(0, a, a)$	*Imma*	3c, 1a
		$(1/2, 1/2, 1/2)$	R_5^-	$(0, a, -a)$	*Imma*	3c
$a^+a^+c^-$	*P*4$_2$*/nmc*	$(0, 1/2, 0)$	X_5^-	$(0, 0, a, a, a, -a)$	*P*4*/nmm*	3c, 1a
		$(1/2, 1/2, 0)$	M_1^+	(a, a, b)	*I*4*/mmm*	3c
		$(1/2, 1/2, 0)$	M_2^+	$(a, -a, 0)$	*I*4*/mmm*	3c
		$(1/2, 1/2, 1/2)$	R_5^-	$(0, 0, a)$	*I*4*/mcm*	3c
$a^+a^+a^+$	*Im*$\bar{3}$	$(1/2, 1/2, 0)$	M_1^+	$(-a, -a, a)$	*Im*$\bar{3}$*m*	3c
		$(1/2, 1/2, 0)$	M_2^+	$(a, a, -a)$	*Im*$\bar{3}$	3c
$a^oa^oc^+$	*P*4*/mbm*	$(1/2, 1/2, 0)$	M_2^+	$(a, 0, 0)$	*P*4*/mbm*	3c

the in-phase and anti-phase tilt modes. In *R*$\bar{3}$*c* and *P*4*/mbm* no secondary modes exist beside the primary ones. In *Im*$\bar{3}$ M_1^+ acts as a secondary induced mode, it leads to size differences between the cuboctahedra A(2a)O_{12} and A(6b)O_{12}. Its isotropy subgroup *Im*$\bar{3}$*m* is a supergroup of *Im*$\bar{3}$. The two mixed tilted structures *Pnma* and *P*4$_2$*/nmc* cannot be achieved by one primary distortion only. At least two primary order parameters must exist in these structures. Both structures possess distortion modes with irreps at all the zone-boundary points X, M and R. They have in common the modes X_5^-, M_2^+ and R_5^-. The latter two modes are the aforementioned in-phase and anti-phase tilts, respectively. X_5^- we do not know yet. In *P*4$_2$*/nmc* the M_1^+-mode, we encountered already in *Im*$\bar{3}$, is active again. In *Pnma*, there exist two additional new modes. The first is M_3^+, which leads to the same isotropy subgroup *P*4*/mbm* as the in-phase tilts M_2^+, and the second mode is R_4^-, which has the same isotropy subgroup *Imma* as the anti-phase tilts R_5^-. All five modes are prospective primary modes. The method to identify the actual hierarchy of these modes will explained next.

Symmetry-Adapted Distortion Mode Analysis of the *Pnma*-Structure

The *Pnma*-structure was chosen to be discussed in more detail. The first information needed is the unit cell transformation that relates the simple cubic *Pm*$\bar{3}$*m* unit cell to the distorted orthorhombic *Pnma* unit cell. The mathematical background of unit cell transformations, in general, can be found in App. E, where also all transformation matrices and their inverses, used in this work, are specified. Here we just want to give in Eqs. 8.4 the vector description, that transforms the basis vectors of the cubic unit cell $(\mathbf{a}_\mathrm{c}, \mathbf{b}_\mathrm{c}, \mathbf{c}_\mathrm{c})$ into those of the orthorhombic unit cell spanned by the basis vectors $(\mathbf{a}_\mathrm{o}, \mathbf{b}_\mathrm{o}, \mathbf{c}_\mathrm{o})$.

$$\mathbf{a}_\mathrm{t} = \mathbf{b}_\mathrm{c} + \mathbf{c}_\mathrm{c} + 1/2 \tag{8.4a}$$

$$\mathbf{b}_\mathrm{t} = 2\mathbf{a}_\mathrm{c} + 1/2 \tag{8.4b}$$

$$\mathbf{c}_\mathrm{t} = \mathbf{b}_\mathrm{c} - \mathbf{c}_\mathrm{c} + 1/2 \tag{8.4c}$$

The initially B-cation centred cubic unit cell transforms into an orthorhombic unit cell with the B-cation at the origin, as indicated by the origin shift of $\boldsymbol{p} = (1/2, 1/2, 1/2)$. Moreover, the transformed cell is doubled along the y-axis, and rotated by 45° about the same axis. As a consequence the unit cell volume quadruples upon this unit cell transformation. With this information the group-subgroup tree for the transformation *Pm*$\bar{3}$*m* → *Pnma* ($\mathcal{G} = 221$, $\mathcal{H} = 62$ and $[i] = 24$) can be obtained, it is given in Fig. 8.4. All isotropy subgroups are highlighted and the corresponding active irreps are given. There are two different kinds of isotropy subgroups in this graph highlighted in blue and red. The blue isotropy subgroups are all associated with Γ-distortions, which in this special case do not have any impact on the occupied Wyckoff positions 1a, 1b and 3c of the parent structure *Pm*$\bar{3}$*m*. Only the red isotropy subgroups with irreps at M, X and R induce displacements of the atoms on 3c, some of them even on 1a, as can be seen in Tab. 8.2. From the group-subgroup graph we can learn already, that M_2^+ and M_3^+ are not the two primary modes, as their simultaneous condensation leads to subgroup *Pbam*, which is a supergroup of *Pnma*. However, any other combination of two irreps is sufficient to reduce the symmetry to *Pnma*.

More information we can only obtain by investigating a specific crystal structure. But first, let us understand to which atomic displacement patterns these distortion modes lead. All five symmetry-adapted distortion modes are visualized in Fig. 8.5 with displacement vectors of arbitrary lengths in the orthorhombic unit cell of the *Pnma*-structure. The R_5^--mode in (a) corresponds to the anti-phase tilts leading to the tilt system $a^-b^oa^-$, the two modes R_4^- in (b) and X_5^- in (c) can be described as shear deformations of the BX_6-octahedra accompanied by different antipolar displacement patterns of the A-atoms in the ac-planes. The M_2^+ mode in (d) is the in-phase tilt $a^ob^+a^o$ and M_3^+ in (e) is characterized by Jahn-Teller distortions of the BX_6-octahedra leading to two shorter and two longer B−X bonds in the ac-plane. This Jahn-Teller distortion is of the M_2^+-type in simple perovskites as described by Carpenter and Howard.[239] Two B−X bonds lengthen/contract while two other bonds within the same BX_6 octahedron contract/lengthen, respectively, the remaining two B−X bonds stay unchanged. Jahn-Teller distortions in adjacent layers along the b-axis are in-phase, as can be seen in (e).

Now we are ready to investigate mode amplitudes and atomic displacements associated with a certain distortion mode. Let us take the optimized equilibrium structure of CaTiO_3 as our specific

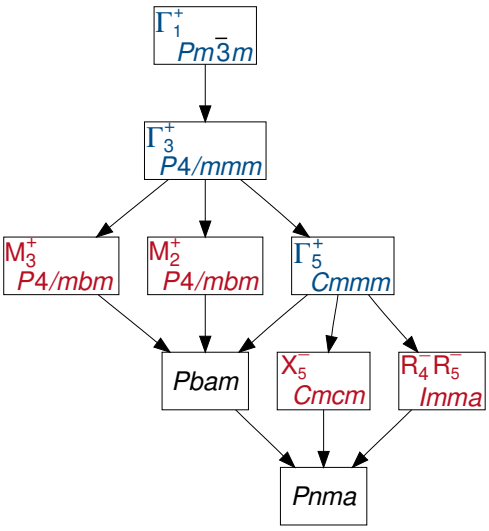

Figure 8.4: Group-Subgroup relations for the transformation $Pm\bar{3}m \rightarrow Pnma$. Isotropy subgroups with their associated irreps are highlighted. The Γ-point distortions are highlighted in blue, because they act only on unoccupied Wyckoff sites, thus they are irrelevant for the studied transition. The relevant irreps and isotropy subgroups are highlighted in red.

example. In Tab. 8.3 the five distortion modes are given with their directions in irrep space, their isotropy subgroups and mode amplitudes. We see that the two tilt modes M_2^+ and R_5^- have the highest amplitudes with values 0.8745 and 1.2631, respectively. The amplitudes of the remaining modes are significantly smaller. Especially, the amplitudes of the Jahn-Teller mode M_3^+ and of the R_4^- antipolar mode are negligibly small. Only the X_5^--mode with 0.4941 has an amplitude of the same order of magnitude as the tilt modes. From the mode amplitudes we can infer, that the two tilt modes together act as primary distortion modes. X_5^- can be ruled out as third primary mode, first because three primary modes are very rare and second because M_2^+ and R_5^- are fully sufficient to reduce the symmetry to *Pnma*.

Table 8.3: Analysis of the symmetry-adapted distortion modes in structurally optimized $CaTiO_3$ at $V_0 = 53.834$. Å^3/f.u.

Irrep	Direction	Isotropy subgroup	Mode Amplitude	Dimension	Distortion type
X_5^-	$(0,0,a,0,0,0)$	*Cmcm*	0.4941	2	BX_6-shear, antipolar
M_2^+	$(a,0,0)$	*P4/mbm*	0.8745	1	$a^o a^o c^+$ tilt
M_3^+	$(a,0,0)$	*P4/mbm*	0.0015	1	Jahn-Teller
R_4^-	$(0,a,a)$	*Imma*	0.0963	2	BX_6-shear, antipolar
R_5^-	$(0,a,-a)$	*Imma*	1.2631	1	$a^- a^- c^o$ tilt

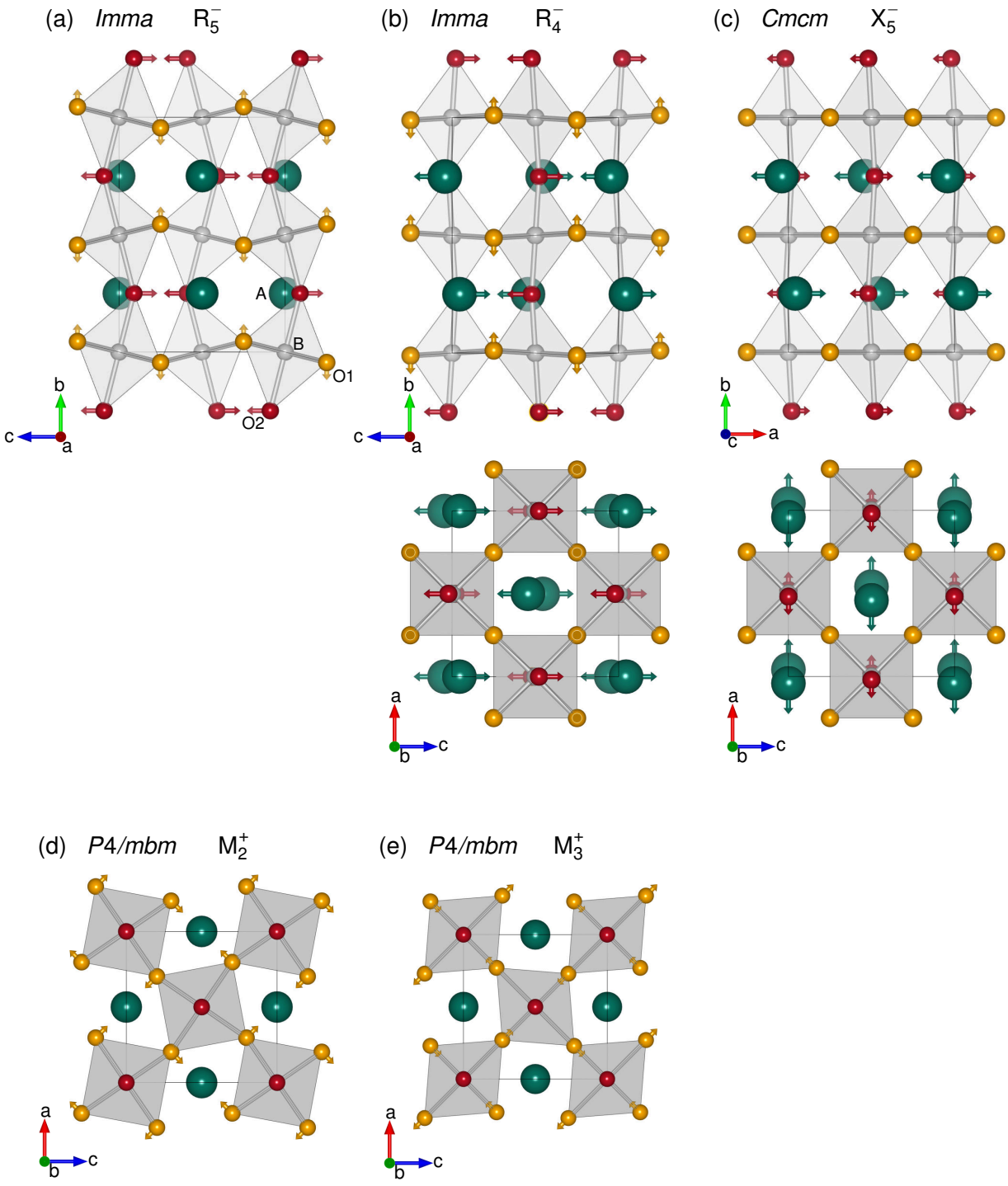

Figure 8.5: Visualization of the symmetry-adapted distortion modes which are active within the orthorhombic *Pnma*-structure: (a) *Imma* R_5^- anti-phase tilt $a^-a^-c^o$, (b) *Imma* R_5^- shear-deformation of octahedra and chequerboard antipolar displacements of A, (c) *Cmcm* X_5^- shear-deformation of octahedra and planar antipolar displacements of A, (d) *P4/mbm* M_2^+ in-phase tilt $a^oa^oc^+$ and (e) *P4/mbm* M_3^+ Jahn-Teller distortion of octahedra.

The fifth column labelled Dimension n in Tab. 8.3 gives not the dimension of the irrep but the dimension of the displacement vector of the distortion, i.e. the number of free parameters in the atomic coordinates. In Tab. 8.4 the atomic displacements are presented with respect to the parent structure given in the low-symmetry setting for the secondary X_5^--mode. The dimension of the displacement vector of this distortion is 2, thus we find two displacement components. The Ca and O2-atoms are displaced in x-direction by 0.2241 and 0.1041 Å, respectively. All other displacement components are zero. The atomic displacements can also be seen as vectors in Fig. 8.5 (c). Mode amplitudes and components of displacement vectors always depend on composition, volume and strain-state of a material. The presence of Jahn-Teller cations like Cu^{2+} (d^9), low-spin Ni^{2+} (d^7) or high-spin Mn^{3+} (d^4) on the B-site can enhance the M_3^+-mode significantly. Interestingly, the ratio of the amplitudes of the two tilt modes R_5^- and M_2^+ is close to $\sqrt{2}$, which means that the resulting tilt system is approximately $a^-a^-a^+$ with equal rotation angles about all Cartesian axes x, y, z irrespective of the rotation sense.

Table 8.4: Atomic displacements resulting from the secondary X_5^--mode in structurally optimized $CaTiO_3$ at $V_0 = 53.834$. Å^3/f.u.

Atom Type	Wyckoff Position	δx [Å]	δy [Å]	δz [Å]
Ca	4c	0.2241	0.0000	0.0000
Ti	4a	0.0000	0.0000	0.0000
O1	8d	0.0000	0.0000	0.0000
O2	4c	0.1041	0.0000	0.0000

8.9 Chemical A-Site Order

Besides atomic displacements, also changes in site occupation can be described in terms of group-subgroup relations. As examples the six different A-site configurations, that will be discussed later in this work, are taken. In a 2×2×2 perovskite supercell there are eight A-atoms situated on a simple cubic sublattice. For the 1:1 stoichiometric ratio of A and A' (exemplary for Na and Bi in $Na_{0.5}Bi_{0.5}TiO_3$) six distinctive arrangements of A-atoms are possible; they are shown in Fig. 8.6. Three of these configurations possess alternating layers of the two cation types along the three

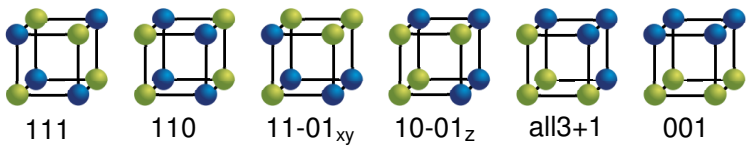

Figure 8.6: A-site configurations in a 2×2×2 perovskite supercell for the stoichiometric ratio 1:1 for A (green) and A' (blue). The simple cubic sublattice of the A/A'-atoms is shown only.

high-symmetry pseudo-cubic directions [001], [110] and [111]. In '$(10\text{-}01)_z$' and '$(11\text{-}01)_{xy}$', there are columns of same cations present. In the '$(10\text{-}01)_z$' configuration these columns are arranged along [10(0)]- and [01(0)]-directions alternately stacked along the z-axis, while in the '$11\text{-}01_{xy}$' configuration they are arranged along [(0)11]- and [(0)01]-directions when looking along x-axis and along [1(0)1]- and [0(0)1]-directions when looking along y-axis. The 'all3+1' configuration is characterized by the fact that in adjacent {001}-planes 3:1 and 1:3 stoichiometries of A and A' are realized. All configurations result from a specific symmetry-lowering associated with a

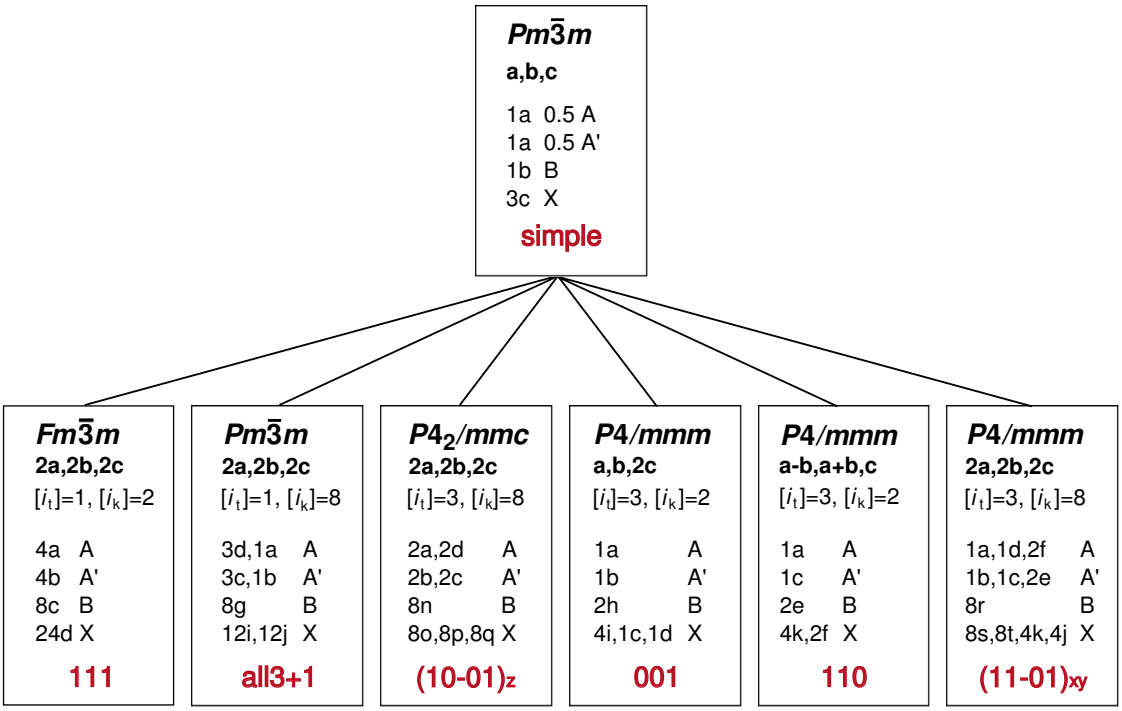

Figure 8.7: Unit cell transformations with transformation indices and splittings of Wyckoff positions for the A-site ordered perovskite structures.

single irrep with respect to the simple perovskite structure with space group $Pm\bar{3}m$. The unit cell transformations and resulting Wyckoff splittings are presented in Fig. 8.7. The structures are sorted from left to right with decreasing symmetry and within the $P4/mmm$-space group with increasing unit cell size. The rock-salt ordered structure '111' with space group $Fm\bar{3}m$ is given in the conventional cubic setting, where the unit cell contains eight formula units. However, there exists a rhombohedral primitive unit cell with two formula units of $A_{1/2}A'_{1/2}BX_3$ only. All atoms in $Fm\bar{3}m$ occupy special positions with all coordinates fixed to specific values. In this structure the only degree of freedom is the unit cell volume (lattice parameter).

All other unit cells are primitive cells. The 'all3+1'-order leads to an isomorphic transformation with an octuplied unit cell $Pm\bar{3}m$. A and A' occupy each two Wyckoff positions with different site symmetries. Positions 1a and 1b keep the octahedral site symmetry $m\bar{3}m$ of the parent structure, but the symmetry of the positions 3c and 3d is reduced to tetragonal $4/mmm$. The X-site is split into 12i and 12j. The X-atoms 12i span the cuboctahedron coordinating the A-atoms on 1a and those on 12j span the cuboctahedron coordinating the A'-atoms on 1b. '$(10\text{-}01)_z$'-order also has an unit cell with eight formula units. All atoms A and A' occupy sites with identical orthorhombic symmetry

mmm but described by different Wyckoff positions (2a-d). The X-site is split into three equivalent sites (8o-q) with monoclinic symmetry *m*. The remaining three order types result in the same space group *P4/mmm*, but their unit cells possess different basis vectors. The layered structure with '001'-order is doubled in z-direction. All atoms A and A' occupy sites with tetragonal symmetry 4*/mmm*. The X-sites is split into three sites with tetragonal symmetry 4*/mmm* (1c, 1d) and orthorhombic symmetry 2*mm*. The layered '110'-order has a doubled unit cell too. But this unit cell is rotated in the ab-plane by 45° instead of doubled along z. Site symmetry of all A and A' is again tetragonal 4*/mmm*. The X-atoms occupy sites with orthorhombic *mmm* (2f) and *m*2*m* (4k) symmetries. The last order is '$(11\text{-}01)_{xy}$', with a unit cell spanned by doubled basis vectors along all three directions. Atoms A and A' each occupy sites with site symmetries 4*/mmm* (1a-d) and *mmm* (2e and 2f) in the ratio 1:1. The X-site is split into four. Two equivalent orthorhombic sites (4k, 4j) with symmetry *m*2*m* and two equivalent monoclinic sites (8s, 8t) with symmetry *m*.
What all these structures have in common is that the B-site never splits and that all A/A'-atoms occupy sites with inversion symmetry $\bar{1}$, which results from the special choice of the supercell geometry. Moreover, A and A' always occupy equivalent sites, which belong to the same Wyckoff sets. This is a result of the stoichiometry.

Table 8.5: Symmetry-adapted distortion modes in A-site ordered perovskite structures. Only active modes are given.

A-site Order	Space group	k-Point	Irrep	Direction	Isotropy subgroup	Wyckoff
111	*Fm*$\bar{3}$*m*					
all3+1	*Pm*$\bar{3}$*m*	$(0, 1/2, 0)$	X_1^+	(a, a, a)	*Pm*$\bar{3}$*m*	1b, 3c
$(10\text{-}01)_z$	*P*4_2*/mmc*	$(0, 1/2, 0)$	X_2^+	$(-a, -b, -a)$	*P*4_2*/mmc*	1b, 3c
001	*P*4*/mmm*	$(0, 1/2, 0)$	X_1^+	$(0, a, 0)$	*P*4*/mmm*	1b,3c
110	*P*4*/mmm*	$(1/2, 1/2, 0)$	M_1^+	$(a, 0, 0)$	*P*4*/mmm*	3c
$(11\text{-}01)_{xy}$	*P*4*/mmm*	$(0, 1/2, 0)$	X_1^+	(a, b, a)	*P*4*/mmm*	1b, 3c

The accompanying displacive distortion modes with their direction vectors and isotropy subgroups are summarized in Tab. 8.5 and visualized in Fig. 8.8. Three different 3-dimensional irreps can be found to be acting on the atoms in Wyckoff positions 1b (B) and 3c (X).
There is no distortion mode associated with the transformation *Pm*$\bar{3}$*m* $\rightarrow$ *Fm*$\bar{3}$*m*. As stated before does the *Fm*$\bar{3}$*m*-structure not possess any degrees of freedom except the volume (lattice parameter). Therefore, no internal distortion mode exists. The X_1^+-mode accompanies 'all3+1', '001' and '$(11\text{-}01)_{xy}$'-order and induces displacements on both the B- and X-atoms. '$(10\text{-}01)_z$'-order leads to an X_2^+-mode acting on both B- and X-atoms, while '110'-order results in a M_1^+-mode acting on the X-atoms only.
All these distortion modes are solely induced by the differences in A-site occupancy. Distortions of this type will later in this work be referred to as *chemically induced* distortion modes. Except for '110', where chemically induced distortions are found for X-atoms only, in all other chemical A-site orders distortions are induced on both B- and X-atoms.

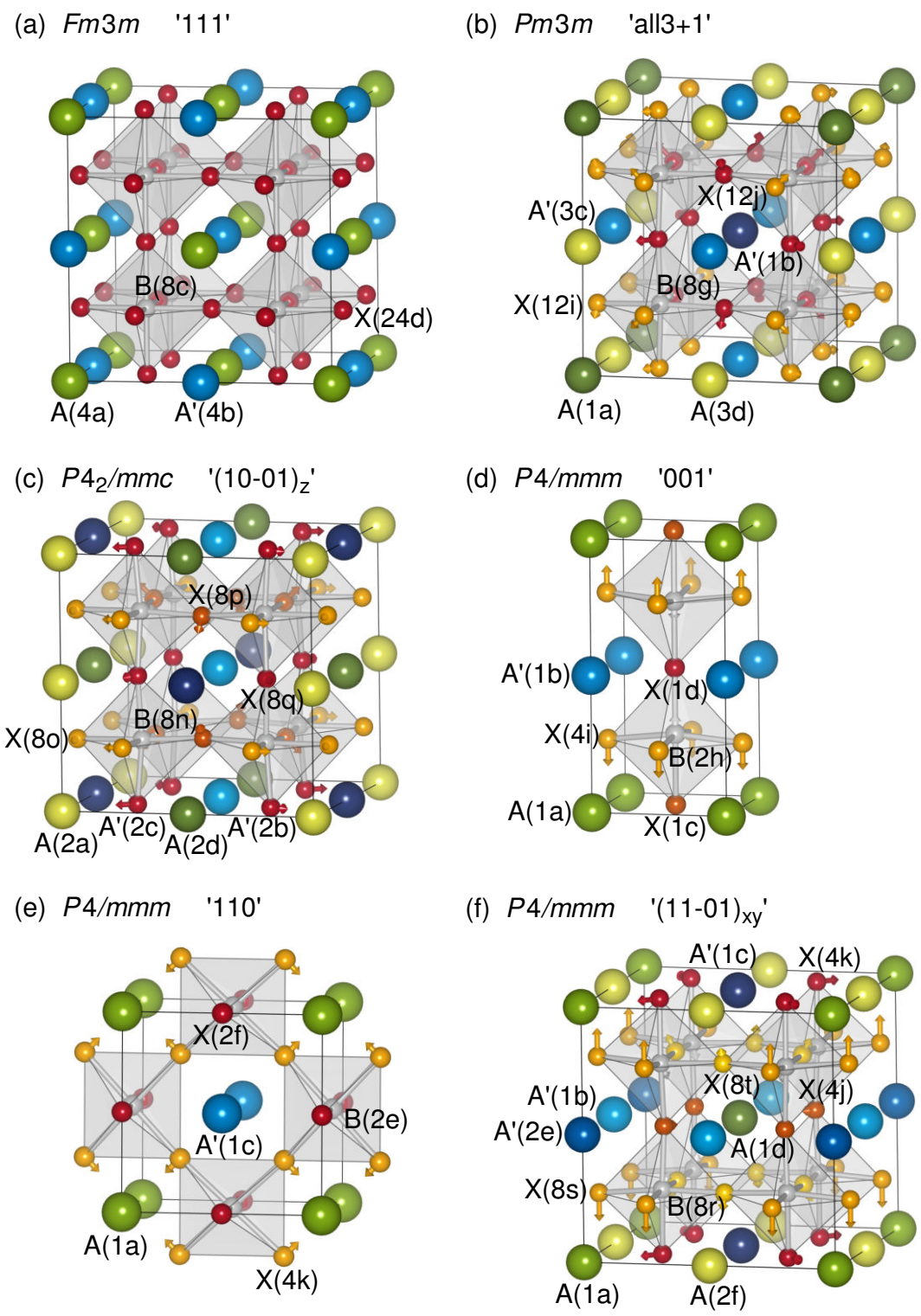

Figure 8.8: Structures and visualization of the chemically induced distortion modes in the the six ordered configurations. Wyckoff positions are indicated by different colors.

Part III

Results

9 Chemical A-site Order

One of the first questions arising when studying a cation mixed system such as $Na_{1/2}Bi_{1/2}TiO_3$ (NBT), is whether there exists chemical order on the mixed crystallographic site or not. This is important as chemical order/disorder is understood to be one of the key ingredients that causes relaxor behaviour in mixed perovskites. In this chapter total energies and densities of states of selected ordered configurations are compared in order to answer this question and to identify driving forces for the ordering process. It is found that chemical order in alternating layers of Na^+ and Bi^{3+} along the $\langle 001 \rangle$ directions is the preferred ground state of NBT. The origin of the high stability of such layers can be found in the enhanced hybridization between Bi $6sp$ and O $2p$ states. The probability of the formation of long-range chemical order at synthesis conditions is discussed. Moreover, the chance of enhancement of chemical ordering in other substituted bismuth titanates is investigated.

9.1 Ordered Configurations

$Na_{1/2}Bi_{1/2}TiO_3$ and all other compounds investigated in this chapter are A-site mixed perovskites. For a 1:1 composition there exist 6 distinctive arrangements of A/A'-atoms, they are shown in Fig. 9.1. These chemically ordered configurations were presented in terms of their symmetry properties in the previous chapter, where space groups and Wyckoff splitting with respect to the simple perovskite structure $Pm\bar{3}m$ are given. '111' and 'all3+1' cation configurations lead to cubic symmetries, while the remaining configurations result in tetragonal structures.

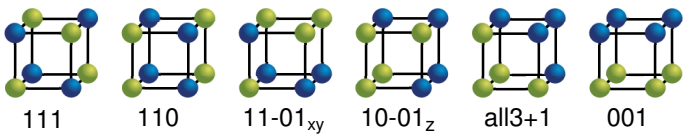

Figure 9.1: 2×2×2 perovskite supercell configurations, the simple cubic sublattice of A-atoms is shown only. (A: green, A': blue)

9.2 $Na_{1/2}Bi_{1/2}TiO_3$

9.2.1 Relative Stabilities of Ordered Configurations

First, we want to compare total energies of the different ordered Bi/Na-configurations in ideal cubic perovskite structures and in relaxed structures at the experimental volume. We focus on the high temperature cubic phase ($a = 3.9137$ Å), where mobility is sufficiently high to allow for cation redistribution. The results are shown in Fig. 9.2 (contributions from ionic and cell shape relaxation are given separately).

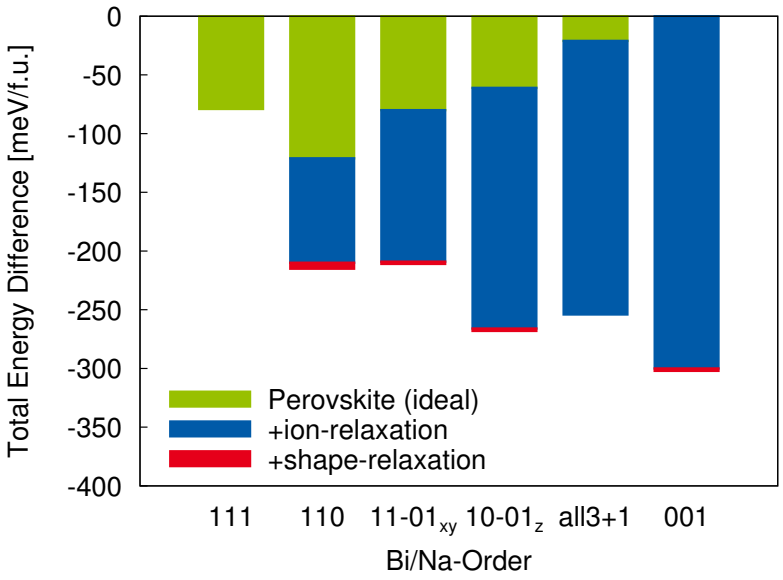

Figure 9.2: Total energy differences from DFT calculations in ideal perovskite (green) and relaxed structures (blue and red). Energy changes from cell shape relaxation (red) are very small.

In the ideal perovskites the different configurations reveal only small variations in total energy of less than 120 meV, with '110' being the most favored and '001' being the most unfavoured order type. Taking structural relaxations into account the maximal difference is almost doubled (220 meV). The most stable structure now is the layered '001' configuration, while the rock-salt ordered system '111' becomes the most unfavoured one. We find that the more unstable a structure is in the ideal perovskite the more energy it can gain from structural relaxation. The rock-salt ordered system does not show any structural relaxation, while all other structures can gain reasonable amounts of energy up to 300 meV. This is demonstrated in Fig. 9.3, where the correlation between DFT relaxation energies and Coulomb lattice sums of the different cation configurations on the ideal perovskite lattice (blue) is shown. The smaller the ionic contribution to the total energy, the larger is the energy gain by local atomic relaxation. Additionally, we show the correlation between DFT total energies and Coulomb energies (green). This correlation is rather poor, indicating that ionic interactions play a minor role and electronic interactions might be more important in this material as commonly assumed.

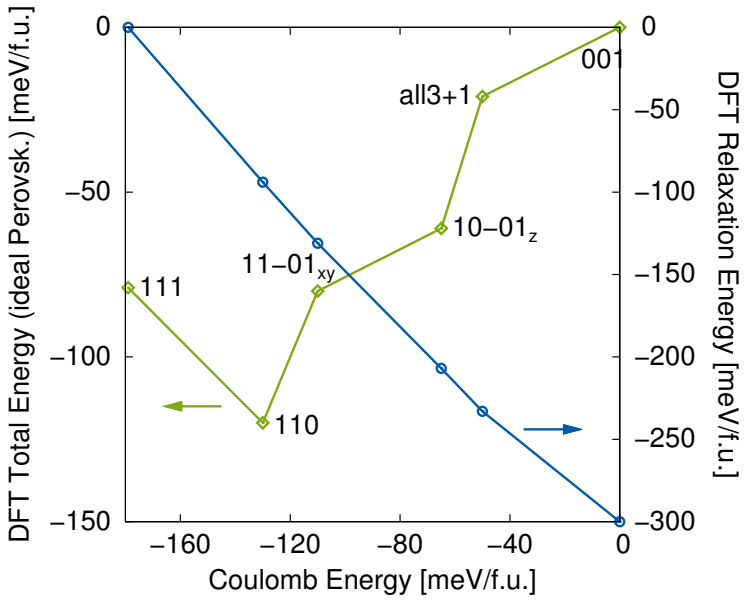

Figure 9.3: Correlation between DFT total energies and Coulomb energies (with $\epsilon_r = 10$) of different cation configurations on the ideal perovskite lattice (green) and between DFT relaxation energies and Coulomb energies (blue). The higher the Coulomb energy of the cation configuration the more energy can the system gain from local structural relaxation.

9.2.2 Structural Relaxation

In the following, we want to investigate the structural changes and stabilizing factors responsible for the high relaxation energies in the '001', '10-01$_z$' and 'all3+1' configurations and the much lower relative stability of the rock-salt ordered structure.
The existence and type of chemical order is determined by the interplay of charge, size and bonding effects. From the electrostatic point of view rock-salt order of the Na^+ and Bi^{3+} ions with alternating layers along the $\langle 111 \rangle$-directions should be the ground state structure of the simple cubic A-site sublattice in NBT, as can be seen from the order of Coulomb lattice sums of the different configurations given in Fig. 9.3. On the other hand, the ionic radii of bismuth and sodium are almost the same: Bi 1.45 Å and Na 1.39 Å[240], but the Bi^{3+} ion size depends, however, strongly on the degree of the $6s^2$ lone pair character. Both ions differ strongly in their bonding properties though, Na forms exclusively ionic bonds while Bi can also contribute covalent bonding parts. Closely related to these cationic properties is the displacing ability of the anionic perovskite sublattice. In the perovskite structure oxygen is quasi-octahedrally coordinated by Bi/Na- and Ti-atoms, with two Ti-atoms in the axial positions of the octahedron at a distance of $a/2$ and four Bi/Na-atoms in the equatorial positions at a distance of $a/\sqrt{2}$, resulting in six possible oxygen environments characterized by the Bi/Na-coordination: $4\times$Na, $4\times$Bi, $1\times$Bi/$3\times$Na, $3\times$Bi/$1\times$Na, and $2\times$Bi/$2\times$Na in cis- or trans-coordination, the latter two are shown in Fig. 9.4. An oxygen ion is expected to displace, if there are significant differences in size, charge or bond strength of the coordinating cations and if the oxygen ion is not an inversion center. Hence, among the six possible coordinations, there are three where no displacement of the oxygen ion is possible (inversion symmetry), namely $4\times$Na, $4\times$Bi and $2\times$Bi/$2\times$Na (trans), one coordination where displacing

is severely facilitated $2\times$Bi/$2\times$Na (cis), while in $3\times$Bi/$1\times$Na and $1\times$Bi/$3\times$Na smaller displacements towards the Bi ions can occur. These displacements can help to release local stresses and to compensate for local charge imbalances, thus stabilizing certain configurations.

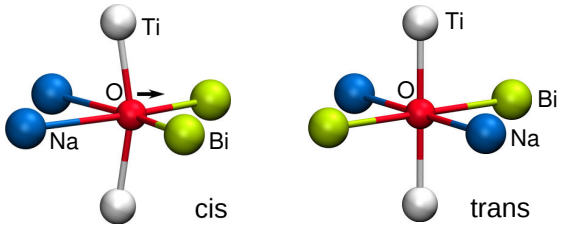

Figure 9.4: Oxygen environments in the $2\times$Bi/$2\times$Na cis- and $2\times$Bi/$2\times$Na trans-coordination.

In Table 9.1 properties of the relaxed structures like c/a-ratio and maximum displacements of Ti and O (Bi/Na do not displace from their ideal positions, because their sites possess inversion symmetry) are summarized. According to the space group symmetries of some A-cation configurations cell shapes may become tetragonal, but c/a-ratios are close to 1.000. We see that the Ti-cations are not considerably displaced. They tend to displace towards Na atoms. Only oxygen anions show significant displacements from their ideal positions. Also given are occurrences of the different oxygen coordinations regarding Bi/Na. All possible oxygen coordinations mentioned above can be found in the six supercell-configurations. $4\times$Na and $4\times$Bi coordinations are only present in the '001' configuration, but $2\times$Bi/$2\times$Na (trans) is present in several configurations, namely the three with the lowest energy gain from relaxation: '111', '110' and '11-01$_{xy}$'. Oxygen ions in these coordinations do not displace from their ideal positions, as expected. The '001' configuration shows the highest relaxation energy and the majority of oxygen anions can be found in

Table 9.1: Properties of the relaxed structures of the Bi/Na-configurations. Also shown are the occurrences of the different oxygen coordinations and electronic bandgaps.

A-Site Configuration	**111**	**110**	**11-01$_{xy}$**	**10-01$_{z}$**	**all3+1**	**001**
Space group	*Fm$\bar{3}$m*	*P4/mmm*	*P4/mmm*	*P4$_2$/mmc*	*Pm$\bar{3}$m*	*P4/mmm*
Relaxed Structures						
c/a-Ratio	1.000	0.989	1.002	1.003	1.000	1.001
Ti Displacement [Å]	0.00	0.00	0.02	0.02	0.03	0.04
Max. O Displacement [Å]	0.00	0.09	0.15	0.14	0.13	0.16
Oxygen Coordination						
$4\times$Na						1/6
$4\times$Bi						1/6
$1\times$Bi/$3\times$Na			1/6	1/3	1/2	
$3\times$Bi/$1\times$Na			1/6	1/3	1/2	
$2\times$Bi/$2\times$Na (cis)		2/3	1/3	1/3		2/3
$2\times$Bi/$2\times$Na (trans)	6/6	1/3	1/3			
Electronic Bandgap [eV]	1.50	1.87	1.80	2.01	1.94	1.90

the $2\times$Bi/$2\times$Na (cis) coordination, where oxygen anions are displaced from their ideal position towards the higher charged and stronger bonding bismuth ions as shown in Fig. 9.4, resulting in size-decreased Bi-polyhedra and size-increased Na-polyhedra, e.g. in the '001' configuration Bi-O distances are decreased from 2.77 Å in the ideal structure to 2.66 Å in the locally relaxed structure. 3+1 coordinated oxygen ions also displace towards the bismuth ions.

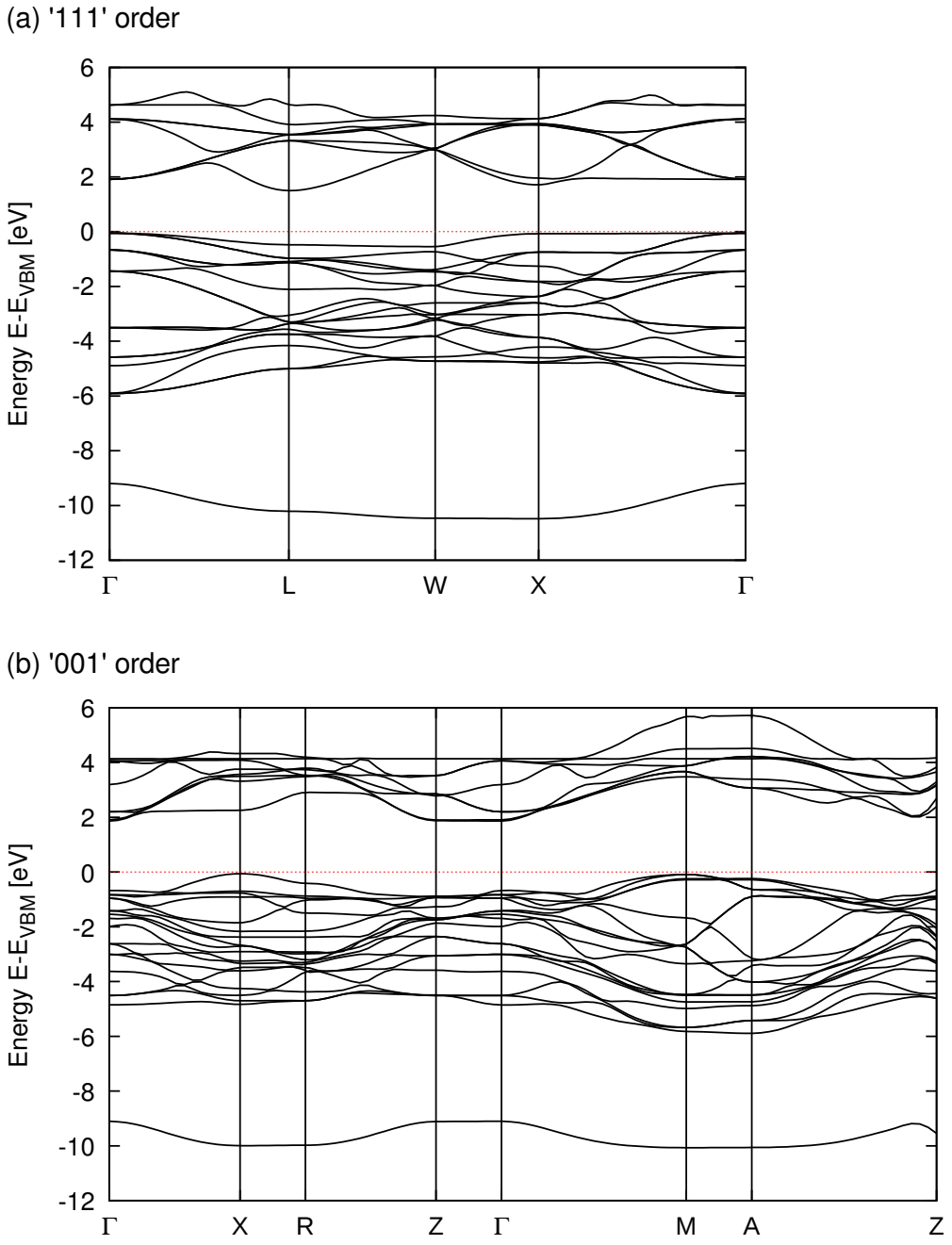

Figure 9.5: Electronic band structures of (a) '111' and (b) '001'-ordered NBT. Band structures were calculated for the primitive rhombohedral and tetragonal unit cells at their equilibrium volumes, respectively.

In summary, local ionic displacements are observed mainly on the oxygen sublattice in the exact way postulated by Woodward,[97,98] while displacements on the titanium sublattice are one order of magnitude smaller. Moreover, structural relaxation can reverse the stability of the considered configurations with respect to the ideal perovskite structure. In the rock-salt ordered structure all oxygen anions are in the $2\times$Bi/$2\times$Na (trans) coordination, which explains why this configuration does not relax at all.
In Table 9.1 also the bandgaps of the relaxed structures are given; they are in the range of 1.50-2.01 eV. Experiments revealed an indirect optical bandgap of 3.20-3.30 eV in thin films.[241] Electronic band structures of the '111' and '001'-ordered structures are shown in Fig. 9.5. In both configurations an indirect bandgap results. It is well known that LDA underestimates bandgaps by up to 100%, but comparison of bandgaps of the same compound only differing in the cation configuration should not be affected by this. We find that local ionic displacements increase the bandgaps, the rock-salt structure has the smallest bandgap which is 0.5 eV below the highest value found in the '10-01$_z$' configuration.

9.2.3 Bader Analysis

In order to investigate electron transfer as a possible driving force for the observed structural relaxations and increased bandgaps, a Bader analysis was applied on the calculated charge densities, which allows to assign electronic charges to every atom. In Fig. 9.6 the Bader charges relative to those in the '111'-ordered structure are given for Bi, Na, Ti and O. The absolute Bader charges in '111' can be found in Tab. 9.2, where the values of the Bader analysis are compared with the nominal charges, which result under the assumption of full ionization (except for Bi(III)). The closer the Bader charge is to the nominal charge the higher is the degree of ionization. The highest value we can find for Na with a ionization of 89%. Bi, Ti and O possess lower ionizations, which are in the same range between 54 and 62%. Thus, bonding between the latter atoms is far from being purely ionic, but possesses considerable covalent contributions.

Table 9.2: Bader charges of Bi, Na, Ti and O in '111'-ordered NBT compared to their nominal values. The accuracy limit of the Bader charges is 0.01e.

Atom	Bader Charge [e]	Nominal Charge [e]	Ionization [%]
Bi	+1.87	+3	62
Na	+0.89	+1	89
Ti	+2.18	+4	54
O	-1.19	-2	59

Fig. 9.6 shows how electron transfer between Bi, Ti and O is increased in all structures relative to '111'-ordered NBT. Also given are the numbers of next bismuth neighbours for Bi and O. The larger the ionic charge difference the higher is the electronic transfer between cations and anions. In all relaxing structures, we find enhanced charge transfer from Ti. The charge of Na in all structures has the same value, its ionization is unchanged irrespective of its coordination. This is in stark contrast to the Bader charges of Bi, which is especially sensitive to the number

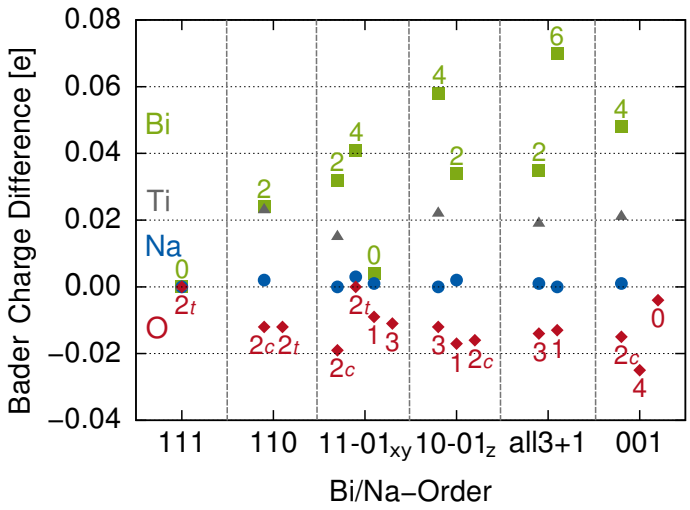

Figure 9.6: Ionic charge differences from Bader analysis given with respect to '111'-order. The accuracy limit is 0.005e.

of next Bi-neighbours. The highest charge difference of 0.07 compared to Bi in '111' shows the Bi atom in 'all3+1-' with six next Bi-neighbours. At charge differences between 0.04 and 0.06 all Bi-atoms with four Bi-neighbours can be found, between 0.02 and 0.04 all those with two Bi-neighbours. The third Bi atom in '11-01_{xy}' has a charge difference close to zero, it has the same A-coordination as Bi in '111'. The charges of the oxygen atoms do not show such strong sensitivity to their coordination. Oxygen atoms in 2×Bi/2×Na (trans)-coordination (2t) can be found in '111', '110' and '11-01_{xy}'. The trans-coordinated O in '11-01_{xy}' has the same charge as O in '111', but the non-relaxing O in '110' has the same charge as the relaxing 2×Bi/2×Na (cis)-coordinated (2c) O in '110', at least within the accuracy limits of the Bader analysis.

Overall, we find some direct correlation between enhanced charge transfer as compared to '111'-order and the relative stabilities of the chemical configurations. The more stable structures show higher charge transfers between Bi, Ti and O, corresponding well with the increased band gaps reported in Tab. 9.1.

9.2.4 Origin of Structural Stability: Density of States

More insights into the driving forces of the structural relaxation we can gain from the analysis of the electronic structure. In the following, densities of states (DOS) are compared. In Fig. 9.7 we show total and site-, l- and m_l-projected densities of states of the '111' and the '001' configurations in ideal perovskite (black dotted line) and structurally relaxed structures (filled). In the '111' configuration, only one type of oxygen is present, 2×Bi/2×Na (trans), while in the '001' configuration we have three different oxygen atoms: 4×Na, 4×Bi and 2×Bi/2×Na (cis) (cf. Table 9.1). There are also two different types of Bi $6p$-orbitals, two lying in the Bi-layer and one perpendicular to it pointing towards the neighbouring Na-layer.

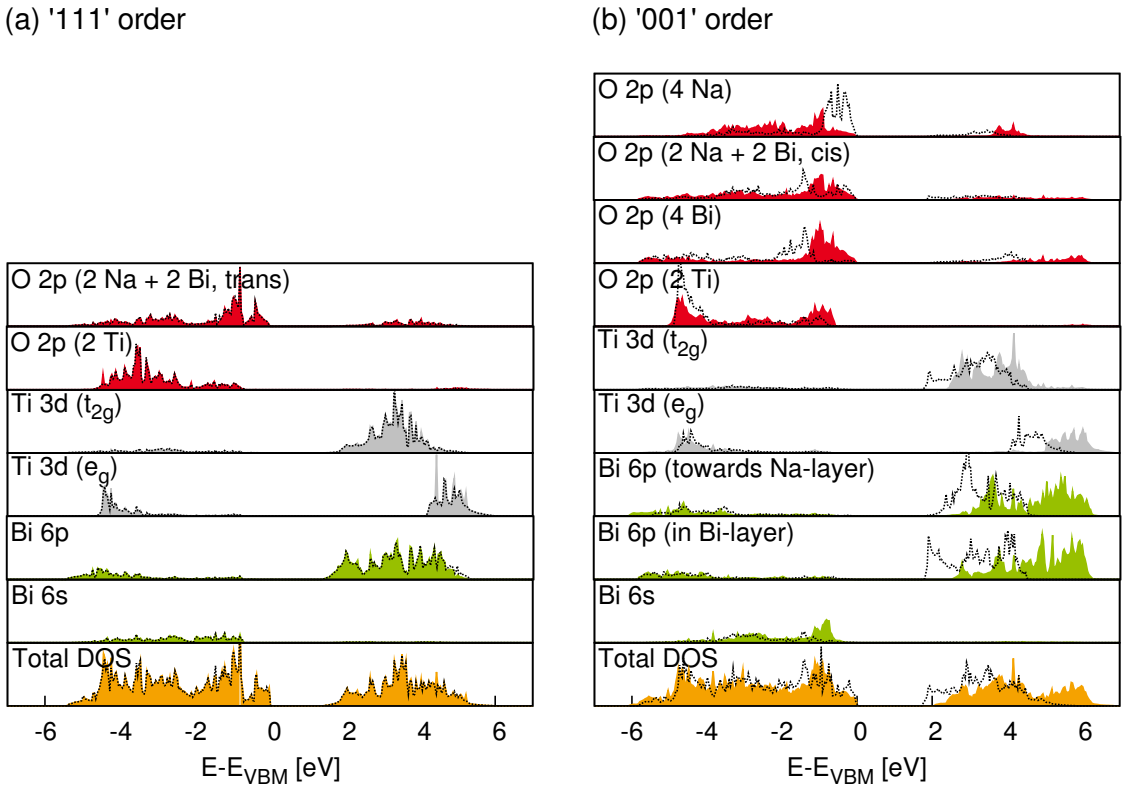

Figure 9.7: Densities of states of configurations '111' (a) and '001' (b) before (black dotted line) and after relaxation (filled) in the cubic perovskite structure. Energies are given relative to the valence band maximum. On structural relaxation - possible in all structures besides the '111' configuration - band gaps are enlarged and changes especially of the Bi $6s$- and O $2p$-state densities occur.

All configurations show a bandgap of 1.5-2.0 eV. The conduction band is formed dominantly by Bi $6p$-states and Ti $3d$-states, which split in the octahedral crystal field into t_{2g} states on the lower energy part of the conduction band and e_g-states, which again split into bonding (in the valence band at -4.5 eV) and anti-bonding (the upper conduction band part above 4.0 eV) states due to interaction with the O $2p$-states. The valence band is formed dominantly by O $2p$-states, with small contributions from Ti $3d$- and Bi $6sp$-states. The maximum of the Bi $6s$-states lies deep below the valence band at -10.0 eV (not shown). The O $2p$-states differ depending on m_l and Bi/Na-coordination of the particular oxygen atom, those orbitals pointing towards Ti show two maxima at the bottom and the top of the valence band, while those orbitals pointing towards Bi/Na show a big maximum only in the upper part of the valence band.

There are three differences between the ideal and relaxed structures' DOS.

- Local oxygen displacements increase the bandgap. The conduction band states are shifted to higher energies by about 0.3 eV in the '001' configuration.
- The order of oxygen states at the valence band maximum (VBM) changes. In the ideal perovskite structure the VBM is formed dominantly by oxygen ions with Na-excess, while oxygen ions with Bi-excess have their density maximum below 0.7 eV. Orbitals with sodium excess are lowered while orbitals with bismuth excess are lifted in energy. These shifts reflect the energy shifts of the coordinating A-cations. The lower lying semi-core states Bi $5d$ and Na $2p$ (not shown) are shifted by +1.0 eV and -0.5 eV, respectively, showing that the on-site Madelung potential of Bi is more favourable in the relaxed structure with local oxygen displacements while that for Na is less favourable.
- Additional Bi $6s$-states arise at the top of the valence band. Although the maximum of $6s$-states stays below the valence band around -10.0 eV, there is a significant increase of the state density in the anti-bonding region above -2 eV, these states mix with both the Bi $6p$-states and the O $2p$-states, which is characteristic for the formation of a stereochemically active Bi^{3+} lone pair.[19,22]

The aforementioned enhanced charge transfer in the '001'-ordered configuration corresponds to the enhanced Bi-O hybridization in the upper valence band region. Although Bi "loses" electrons in the charge-transfer process, it gets back these additional states, which can be understood as a partial re-transfer by sharing.

9.2.5 Chemical Ordering

Generally, chemical ordering will occur if there is a decisive energy difference between the most stable ordered configuration and the disordered state. As we have no possibility to assess energies and entropies of the disordered state by DFT calculations, we can only estimate a lower limit. Thus we assume, first, that the entropy of the ordered state is zero and that the entropy of the disordered state can be approximated by the configurational entropy of an ideal solution with $x_{\mathrm{Bi}} = x_{\mathrm{Na}} = 0.5$,

$$-T\Delta S = -k_{\mathrm{B}}T[-x_{\mathrm{Bi}} \ln x_{\mathrm{Bi}} - x_{\mathrm{Na}} \ln x_{\mathrm{Na}}] \tag{9.1}$$

Second we assume a lower limit for the energy of the disordered state. We know that the energy should be higher than in the ordered state, but we do not know whether it is closer to the energy of '111' order or to any other order we investigated. Thus, we take the worst case scenario and take the energy of the second most stable configuration '10-01_z'. Thus, the problem reduces to a comparison of the energy difference between the two most stable configurations '001' and '10-01_z', which is 34 meV, and the configurational entropy of the disordered state.
Both free energy contributions are presented in Fig. 9.8. At sintering conditions the energy equivalent $T\Delta S$ is more than twice the obtained energy difference between the two most stable ordered

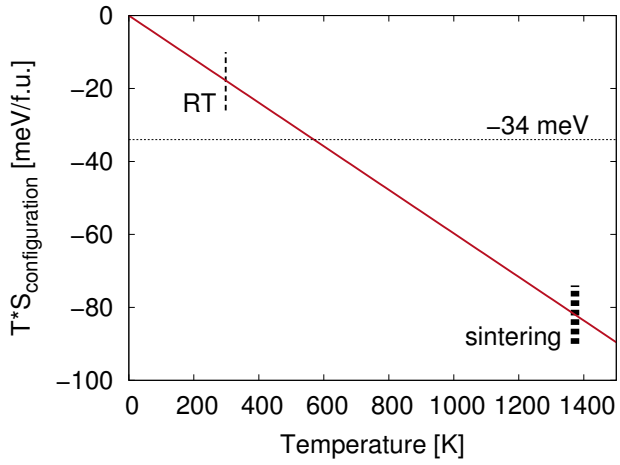

Figure 9.8: Entropy contribution of mixing to the free energy in the disordered state as a function of temperature. RT stands for room temperature.

states, therefore the disordered state is favoured. The critical temperature of the order-disorder transition is about 570 K. Chemical long-range ordering can therefore be ruled out, but short-range ordering with alternating layers of Bi and Na along $\langle 001 \rangle$-directions is still possible to occur.
This approximation gives a lower limit for the ordering temperature, since the ideal solution model is overestimating the mixing entropy and it can be anticipated that the energy of the disordered state is higher than the energy that was chosen.

9.2.6 Volume Dependence of Relative Stabilities

Finally, we will discuss how the relative stabilities of the different chemical orders depend on the unit cell volume. Up to now, we only compared energies for the experimental volume of the cubic phase $V_{\text{exp}} = 59.946$ Å^3/f.u. In Fig. 9.9 the relative stabilities of the less stable configurations with respect to '001' are given as a function of the unit cell volume. The given volume range corresponds to pressures between +40 and -20 GPa. We find that the energies of the chemical configurations possess different dependences on the unit cell volume (or hydrostatic pressure), 'all3+1', '11-01$_{\text{xy}}$' and '111' are destabilized with increasing volume, while '10-01$_{\text{z}}$' and '110' become more stable, leading to changes in the order of the different configurations with changes in volume. The largest energy difference between '001' and the next most stable configuration we find at a volume of about 55 Å^3/f.u. (corresponding to a hydrostatic pressure of 5 GPa), where 'all3+1' and '10-01$_{\text{z}}$' are degenerate in energy. At smaller volumes 'all3+1' is the second most stable configuration, at larger volumes it is '10-01$_{\text{z}}$'. In comparison to the experimental volume of the cubic phase, where the energy difference between '001' and '10-01$_{\text{z}}$' is 34 meV, the maximum energy difference at 55 Å^3/f.u. is only 7 meV higher. Thus, application of hydrostatic pressure has only a minor influence on the tendency of chemical ordering.

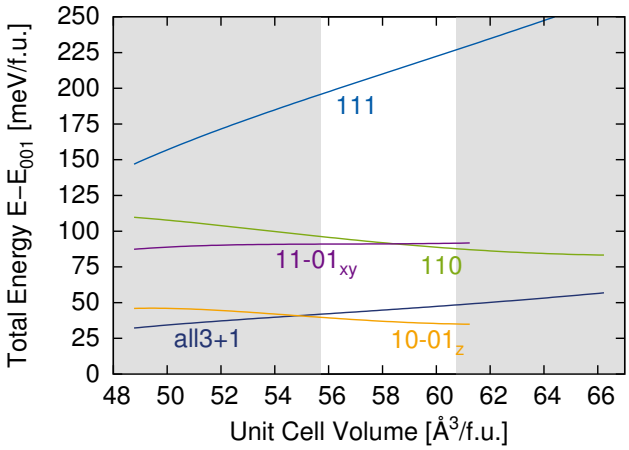

Figure 9.9: Energies of less stable configurations with respect to '001' in NBT under variation of the unit cell volume. The white coloured background corresponds to the volume range accessible in bismuth titanates $M_{1/2}Bi_{1/2}TiO_3$ discussed in Ch. 9.3.

9.3 Enhancement of Chemical Ordering by Substitution

In order to investigate the possibility of the enhancement of chemical ordering from short-range towards larger length-scales - which can be more easily detected by scattering techniques - by inducing chemical changes, i.e. by alloying or doping with other monovalent cations, the structure optimizations were repeated for the compounds $M_{1/2}Bi_{1/2}TiO_3$ with M=Li, Na, Ag, K, Rb, Tl and Cs. Besides NBT only the K-substituted material has been synthesized under ambient pressure, $Ag_{1/2}Bi_{1/2}TiO_3$ could be synthesized at 14.5 GPa.[242] All other compounds are not reported in literature and have to be considered as metastable (at best). Due to the lack of experimental volumes in most cases, all calculations were performed at the equilibrium volume of the respective '111'-ordered configuration in order to have a defined reference framework.

9.3.1 Relative Stabilities of Ordered Configurations

We want to start by comparing total energies of fully relaxed structures of the different chemical orders, this time not only as a function of the order itself but also of the alkali metal M. In Fig. 9.10 the energy differences are given for all compounds MBT with M=Li, Na, Ag, K, Rb, Tl and Cs as a function of their equilibrium volumes. There are three groups of elements, the light alkali metals Li, Na and K, for which the energies depend nearly linearly on the equilibrium volume. The heavy alkali metals Rb and Cs, which exhibit some "chaotic" dependence for the two configurations '10-01$_z$' and '11-01$_{xy}$' as compared to the light alkali metals. The third group is formed by Ag and Tl, which for some configurations are more similar to the light alkali metals. Although Ag and Tl do not belong to the alkali group and have quite different electron configurations (Ag^+ $5d^{10}\,6s^0$ and Tl^+ $5d^{10}\,6s^2$), the stabilities of their ordered bismuth titanates correspond well to those of the alkali bismuth titanates.

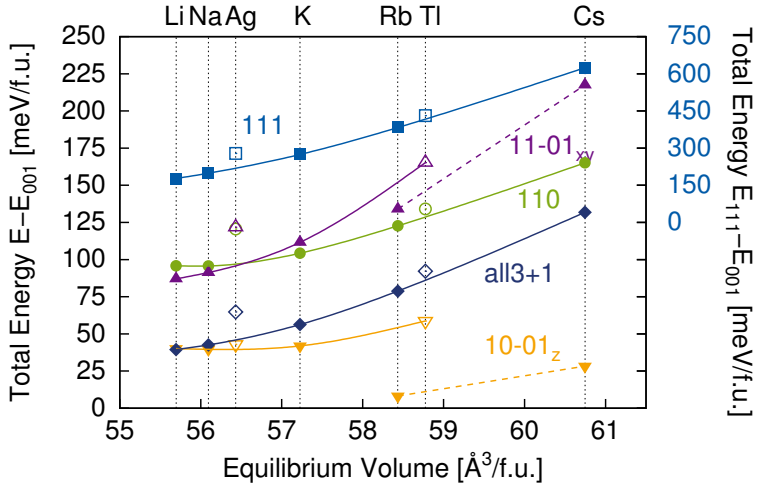

Figure 9.10: Energies of less stable configurations with respect to '001' for the substituted bismuth titanates MBT with M=Li, Na, Ag, K, Rb, Tl and Cs.

The decisive energy difference for chemical ordering, however, is the one for '10-01$_z$' order, which shows little variation for the light alkali metals and for silver. Overall their energy variations are in the same order of magnitude as those for pure NBT under variation of the volume, as shown in Fig. 9.9. Only substitution of sodium by thallium leads to an increase of this energy up to 58 meV, which corresponds to a critical temperature for the order-disorder transition of about 1000 K. As stated above, the energies of the heavy alkali metals for configuration '10-01$_z$' are somewhat out of line, leading to energy differences lower than for the light alkali metals.
These results suggest, that the only possibility to enhance the tendency of chemical ordering in NBT is the incorporation of thallium. As Tl is almost as poisonous as lead, it can only be of restricted academical interest to further investigate $Tl_{1/2}Bi_{1/2}TiO_3$ experimentally.
The largest energy variation can be found for '111', which is probably due to the fact that in this structure the only free parameter is the unit cell volume to adapt to A-cations of different sizes, no internal relaxation is possible to compensate for the size mismatches. Relaxation ability and stability limits of the perovskite structure are the topics, we want to address in the last part of this chapter.

9.3.2 Structural Relaxation Processes and Analysis of Distortion Modes

In the following we want to investigate the individual energy contributions from ionic and shape relaxation in more detail and how they are related to structural changes. The individual energy contributions from ionic and shape relaxation were determined as in Sec. 9.2.1 from the total energies, obtained for static and different relaxed calculations, by subtraction. Both energy contributions will be compared with those quantities, that characterize the underlying structural changes. These are the mode amplitudes of the chemically induced distortion modes and the aspect ratios of the tetragonal structures (both determined in the fully relaxed structures).
First, let us have a look on the shape relaxation. Energies gained by this process are shown in Fig. 9.11 (a). Largest contributions we find for the heavy alkali metals Rb and Cs. In these structures large size mismatches have to be compensated by structural relaxation leading to enhanced internal (atomic positions) and external (unit cell parameters) distortions. Only tetragonal structures can gain energy from shape relaxation resulting in aspect ratios different from unity, these are '110', '11-01$_{xy}$', '10-01$_z$' and '001'. The evolution of the aspect ratios are presented in (b). The largest energy gain can be found in the '110'-ordered structures. The aspect ratio changes from 0.996 for Li to 0.960 for Cs, giving an increase in lattice strain from -0.4 to -4.0%. In a similar range variations in the aspect ratios of '001'-ordered structures are found, which changes from elongation ($c/a > 1$) for the small alkali metals Li and Na, and Ag to contraction ($c/a < 1$) for the large alkali metals Rb and Cs, and Tl. For K the aspect ratio is close to unity, accordingly, we find zero relaxation energy for K and increasing relaxation energies the stronger the unit cell distortion is for the remaining alkali metals. A non-continuous behaviour in both energies and aspect ratios show the more "complex" orders '10-01$_z$' and '11-01$_{xy}$' in Fig. 9.11. For Li, Na, K, Ag and Tl only small lattice strains are found in both configurations. For Rb and Cs the unit cells of '10-01$_z$' exhibit large deviations from the cubic structure, which lead to large energy gains. Compounds with the '11-01$_{xy}$'-order exhibit the lowest shape relaxation energies, which corresponds to small variation of aspect ratios between 1.000 and 1.010.

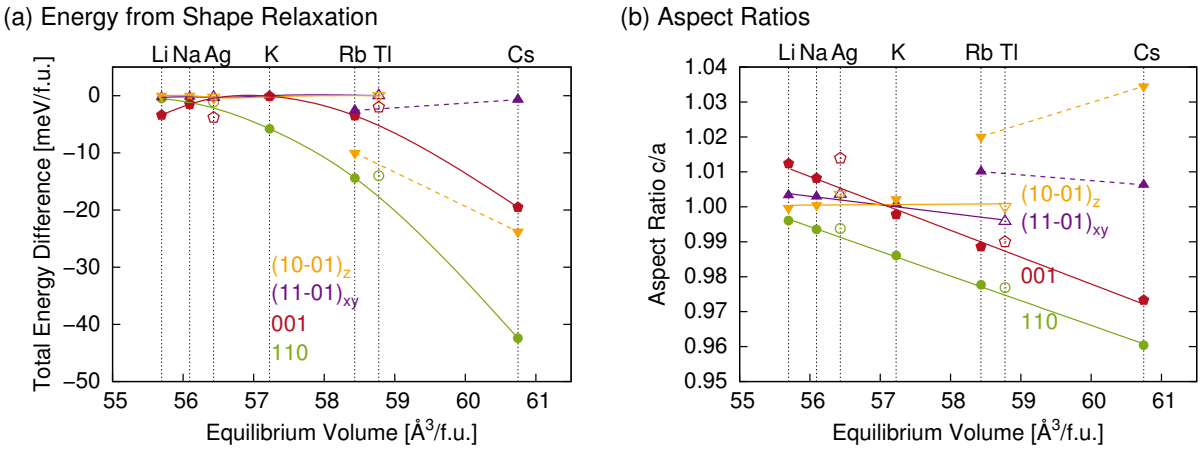

Figure 9.11: Comparison of energy contributions originating from shape relaxation (a) and resulting aspect ratios c/a (b) in the tetragonal structures '110', '11-01$_{xy}$','10-01$_z$' and '001'.

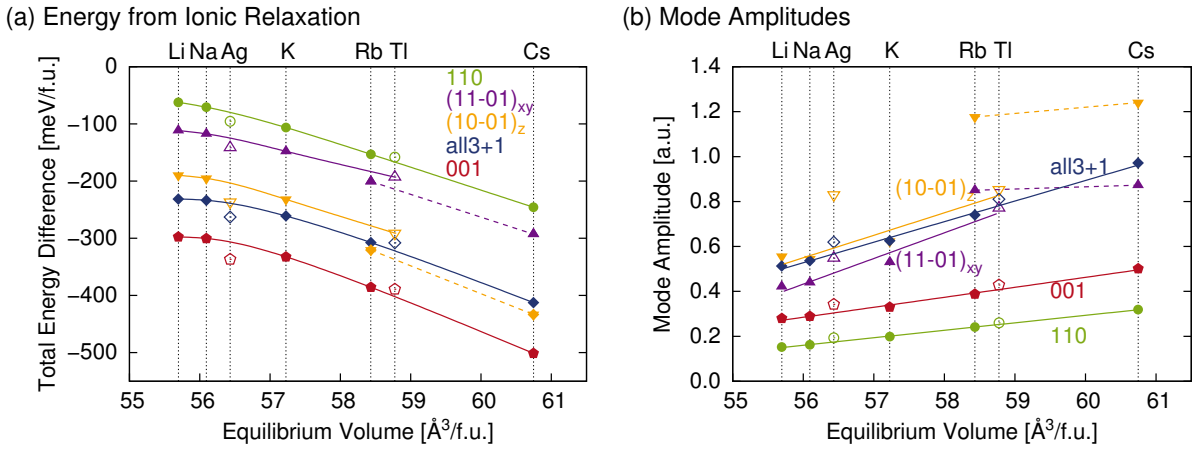

Figure 9.12: Comparison of energy contributions originating from ionic relaxation (a) and resulting mode amplitudes (b) in the structures 'all3+1', '110', '11-01$_{xy}$','10-01$_z$' and '001'.

Now, let us focus on the ionic relaxation. Energy contributions from this process are given in Fig. 9.12 (a) and mode amplitudes in (b). The energies gained in this "internal" relaxation process are the dominating contribution to the total energies. The ionic relaxation energies increase strongly with increasing equilibrium volume. Ionic relaxation energies of the Li and Na compounds are very similar in all configurations. For heavier alkali ions they depend almost linearly on the equilibrium volume leading to energy differences between Li and Cs of about 200 meV/f.u. Only configuration '10-01$_z$' shows exceptional behaviour. The relaxation energies for M=Li, Na, K in configuration '10-01$_z$' are smaller than those of 'all3+1' by about 40 meV, while for the heavier homologues they are greater by about 20 meV. This corresponds very well with the highly increased amplitudes of the chemically induced distortion mode shown in Fig. 9.12 (b) and of the aspect ratio given in Fig. 9.11 (b) for the '10-01$_z$'-ordered compounds with M=Rb, Cs. Generally, amplitudes of these types of distortion can be assumed to be proportional to the equilibrium volume. This assumption is confirmed by almost all configurations, the mode amplitudes of '110', '001' and 'all3+1' depend almost linearly on the equilibrium volume, only '10-01$_z$' and '11-01$_{xy}$' show deviations from this behaviour. For these two, the linearity is found only for M=Li, Na, K and Tl but not in case of the larger homologues Rb and Cs, for which the amplitudes are very high and almost constant. The smallest mode amplitudes are found for '110'-order and the largest in 'all3+1'. This can be easily explained by the number of atoms involved in the distortion mode, as the mode amplitude becomes larger, the more atoms displace and the further they move. In '110' only O1 atoms displace, which are 40% of all atoms, while in 'all3+1','11-01$_{xy}$' and '10-01$_z$' only Na and Bi atoms are fixed, thus 80% of the atoms are involved in the distortion mode, leading to larger mode amplitudes.

In Fig. 9.13 the atomic displacements associated with the chemically induced distortion modes in chemical configurations 'all3+1' and '10-01$_z$' are shown (a visualization of the atoms and distortion modes can be found in Fig. 8.8). In both structures we can observe, how Ti favours in general displacements towards the lower charged monovalent ions, but in case of Cs this ion takes so much space, that Ti atoms are displaced towards Bi instead. In 'all3+1' all atomic displacements are

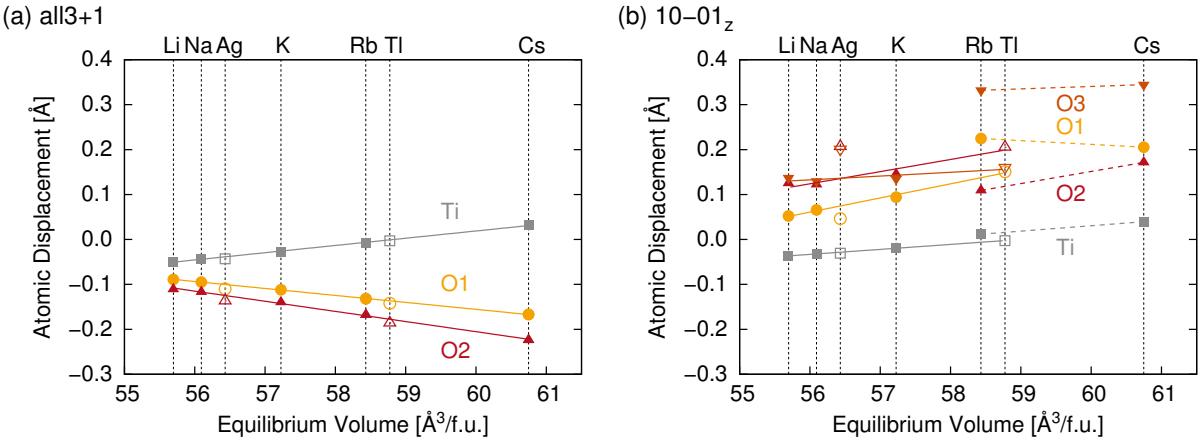

Figure 9.13: Atomic displacements associated with the chemically induced distortion modes in (a) 'all3+1'and (b) '10-01$_z$'.

enhanced by about 0.1 Å if lithium is exchanged by caesium. O2 with coordination 3×Na/1×Bi exhibits larger displacements than O1, which is coordinated by 1×Na/3×Bi. In '10-01$_z$' largest displacements of almost equal magnitude exhibit O2 and O3. O2 has coordination 3×Na/1×Bi and O3 is 2×Na/2×Bi (cis)-coordinated. Atomic displacements of O1 are about 0.1 Å smaller than those of O2 and O3. O1 is coordinated by 1×Na/3×Bi. For the heavy alkali ions Rb and Cs oxygen displacements are irregularly enhanced and suppressed. Similar is the situation in '11-01$_{xy}$', whose atomic displacements can be found together with those of the remaining chemical orders in App. B.

Well-defined linear correlations between relaxation energies or structural properties and the equilibrium volumes of the compounds MBT are found for the light alkali homologues Li, Na and K and for Ag and Tl in all chemically ordered configurations. Rb and Cs in contrast show strong deviations from linearity in case of the configurations '10-01$_z$' and '11-01$_{xy}$'. These two structures have the lowest symmetries, which is expressed in the high degree of Wyckoff splittings and the large sizes of the unit cells (8 f.u.). The higher symmetric structures like '001', '110' and 'all3+1' offer better possibilities to accommodate the size mismatches between M^+ and Bi^{3+} and the TiO_6 octahedral backbone of the perovskite structure. The structural relaxations of '10-01$_z$' and '11-01$_{xy}$' becoming "chaotic" probably reflects the fact, that for the Rb and Cs compounds the perovskite structure is just not stable, because the alkali ions are simply too large to be incorporated on the A-site.
These size mismatches can be quantified by the Goldschmidt tolerance factor t[243] of the $(M\mathrm{TiO_3})^-$ components:

$$t = \frac{r_\mathrm{M} + r_\mathrm{O}}{\sqrt{2}\,(r_\mathrm{Ti} + r_\mathrm{O})}. \tag{9.2}$$

This factor is based on the assumption that atoms i behave like hard spheres with radii r_i. It is a measure of the size mismatch of M, Ti and O. The closer the value of t is to unity, the better the atoms fit together.

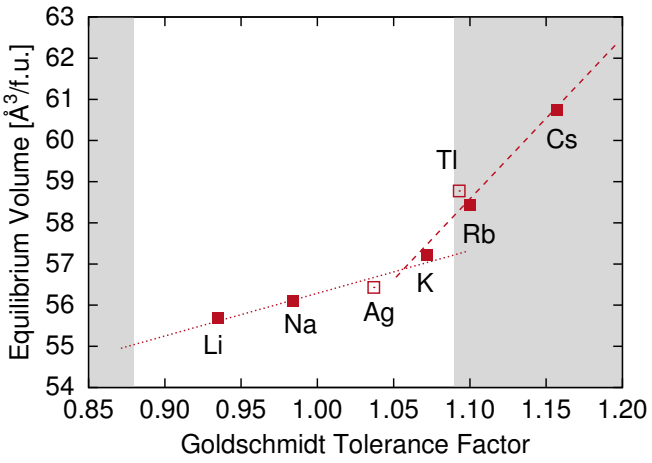

Figure 9.14: Calculated equilibrium volumes of 111-ordered $M_{1/2}Bi_{1/2}TiO_3$ compared with the Goldschmidt tolerance factors determined for the $(M\mathrm{TiO_3})^-$ components using the revised effective ionic radii of Shannon[240] (coordination number 12: Li^+ 1.25 Å, Na^+ 1.39 Å, K^+ 1.64 Å, Ag^+ 1.54 Å, Rb^+ 1.72 Å, Tl^+ 1.70 Å, Cs^+ 1.88 Å, and coordination number 6: Ti^{4+} 0.605 Å, O^{2-} 1.40 Å). Grey shaded areas indicate the ranges of Goldschmidt tolerance factor, where the perovskite structure becomes unstable according to Eitel.[42]

In Fig. 9.14 the Goldschmidt factors of components $(M\mathrm{TiO_3})^-$ are given together with the equilibrium volumes of the respective MBT compounds. The values of the Goldschmidt tolerance factor vary between 0.935 for the Li component and 1.157 for the Cs component. For the component $(\mathrm{BiTiO_3})^+$ a value of 1.005 results, which is close to the one of Na. In literature different ranges of t for the stability of the perovskite structure are reported depending on the ionic radii used. Goldschmidt himself gave as limits $0.8 < t < 1.0$[243], Randall used the effective ionic radii of Shannon and Prewitt[244] and found $0.78 < t < 1.05$[245]. In Fig. 9.14 the limits $0.88 < t < 1.09$ are indicated, as they were reported by Eitel[42] using the revised effective ionic radii of Shannon[240] and considering the correct coordination numbers.

We find two regimes of correlation between the Goldschmidt factors and the calculated equilibrium volumes. Within the perovskite stability limits a linear correlation with a shallow slope is found. For those components with t close to and beyond the upper limit (Tl, Rb and Cs) also a linear correlation is found, but the slope is four times larger than in the first regime. K seems to be a borderline case as it is situated right in the cross section of the two regimes.

It has to be stressed that the effective ionic radius of Li^+ needs to be used very cautiously, because this value was extrapolated from data for the smaller coordination numbers 4, 6 and 8. Li^+ obviously prefers small coordination numbers and does not fit well in the cuboctahedral A-site of the perovskite structure. The ionic radii of the remaining alkali metal ions increase by maximal 15% when increasing the coordination number from 8 to 12, in case of the extrapolated value for Li^+ the increase amounts to 26%. Assuming an increase of less than 20% for the effective ionic radius of Li^+ we obtain a Goldschmidt tolerance factor below the lower stability limit of the perovskite structure at $t = 0.88$.

These results indicate that the Goldschmidt tolerance factor provides a quite reliable rule of thumb for the stability of the perovskite structure. Even for compounds (not solid solutions) it is manda-

tory, that both (hypothetical) individual components ABX_3 and A'BX_3 possess tolerance factors within the stability limits of the perovskite structure not only the averaged compound. This condition is indeed only reliably fulfilled for Na, Ag and K studied here, which have been synthesized successfully.[147,242]
The Goldschmidt factor of $(TlTiO_3)^-$ at the upper stability limit implies, that $Tl_{1/2}Bi_{1/2}TiO_3$ might not be a stable compound. The relative energies discussed above and the "regular" behaviour of the induced distortions in '10-01$_z$' and '11-01$_{xy}$' indicate though, that probably due to the additional lone-pair effect of Tl^+, this material can be stabilized despite the high Goldschmidt factor.

9.4 Summary

In this chapter structural and electronic structure properties of NBT depending on Bi/Na-order were investigated. The importance of structural relaxation in the ordered states was demonstrated and the driving force for this process identified. Most energy is gained by charge transfer between and hybridization of Bi $6sp$-O $2p$ states. This hybridization leading to stereochemically active Bi^{3+} lone pairs increases the stability especially of structures with layers of high Bi-concentrations in $\{001\}$-planes. This kind of planes was considered by Kreisel *et al.* to explain the diffuse scattering patterns indicative for Guinier-Preston-Zones.[126] However, an estimation of the free energy differences between the ordered and disordered structures showed that at temperatures higher than 570 K chemical ordering is unlikely, but different degrees of short-range order can occur depending on synthesis conditions.
Moreover, it was investigated if there is a way to enhance the tendency of chemical ordering by volume changes or substitution of Na by other monovalent metals. Unfortunately, it seems that there is only one way to stimulate long-range chemical order in this type of bismuth titanates, which is the substitution of sodium by thallium. Thallium, however, is almost as poisonous as lead and can thus not be a reasonable alternative.

10 Ground State Structures

After having studied the effect of chemical A-site order, we can dare to increase the complexity of our system by introducing further lattice instabilities such as ferroelectric distortions and octahedral tilts. We carry out a search for the ground state structures of all six types of chemical order at different pressures by including various tilt systems and polar and antipolar displacements. We will discover, that two different types of phase diagrams exist determined by the chemical configuration. For example 111-ordered regions prefer an *R*3*c*-like structure at zero pressure, while 001-ordered regions adopt a *Pbnm*-like structure. The latter is identical to the high-pressure phase of all chemical configurations. Under tensile conditions *P*4*mm*-like structures become energetically stable. The probability of a mixed phase ground state in the vicinity of zero pressure is investigated and the possible shape and size of the *Pbnm*-like regions discussed.

10.1 Phase Stabilities under Pressure

In order to study the influence of chemical order on phase stabilities and pressure-induced phase transitions, we calculated enthalpies for six different cation arrangements in eight different structure types. The cation configurations and tilted structure types were introduced in chapters 8.9 and 8.8, respectively.

We have studied the enthalpies for two conditions: isotropic strain and isotropic stress. We started with the pseudo-cubic lattice parameters, because we wanted first to investigate the interaction between polarization, octahedral tilting and chemical order before additionally including anisotropic lattice strain. This is also from a structural point of view reasonable, as cell parameters of NBT both in the low-temperature rhombohedral phase and the high-temperature tetragonal phase are very close to cubic.[14] Moreover, in a disordered material a more or less locally stressed final state will result.
The two conditions of isotropic strain and isotropic stress represent the possible boundary limits one can encounter in a disordered crystal depending on the response of the matrix to mechanical stresses. In a chemically disordered system like NBT, even if the whole crystal is stress-free, there will arise mechanical stresses on the local scale due to the chemical disorder. Thus unit cells will be strained with respect to their ‘ideal’ equilibrium volumes and shape as they result from first-principles supercell calculations. For this reason the two boundary conditions of isotropic strain and isotropic stress will be discussed.

10.1.1 Isotropic Strain

In a first set of calculations all cell parameters were isotropically rescaled and the pressure was taken from the trace of the stress tensor. In this case two variants of pressure phase-diagrams can be discerned. The first variant shows three stable phases and is adopted by the chemical configurations '110', '11-01$_{xy}$' and '111'. In Fig. 10.1 (a) the phase diagram of '111' is given as an example for this variant. The enthalpies $H(P) - H_{\text{cubic}}(P)$ are shown relative to the respective cubic phases in the pressure range between -15 and $+20$ GPa. At zero pressure the structure type $x^-_+y^-_+z^-_+$ is most stable exhibiting both anti-phase tilts and polarization along the [111]-axis (*R*3*c*-like). Above 2.5 GPa this structure type becomes unstable and a phase transition to $x^-_-y^-_-z^+_0$ takes place (*Pbnm*-like), with one tilt changing to in-phase and polar displacements changing to anti-polar. The transition pressures of this phase transformation are in the range of $2.6 - 3.4$ GPa depending on the chemical configuration, which is in good agreement with transition pressures of $1.6 - 5.0$ GPa (at room temperature) reported in literature.[113,122,126] At negative pressures below -13 GPa another phase transition to structure type $x^o_oy^o_oz^o_+$ (*P*4*mm*-like) without tilts but polarization along the [001]-direction can be observed. Almost identical in enthalpy is the non-tilted rhombohedral structure type $x^o_+y^o_+z^o_+$ ($R3m$-like). The remaining pure and mixed three-tilt systems $x^+_oy^+_oz^+_o$, $x^-_oy^-_oz^-_o$ and $x^-_-y^+_oz^+_o$ are metastable. This holds also true for the structure type with the one-tilt system $x^0_0y^0_0z^+_0$. In general, the more in-phase tilts are present the higher the enthalpy. Highest enthalpies at positive pressures have the non-tilted and the one-tilt system $x^o_oy^o_oz^+_o$. But at negative pressure non-tilted structures become favoured over all tilted structure types. This reflects the tendency of pressure to suppress ferroelectricity and to favour octahedral tilting as observed by Samara.[48]

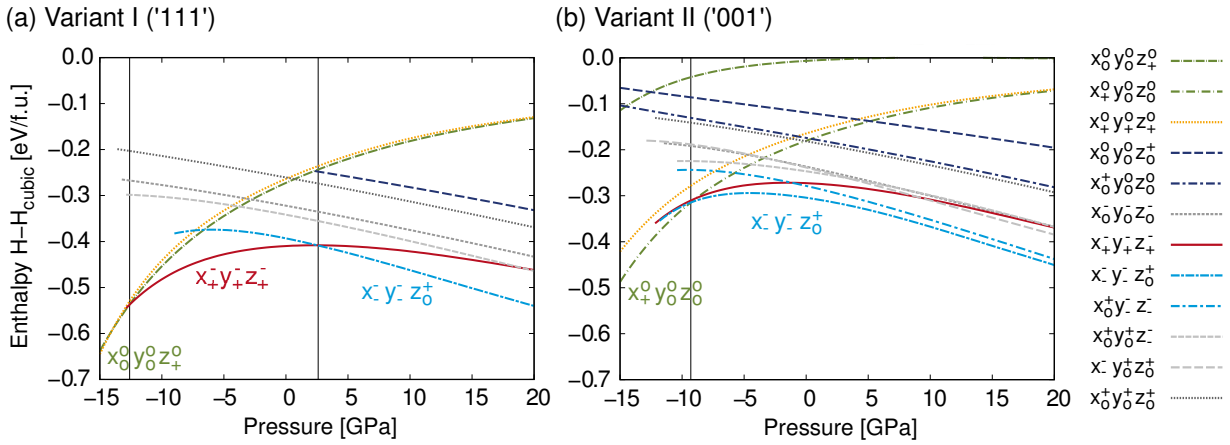

Figure 10.1: Pressure phase diagram variants I and II for $Na_{1/2}Bi_{1/2}TiO_3$ in chemical configurations (a) '111' and (b) '001'. Enthalpies are given relative to the respective ideal cubic perovskite phases.

The second variant of phase diagram is found for the chemical configurations '10-01$_z$', 'all3+1' and '001'. In Fig. 10.1 (b) the phase diagram of chemical configuration '001' is given as an example for this variant. Due to the highly anisotropic chemical order several structure types can be found twice as chemically ordered layers and tilts/polarization can be oriented along different directions

relative to each other. In this second variant we find only two stable phases. Under compression both orientations of the mixed tilted structure type $x^-_-y^-_-z^+_0$ (*Pbnm*-like) are more stable than $x^-_+y^-_+z^-_+$ (*R*3*c*-like) in contrast to the aforementioned chemical configurations. Below a negative pressure of -9 GPa a phase transition to the non-tilted [100]-polarized structure type takes place just as before (*P*4*mm*-like). The second non-tilted tetragonal structure with polarization in [001]-direction is highest in enthalpy. Local depolarizing fields in z-direction due to the chemical order of Bi^{3+} and Na^+ suppress the polarization along [001] leading to the cubic reference structure at positive pressures.
It is noteworthy that the structure type with the lowest energy, $x^-_-y^-_-z^+_o$, is identical to the one identified by Burton *et al.*[246] In contrast to their calculations, however, we do not find the cation arrangement labelled '10-01$_z$' to have lowest energy but the layered chemical configuration '001'.

Next, we want to compare all chemical configurations in their *R*3*c*- and *Pbnm*-like structures. The total energies for the *R*3*c*-like and *Pbnm*-like structure types relative to the lowest value are shown in Fig. 10.2. Also given are the deviations of the volumes and bulk moduli from their average values for the two structure types. Compared to the previous chapter on order phenomena in the high-temperature phase of NBT, the stability sequence of the different chemical configurations does not change in the lower symmetry phases. Chemical configurations '111', '110' and '11-01$_{xy}$' have higher energies than '10-01$_z$', 'all3+1' and '001' in both structure types (and in all others). For every chemical configuration the ground state is marked with $\star$ in Fig. 10.2. It can be seen that the less stable chemical configurations adopt *R*3*c*-like structures and the more stable chemical configurations adopt *Pbnm*-like structures as their zero pressure ground states. The difference between the lowest energy *Pbnm*-like and *R*3*c*-like structures (chemical configuration '001') is quite large with 31 meV/f.u. and becomes even larger if averaging is only over the marked ground states (81 meV/f.u.). Although the *R*3*c*-like structures do not comprise the minimum energy, their average over all chemical configurations gives a 5 meV/f.u. lower value as compared to the *Pbnm*-like structures. Another peculiarity of the *R*3*c*-like structures is the low statistical spread in the volumes and bulk moduli. The respective values of the *Pbnm*-like structures show a much broader scattering than the values of the *R*3*c*-like structures, especially the bulk moduli differ by up to 18% from their average. The experimental value of the volume linearly extrapolated from Jones' temperature dependent data[14] to 0 Kelvin gives 58.5 Å^3, thus 3.8% larger than the theoretical volume V^{R3c}_{ave}.

10.1.2 Isotropic Stress

So far we focused on isotropically strained structures. In the following, we want to expand our discussion to anisotropic lattice strains. It is well-known that tetragonal lattice strain strongly couples to polarization,[46] hence we expect a more pronounced effect for tetragonal structures.
The enthalpies $H(P)-H_{\text{cubic}}(P)$ for chemical configurations '111' and '001' are given in Fig. 10.3. Not all structures presented before were considered, only those relevant for the ground state in the isotropically strained regime were taken into account, i.e. $x^-_+y^-_+z^-_+$, $x^-_-y^-_-z^+_o$, $x^o_oy^o_oz^o_+$, $x^o_+y^o_+z^o_+$ and $x^o_oy^o_oz^+_o$. The $H(P) - H_{\text{cubic}}(P)$-diagrams show that the overall relative phase stabilities do

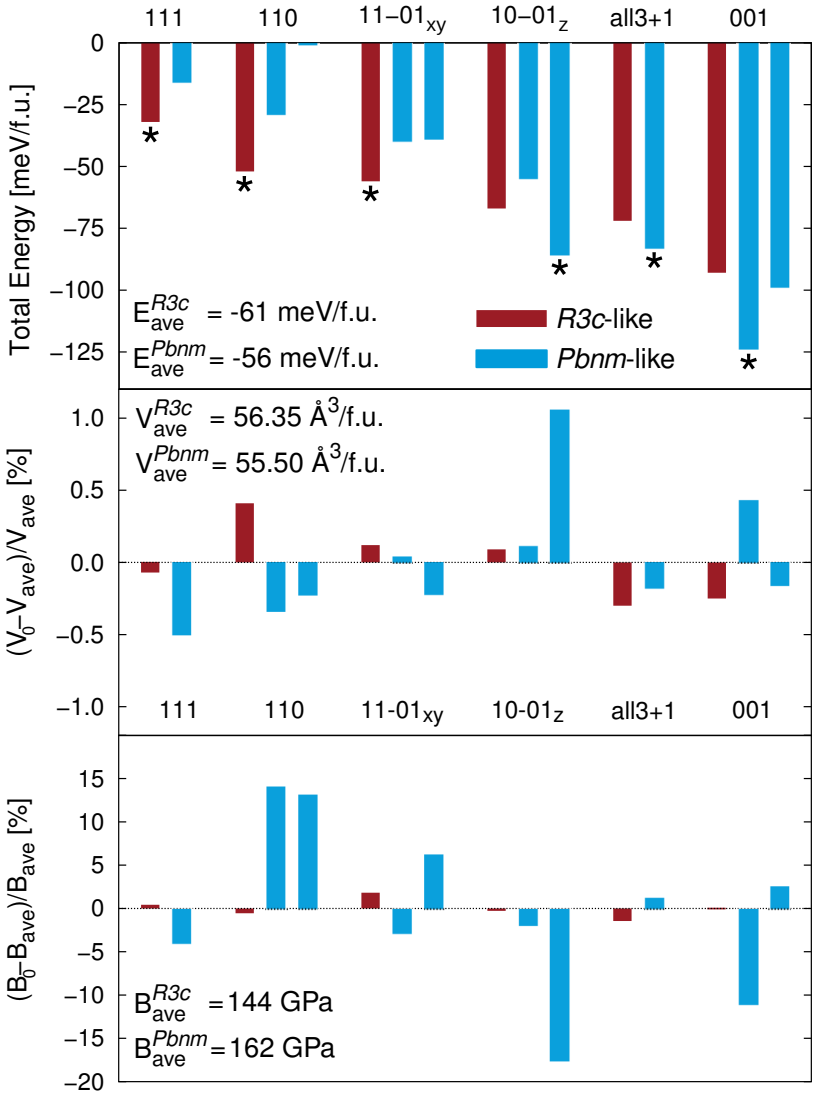

Figure 10.2: Comparison of the Birch-Murnaghan fitting parameters. Absolute zero pressure energies (top) for all six chemical configurations in *R*3*c*-like (red) and *Pbnm*-like structures (blue) are given relative to the lowest value in meV per formula unit (f.u.). Ground states of the different chemical configurations are marked with $\star$. Also given are the relative deviations of equilibrium volumes V_0 (middle) and Bulk moduli B_0 (bottom) with respect to the average values of *R*3*c*-like and *Pbnm*-like structures.

not change if strain is taken into account. For chemical configuration '111' still $x_+^- y_+^- z_+^-$ is most stable at zero pressure, while for chemical configuration '001' the $x_-^- y_-^- z_0^+$ structure types have lower enthalpy than $x_+^- y_+^- z_+^-$. Mainly a substantial up-shift to -5 GPa of the pressures of phase transitions occurring at negative pressure

$$x_o^o y_o^o z_+^o \rightleftharpoons x_+^- y_+^- z_+^- \tag{10.1a}$$

$$x_+^o y_o^o z_o^o \rightleftharpoons x_-^- y_-^- z_o^+ \tag{10.1b}$$

can be observed in both chemical configurations. The pressure of the second phase transition

$$x_+^- y_+^- z_+^- \rightleftharpoons x_-^- y_-^- z_o^+ \tag{10.2}$$

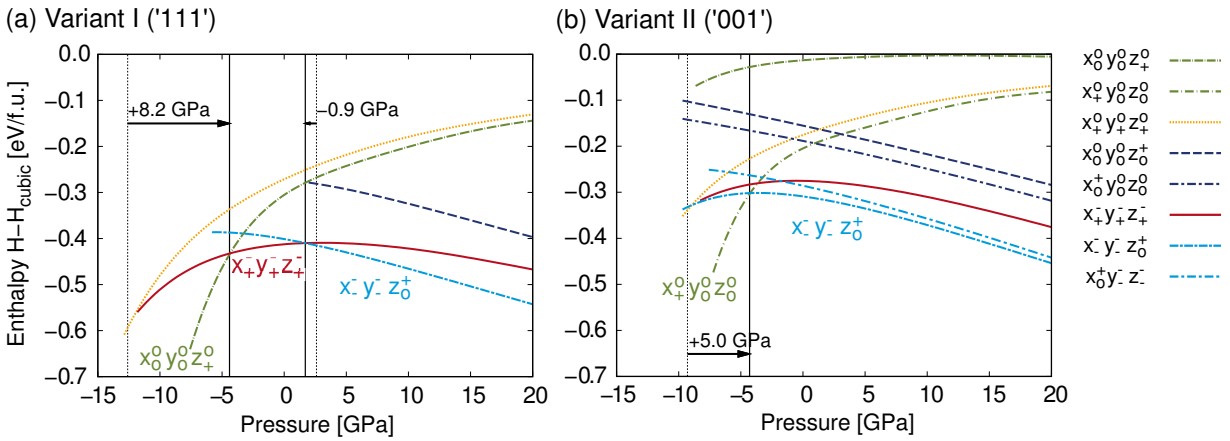

Figure 10.3: Pressure phase diagram for $Na_{1/2}Bi_{1/2}TiO_3$ in chemical configurations (a) '111' and (b) '001' under consideration of anisotropic lattice strain (but isotropic stress). Enthalpies are given relative to the respective ideal perovskite phases.

present in chemical configuration '111', is only slightly reduced. Comparing Fig. 10.1 and Fig. 10.3 we find that strain has only small impact on enthalpies of structures, which are rhombohedral or orthorhombic on average. Yet, highly affected by lattice strain are enthalpies of the tetragonal structures $x^o_oy^o_oz^o_+$ and $x^o_oy^o_oz^+_o$ as was expected.

10.1.3 Pressure-Induced Phase Transitions

Depending on chemical order we find two variants of pressure phase diagrams for the mixed perovskite $Na_{1/2}Bi_{1/2}TiO_3$. All chemical configurations adopt the tetragonal polar-distorted non-tilted structure type $x^0_0y^0_0z^0_+$ (*P*4*mm*-like) at negative pressures below -5 GPa. This corresponds to the structure type reported for several solid solutions of NBT with perovskites having large cations on the A-site like $BaTiO_3$ or $K_{1/2}Bi_{1/2}TiO_3$.

At positive pressures above $+3$ GPa, in contrast, the anti-polar distorted mixed-tilted structure type $x^-_-y^-_-z^+_0$ (*Pbnm*-like) is favoured, in excellent agreement with experiments.[113,122,126] We find, however, no evidence for another tetragonal high-pressure phase up to $+20$ GPa, which was reported by Kreisel.[126] Between -5 GPa and $+3$ GPa either the high-pressure phase or a third structure type is found. One half of the investigated chemical configurations adopts the rhombohedral polar-distorted anti-phase tilted structure type $x^-_+y^-_+z^-_+$ (*R*3*c*-like). The other half stays in the structure type of the high-pressure phase, i.e. $x^-_-y^-_-z^+_0$.

Thus, we find two different ground states at zero pressure depending on the chemical configuration. Different chemical arrangements prefer different tilts (in-phase and anti-phase) and displacements (polar and anti-polar) leading to a structural frustration in the disordered system. Structurally frustrated systems generally have several possibilities to overcome their ambivalences. Reaney *et al.*[248] reviewed the formation of intermediate structures in Pb-based mixed perovskites and solid solutions between displacive variants. In solid solutions between compounds exhibiting different displacive instabilities structural frustration can result in either incommensurate

phase modulations (detectable in diffuse scattering or satellite peaks) or mixed anti-polar/polar order (leading to cell-doubling or monoclinic states). In the case of mixed compounds the end member phases are hypothetical, but still intermediate structures can occur containing different displacive elements, which are stabilized on short length scales due to chemical heterogeneity. $Na_{1/2}Bi_{1/2}TiO_3$ can be regarded as such a chemically frustrated system as well, although it does not contain lead. Depending on the local chemical configuration anti-phase tilts and in-phase tilts compete with each other leading to a complex ground state structure with both polar and anti-polar cation displacements.

10.2 Mixed Phase State

10.2.1 Stability of a Mixed Phase Ground State

In the previous chapter we found that chemical long-range order does not exist in NBT. Only '001'-short-range order can be expected. The $x^-_-y^-_-z^+_0$ local structure is coupled to chemically '001'-ordered regions, while the $x^-_+y^-_+z^-_+$ local structure is coupled to the chemical '111'-order. In the following, we want to investigate whether '001'-ordered regions can exist as chemical nanoregions (CNRs) within a '111'-ordered matrix.
However, the introduction of a second structure type (phase) into the matrix introduces local stresses in the interfacial regions due to lattice and tilt misfits. In z-direction only misfit strains due to different c-lattice parameters can arise, but in x- and y-directions also tilt-misfits will develop when the transition from in-phase to anti-phase tilts has to be accomplished by deformation of TiO_6-octahedra in every second layer along the z-direction.
In the following, we discuss whether a mixed phase state $x^-_+y^-_+z^-_+/x^-_-y^-_-z^+_0$ or a pure $x^-_+y^-_+z^-_+$ phase for matrix and CNRs is preferred. For quantifying energy contributions of lattice and tilt misfits, we compare total energies of large supercells containing both structures '111'-ordered $x^-_+y^-_+z^-_+$ and '001'-ordered $x^-_-y^-_-z^+_0$, separated by distorted interfaces, and total energies of the two pure states $x^-_+y^-_+z^-_+$ and $x^-_-y^-_-z^+_0$ with the same mixed '111'/'001' cation order. There are several ways to accomplish an interface between the two crystal structures. On the basis of a study by Beanland[249] on planar defects, such as antiphase boundaries and twin boundaries, in the $a^-a^-a^-$ tilt system we chose the (001)-plane interface for our calculations. Beanland could show that planar defects on general planes lead to a suppression of all tilts, which we consider as energetically unfavoured. Only the (001)-twin boundary conserves tilts about all axes by reversing the rotation sense of the tilts about the z-axis which results in the tilt system $a^-a^-c^+$. Therefore also in case of an incommensurate interface between these two tilt systems, the (001)-plane should be the thermodynamically favoured one, as it requires the minimal distortion of the octahedra in the interface region. In the interfacial regions the chemical configuration '11-01_{xy}' results. At least half of the octahedra in the interfacial regions are distorted due to the tilt misfit. By constructing the interface it has to be taken into account, that the polarization in both phases has the same direction in order to avoid head-to-head and tail-to-tail configurations across the interface, which are not stable.

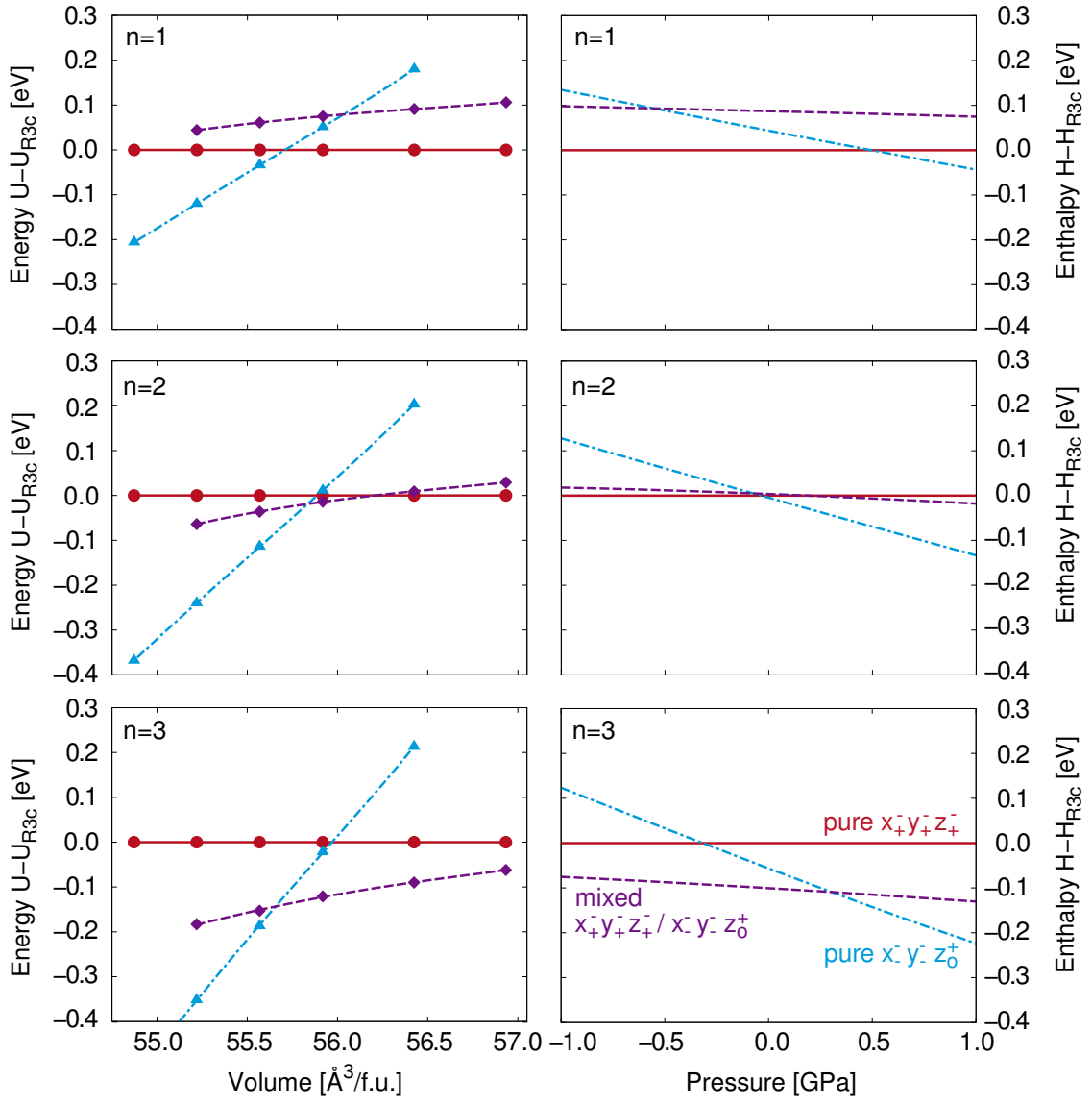

Figure 10.4: Total energies (left panel) and enthalpies (right panel) of supercells relative to the pure $x_+^-y_+^-z_+^-$-states depending on the cell volume and pressure, respectively, given for different numbers of unit cells n in the slabs as shown in Fig. 6.1.

Two scenarios are possible, either the volume is spatially homogeneous or the pressure, depending on the ability for local relaxations i.e. stress release within the two phase regions. In the first scenario energies $U(V)$ have to be compared in the second scenario enthalpies $H(P)$. The total energies depending on the cell volume $U(V)$ given relative to the energy of a pure $x_+^-y_+^-z_+^-$-phase for different numbers of unit cells in the slabs are shown in the left panel of Fig. 10.4. For the same cases we give enthalpies depending on pressure $H(P)$ in the right panel of Fig. 10.4. As the cell sizes become very large (160 atoms for $n = 3$) only four data points were calculated. Both scenarios lead to the same phase stabilities for $n = 1$ and $n = 3$, and only a slightly different behaviour for $n = 2$. For a slab size of only one unit cell solely pure phases $x_+^-y_+^-z_+^-$ and $x_-^-y_-^-z_0^+$ are stable. The tilts in the misfit layer of the mixed state become completely suppressed, not only in the interfacial regions but in the whole layer, leading to higher energies (enthalpies) than in the

pure phases. This confirms our assumption that the suppression of tilts leads to higher interface energies. But with increasing slab size the energy gain resulting from the phase transformation according to Eq. 10.2 stabilizes the mixed phase state $x_+^- y_+^- z_+^- / x_-^- y_-^- z_0^+$. The transition from pure phases to the mixed phase state occurs at a slab size of $n = 2$. Here, in both scenarios a region exists, where all three states have similar energies (enthalpies). As soon as the slab size reaches $n = 3$ the mixed state is stable at volumes higher than 55.66 Å^3/f.u. or pressures lower than 0.30 GPa. At smaller volumes/higher pressures a pure $x_-^- y_-^- z_0^+$-phase becomes stable. In the shown range of volumes/pressures the pure $x_+^- y_+^- z_+^-$-phase does not occur. In Fig. 10.5 the relaxed structures for the mixed states with $n = 2, 3$ are presented. It can be seen that in the interfacial layers two types of octahedra are formed, both are not tilted about the z-axis, but the first one has perfect 90° O-Ti-O angles (marked in white), while the second one has angles of 82° and 78° (marked in black). This shows that '001'-chemically ordered regions will transform to the $x_+^- y_+^- z_+^-$-structure only if the ordered regions are very small, otherwise they will adopt their favoured $x_-^- y_-^- z_0^+$-structure. These results approve the general assumption that tilts are rather "soft" and can be easily changed. The chemically ordered nanoregions have the same local structure as the high-pressure phase. Thus, they can act as precursors for the high-pressure $x_-^- y_-^- z_0^+$-phase.

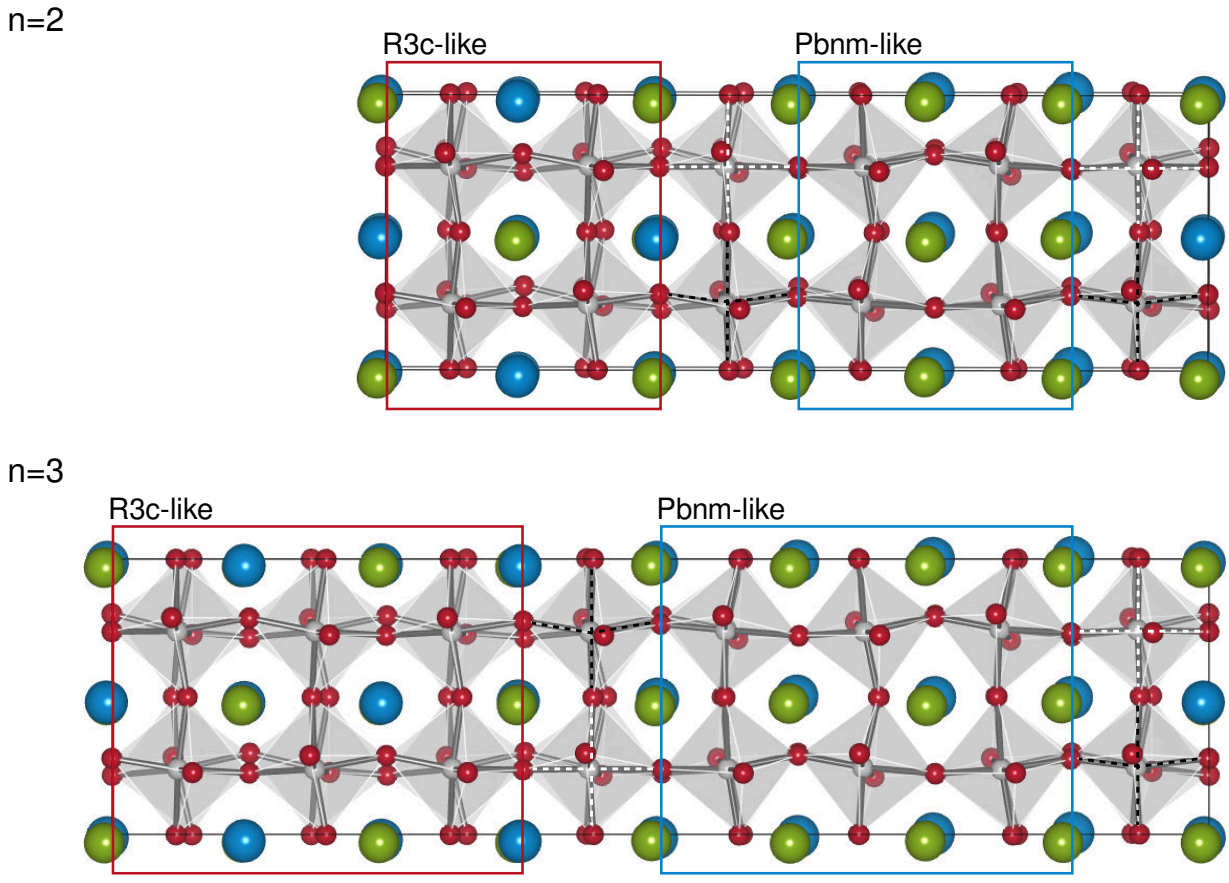

Figure 10.5: Structurally optimized structures in mixed supercells with $n = 2$ (top) and $n = 3$ (bottom) at $V = 55.92$ Å^3/f.u. Distortions are mainly found in the interfacial layers, where two types of not tilted octahedra are present.

10.3 Shape and Local Structure of Chemically Ordered Nanoregions

The favoured shape of the chemically ordered nanoregions depends on the elastic anisotropy of the two structure types adopted by matrix and nanoregions. The matrix has a rhombohedral average symmetry and is thus isotropic in all pseudo-cubic $\langle 001 \rangle$-directions, while the orthorhombic symmetry of the chemically ordered nanoregions leads to anisotropic properties. Hence, interface energies of pseudo-cubic (100) and (010)-interfaces will be higher than that of the (001)-interface of the $x^-_- y^-_- z^+_0$-CNRs embedded in the $x^-_+ y^-_+ z^-_+$-matrix, leading to a non-spherical shape of the chemically ordered nanoregions like flattened ellipsoids or thin discs. Both CNR-shapes are schematically shown in Fig. 10.6. Thin discs on unit-cell scale become equivalent to regular or irregular incommensurate phase modulation leading to planar defects as the planar segregation areas discussed by Kreisel *et al.*,[126] the tilt stacking faults proposed by Dorcet and Trolliard[110] or the modulated domain structure reported by Thomas *et al.*.[127] Another explanation for a preference of rather two dimensional small CNRs can be given by considering electrostatics. Perfect layers of Na^+ and Bi^{3+} along $\langle 001 \rangle$-directions lead to local electrostatic fields comparable to those present in a (multilayer) parallel plate capacitor. The higher the number of layers the higher is the stored energy of the capacitor for equal values of accumulated area (not active area), distance (i.e. the lattice parameter) and bound charge. Hence, it is favourable to have very thin discs. Another way to reduce the stored energy is to reduce the amount of bound charge, i.e. the formation of imperfect layers. The chemical configuration '001' is just one out of three that stabilizes the $x^-_- y^-_- z^+_0$ structure type. The Bi/Na-layers do not need to be perfect, they can host up to 33% "antisites". The in-phase tilts of the $x^-_- y^-_- z^+_0$ structure type present in the CNRs introduce anti-polar displacements in the A-sublattice in contrast to the polar ferroelectric distortion present in the structure type $x^-_+ y^-_+ z^-_+$ of the matrix. Generally, the orthorhombic space group *Pbnm* is associated with antiferroelectric behaviour, which is correct in case of simple perovskites, but not in case of mixed systems like $Na_{1/2}Bi_{1/2}TiO_3$. Anti-polar displacements within the mixed A-sublattice do not inevitably imply antiferroelectric behaviour of the material. Chemical order breaks the ideal *Pbnm*-symmetry leading in most cases to polar space groups (cf. C), e.g. the '001'-chemical configuration possesses $Pmc2_1$-symmetry, which leads to a considerable spontaneous polarization.
Synthesis conditions will have a strong influence on the size and the shape of the chemically ordered nanoregions in NBT. As both parameters directly influence the occurrence of the mixed phase state, synthesis conditions and also sample history will strongly affect the local structure.

10.4 Summary

The mixed perovskite $Na_{1/2}Bi_{1/2}TiO_3$ resembles a complex system including ferroelectric distortions, octahedral tilting, lattice strain as well as chemical and polar displacive disorder. In this chapter we investigated the interplay of these order parameters.
We studied the effect of pressure on the phase stability for differently ordered chemical configurations. All chemical configurations favour the tetragonal polar-distorted non-tilted structure $x^0_0 y^0_0 z^0_+$

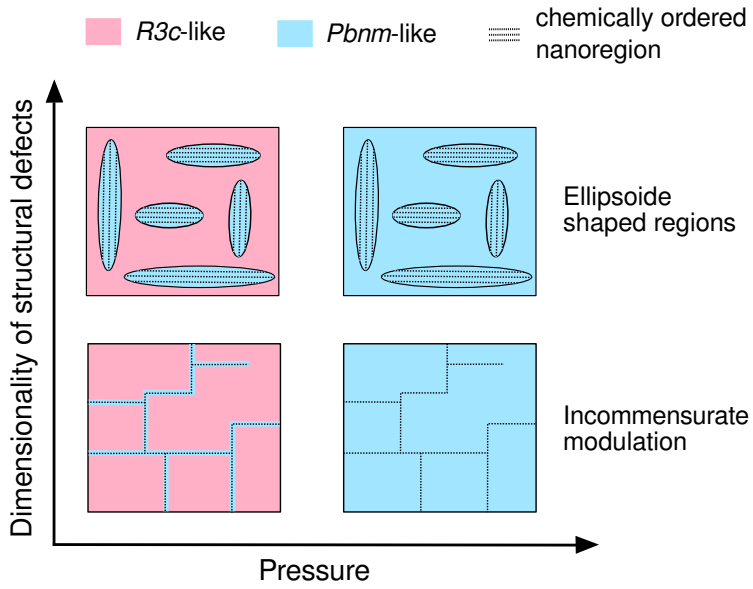

Figure 10.6: Structure models for chemically ordered nanoregions in $Na_{1/2}Bi_{1/2}TiO_3$. Depending on the difference in interface energies induced by the in-phase tilts in z-direction, CNRs can arise as planar stacking faults also describable as incommensurate phase modulation or as bulky ellipsoidal regions. At low-pressure the *Pbnm*-like CNRs are embedded in the *R*3*c*-like matrix. Between about 1.5 and 3 GPa the matrix undergoes a phase transition and transforms into the *Pbnm*-like structure of the CNRs.

(*P*4*mm*-like) at negative pressures below -5 GPa and at positive pressures above $+3$ GPa an antipolar-distorted mixed-tilted structure $x^-_-y^-_-z^+_0$ (*Pbnm*-like). In the pressure range in-between two different structure types are stable depending on the cation configuration. One subset of the investigated chemical configurations adopts a rhombohedral polar-distorted anti-phase tilted structure $x^-_+y^-_+z^-_+$ (*R*3*c*-like). The other subset favours the structure type of the high-pressure phase $x^-_-y^-_-z^+_0$. Thus, at zero pressure as a material with locally varying chemical short-range order NBT is a structurally frustrated system. Moreover, in contrast to solid solutions, where the average crystal structure can be changed by variation of the composition, NBT is one rare example where the structure depends on the type and degree of chemical order.

Our results suggest the existence of chemically ordered nanoregions CNRs, which adopt a different local structure (*Pbnm*-like) than the chemically disordered matrix (*R*3*c*-like). Due to the anisotropy of the structure adopted by the CNRs, the nanoregions are expected to have the shape of flattened ellipsoids or thin discs. The thickness has to be at least three unit cells in order to compensate for the tilt misfit resulting in the interfacial regions where in-phase and anti-phase tilts meet. This structure model is in good agreement with earlier experimental reports.[106,109,113,126]

We demonstrated that the local NBT structure arises from a delicate balance between octahedral tilting and ferroelectric distortions depending on the local chemical configuration. Chemical short-range order is responsible for local deviations from the average crystal structure leading to structurally different chemical nanoregions.

11 Analysis of Order Parameters: Octahedral Tilting and Polarization

In this chapter the tools of group-subgroup relations and symmetry-adapted distortion mode analysis, which were extensively introduced in Ch. 8, will be seen in action. The aim of this analysis is the comparison of the *R*3*c*-like, *Pbnm*-like and *P*4*bm*-like structures with chemical orders '111' and '001'. The chemical orders break the symmetry with respect to the simple perovskite structure ABX_3, increasing in some cases the number of distortion modes.

A common characteristic of all phases that are discussed in this chapter is the coexistence of (anti)polar displacements and octahedral tilts, which are described by independent order parameters. Aside from this, the distorted structures can be related to two different parent structures, first to the chemically ordered undistorted perovskite structures $Fm\bar{3}m$ and *P*4*/mmm* and second to the (anti)polar and tilted simple perovskite structures *R*3*c*, *Pbnm* and *P*4*bm*. In the first part of this chapter, we follow the first choice, because we are interested in the appearance and hierarchy of the symmetry-adapted distortion modes, which can be more easily understood if one compares the distorted structures with undistorted high-symmetry structures.
In the second part, we will pursue the alternative path in order to learn how chemical order changes locally the average crystal structure. Hence, we compare the distortion modes, that are active in the $Pm\bar{3}m$-derived distorted structures with those we found in the chemically ordered correspondents.
Finally, transformation indices are compared in order to discuss how chemical ordering affects the number of domains in the distorted phases.

11.1 Chemical '111'-Order: $Fm\bar{3}m$ Parent Structure

11.1.1 Wyckoff Splitting

The symmetries *R*3*c* (No. 161), *Pbnm* (No. 62) and *P*4*bm* (No. 100) of the ideal perovskite ABX_3 with space group $Pm\bar{3}m$ (No. 221) are reduced by chemical rock-salt order in the mixed perovskite $A_{1/2}A'_{1/2}BX_3$ with symmetry $Fm\bar{3}m$ (No. 225) to space groups *R*3 (No. 146), $Pmn2_1$ (No. 31) and $P4_2nm$ (No. 142), respectively. These symmetry reductions are accompanied by several splittings of the occupied Wyckoff-positions 4a (A=Bi), 4b (A'=Na), 8c (B=Ti) and 24d (X=O) of $Fm\bar{3}m$, which are summarized in Tab. 11.1. The cubic unit cell of $Fm\bar{3}m$ contains eight formula units $Na_{1/2}Bi_{1/2}TiO_3$, the hexagonal cell of *R*3 contains six and the orthorhombic $Pmn2_1$ and tetragonal $P4_2nm$ unit cells both contain four formula units. As can be seen from Tab. 11.1 occupy Bi and

Table 11.1: Wyckoff-Splitting in $Fm\bar{3}m$ parent structure.

Atom	$Fm\bar{3}m$ (No. 225)	Symmetry	$R3$ (No. 146)	Symmetry	$Pmn2_1$ (No. 31)	Symmetry	$P4_2nm$ (No. 102)	Symmetry
Bi	4a	$m\bar{3}m$	3a	3	2a	m	2a	$2mm$
Na	4b	$m\bar{3}m$	3a	3	2a	m	2a	$2mm$
Ti	8c	$\bar{4}3m$	3a (1.1)	3	4b	1	4b	2
			3a (1.2)	3				
O	24d	mmm	9b (1)	1	4b (1.1)	1	4c (1.1)	m
			9b (2)	1	4b (1.2)	1	4c (1.2)	m
					2a (2)	m	4b (2)	2
					2a (3)	m		

Na in all structures sites of identical symmetries and do not experience any Wyckoff splitting, which means that both ions occupy equivalent sites in all structures (sites forming a Wyckoff set). The (cub)octahedral site symmetry $m\bar{3}m$ of the A-sites is reduced to trigonal 3, monoclinic m and orthorhombic $2mm$. The Ti-site experiences Wyckoff-splitting only in the $R3$ structure. The tetrahedral site (symmetry $\bar{4}3m$) is split into two equivalent sites in $R3$, retaining only the trigonal symmetry element 3. In $Pmn2_1$ and $P4_2nm$ no splitting of the Ti-sites occurs, but symmetries are reduced to triclinic 1 and monoclinic 2, respectively. The highest degree of Wyckoff-splitting experiences the O-site. In $R3$ the orthorhombic site with symmetry mmm is split into two equivalent sites, O1 in the Bi-layers and O2 in the Na-layers, under loss of all symmetry elements (except the identity). In $Pmn2_1$ the O-site is split into two groups, two equivalent sites with triclinic symmetry 1 occupied by four oxygen ions each (O1.1 and O1.2 on 4b in the Ti-layers) and two more sites with monoclinic symmetry m occupied by two oxygen ions each (O3 and O4 on 2a in the Bi/Na-layers). In $P4_2nm$ three different oxygen sites can be found. One third of the oxygen ions occupies positions with monoclinic symmetry 2 (O2 on 4b in the Bi/Na-layers) and the remaining two third occupy two equivalent sites with monoclinic symmetry m (O1.1 and O1.2 on 4c in the Ti-layers). The numbering O1.1/O1.2 indicates that these oxygen atoms are crystallographically different, but chemically identical, it means that they show the same displacements.

11.1.2 *R*3-Structure

The unit cell transformation from the *Fm*$\bar{3}$*m* cubic setting to the *R*3 hexagonal setting is represented by the vector transformations described by Eqs. (11.1). Direction $[1\bar{1}1]$ of the cubic unit cell becomes the 3-fold rotation axis c_h of the hexagonal unit cell, which is also the polar axis.

$$\mathbf{a}_\mathrm{h} = -1/2\,\mathbf{a}_\mathrm{c} + 1/2\,\mathbf{c}_\mathrm{c} \tag{11.1a}$$

$$\mathbf{b}_\mathrm{h} = -1/2\,\mathbf{b}_\mathrm{c} - 1/2\,\mathbf{c}_\mathrm{c} \tag{11.1b}$$

$$\mathbf{c}_\mathrm{h} = \mathbf{a}_\mathrm{c} - \mathbf{b}_\mathrm{c} + \mathbf{c}_\mathrm{c} \tag{11.1c}$$

The details of the distortion modes present in the optimized structures are summarized in Tab. 11.2 with their directions in the irrep subspaces, their isotropy subgroups and the dimensions of the displacement vectors. All modes correspond to irreducible representations at the Brillouin zone center. There are two chemically induced modes acting separately on the Ti-atoms (Γ_5^+) and on the O-atoms (Γ_2^-). The resulting isotropy subgroups are *R*$\bar{3}$*m* and *F*$\bar{4}$3*m*, respectively. In Fig. 11.1 (a) and (b) are the structures given, as they result from these two distortion modes only. The Γ_5^+-mode causes Ti-atoms to displace along the c-axis towards the Na-layers, both atoms Ti1.1 and Ti1.2 move by the same amount but in opposite directions. The effect of Γ_2^- is a distortion of the TiO_6-octahedra due to small displacements of the oxygens O1 and O2. This distortion leads to a slight volume difference between the Ti1.1- and Ti1.2-centred octahedra, the latter ones being smaller.

The polar mode Γ_4^- acts on all six atom types. The resulting isotropy subgroup is *R*3*m*. The structure is shown in Fig. 11.1 (c). The largest displacements exhibit the Bi-atoms, the smallest displacements show Ti-atoms and O1-atoms. As it is typical for a polar mode, cations and anions displace in opposite directions.

The fourth mode is the anti-phase tilt Γ_5^--mode, whose tilt pattern is represented by the Glazer-notation as $a^-a^-a^-$. The displacement vector is 2-dimensional, because the two oxygen atoms O1 and O2 can be displaced by slightly different amounts leading to small deformations of the TiO_6-octahedra. The resulting isotropy subgroup is *R*32.

As none of the isotropy subgroups is identical with the space group of the distorted structure *R*3, there must exist at least two primary modes. Inspection of the group-subgroup graph in Fig.11.2 ($\mathcal{G} = 225$, $\mathcal{H} = 146$, index $[i] = 16$) shows us that there are only two possible combinations leading to *R*3. Either the two last modes Γ_4^- and Γ_5^- or Γ_2^- and Γ_5^- can be these primary modes.

Table 11.2: Details of the symmetry-adapted distortion modes in R3.

k-point	Irrep	Direction	Isotropy subgroup	Dimension	Distortion type
(0,0,0)	Γ_5^+	$(-a,-a,a)$	*R*$\bar{3}$*m*	1	chemically induced (Ti)
(0,0,0)	Γ_2^-	(a)	*F*$\bar{4}$3*m*	1	chemically induced (O)
(0,0,0)	Γ_4^-	$(-a,a,-a)$	*R*3*m*	6	polar mode $[111]_\mathrm{c} = c_\mathrm{h}$
(0,0,0)	Γ_5^-	$(-a,-a,a)$	*R*32	2	$a^-a^-a^-$ tilt

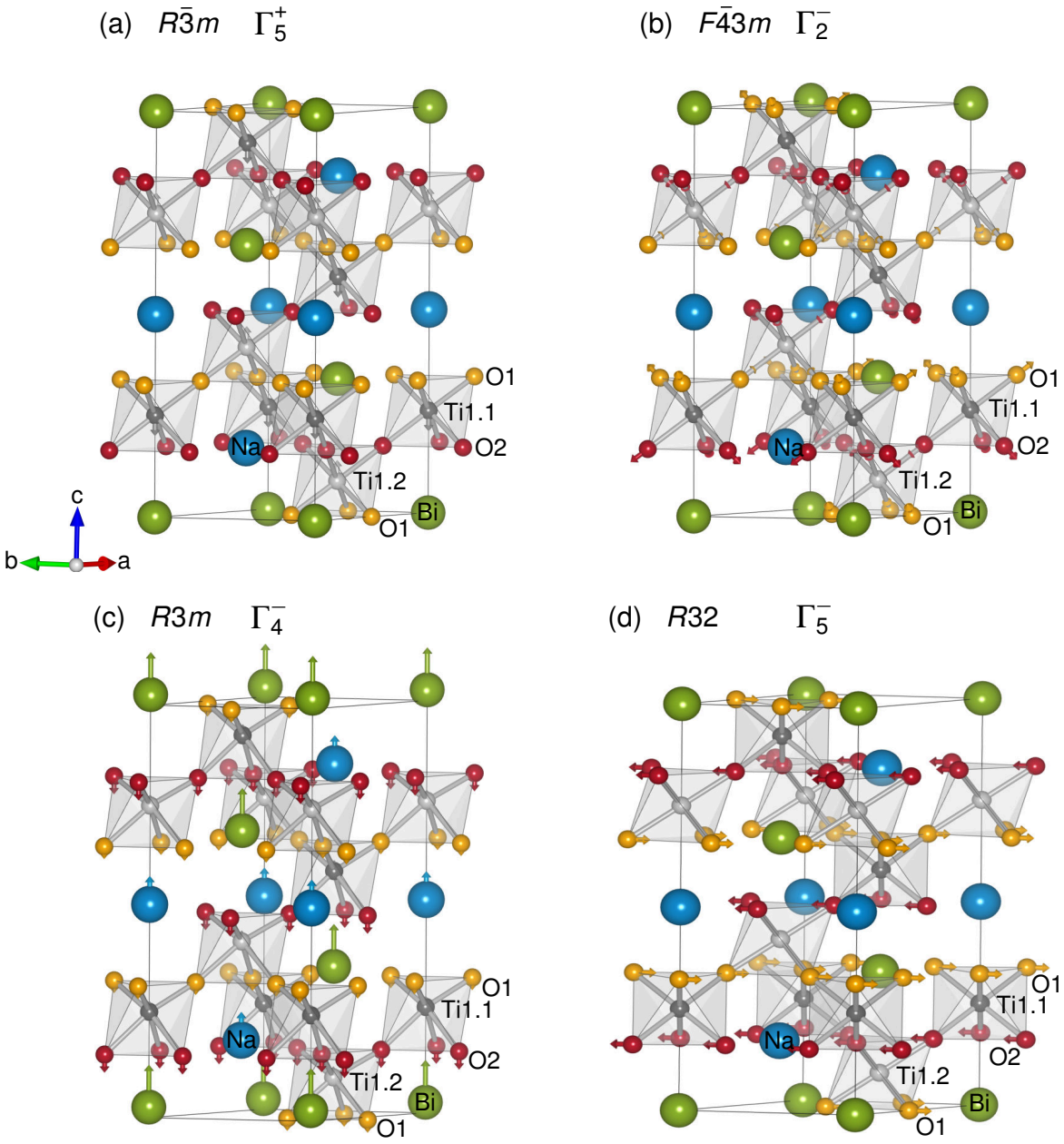

Figure 11.1: Visualization of the symmetry-adapted distortion modes within the hexagonal $R3$-structure. Structures are shown for the volume $V = 56.62$ Å^3/f.u., which is very close to the equilibrium volume $V_0 = 56.09$ Å^3/f.u. The atom positions are exactly as if the presented distortion mode would exist exclusively, displacement vectors are given with the following scaling factors: (a) $\times 40$, (b) $\times 400$, (c) $\times 4$ and (d) $\times 2$.

In Fig. 11.3 the mode amplitudes depending on the cell volume are given. The two chemically induced modes Γ_5^+ and Γ_2^- are clearly secondary distortion modes with very small amplitudes at any volume. The dominating modes are the anti-phase tilt mode Γ_5^- and the polar mode Γ_4^-. Both distortion modes respond differently to increasing volume. The tilt mode decreases, while the polar mode increases linearly with increasing volume. This could be seen already in Ch. 10 on

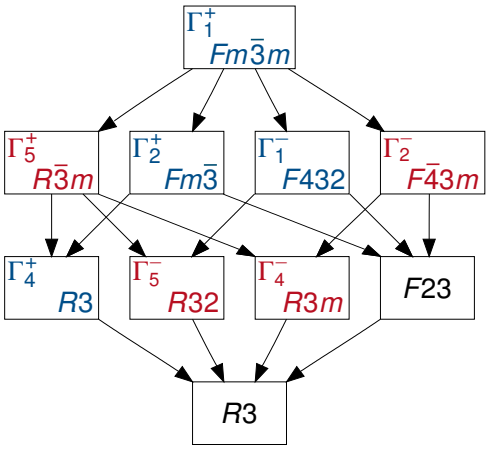

Figure 11.2: Graph of minimal subgroups connecting the space group $Fm\bar{3}m$ and its subgroup $R3$.

the phase stability of NBT, where tilted phases became unfavoured at large volumes while stability of polar phases was reduced at small volumes. In Fig. 11.3 (c) is shown how the hexagonal aspect ratio c/a, given by the following equation, depends on volume:

$$\frac{c}{a} = \frac{c_\mathrm{h}}{a_\mathrm{h}} \cdot \left(\frac{c_\mathrm{h}}{a_\mathrm{h}}\right)^{-1}_{\mathrm{ideal}} = \frac{c_\mathrm{h}}{a_\mathrm{h}} \cdot \left(\frac{a_\mathrm{c} \cdot \sqrt{3}}{a_\mathrm{c}/\sqrt{2}}\right)^{-1} = \frac{c_\mathrm{h}}{a_\mathrm{h}} \cdot \frac{1}{\sqrt{6}} \tag{11.2}$$

Below 54 Å^3/f.u. the hexagonal unit cell is compressed along the c_h-axis, while at volumes above 54 Å^3/f.u. it is elongated with respect to the ideal hexagonal ratio. Not only the polar mode but also the unit cell deformation (lattice strain) increases linearly with increasing volume.

The atomic displacements for both the polar and the anti-phase tilt mode are given in Fig. 11.3 (b) and (d). For the tilt mode displacements of O1 and O2 were averaged. Like the mode amplitudes also the atomic displacements depend nearly linearly on the volume. Only for Na a deviation from this is observed at small volumes. At the smallest volume, Bi and Na are displaced by almost the same amount but with increasing volume the displacements of Bi become significantly larger. At the equilibrium volume of $V_0 = 56.09$ Å^3/f.u. the difference between Bi and Na displacements is as large as 0.12 Å. It can be seen that cations on both A- and B-sites are ferroelectrically active. This finding is in strong contrast to an earlier study, where the softness of polar A- and B-atom displacements in $(1-x)\mathrm{Na_{1/2}Bi_{1/2}TiO_3}$-$x\mathrm{BaTO_3}$ were probed separately in the cubic perovskite structure.[47] In that earlier study it was found that only the A-atoms are ferroelectrically active in pure NBT while Ti-atoms are most stable at their ideal positions. Now we can see that, although the displacements of Ti are much smaller than those of the A-atoms, the contribution of Ti to the overall polarization will still be large due to its higher charge. The oxygen atoms situated in the Bi-layers (O1) show smaller displacements than the oxygen atoms situated in the Na-layers (O2). Comparing the oxygen displacements resulting from the polar mode with those from the tilt mode, we find that the maximum displacements resulting from the tilt mode are about twice as large as those resulting from the polar mode. Overall both distortion modes lead to atomic displacements of the same order of magnitude.

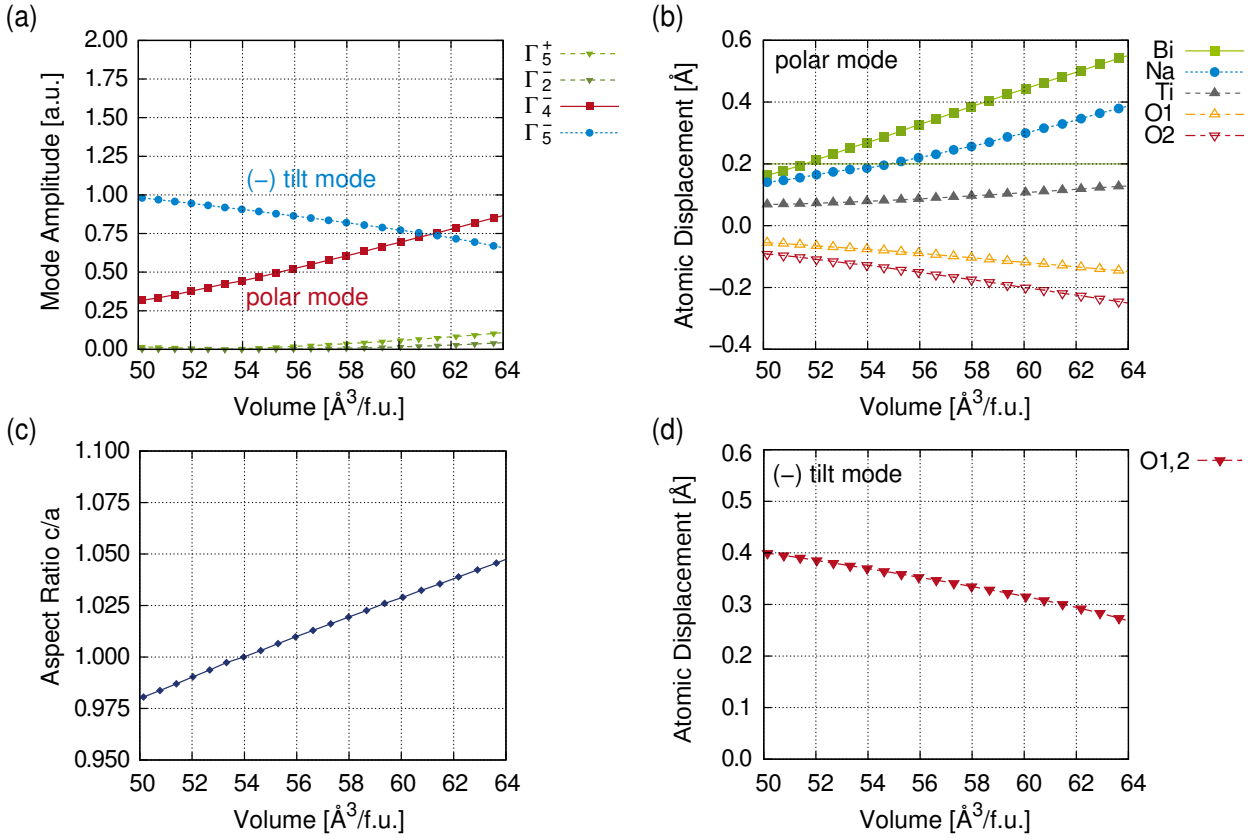

Figure 11.3: Analysis of the symmetry-adapted distortion modes in the *R*3-structures depending on volume. In (a) amplitudes of all distortion modes are given. (b) and (d) show the atomic displacements associated with the polar mode Γ_4^- and the anti-phase tilt mode Γ_5^-. (c) presents the evolution of the hexagonal aspect-ratio c/a with volume.

11.1.3 *Pmn*2_1-Structure

The unit cell transformation *Fm*$\bar{3}$*m* $\rightarrow$ *Pmn*2_1 is described by the vector transformations in Eqs. (11.3). Direction $[001]$ of the cubic unit cell becomes the a_o-axis with the perpendicular mirror plane *m* of the orthorhombic unit cell, about this axis the in-phase tilt occurs. The polar axis of the orthorhombic unit cell is c_o, while the axis of antipolar displacements is b_o. Upon the unit cell transformation the cell volume is reduced to one half of the initial volume:

$$\mathbf{a}_\mathrm{o} = \mathbf{c}_\mathrm{c} - {}^1\!/_8 \tag{11.3a}$$

$$\mathbf{b}_\mathrm{o} = {}^1\!/_2\,\mathbf{a}_\mathrm{c} - {}^1\!/_2\,\mathbf{b}_\mathrm{c} - {}^3\!/_8 \tag{11.3b}$$

$$\mathbf{c}_\mathrm{o} = {}^1\!/_2\,\mathbf{a}_\mathrm{c} + {}^1\!/_2\,\mathbf{b}_\mathrm{c} + {}^1\!/_2 \tag{11.3c}$$

A summary of the distortion modes is given in Tab. 11.3. There are six different distortion modes active in the *Pmn*2_1-structure. These are visualized in Fig. 11.4 for the optimized structure at the volume $V = 55.31$ Å. The oxygen atoms O1.1 and O1.2 are chemically equivalent, although they occupy crystallographically different positions, which means that all O1 atoms experience the same atomic displacements.
Again a chemically induced mode transforming as irrep Γ_5^+ is acting on the Ti-ions, as presented in Fig.11.4 (a). The displacements are restricted to the direction perpendicular to the mirror plane in the bc-plane resulting in displacements along the a_o-axis, these displacements are directed towards the O3-atoms. The resulting isotropy subgroup is *Immm*.
In (b) the anti-phase tilt mode is shown, as described by the irrep Γ_5^-, which corresponds to the tilt system $a^-a^-c^o$. All oxygen atoms O1-3 are involved in the anti-phase tilts about the orthorhombic b_o-axis. Oxygen atoms O2 and O3 have to displace farther by a factor of about $\sqrt{2}$ compared to the O1 atoms in this mode in order to maintain the rigidity of the octahedra.
The polar mode in (c) is represented by the irrep Γ_4^-, the direction of the polar displacements is along the c_o-axis. The polar mode is dominated by displacements of the atoms Bi, Ti and O2.
These two distortions Γ_5^- and Γ_4^- both lead to the same isotropy subgroup *Imm*2, but they correspond to different cell transformations, the latter includes a translation, the first one does not.

Table 11.3: Details of the symmetry-adapted distortion modes in *Pmn*2_1.

k-point	Irrep	Direction	Isotropy subgroup	Dimension	Distortion type
(0,0,0)	Γ_5^+	$(a,0,0)$	*Immm*	1	chemically induced (Ti)
(0,0,0)	Γ_4^-	$(a,a,0)$	*Imm*2	6	polar mode $[110]_\mathrm{c} = c_\mathrm{o}$
(0,0,0)	Γ_5^-	$(0,a,-a)$	*Imm*2	2	$a^-a^-c^o$ tilt
(0,1,0)	X_2^+	$(0,a,0)$	*P*4_2*/mnm*	2	$a^oa^oc^+$ tilt
(0,1,0)	X_3^+	$(0,a,0)$	*P*4*/mnc*	1	Jahn-Teller distortion (+)
(0,1,0)	X_5^-	$(0,0,a,0,0,0)$	*Pmmn*	5	antipolar mode $[1\bar{1}0]_\mathrm{c} = b_\mathrm{o}$

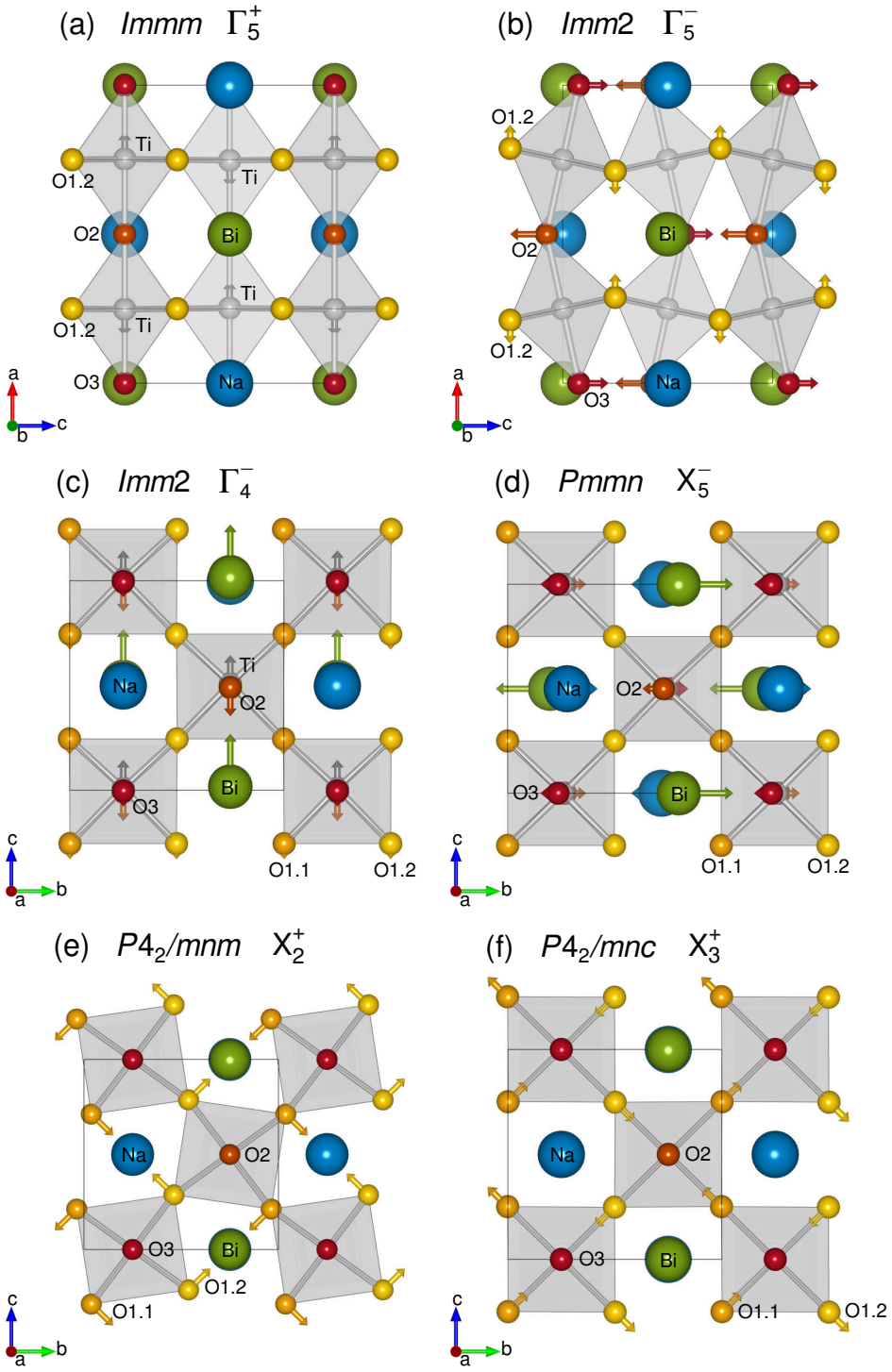

Figure 11.4: Visualization of the symmetry-adapted distortion modes, which are active within the orthorhombic *Pmn*2_1-structure. Structures are shown for the volume $V = 55.31$ Å^3/f.u. The atomic positions are exactly as if the presented distortion mode would exist exclusively, while displacement vectors are given with the following scaling factors: (a) $\times 40$ and (b) $\times 2$, (c) $\times 15$ and (d) $\times 4$, (e) $\times 3$ and (f) $\times 80$. The oxygen atoms O1.1 and O1.2 are chemically equivalent.

However, the fact that they possess the same isotropy subgroup has some special implication on the interaction between the two modes, as we will see in Ch. 12.
In (d) the distortion associated with irrep X_5^- is shown, which is antipolar and leads to the isotropy subgroup *Pmmn*. Atomic displacements develop along the b_o-axis, atoms of the same type but in different layers perpendicular to the a_o-axis are displaced in opposite directions. Anions and cations within the same layer are displaced in opposite directions just as in a polar mode. Thus dipole moments develop in every AO-layer ($x = 0$ and $x = 0.5$), which exactly cancel each other. Similar dipole moments develop in the TiO_2-layers resulting from anti-phase displacements of Ti in the layers $x = 0.25$ and $x = 0.75$. Overall, the displacements linked with this antipolar mode are one order of magnitude larger than those linked with the polar mode (scaling factors of the shown displacement vectors are 4 and 15, respectively). Both modes are dominated by the displacements of the Bi-atoms, but in the antipolar mode there are also considerable contributions from the Na-atoms. Displacements of Ti-atoms play a minor role and O1-atoms are not involved at all in the antipolar mode.
The in-phase tilt mode in (e) is associated with the irrep X_2^+ and leads to the isotropy subgroup *P*4_2*/mnm*. This tilt mode acts only on the O1-atoms and results in octahedral tilts about the a_o-axis. A second distortion mode acting on the O1-atoms only is the Jahn-Teller distortion described by the irrep X_3^+, which leads to isotropy subgroup *P*4_2*/mnc*. This Jahn-Teller distortion is of the same type as the one we saw in the *Pnma*-structure of $CaTiO_3$ in Fig. 8.5 (e). Jahn-Teller distortions in adjacent layers along the a_o-axis are in-phase, as can be seen in (f).

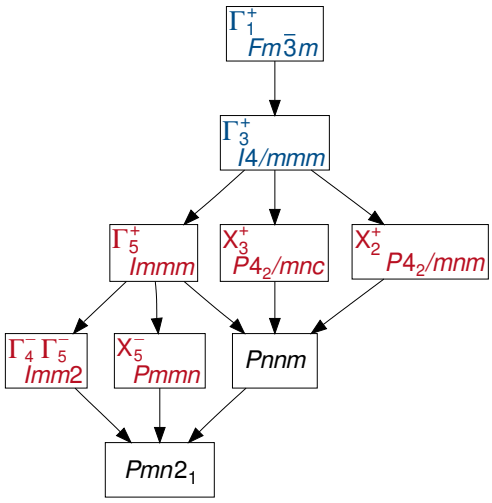

Figure 11.5: Graph of minimal subgroups connecting the space group *Fm*$\bar{3}$*m* and its subgroup *Pmn*2_1.

For the transformation *Fm*$\bar{3}$*m* $\rightarrow$ *Pmn*2_1 ($\mathcal{G} = 225$, $\mathcal{H} = 31$, index $[i] = 24$) the group-subgroup graph is given in Fig. 11.5. There are in total 15 prospective combinations of two primary distortion modes. But some combinations can be ruled out from symmetry considerations, for example Γ_5^+ can be completely ruled out as primary mode, as it in whatever combination always leads to a super group of *Pmn*2_1. Moreover, the combination of X_2^+ and X_3^+ is impossible, as it results in *Pnnm*, only. Another impossible combination is Γ_4^- or Γ_5^-, which gives *Imm*2. But any of the

remaining eight combinations of two irreps can explain the symmetry lowering to *Pmn*2_1. As we do not expect a Jahn-Teller distortion to be dominating, five couples combining (anti)polar and tilt modes only are left.

In the following, the mode amplitudes and the atomic displacements associated with the polar, antipolar and tilt modes, as they change with volume, will be discussed in detail in order to identify the actual primary and secondary modes. In Fig. 11.6 the amplitudes of all six modes depending on the unit cell volume are shown. Data were obtained just up to 58 Å^3/f.u., as this structure is stable in the high-pressure regime only.
The chemically induced mode Γ_5^+ and the Jahn-Teller distortion X_3^+ have very small amplitudes in the whole volume range and can be considered as induced secondary distortion modes. Overall, the anti-phase tilt mode Γ_5^- and the in-phase tilt mode X_2^+ are dominating, especially at small volumes. From this behaviour we can infer that the two tilt modes are primary distortion modes at small volumes. At large volumes, however, the antipolar and polar modes become equally important. Thus, no clear distinction between primary and secondary modes is possible.
The amplitude of the anti-phase tilt mode is almost constant in the whole volume range. Similarly, the antipolar mode changes only slightly with volume, at large volumes the amplitude increases slowly in contrast to the polar mode whose amplitude increases by almost 300%. At volumes larger than 54 Å^3/f.u the polar mode Γ_4^- starts to increase almost linearly with increasing volume. Simultaneously, the in-phase tilt mode X_2^+ decreases by almost equal amounts as polarization increases. It seems that these two modes are strongly coupled to each other. In the whole volume range the amplitude of the polar mode is smaller than the amplitude of the antipolar mode. In Fig. 11.6 (c) the evolution of the two orthorhombic aspect ratios b/a, calculated by the following equation, and c/a, calculated in the respective way, with volume is shown:

$$\frac{b}{a} = \frac{b_\mathrm{o}}{a_\mathrm{o}} \cdot \left(\frac{b_\mathrm{o}}{a_\mathrm{o}}\right)^{-1}_{\text{ideal}} = \frac{b_\mathrm{o}}{a_\mathrm{o}} \cdot \left(\frac{a_\mathrm{c}/\sqrt{2}}{a_\mathrm{c}}\right)^{-1}_{\text{ideal}} = \frac{c_\mathrm{t}}{a_\mathrm{t}} \cdot \sqrt{2} \tag{11.4}$$

The onset of increasing polarization along the c_o-axis corresponds to an analogue progression in the c/a-ratio, which is constant up to 54 Å^3/f.u and then increases strongly, just as the amplitude of the polar mode. The amplitude of the in-phase tilt shows the inverse behaviour, it decreases slowly almost linearly at small volumes and has a kink with a much stronger decrease at larger volumes when the c/a-jump sets in around 55 Å^3/f.u. The smaller increase of the antipolar mode can be similarly matched with the continuous but weak increase of the b/a-ratio. The lattice parameter b is always larger than c, just as the antipolar mode is always larger than the polar mode.

The atomic displacements arising from the polar, antipolar and the in-phase and anti-phase tilt modes are given in Fig. 11.6 (b), (d) and (e). As we know from the mode amplitudes already, the atomic displacements associated with the polar mode are much smaller than those resulting from the antipolar mode. Both modes are dominated by displacements of Na/Bi-atoms and O2-atoms. In the polar mode Na-atoms displace at small volumes in the opposite direction than Bi-atoms. Only at volumes larger than 56 Å^3/f.u. all cations displace in the opposite direction than the anions, as it is typical for a polar mode. These antiparallel displacements of Bi and Na at small volumes are a remainder of the *Pbnm*-phase, the second parent phase of this structure. Overall, except for

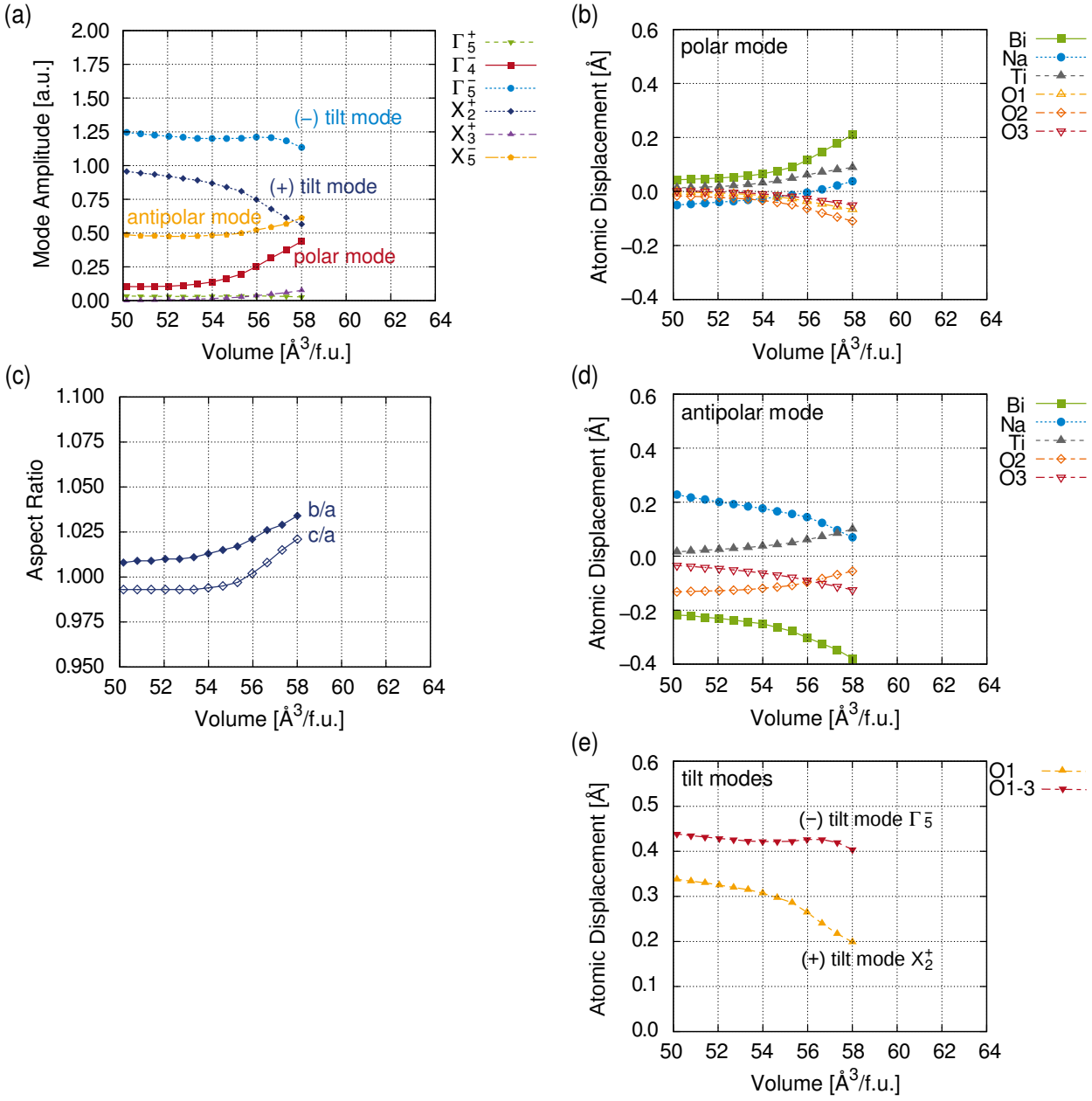

Figure 11.6: Analysis of the symmetry-adapted distortion modes in the *Pmn*2_1-structures depending on volume. In (a) amplitudes of all distortion modes are given. (b), (d) and (e) show the atomic displacements associated with the polar mode Γ_4^-, the antipolar mode X_5^-, and the in-phase tilt mode X_2^+ together with the anti-phase tilt mode Γ_5^-, respectively. (c) presents the evolution of the orthorhombic aspect-ratios b/a and c/a with volume.

the Na-atoms, atomic displacements increase with increasing volume. The same can be found for the antipolar mode in (d). At the smallest volume Na-atoms and Bi-atoms show almost equal atomic displacements of 0.2 Å. On increasing volume the Bi-displacements increase while the Na-displacements are reduced. The atomic displacements arising from the tilt modes are given in (e). The displacements resulting from the anti-phase tilt mode are almost constant, only those resulting from the in-phase tilt mode show a strong variation with volume.

11.1.4 *P*4_2*nm*-Structures

The unit cell transformation from the *Fm*$\bar{3}$*m* cubic setting to the *P*4_2*nm* tetragonal setting with basis vectors $(\mathbf{a}_t, \mathbf{b}_t, \mathbf{c}_t)$ is represented by the vector transformation described by Eqs. (11.5). Basis vector $\mathbf{c}_c$ of the cubic unit cell becomes basis vector $\mathbf{c}_t$ of the tetragonal unit cell. About this c-axis the in-phase tilt develops, it is also the polar axis. Upon the unit cell transformation the cell volume is reduced to one half of the initial volume:

$$\mathbf{a}_t = {}^1\!/_2\,\mathbf{a}_c - {}^1\!/_2\,\mathbf{b}_c, \tag{11.5a}$$

$$\mathbf{b}_t = {}^1\!/_2\,\mathbf{a}_c + {}^1\!/_2\,\mathbf{b}_c, \tag{11.5b}$$

$$\mathbf{c}_t = \mathbf{c}_c. \tag{11.5c}$$

Table 11.4: Details of the symmetry-adapted distortion modes in *P*4_2*nm*.

k-point	Irrep	Direction	Isotropy subgroup	Dimension	Distortion type
(0,0,0)	Γ_4^-	$(0,0,a)$	*I*4*mm*	6	polar mode $[001]_c = c_t$
(0,1,0)	X_2^+	$(0,a,0)$	*P*4_2*/mnm*	2	$a^o a^o c^+$ tilt

Only two different modes can be found with irreps Γ_4^- and X_2^+ leading to the isotropy subgroups *I*4*mm* and *P*4_2*/mnm*. A summary of the distortion modes is given in Tab. 11.4. As none of the two modes is sufficient to reduce the symmetry to *P*4_2*nm*, both modes must be primary modes. This is confirmed by the group-subgroup relation illustrated in Fig. 11.7.

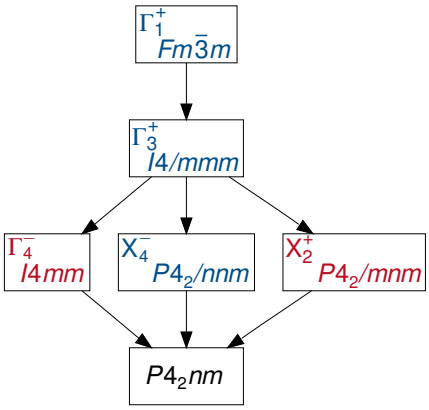

Figure 11.7: Graph of minimal subgroups connecting the space group *Fm*$\bar{3}$*m* and its subgroup *P*4_2*nm*.

In Fig. 11.8 the two modes are visualized for the optimized structure at the volume $V = 56.07$ Å^3/f.u. The oxygen atoms O1.1 and O1.2 are chemically equivalent, although they occupy crystallographically different positions, therefore all O1 atoms experience the same atomic displacements.

The polar mode corresponding to irrep Γ_4^- is shown in Fig. 11.9 (a). It leads to the isotropy subgroup *I*4*mm* and is dominated by displacements of Bi-atoms and O1-atoms. In (b) the in-phase tilt mode is visualized, as described by the irrep X_2^+, which corresponds to the tilt system

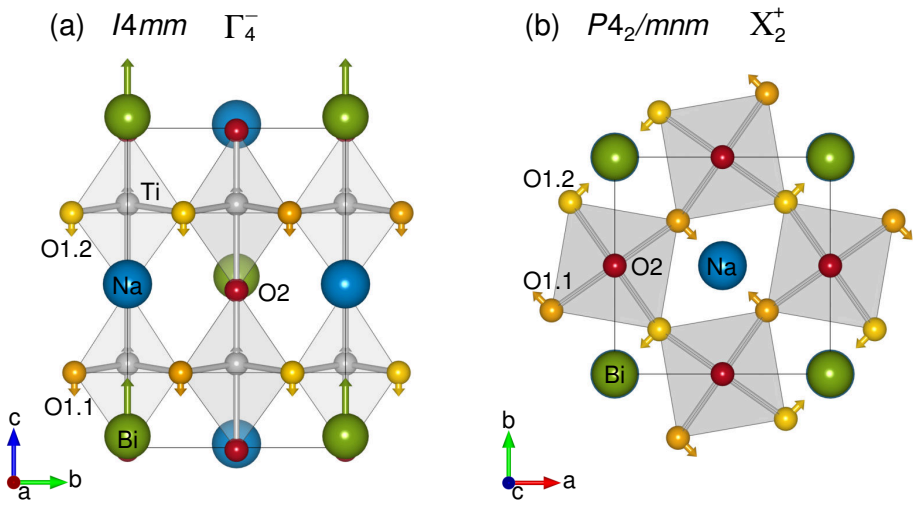

Figure 11.8: Visualization of the symmetry-adapted distortion modes within the tetragonal *P*4$_2$*nm*-structure. Structures are shown for the volume $V = 56.07$ Å^3/f.u. The atom positions are exactly as if the presented distortion mode would exist exclusively. Displacement vectors are given with the following scaling factors: (a) $\times 5$ and (b) $\times 2$. The oxygen atoms O1.1 and O1.2 are chemically equivalent.

$a^o a^o c^+$. Only O1-atoms are involved in this tilt about the tetragonal c_t-axis. At the chosen volume both distortion modes are similarly strong.

However, a sequence of phase transitions *P*4$_2$*/mnm* $\rightleftharpoons$ *P*4$_2$*nm* $\rightleftharpoons$ *I*4*mm* is evidently reflected in the mode amplitudes at different volumes presented in Fig. 11.9. The differently coloured background indicates the stability ranges of the various phases. At volumes $V < 54.1$ Å^3/f.u. only the tilt is present, while polarization is zero, in accordance with the non-polar space group *P*4$_2$*/mnm*. With increasing volume the polar mode becomes activated, resulting in the tilted and polar intermediate structure *P*4$_2$*nm*. At volumes $V > 57.4$ Å^3/f.u. tilts become unfavoured and drop to zero, the polar structure *I*4*mm* results.

The tetragonal aspect ratios c/a within the different phases given by

$$\frac{c}{a} = \frac{c_\mathrm{t}}{a_\mathrm{t}} \cdot \left(\frac{c_\mathrm{t}}{a_\mathrm{t}}\right)^{-1}_{\text{ideal}} = \frac{c_\mathrm{t}}{a_\mathrm{t}} \cdot \left(\frac{a_\mathrm{c} \cdot \sqrt{2}}{a_\mathrm{c}}\right)^{-1}_{\text{ideal}} = \frac{c_\mathrm{t}}{a_\mathrm{t}} \cdot \frac{1}{\sqrt{2}} \tag{11.6}$$

are shown in Fig. 11.9 (c). In the purely tilted phase *P*4$_2$*/mnm* the aspect ratio c/a decreases slowly with increasing volume, while it increases strongly in the purely polar phase *I*4*mm*. In the bridging phase *P*4$_2$*nm* the aspect ratio goes through a small maximum, resulting from the competition between the two order parameters tilt and polarization which couple in opposite ways to the lattice strain.

The atomic displacements accompanying the two distortion modes are presented in Fig. 11.9 (b) for the polar mode and in (d) for the in-phase tilt mode. At the lower stability limit of the *P*4$_2$*nm* bridging phase the polar mode is dominated by displacements of Na and O1. The displacements

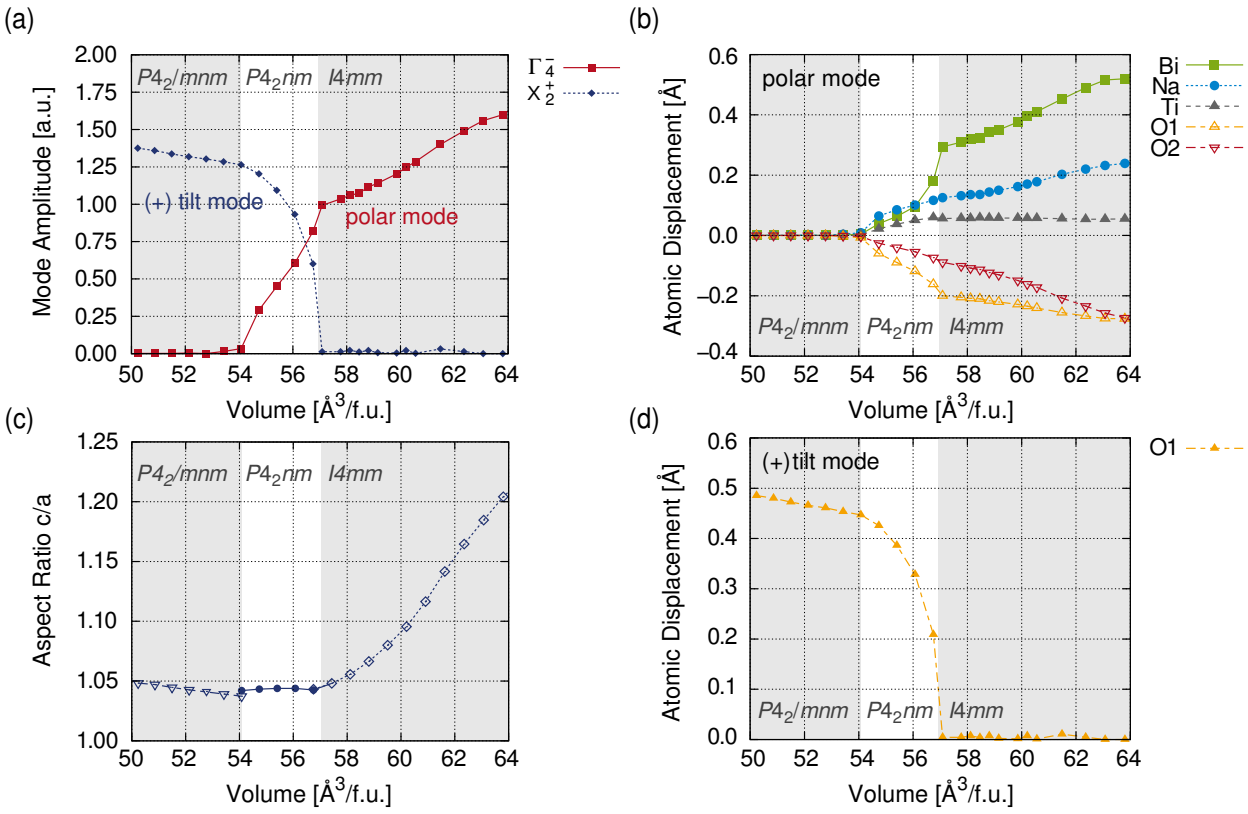

Figure 11.9: Analysis of the symmetry-adapted distortion modes in the $P4_2nm$-structures depending on volume. In (a) amplitudes of all distortion modes are given. (b) and (d) show the atomic displacements associated with the polar mode Γ_4^- and the anti-phase tilt mode X_2^+, respectively. (c) presents the evolution of the tetragonal aspect-ratio c/a with volume.

of Bi become dominating only in the upper half of the stability range of this phase. While the displacements of Na, Ti and O2 show a linear dependence on the unit cell volume, those of Bi and O1 exhibit more an exponential-like dependence at volumes between 54.1 and 57.4 Å^3/f.u. However, the largest displacements are observed in the purely polar phase *I*4*mm*. They are in the same order of magnitude as those we found in the rhombohedral *R*3-structure before. The O1-displacements resulting from the in-phase tilt mode X_2^+ in (d) show the opposite behaviour. They are maximal at small volumes, and with 0.5 Å they are indeed the largest displacements we met up to now associated with a tilt mode. In the purely tilted phase $P4_2/mnm$ the tilt-related atomic displacements decrease linearly with increasing unit cell volume. In the bridging phase the displacements immediately start to drop and reach zero at the upper stability limit of the bridging phase $P4_2nm$.

Similar to the $Pmn2_1$-structure discussed in the previous section, the polar mode Γ_4^- and the in-phase tilt mode X_2^+ show a strong interaction. They are competing distortion modes, which is clearly evident from the phase sequence resulting in the *P*4*bm*-like structures with a very small volume range where both modes can coexist. At small volumes tilts win the competition and at large volumes polarization prevails.

11.2 Chemical '001'-Order: *P*4*/mmm* Parent Structure

11.2.1 Wyckoff Splitting

Chemical A-site order with alternating layers of Bi^{3+} and Na^{+} along one of the $\langle 001 \rangle$-axes of the cubic perovskite unit cell results in the P4*/mmm* parent structure. This parent structure is tetragonal and thus possesses a four-fold rotation axis, which can be oriented in different ways relative to the in-phase tilt axes in the *Pbnm*- and *P*4*bm*-derived structures. In order to keep things simple and to reduce the number of distortion modes not related to polarization or octahedral tilting, only the orientations with the higher resulting symmetries are investigated. These are the structures, where ordered layers and in-phase tilts possess the same symmetry axis. It should be noted, that the structures with higher symmetry are not necessarily those with the lowest energies. This is especially in the *P*4*bm*-derived structure the case, where polarization has to develop perpendicular to the layers of Na/Bi.

The symmetries *R*3*c* (No. 161) and *Pbnm* (No. 62) of the ideal perovskite ABX_3 with space group $Pm\bar{3}m$ (No. 221) upon chemical '001'-ordering are reduced to the space groups *Pc* (No. 7) and $Pmc2_1$ (No. 26). Space group *P*4*bm* (No. 100) is unchanged, as it is commensurate (compatible) with this type of chemical order. The symmetry reductions from the *P*4*/mmm* parent structure are accompanied by several splittings of the occupied Wyckoff-positions 1a (Bi), 1b (Na), 2h (Ti) and 4i (O1), 1c (O2), and 1d (O3) as summarized in Tab. 11.5.

The tetragonal unit cell of *P*4*/mmm* contains two formula units $Na_{1/2}Bi_{1/2}TiO_3$. The monoclinic cell of *Pc* as well as the orthorhombic $Pmc2_1$ and tetragonal *P*4*bm* unit cells all contain four formula units. All symmetry reductions are accompanied by a cell doubling. As can be seen from Tab. 11.5 Bi and Na occupy also in these structures sites of identical symmetries and do not experience any Wyckoff splitting. All A-sites are equivalent. The tetragonal site symmetry 4*/mmm* of the A-sites is reduced to triclinic 1, monoclinic *m* and orthorhombic 2*mm*, respectively. The Ti-

Table 11.5: Splittings of Wyckoff positions in the *P*4*/mmm*-derived low-symmetry structures *Pc*, $Pmc2_1$ and *P*4*bm*.

Atom Type	*P*4*/mmm* (No. 123)	Site Symmetry	*Pc* (No. 7)	Site Symmetry	$Pmc2_1$ (No. 26)	Site Symmetry	*P*4*bm* (No. 100)	Site Symmetry
Bi	1a	4*/mmm*	2a	1	2a	*m*	2b	2*mm*
Na	1b	4*/mmm*	2a	1	2b	*m*	2b	2*mm*
Ti	2h	4*mm*	2a (1)	1	4c	1	2a (1)	4
			2a (2)	1			2a (2)	4
O	4i (1)	2*mm*	2a (1.1)	1	4c (1.1)	1	4c (1.1)	1
			2a (1.2)	1	4c (1.2)	1	4c (1.2)	1
			2a (1.3)	1				
			2a (1.4)	1				
	1c (2)	4*/mmm*	2a (2)	1	2a (2)	*m*	2a (2)	4
	1d (3)	4*/mmm*	2a (3)	1	2b (3)	*m*	2a (3)	4

site of tetragonal symmetry $4mm$ experiences Wyckoff-splitting in the *Pc* and P$4bm$ structures, accompanied by symmetry reductions to triclinic 1 and tetragonal 4. In P$mc\,2_1$ no splitting of the Ti-sites occurs, but all symmetry elements are lost except the identity 1. Again the highest degree of Wyckoff-splitting experiences the O-site. The orthorhombic site with symmetry $2mm$, which is located in the Ti-layers, is split into several chemically equivalent sites with triclinic symmetry 1 in all structures. The two tetragonal sites with symmetry $4/mmm$, which are O2 in the Bi-layers and O3 in the Na-layers, are not further split, but their symmetries are reduced to triclinic 1 in *Pc*, monoclinic *m* in *Pmc* 2_1 and tetragonal 4 in *P*$4bm$.

11.2.2 *Pc*-Structures

The unit cell transformation *P*$4/mmm$→*Pc* (unique axis b) is performed by the vector operations in Eqs. (11.7). Basis vector $\mathbf{c}_\mathrm{t}$ of the tetragonal parent phase becomes basis vector $\mathbf{a}_\mathrm{m}$ of the monoclinic cell, as a consequence the Na/Bi-layers are oriented along the a_m-axis. In this setting spontaneous polarization has components developing in two directions, along $\mathbf{a}_\mathrm{m}$ and along $\mathbf{c}_\mathrm{m}$. Moreover, the tilt mode $a^-a^-a^-$ is split into two separate modes $a^-a^-c^o$ and $a^oa^oc^-$ due to the anisotropy resulting from the chemical order, prospectively resulting in the tilt system $a^-a^-c^-$. Upon the unit cell transformation the cell volume is doubled:

$$\mathbf{a}_\mathrm{m} = \mathbf{c}_\mathrm{t} + {}^1\!/_4, \tag{11.7a}$$

$$\mathbf{b}_\mathrm{m} = \mathbf{a}_\mathrm{t} + \mathbf{b}_\mathrm{t} + {}^1\!/_4, \tag{11.7b}$$

$$\mathbf{c}_\mathrm{m} = -\mathbf{a}_\mathrm{t} + \mathbf{b}_\mathrm{t}. \tag{11.7c}$$

Due to the very low symmetry of the distorted structure, a large variety of distortion modes can be observed. In total ten distortion modes can be identified in the optimized crystal structures, they are summarized in Tab. 11.6. Besides the already discussed modes associated with polarization, octahedral tilting or chemically induced and Jahn-Teller distortions, we also find more complex deformations of the TiO_6 octahedra. Surprisingly, besides the two expected anti-phase tilt modes $a^-a^-c^o$ and $a^oa^oc^-$, also an in-phase tilt mode $a^oa^oc^+$ is active. All distortion modes are visualized in Fig. 11.10 and Fig. 11.11. First, the distortions linked with polarization and octahedral tilts will be discussed, they are given in Fig. 11.10. The first polar mode Γ_5^-, shown in (a) from two different perspectives, leads to the orthorhombic isotropy subgroup *Amm*2. This mode is dominated by displacements of Bi, Na and O2 and results in a polarization along the $\mathbf{c}_\mathrm{m}$-axis, which is in-plane with respect to the Na/Bi-layers. Bi-atoms displace much stronger than Na-atoms.
In (b) the second polar mode Γ_3^-, which leads to the tetragonal isotropy subgroup *P*$4mm$, is given. The polarization along the $\mathbf{a}_\mathrm{m}$-axis is characterized by very strong contributions from the Na-atoms, Bi-atoms - in contrast - show only minor displacements. This mode leads to out-of-plane polarization, which is perpendicular to the Na/Bi-layers. Overall, displacements originating from Γ_5^- are larger than those resulting from Γ_3^-.
In (c) the M_5^- mode leading to $a^-a^-c^o$ tilts and the subgroup *Pmma* can be seen, which involves all oxygen atoms O1-3. O2 and O3 have to move farther than O1 by a factor of $\sqrt{2}$ in order to maintain rigid TiO_6-units.

Table 11.6: Details of the symmetry-adapted distortion modes in *Pc*.

k-point	Irrep	Direction	Isotropy subgroup	Dimension	Distortion type
(0,0,0)	Γ_1^+	(a)	*P4/mmm*	2	chemically induced (Ti,O)
(0,0,0)	Γ_5^+	(a,a)	*C2/m*	3	octahedron deformation
(0,0,0)	Γ_3^-	(a)	*P4mm*	6	polar mode $[001]_\mathrm{t} = a_\mathrm{m}$
(0,0,0)	Γ_5^-	$(a,-a)$	*Amm2*	7	polar mode $[\bar{1}10]_\mathrm{t} = c_\mathrm{m}$
(½,½,0)	M_2^+	(a)	*P4/mbm*	1	$a^o a^o c^+$ tilt
(½,½,0)	M_3^+	(a)	*P4/mbm*	1	Jahn-Teller distortion (+)
(½,½,0)	M_5^+	$(0,-a)$	*Pmna*	2	octahedron deformation
(½,½,0)	M_1^-	(a)	*P4/nbm*	1	Jahn-Teller distortion (-)
(½,½,0)	M_4^-	(a)	*P4/nbm*	1	$a^o a^o c^-$ tilt
(½,½,0)	M_5^-	$(0,-a)$	*Pmma*	6	$a^- a^- c^o$ tilt

In (d) and (e) are the in-phase and anti-phase tilts about the a_m-axis presented, they are associated with the irreps M_2^+ and M_4^-. The in-phase tilts are much weaker than the anti-phase tilts, but they still lead to a significant distortion of the structure.

Second, the distortions related to chemical occupation, Jahn-Teller distortions and the complex TiO_6 octahedron deformations will be discussed, they are shown in Fig. 11.11. The chemically induced mode Γ_1^+ shown in (a), which is a so-called trivial secondary mode, as it has the symmetry of the parent structure, results in displacements of Ti-atoms towards the Na-layers and of O1-atoms, in the opposite direction, towards the Bi-layers. This mode is observed in all *P4/mmm*-derived structures and has its origin in the chemical order.
The next two modes describe complex deformations of the TiO_6 octahedra. The M_5^+ mode in (b) is dominated by displacements of Ti and O1. Ti-atoms move along the monoclinic $\mathbf{b}_\mathrm{m}$-axis, while O1-atoms displace along the $\mathbf{a}_\mathrm{m}$-axis. O1.1/O1.3 and O1.2/O1.4 displace in opposite directions, which leads to a shear-like deformation of the octahedra. However, this mode is a secondary distortion mode with a very low amplitude. In contrast to Γ_5^+, which is as strong as Γ_1^+ and leads to a significant deformation. It can be understood as $\mathrm{Ti}-\mathrm{O}$ bond bending accompanied by off-centring of the Ti-atoms along the $\mathbf{c}_\mathrm{m}$-axis. As a result two of the four $\mathrm{O1}-\mathrm{Ti}-\mathrm{O1}$ bond angles are changed to $92.22°$ and $87.78°$. Ti1- and Ti2-octahedra deform in opposite directions.
The remaining two distortion modes are in-phase and anti-phase Jahn-Teller distortions M_3^+ and M_1^- shown in (d) and (e), respectively. In (e) O1.1 and O1.2 move in opposite directions than O1.3 and O1.4. Both Jahn-Teller distortions are secondary modes with very small amplitudes.

The enormous number of distortion modes is also reflected in the complexity of the group-subgroup graph for the transformation *P4/mmm*→*Pc* ($\mathcal{G} = 123$, $\mathcal{H} = 7$, index $[i] = 16$). It is given in Fig. 11.12. In this structure even more than two primary modes are necessary to accomplish the symmetry lowering from *P4/mmm* to *Pc*. Next, we will find the most suitable candidates for these primary modes.

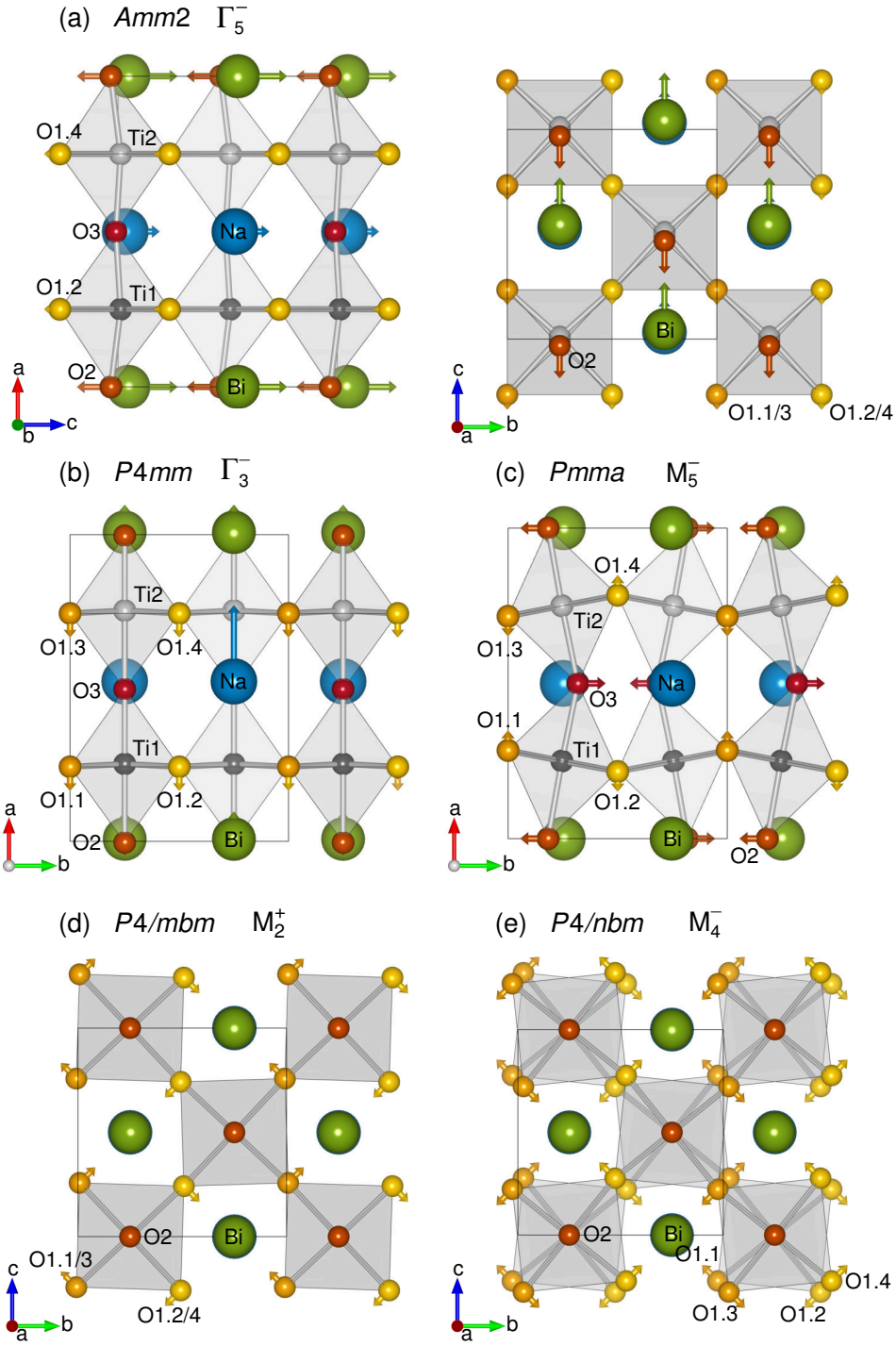

Figure 11.10: Visualization of the symmetry-adapted distortion modes of polar and tilt distortions within the monoclinic *Pc*-structure. Structures are shown for the volume $V = 56.11$ Å^3/f.u. The atom positions are exactly as if the presented distortion mode would exist exclusively. Displacement vectors are given with the following scaling factors: (a) $\times 5$ and (b) $\times 12$, (c) $\times 2$ and (d) $\times 10$, and (e) $\times 3$.

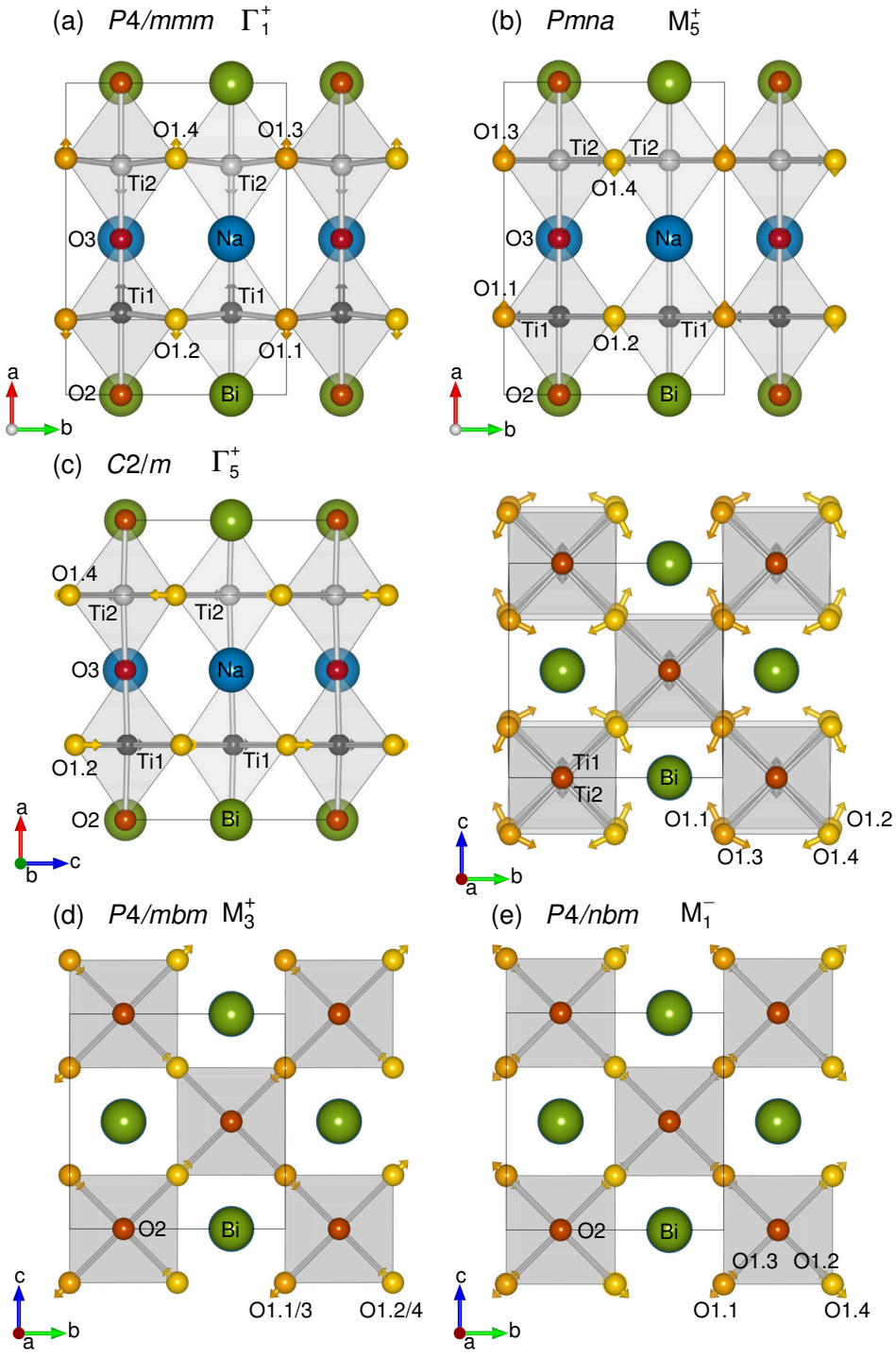

Figure 11.11: Visualization of the symmetry-adapted distortion modes of Jahn-Teller and TiO_6-octahedron distortions within the monoclinic *Pc*-structure. Structures are shown for the volume $V = 56.11$ Å^3/f.u. The atom positions are exactly as if the presented distortion mode would exist exclusively. Displacement vectors are given with the following scaling factors: (a) $\times 8$ and (b) $\times 400$, (c) $\times 10$ and (d) $\times 150$, and (e) $\times 400$.

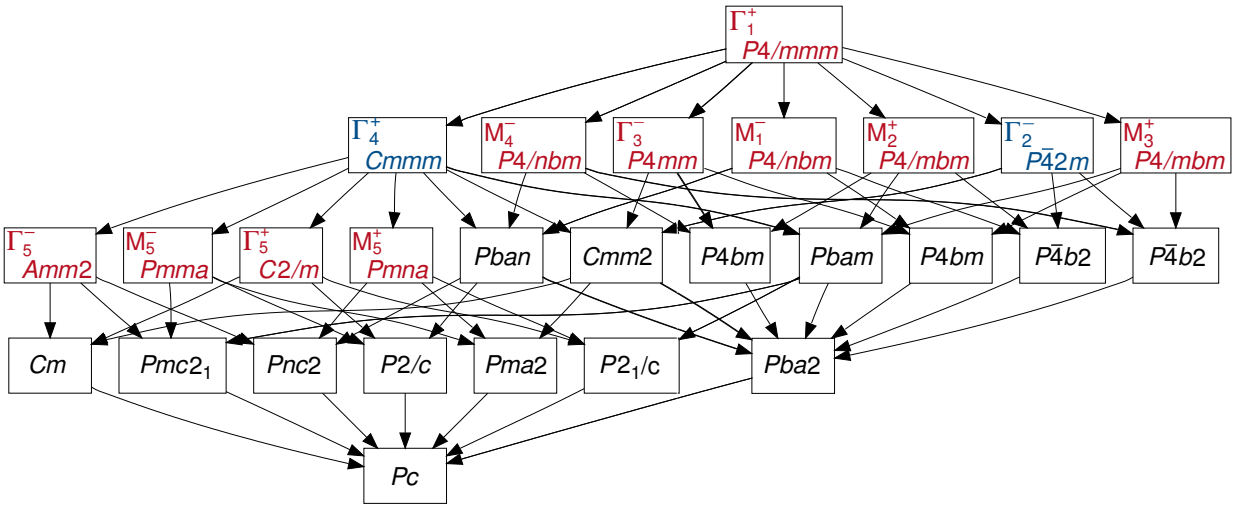

Figure 11.12: Graph of minimal subgroups connecting the space group *P4/mmm* and its subgroup *Pc*.

The mode amplitudes as they vary with volume are shown in Fig. 11.13. As mentioned earlier the three modes M_3^+, M_5^+ and M_1^- are secondary induced modes with very small amplitudes in the whole volume range.

At small volumes the anti-phase tilt modes M_4^- and M_5^- are dominating. The latter decreases linearly with volume, while the first shows a more complex behaviour. It stays constant up to 52 Å^3/f.u. and then decreases linearly with increasing volume. Moreover, it seems to be coupled to the bond bending deformation Γ_5^+, which shows exactly the same behaviour.

At large volumes the in-plane polar mode Γ_5^- becomes strongest. It shows a linear dependency on volume, while the out-of-plane polar mode Γ_4^- saturates at about 56 Å^3/f.u. at a value which is approximately one third of the amplitude of the in-plane polar mode.

The remaining two distortion modes, the chemically induced distortion Γ_1^+ and the in-phase tilt mode M_2^+, have only intermediate amplitudes with values below 0.3. Γ_1^+ increases slightly with increasing volume, M_2^+ exhibits low variation with volume up to 58 Å^3/f.u., where it starts to slightly decrease.

In Fig. 11.13 (c) is shown how the aspect ratios a/b, determined by

$$\frac{a}{b} = \frac{a_\mathrm{m}}{b_\mathrm{m}} \cdot \left(\frac{a_\mathrm{m}}{b_\mathrm{m}}\right)^{-1}_{\text{ideal}} = \frac{a_\mathrm{m}}{b_\mathrm{m}} \cdot \left(\frac{2 \cdot a_\mathrm{sc}}{\sqrt{2} \cdot a_\mathrm{sc}}\right)^{-1}_{\text{ideal}} = \frac{a_\mathrm{m}}{b_\mathrm{m}} \cdot \frac{1}{\sqrt{2}} \tag{11.8}$$

and c/b of the monoclinic unit cell and the angle β evolve with the unit cell volume. The tetragonal unit cell of the parent structure *P4/mmm* is doubled along the c_t-axis with respect to the simple cubic perovskite unit cell. So, it is easier to express the monoclinic cell parameters in terms of the simple cubic unit cell (sc). The aspect ratio c/b correlates perfectly well with the out-of-plane component of the spontaneous polarization associated with irrep Γ_5^-. Likewise, the aspect ratio a/b correlates with the in-plane component of the spontaneous polarization arising from irrep Γ_3^-. The monoclinic angle β up to 58 Å^3/f.u. depends almost linearly on the volume and passes through a maximum at about 61 Å^3/f.u.. The kink in the amplitudes of the anti-phase tilt mode M_4^- and the bond bending deformation Γ_5^+ coincide with $\beta = 90°$.

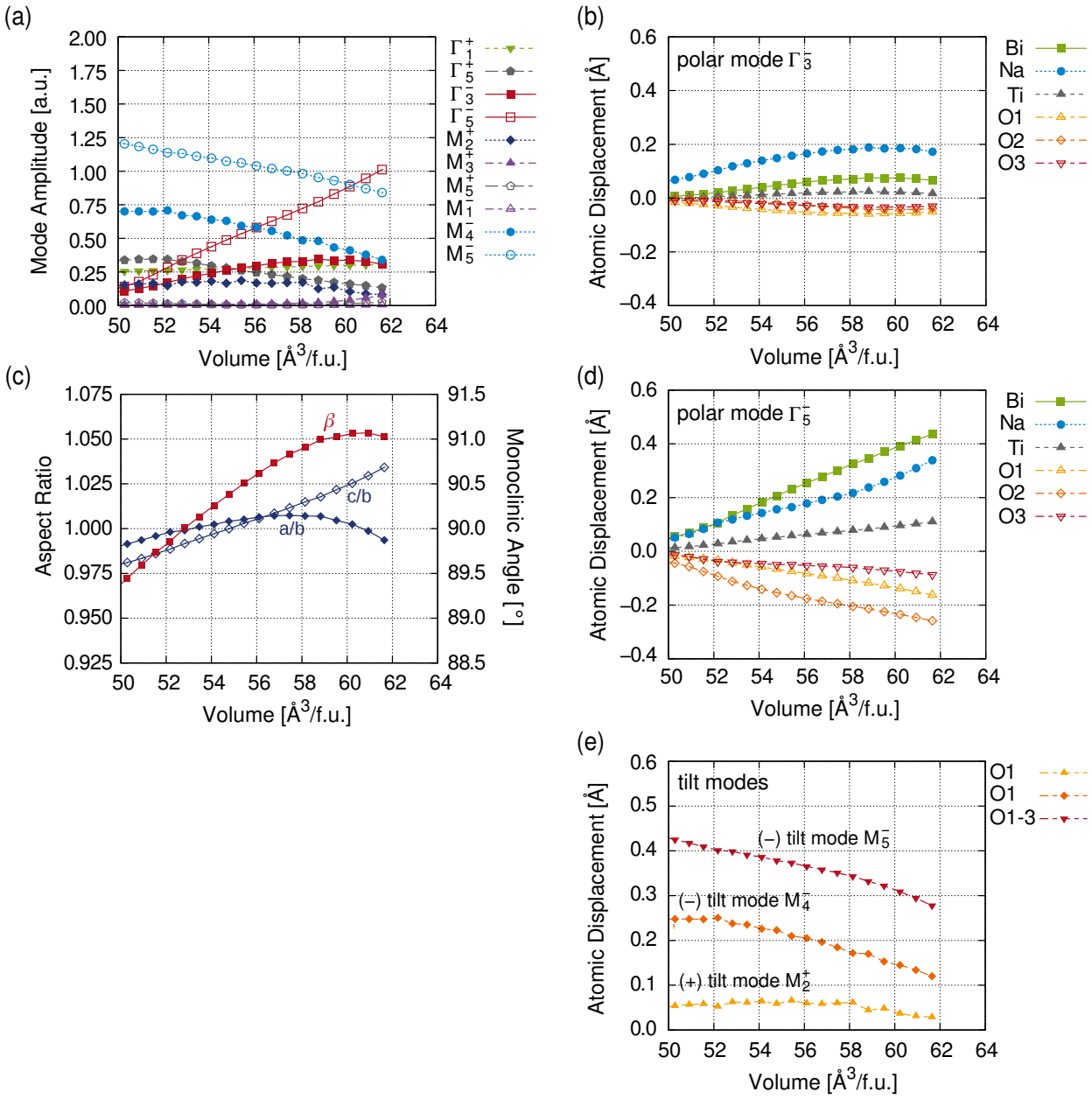

Figure 11.13: Analysis of the symmetry-adapted distortion modes in the *Pc*-structures depending on volume. In (a) the amplitudes of all distortion modes are given. (b) and (d) show the atomic displacements associated with the two different polar modes Γ_3^- and Γ_5^-, respectively. In (e) the amplitudes of the three tilt modes M_2^+, M_4^- and M_5^- are given. (c) presents the evolution of the monoclinic aspect-ratios a/b and the c/b as well as of the monoclinic angle β with volume.

Now we want to gain some deeper insights into the atomic displacements due to the polar and tilt modes and how they evolve quantitatively with varying volume. These atomic displacements are given in Fig. 11.13 (b), (d) and (e). First, we want to compare the two polar modes Γ_3^- and Γ_5^-, which lead to components of the spontaneous polarization along the $\mathbf{a}_\mathrm{m}$-axis and the $\mathbf{c}_\mathrm{m}$-axis, respectively, i.e. out-of-plane and in-plane with respect to the Na/Bi-layers. At intermediate and

large volumes the out-of-plane components (Γ_3^-) of the spontaneous polarization vector are much smaller than the in-plane components (Γ_5^-). At very small volumes, all displacements related to spontaneous polarization are small, except the displacements of Na which exceed even those of Bi at volumes $V < 52$ Å^3/f.u. Up to 52 Å^3/f.u the in-plane components of Na and Bi are equal, but the out-of-plane component of Na is eight times larger than that of Bi. With increasing volume the in-plane component of Bi increases faster than that of Na. All out-of-plane displacements show some saturation at volumes larger than 56 Å^3/f.u, above 59 Å^3/f.u even a slight decrease can be observed. All in-plane displacements increase with increasing volume leading to large polarization at large volumes.
The opposite effect is found for the tilt displacements. It is interesting to compare the two anti-phase tilts M_4^- and M_5^-. If we would have equal rotation angles about all pseudocubic axes ($a^-a^-a^-$), the displacements should fulfil the relation M_5^-:M_4^-=$\sqrt{2}$. Here the ratio of M_5^-:M_4^- is in the whole volume range larger than $\sqrt{2}$, indicating that the tilt angle of $a^oa^oc^-$ is much smaller than those of $a^-a^-c^o$. An explanation might be the simultaneous presence of the in-phase tilt $a^oa^oc^+$ due to the M_2^+-mode, which suppresses the M_4^--mode.

The dominating modes are the two anti-phase tilt modes M_5^- and M_4^-, and the two polar modes Γ_3^- and Γ_5^-, but also the in-phase tilt mode M_2^+ and the octahedron deformation mode Γ_5^+ possess considerable mode amplitudes. Almost any combination of at least three out of these six modes can act as primary modes. Yet, the three dominating modes at small volumes M_5^-, M_4^- and Γ_5^+ are not sufficient, they lead to *P2/c* only, addition of at least one of the remaining modes is necessary. At larger volumes, where the polar mode Γ_5^- becomes stronger than Γ_5^+, the combination of M_5^-, M_4^- and Γ_5^- is sufficient to describe the symmetry lowering to *Pc*.

11.2.3 *Pmc*2_1-Structures

The unit cell transformation from the tetragonal unit cell *P4/mmm* to the *Pmc*2_1 orthorhombic setting is represented by the vector transformation described by Eqs. (11.9). Since basis vector $\mathbf{c}_\mathrm{t}$ of the tetragonal unit cell transforms into basis vector $\mathbf{a}_\mathrm{o}$ of the orthorhombic cell, the Bi/Na-layers are stacked along the $\mathbf{a}_\mathrm{o}$-axis. In this setting spontaneous polarization develops along the direction of $\mathbf{c}_\mathrm{o}$:

$$\mathbf{a}_\mathrm{o} = \mathbf{c}_\mathrm{t} + {}^3\!/_4, \tag{11.9a}$$

$$\mathbf{b}_\mathrm{o} = \mathbf{a}_\mathrm{t} - \mathbf{b}_\mathrm{t} + {}^1\!/_4, \tag{11.9b}$$

$$\mathbf{c}_\mathrm{o} = \mathbf{a}_\mathrm{t} + \mathbf{b}_\mathrm{t}. \tag{11.9c}$$

The analysis of the symmetry-adapted distortion modes in the optimized structures reveals that in total five modes are active in the *Pmc*2_1-structures. The details of these distortion modes are summarized in Tab. 11.7. Besides the chemically induced mode represented by the irrep Γ_1^+, that we already found in the *Pc*-structures, there is one polar mode Γ_5^- responsible for spontaneous polarization along the c_o-axis with isotropy subgroup *Amm*2. The remaining three modes act mainly on the oxygen atoms, although the anti-phase tilt M_5^- induces also very small displacements on

Table 11.7: Details of the symmetry-adapted distortion modes in $Pmc2_1$.

k-point	Irrep	Direction	Isotropy subgroup	Dimension	Distortion type
(0,0,0)	Γ_1^+	(a)	*P4/mmm*	2	chemically induced (Ti,O)
(0,0,0)	Γ_5^-	(a,a)	*Amm2*	7	polar mode $[110]_t = c_o$
(½,½,0)	M_2^+	(a)	*P4/mbm*	1	$a^o a^o c^+$ tilt
(½,½,0)	M_3^+	(a)	*P4/mbm*	1	Jahn-Teller distortion (+)
(½,½,0)	M_5^-	$(a,0)$	*Pmma*	6	$a^- a^- c^o$ tilt

other atoms, that is why it has dimension 6. The in-phase tilt mode M_2^+ and the Jahn-Teller distortion M_3^+ both lead to the same isotropy subgroup *P4/mbm*. In Fig. 11.15 the distortion modes are visualized. We know all of them already from the *Pc*-structures. $Pmc2_1$ is a supergroup of *Pc*. The trivial secondary mode Γ_1^+ is shown in (a). Ti-atoms move towards the Na-layers, while O1-atoms displace in the opposite direction towards the Bi-layers. In (b) the anti-phase tilt mode is given associated with irrep M_5^-. The polar mode Γ_5^- with isotropy subgroup *Amm*2 is shown in (c), main contributions to spontaneous polarization arise from displacements of Bi and O2. In (d) and (e) the in-phase tilt and Jahn-Teller distortion can be seen, respectively. The latter possesses only a very small amplitude.

The group-subgroup relation for the transformation *P4/mmm* $\rightarrow$ $Pmc2_1$ ($\mathcal{G} = 123$, $\mathcal{H} = 26$, index $[i] = 8$) in Fig. 11.14 bears some similarities with the one of the analogue transformation for the '111'-chemical order in Fig. 11.5.

In comparison with the '111'-ordered $Pmn2_1$-structures we do not find an individual antipolar mode in the '001'-ordered $Pmc2_1$-structures. Small antipolar displacements of Bi and Na though are included in the anti-phase tilt dominated M_5^- mode. Moreover, a strong polar mode is present. As we do not expect the Jahn-Teller distortion M_3^+ to be a dominating mode, any combination of (at least) two modes out of M_2^+, M_5^- and Γ_5^- can act as primary distortion modes.

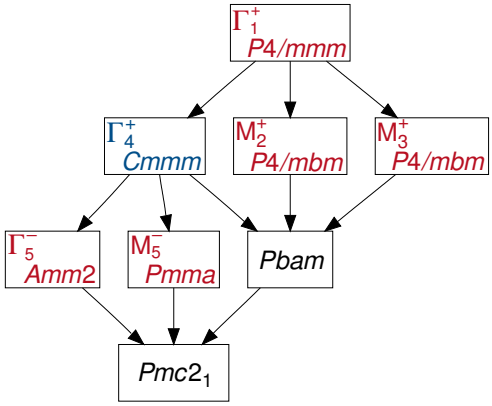

Figure 11.14: Graph of minimal subgroups connecting the space group *P4/mmm* and its subgroup $Pmc2_1$.

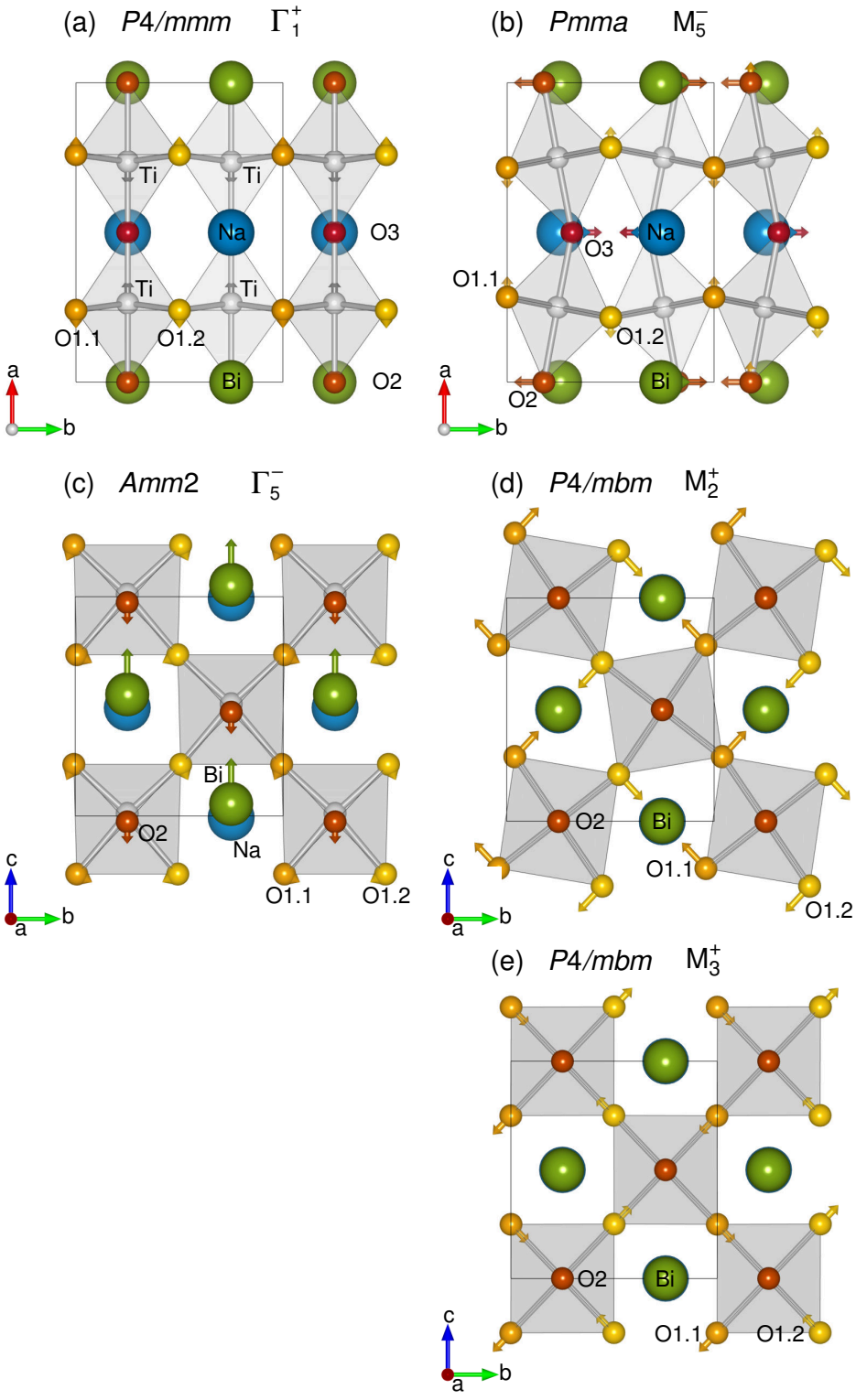

Figure 11.15: Visualization of the symmetry-adapted distortion modes within the orthorhombic *Pmc*2_1-structure. Structures are shown for the volume $V = 55.97$ Å^3/f.u. The atom positions are exactly as if the presented distortion mode would exist exclusively. Displacement vectors are given with the following scaling factors: (a) $\times 6$ and (b) $\times 2$, (c) $\times 4$ and (d) $\times 3$, and (e) $\times 130$.

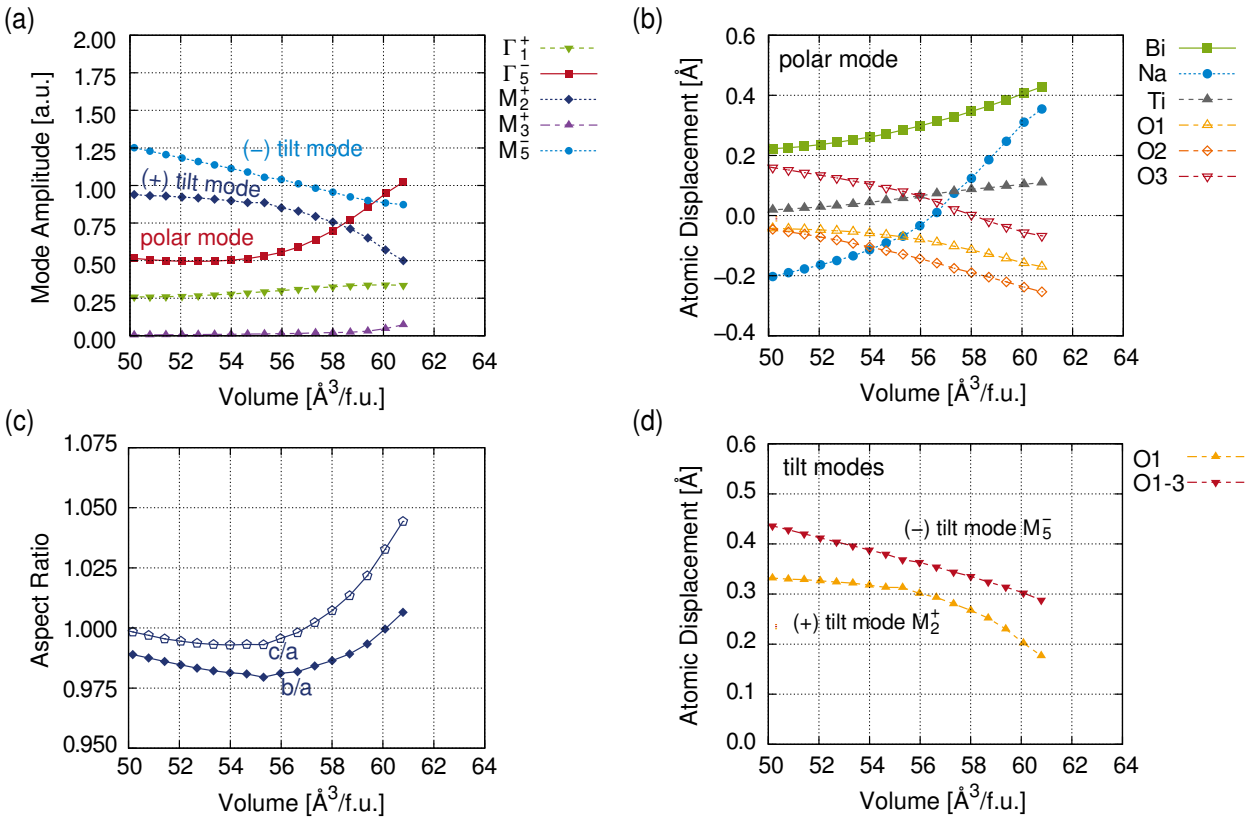

Figure 11.16: Analysis of the symmetry-adapted distortion modes in the *Pmc*2_1-structures depending on volume. In (a) amplitudes of all distortion modes are given. (b) and (d) show the atomic displacements associated with the polar mode Γ_5^- and with the two tilt modes M_2^+ and M_5^-, respectively. (c) presents the evolution of the orthorhombic aspect-ratios b/a and c/a with volume.

In Fig. 11.16 (a) the amplitudes of the five distortion modes are shown. At small and intermediate volumes the dominating modes are the anti-phase tilt mode M_5^- and the in-phase tilt mode M_2^+. M_5^- shows a linear dependence on the unit cell volume. In contrast, the in-phase tilt mode has a nearly constant amplitude up to 55 Å^3/f.u., and at larger volumes it drops faster than the anti-phase tilt mode decreases with increasing volume. At large volumes another mode becomes strongest. The polar mode behaves contrary to the in-phase tilt. Its mode amplitude is nearly constant below 55 Å^3/f.u., at larger volumes it rises fast and above 59.5 Å^3/f.u. the polar mode is the dominating one. In the low volume range the polar mode has an amplitude of 0.5, comparable to the amplitude of the antipolar mode in the *Pmn*2_1-structures at the same volumes. The absence of an individual antipolar mode in *Pmc*2_1 leads to a substantial enhancement of the spontaneous polarization, leading to mode amplitudes in the same order of magnitude as spontaneous polarization in the typical polar structures *R*3 and *Pc* at their equilibrium volumes.

It seems that the assignment of primary and secondary order parameters becomes ambiguous with increasing volumes. A clear distinction can only be made by investigating the interactions of the three dominating modes, which will be done in the following chapter.

The chemically induced trivial secondary mode Γ_1^+ depends weakly on the volume. Its amplitudes are almost equal to those in the Pc-structures. It seems this mode does not couple to other order

parameters except the lattice strain along the a_o-axis, which is illustrated by the aspect ratios b/a and c/a in Fig.11.16 (c).
The orthorhombic aspect ratios are calculated with respect to the ideal aspect ratio in a pseudocubic unit cell, as it is given in Eq. 11.10 for b/a. The second aspect ratio c/a is obtained by the same way, by

$$\frac{b}{a} = \frac{b_o}{a_o} \cdot \left(\frac{b_o}{a_o}\right)^{-1}_{\text{ideal}} = \frac{b_o}{a_o} \cdot \left(\frac{\sqrt{2} \cdot a_{sc}}{2 \cdot a_{sc}}\right)^{-1}_{\text{ideal}} = \frac{b_o}{a_o} \cdot \sqrt{2} \tag{11.10}$$

The behaviour of the two aspect ratios is rather complex, because of the simultaneous presence of two independent tilt systems and spontaneous polarization, each affecting one or two of the lattice parameters. Up to volumes of 55 Å^3/f.u. both aspect ratios decrease gently with increasing volume, at larger volumes they increase strongly. The reason for the initial decrease is that lattice parameter a_o increases faster than b_o and c_o, which is reversed at larger volumes. The lattice parameter a_o is only affected by the anti-phase tilt, which decreases faster than the in-phase tilt in this volume range. Lattice parameter c_o is enhanced by decreasing in-phase tilt and by growing polarization. On lattice parameter b both tilt reductions have an enhancing effect.

Finally, we want to have a look at the atomic displacements resulting from the polar and the two tilt modes in Fig. 11.16 (b) and (d), respectively.
At small volumes the polar mode in (b) still bears some resemblance with the antipolar mode of its distorted parent structure *Pnma* with sodium and bismuth experiencing displacements in opposite directions by exactly the same distance and O3 displacing in the opposite direction than O1 and O2. At about 57 Å^3/f.u. we find a crossover, where the displacements of both Na and O3 have zero values. At larger volumes the displacements show typical polar behaviour, with cations and anions moving in opposite directions with values comparable to the displacements resulting from the strong polar Γ_5^--mode in the *Pc*-structures in the same volume range. Thus, at large volumes Γ_5^- in *Pmc*2_1 is a typical polar mode despite the simultaneous presence of the tilt pattern $a^-a^-a^+$, which is generally associated with antiferroelectric behaviour (antipolar displacements). Furthermore, spontaneous polarization of the *Pbnm*-like phase is comparable to that in the *R*3*c*-like phase. The atomic displacements of the oxygen atoms associated with the two tilt modes in (d) show that the displacements linked with the anti-phase tilts are equal to those of the same mode in the *Pc*-structures in Fig. 11.13. Whereas, the in-phase tilts are stronger than M_2^+ and M_4^- in summation.

11.2.4 *P4bm*-Structures

Finally, we want to discuss the *P4bm*-phase. In this case the chemical order does not break the symmetry.
The two tetragonal unit cells of the distorted structure *P4bm* and of the parent structure *P4/mmm* are related to each other by the vector transformation given in Eqs. (11.11). The transformed tetragonal unit cell spanned by the basis vectors $(\mathbf{a}_{t'}, \mathbf{b}_{t'}, \mathbf{c}_{t'})$ is rotated about the old $\mathbf{c}_t$-axis by 45° and the origin is shifted by $(1/2, 1/2, 0)$. As $\mathbf{c}_{t'} = \mathbf{c}_t$ the Na/Bi-layers are stacked along $\mathbf{c}_{t'}$ in the transformed tetragonal unit cell:

$$\mathbf{a}_{t'} = \mathbf{a}_t - \mathbf{b}_t + 1/2, \tag{11.11a}$$

$$\mathbf{b}_{t'} = \mathbf{a}_t + \mathbf{b}_t + 1/2, \tag{11.11b}$$

$$\mathbf{c}_{t'} = \mathbf{c}_t. \tag{11.11c}$$

Table 11.8: Details of the symmetry-adapted distortion modes in *P4bm*.

k-point	Irrep	Direction	Isotropy subgroup	Dimension	Distortion type
(0,0,0)	Γ_1^+	(a)	*P4/mmm*	2	chemically induced (Ti,O)
(0,0,0)	Γ_3^-	(a)	*P4mm*	6	polar mode $[001]_{pc} = c_t$
(½,½,0)	M_2^+	(a)	*P4/mbm*	1	$a^o a^o c^+$ tilt
(½,½,0)	M_4^-	(a)	*P4/nbm*	1	$a^o a^o c^-$ tilt

The analysis of the optimized structures reveals the presence of four different distortion modes, which we all know already from the *Pc*-structures. *P4bm* is another supergroup of *Pc*. There are the chemically induced displacements of Ti and O1 associated with the trivial secondary mode Γ_1^+. The polar mode leads to spontaneous polarization along the $c_{t'}$-axis with isotropy subgroup *P4mm*. The remaining two modes lead to in-phase and anti-phase tilts about the polar axis, they transform like the irreps M_2^+ and M_4^-.

In Fig. 11.17 the four modes are visualized for the optimized structure with volume $V = 59.50$ Å^3/f.u. The oxygen atoms O1.1 and O1.2 are chemically equivalent, although they occupy crystallographically different positions.

In Fig. 11.17 (a) we can see the Γ_1^+-mode, which is a bit more pronounced in this structure due to the larger volume (and larger c/a-ratio) as compared to the corresponding pictures of the same mode within the *Pc* and *Pmc*2_1-structures. The polar Γ_3^--mode in (b) is similar to the Γ_3^--distortion in the *Pc*-structure, in the sense that the main contribution to spontaneous polarization originates from the Na-atoms which experience the largest displacements. In (c) and (d) are the tilt modes shown. The in-phase tilt leads to large displacements of the O1-atoms, while the displacements due to the anti-phase tilt about the same axis, leading to displacements of O1.1 and O1.2 in opposite directions, are very small. This is a strong indication that the latter is an induced secondary mode,

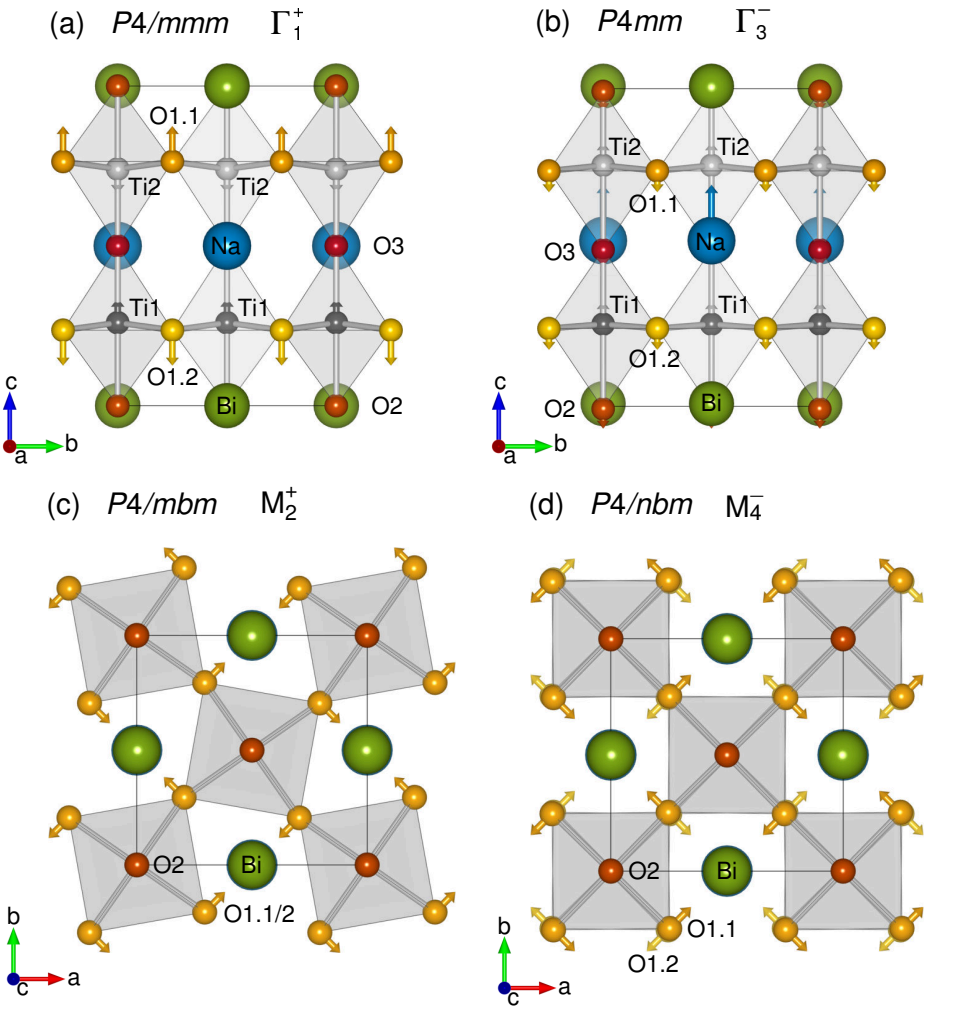

Figure 11.17: Visualization of the symmetry-adapted distortion modes within the tetragonal *P*4*bm*-structure. Structures are shown for the volume $V = 59.50$ Å^3/f.u. The atom positions are exactly as if the presented distortion mode would exist exclusively. Displacement vectors are given with the following scaling factors: (a) $\times 8$ and (b) $\times 8$, (c) $\times 2$ and (d) $\times 30$.

only.

A finding that is supported by a view on the group-subgroup relations in Fig. 11.18 ($\mathcal{G} = 123$, $\mathcal{H} = 100$, index $[i] = 4$).[1] Space group *P*4*bm* is a common subgroup of the isotropy subgroups *P*4*mm*, *P*4/*nbm* and *P*4/*mbm*. Here, any combination of two of these isotropy subgroups leads to space group *P*4*bm*. Which confirms our finding that we have two primary modes Γ_3^- and M_2^+ and the third mode M_3^+ as an induced secondary distortion. Yet, any other combination of two modes being primary is equally possible.

[1] The given graph is the contracted graph. The combination of the in-phase and anti-phase Jahn-Teller distortions M_3^+ and M_1^- can also result in a $P4bm$-structure, which can be easily differentiated from the tilted structure as it does not possess the origin shift of $(1/2, 1/2, 0)$.

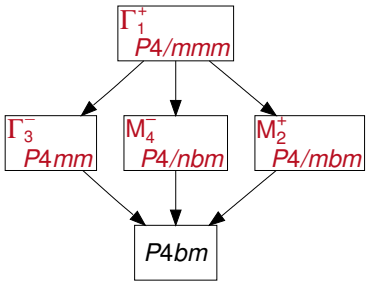

Figure 11.18: Graph of minimal subgroups connecting the space group *P4/mmm* and its subgroup *P4bm*.

Let us come to the evolution of the distortion modes with the unit cell volume. In Sec. 11.1.4 about the '111'-ordered $P4_2nm$-structures we learnt, that tilts and spontaneous polarization are strongly competing with each other in the *P4bm*-structure type resulting in a very small volume range where both lattice instabilities can coexist. The same we can find in the *P4bm*-structures reviewed now.

In Fig. 11.19 the results of the analysis of the symmetry-adapted distortion modes within the *P4bm*-structures are presented. In all figures three different phase regions are marked. At volumes $V < 57.5$ Å^3/f.u. the in-phase tilted *P4/mbm*-structure is stable. Between 57.5 and 62.3 Å^3/f.u. the tilted polar *P4bm*-structure can be found and at volumes $V > 62.3$ Å^3/f.u. the purely polar *P4mm*-structure develops. Thus, the following phase sequence is found:

$$P4/mbm \rightleftharpoons P4bm \rightleftharpoons P4mm. \tag{11.12}$$

At small and intermediate volumes the in-phase tilt mode has a huge amplitude of more than 1.0. In the small coexistence region, the additional anti-phase tilt mode can be seen, although its tiny amplitude makes it almost negligible. Yet, the amplitude of the polar mode shows a steep ascent with increasing volume and reaches at the upper stability limit about 1.0. The amplitude of the in-phase tilt mode decreases with a larger slope in the coexistence region, but never falls below 0.7, before it drops to zero at 62.3 Å^3/f.u. The polar mode exhibits a small jump at that volume and increases with almost the same slope as in the coexistence region. With the onset of spontaneous polarization at 57.5 Å^3/f.u. also the chemically induced distortion mode Γ_1^+ shows an overall increase by 100% up to 64 Å^3/f.u. This strong increase coincides with the steep ascent of the tetragonal aspect ratio c/a, calculated by

$$\frac{c}{a} = \frac{c_\mathrm{t}}{a_\mathrm{t}} \cdot \left(\frac{c_\mathrm{t}}{a_\mathrm{t}}\right)^{-1}_{\mathrm{ideal}} = \frac{c_\mathrm{t}}{a_\mathrm{t}} \cdot \left(\frac{2 \cdot a_\mathrm{sc}}{\sqrt{2} \cdot a_\mathrm{sc}}\right)^{-1}_{\mathrm{ideal}} = \frac{c_\mathrm{t}}{a_\mathrm{t}} \cdot \frac{1}{\sqrt{2}} \tag{11.13}$$

The aspect ratio c/a decreases linearly with increasing volume in the *P4/mbm*-phase. Tilts are essentially a way to decrease the lattice parameters within the plane of octahedral rotation, which is here the ab-plane. When the rotation reduces the respective lattice parameters can elongate, leading to a reduction of the c/a-ratio approaching 1.0 with increasing volume. Polarization couples in the opposite way to lattice strain, it leads to elongation along the polar axis, which is here c_t, resulting in an enhancement of c/a with increasing volume. At large volumes we can even speak of supertetragonality, as the lattice strain exceeds 10%.

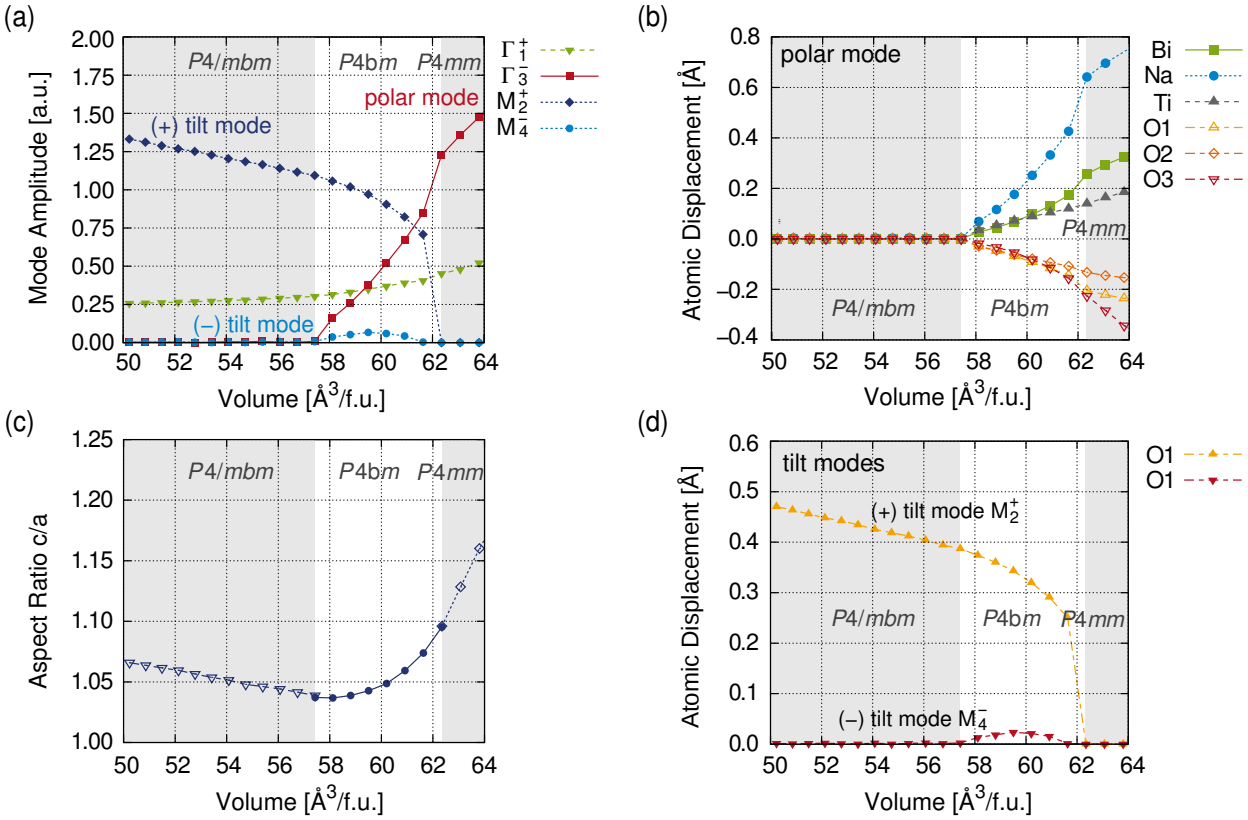

Figure 11.19: Analysis of the symmetry-adapted distortion modes in the *P*4*bm* structures depending on volume. In (a) amplitudes of all distortion modes are given. (b) and (d) show the atomic displacements associated with the polar mode Γ_3^- and with the two tilt modes M_2^+ and M_4^-, respectively. (c) presents the evolution of the tetragonal aspect-ratio c/a with volume.

The atomic displacements associated with the polar mode and the two tilt modes are given in (b) and (d), respectively. As stated before, the polar mode in (b) is dominated by displacements of the Na-atoms similar to the Γ_3^--mode in the *Pc*-structures. Yet, the Na-displacements in the structures with space group *P*4*bm* and *P*4*mm* are larger by a factor of 2 and 4, respectively. Even in comparison with other polar structures the displacements of sodium are huge, which is probably linked to the supertetragonality of the *P*4*mm*-phase. The displacements of bismuth adopt values comparable to those in the stronger polar mode Γ_5^- in the *Pc*-structures at large volumes.
The displacements of the O1-atoms resulting from the in-phase tilt are almost as large as those in the corresponding '111'-ordered structures. The displacements originating from the anti-phase tilts arising in the coexistence region are one order of magnitude smaller than those from the in-phase tilts and never exceed 0.025 Å.

11.3 Comparison of Chemical Orders '111' and '001'

11.3.1 Wyckoff Splitting

Let us first have a brief look on the splittings and symmetry changes that the Wyckoff positions experience upon the transformations in the simple perovskite unit cell from $Pm\bar{3}m$ to $R3c$, $Pbnm$ and $P4bm$. They are specified in Tab. 11.9.

Table 11.9: Wyckoff splitting in distorted structures derived from the $Pm\bar{3}m$ parent structure.

Atom	$Pm\bar{3}m$ Wyckoff	(No. 221) Symmetry	$R3c$ Wyckoff	(No. 161) Symmetry	$Pbnm$ Wyckoff	(No. 62) Symmetry	$P4bm$ Wyckoff	(No. 100) Symmetry
$Na_{1/2}Bi_{1/2}$	1a	$m\bar{3}m$	6a	3	4c	$\bar{1}$	2b	$2mm$
Ti	1b	$m\bar{3}m$	6a	3	4a	$\bar{1}$	2a	4
O	3c	$4/mmm$	18b	1	8d (1)	1	4c (1)	m
					4c (2)	$\bar{1}$	2a (2)	4

In the high-symmetry parent structure $Pm\bar{3}m$ bismuth and sodium have to be treated as a single "averaged atom" $Na_{1/2}Bi_{1/2}$. This averaged atom and titanium both occupy Wyckoff positions 1a and 1b of the same Wyckoff set with (cub)octahedral $m\bar{3}m$ site symmetry, while the oxygen-site has tetragonal $4/mmm$ symmetry. The cubic unit cell contains one formula unit, only.
None of the Wyckoff positions experiences splitting in the $R3c$-structure, but site symmetries are reduced. $Na_{1/2}Bi_{1/2}$ and Ti occupy different orbits of the same Wyckoff position 6a with trigonal 3 site symmetry. The oxygen atoms are situated on the general Wyckoff position 18b with triclinic 1 symmetry. The conventional hexagonal unit cell contains six formula units, but there exists a primitive rhombohedral unit cell with two formula units.
The highest degree of symmetry reduction undergo the positions in the orthorhombic $Pbnm$ structure. There are two different O-sites with triclinic 1 (8d) and monoclinic $\bar{1}$ (4c) site symmetry. $Na_{1/2}Bi_{1/2}$ and Ti again occupy Wyckoff positions, that belong to the same Wyckoff set with monoclinic $\bar{1}$ site symmetry. The orthorhombic unit cell contains four formula units.
The tetragonal unit cell of the $P4bm$ structure is the smallest, it comprises only two formula units. $Na_{1/2}Bi_{1/2}$ is located on an orthorhombic site $2mm$, whereas Ti occupies a tetragonal site with symmetry 4. Two different O-sites can be found, two third of the oxygen atoms occupy a monoclinic site m (4c), and the remaining one third a tetragonal 4 site (2a).

11.3.2 *R*3*c*-like Structures

The hexagonal unit cell of the *R*3*c* structure can be obtained by applying the vector operations

$$\mathbf{a}_\mathrm{h} = -\mathbf{b}_\mathrm{c} + \mathbf{c}_\mathrm{c}, \tag{11.14a}$$

$$\mathbf{b}_\mathrm{h} = \mathbf{a}_\mathrm{c} - \mathbf{c}_\mathrm{c}, \tag{11.14b}$$

$$\mathbf{c}_\mathrm{h} = \mathbf{a}_\mathrm{c} + \mathbf{b}_\mathrm{c} + \mathbf{c}_\mathrm{c}, \tag{11.14c}$$

on the basis vectors of the simple cubic perovskite *Pm*$\bar{3}$*m* unit cell. The hexagonal $\mathbf{c}_\mathrm{h}$-vector points along the [111]-direction of the cubic unit cell, which is also the polar axis. This hexagonal unit cell has the same size as the one of the *R*3 structure.

The symmetry adapted distortion modes within the *R*3*c* structure are given in Tab. 11.10. We find two active modes in the *R*3*c* structure. First, there is the zone-center mode Γ_4^- with isotropy subgroup *R*3*m*, that generates spontaneous polarization along the 3-fold rotation axis. The second mode is the zone-boundary mode R_5^- with isotropy subgroup *R*$\bar{3}$*c*, that induces anti-phase tilts about the same axis resulting in the tilt system $a^-a^-a^-$. In Tab. 11.11 we find a comparison of the distortion modes present in the simple perovskite parent *R*3*c* and the chemically ordered structures *R*3 and *Pc*. In the '111'-ordered structure we find the same polar mode Γ_4^- with isotropy subgroup *R*3*m* and an equivalent anti-phase tilt mode, which is in this structure associated with the zone-center mode Γ_5^- with isotropy subgroup *R*32. The dimensions of the displacement vectors are increased from 4 to 6 for the polar mode and from 1 to 2 for the tilt mode. Moreover, we find two additional chemically induced modes Γ_5^+ and Γ_2^- which possess both one-dimensional displacement vectors and act separately on the titanium and oxygen atoms. In total, the number of free parameters increases from 5 to 10 for the atomic positions in the *R*3 structure.
Much more complex becomes the situation in the '001'-ordered *Pc* structure. In total ten active modes can be distinguished. The polar and the tilt mode are both split into two modes: one having a one-dimensional irrep and the other one having a two-dimensional irrep, instead of a single three-dimensional irrep as in the parent structure. The polar mode Γ_3^- is responsible for out-of-plane polarization with respect to the Bi/Na-layers (along axis a_m), while Γ_5^- leads to in-plane polarization (along axis c_m). The displacement vectors of the two polar modes possess 6 and 7 components, respectively. Similarly, the tilt mode is split into M_4^-, which is the origin of the tilt $a^oa^oc^-$ about axis a_m, and M_4^- resulting in the tilts $a^-a^-c^o$ about the b_m-axis. The chemically induced mode is the trivial secondary mode associated with irrep Γ_1^+, which we can find in any of the *P*4*/mmm*-derived structures. Five more modes are present in the *Pc* structure, they all have in common, that they lead to atomic displacements within the TiO_6-framework, only. Mode M_2^+ represents an additional in-phase tilt about the a_m-axis, whereas M_3^+ and M_1^- describe Jahn-Teller

Table 11.10: Details of the symmetry-adapted distortion modes in the *R*3*c* structure.

k-point	Irrep	Direction	Isotropy subgroup	Dimension	Distortion type
(0,0,0)	Γ_4^-	(a,a,a)	*R*3*m*	4	polar mode $[111]_\mathrm{c} = c_\mathrm{h}$
$(1/2,1/2,1/2)$	R_5^-	(a,a,a)	*R*$\bar{3}$*c*	1	$a^-a^-a^-$ tilt

Table 11.11: Comparison of the symmetry-adapted distortion modes in the simple and chemically ordered *R*3*c*-like structures. Given for every distortion mode are in the first line the irrep, the direction of the associated vector in the irrep subspace and the dimension of the displacement vector and in the second line the isotropy subgroup.

Distortion Type	*R*3*c*	*R*3	*Pc*
anti-phase tilt	R_5^- (a,a,a) 1	Γ_5^- $(-a,-a,a)$ 2	M_4^- (a) 1
	*R*3*c*	*R*32	*P*4*/nbm*
			M_5^- $(0,-a)$ 6
			Pmma
polar	Γ_4^- (a,a,a) 4	Γ_4^- (a,a,a) 6	Γ_3^- (a) 6
	*R*3*m*	*R*3*m*	*P*4*mm*
			Γ_5^- $(a,-a)$ 7
			*Amm*2
chemically induced		Γ_5^+ $(-a,-a,a)$ 1	Γ_1^+ (a) 2
		R$\bar{3}$*m*	*P*4*/mmm*
		Γ_2^- (a) 1	
		F$\bar{4}$3*m*	
in-phase tilt			M_2^+ (a) 1
			*P*4*/mbm*
Jahn-Teller			M_3^+ (a) 1
			*P*4*/mbm*
			M_1^- (a) 1
			*P*4*/nbm*
octahedral shear			Γ_5^+ (a,a) 3
			*C*2*/m*
			M_5^+ $(0,-a)$ 2
			Pmna

distortions in layers stacked in-phase and anti-phase along the same axis. The last two modes Γ_5^+ and M_5^+ induce different shear-like deformations of the octahedra. In total, the number of free parameters increases from 5 to 30 for the atomic positions in the *Pc* structure.

Chemical '001'-ordering severely disturbs the average *R*3*c* structure, while '111'-ordering only induces minor deviations. The main feature of '111'-order is that the polar displacements of bismuth and sodium differ by about 0.12 Å at the equilibrium volume of 56.09 Å^3/f.u., as can be seen in Fig. 11.3 (b). The calculated hexagonal strain of 1.25% at that volume is comparatively

high (compared to the experimental value of 0.4%[113]). It is twice the lattice strain of 0.6% for '001'-order (cf. Fig. 11.13 (c)), where an additional shear strain manifests in the monoclinic angle of $\beta = 89.38°$. The main deviations from the average structure induced by '001'-ordering result from the additional in-phase tilt originating from the M_2^+ mode. This in-phase tilt mode suppresses the anti-phase tilt about the same axis and has also impact on the out-of-plane spontaneous polarization. Thus, along the stacking direction of the Na/Bi-layers not only an additional in-phase tilt exists, but also the polarization is suppressed and exhibits an anomalous displacement vector due to the inhibition of the Bi-displacements. As a consequence, there exists a very strong correlation between chemical '001'-order and displacive polar order in the *R*3*c*-like structure.

11.3.3 *Pbnm*-like Structures

The transformation $Pm\bar{3}m \rightarrow Pbnm$ was described in detail already in the introductory part on p. 65, where also illustrations of the arising distortion modes can be found. [2]
In total, we found five distortion modes to be active in this transformation. There are the two tilt modes M_2^+ and R_5^-, responsible for in-phase $a^o a^o c^+$-tilt and anti-phase $a^- a^- c^o$-tilts, respectively. Moreover, there exist two antipolar modes, that introduce also shear deformations of the octahedra, they are associated with irreps X_5^- and R_4^-. The last mode M_3^+ leads to Jahn-Teller distortions.

Table 11.12: Comparison of the symmetry-adapted distortion modes in the simple and chemically ordered *Pbnm*-like structures.

Distortion Type	*Pbnm*	*Pmn*2_1	*Pmc*2_1
in-phase tilt	M_2^+ $(0,0,a)$ 1	X_2^+ $(0,a,0)$ 2	M_2^+ (a) 1
	*P*4*/mbm*	*P*4_2*/mnm*	*P*4*/mbm*
anti-phase tilt	R_5^- $(0,a,-a)$ 1	Γ_5^- $(0,a,-a)$ 2	M_5^- $(a,0)$ 6
	Imma	*Imm*2	*Pmma*
(anti)polar	X_5^- $(0,0,a,0,0,0)$ 2	X_5^- $(0,0,a,0,0,0)$ 5	Γ_5^- (a,a) 7
	Cmcm	*Pmmn*	*Amm*2
	R_4^- $(0,a,a)$ 2	Γ_4^- $(a,a,0)$ 6	
	Imma	*Imm2*	
Jahn-Teller	M_3^+ $(a,0,0)$ 1	X_3^+ $(0,a,0)$ 2	M_3^+ (a) 1
	*P*4*/nbm*	*P*4*/mnc*	*P*4*/nbm*
chemically induced			Γ_1^+ (a) 2
			*P*4*/mmm*

[2] Please note, that the two structures *Pbnm* and *Pnma* belong to the same space group type, they can be converted into each other by a simple rotation of the coordinate system. In literature both notations can be found, *Pbnm* is more commonly used by people from the field of crystallography (e.g. Ref. 113,126), while *Pnma* is more often found in reports about electron microscopy (e.g. Ref. 109,110).

Tab. 11.12 provides information about how these distortion modes change upon chemical ordering. The in-phase and anti-phase tilts in both ordered structures are similar to those in the distorted parent structure *Pbnm*, mainly the dimensions of the displacement vectors change. Similarly, the Jahn-Teller distortion persists, which is described by modes X_3^+ in the '111'-ordered structures and M_3^+ in the '001'-ordered structures.
Most fundamental changes undergo the antipolar modes X_5^- and R_4^- of the distorted parent structure. In the '111'-ordered *Pmn*2_1 structures, there exists a corresponding antipolar X_5^--mode that leads to similar displacements as the original planar antipolar X_5^--mode (compare Fig. 11.4 (d) and Fig. 8.5 (c)), but no comparable antipolar mode can be identified in the '001'-ordered structures. As both structures are characterized by polar space groups *Pmn*2_1 and *Pmc*2_1 -in contrast to the centrosymmetric parent structure *Pbnm*-, both ordered structures possess polar modes Γ_4^- and Γ_5^-, respectively. The cation displacement pattern induced by Γ_5^- in *Pmc*2_1 though exhibits some resemblance with the original antipolar mode X_5^- in *Pbnm* (compare Fig. 11.15 (c) and Fig. 8.5 (c)). The displacements originating from Γ_4^-, that arises upon '111'-ordering in the *Pmn*2_1 structure, are more similar to those of the original chequerboard antipolar R_4^--mode (compare Fig. 11.4 (c) and Fig. 8.5 (b)). The antipolar displacements resulting from M_5^- mode in *Pmc*2_1 also follow a chequerboard like pattern, but Na and Bi in the same column displace in the same direction and not in opposite directions as in the original chequerboard antipolar R_4^--mode.
Next we want to compare the deviations from the average crystal structure resulting from chemical ordering. On '111'-ordering only a weak polar mode arises, while the antipolar mode X_5^- has the same amplitude at the equilibrium volume (cf. Fig.11.6) as the antipolar mode in the parent structure given in Tab. 8.3 for $CaTiO_3$. The amplitudes of the two tilt modes as well are almost equal to those in the *Pbnm* structure. Therefore, besides the introduction of a very weak polar mode, chemical '111'-ordering does not induce significant changes in the crystal structure compared to the *Pbnm* structure of $CaTiO_3$.
In strong contrast to that, '001'-ordering causes huge changes. Not only the antipolar modes vanish, but also a strong polar mode is induced with amplitudes in the same order of magnitude not only as the original antipolar X_5^- mode in *Pbnm*, but also as the polar Γ_5^- mode in the *Pc*-structures, which is responsible for the in-plane spontaneous polarization. The atomic displacements arising from the polar Γ_5^- mode in *Pmc*2_1 resemble at small volumes more those of the antipolar X_5^- mode (c.f. Fig. 8.5 (c)) with bismuth and sodium displacing in opposite directions, as well as O2 and O3, which are situated in the same layers as bismuth and sodium. But at large volumes the displacements of all atom types are almost equal to those of the polar Γ_5^- mode in the *Pc*-structure (compare Fig. 11.16 (b) and Fig. 11.13 (d)).
To summarize, '001'-ordering induces huge deviations from the *Pbnm* average structure. The resulting *Pmc*2_1 structure has to be regarded more as typically polar than as antipolar. The *Pbnm*-like structure allows for almost the same spontaneous polarization as in the *R*3*c*-like structure without the competition between in-phase and anti-phase tilts associated with the irreps M_2^+ and M_4^-. The anti-phase tilt M_4^- is missing in the *Pbnm*-like structure.

11.3.4 *P*4*bm*-like Structures

The unit cell transformation from cubic $Pm\bar{3}m$ to tetragonal $P4bm$ is accomplished by the basis vector transformation described by

$$\mathbf{a}_\mathrm{t} = \mathbf{a}_\mathrm{c} + \mathbf{b}_\mathrm{c} + {}^1\!/_2, \tag{11.15a}$$
$$\mathbf{b}_\mathrm{t} = -\mathbf{a}_\mathrm{c} + \mathbf{b}_\mathrm{c} + {}^1\!/_2, \tag{11.15b}$$
$$\mathbf{c}_\mathrm{t} = \mathbf{c}_\mathrm{c}. \tag{11.15c}$$

The polar axis is oriented along $\mathbf{c}_\mathrm{t}$, which is at the same time the axis, about which the in-phase tilt develops.

Table 11.13: Details of the symmetry-adapted distortion modes in *P*4*bm*.

k-point	Irrep	Direction	Isotropy subgroup	Dimension	Distortion type
(0,0,0)	Γ_4^-	$(0,0,a)$	*P*4*mm*	4	polar mode $[001]_\mathrm{c} = c_\mathrm{t}$
($1/2, 1/2$,0)	M_2^+	$(0,0,a)$	*P*4*/mbm*	1	$a^o a^o c^+$ tilt

Tab. 11.13 summarizes the distortion modes responsible for the phase transformation $Pm\bar{3}m \rightarrow P4bm$. Two modes are active, the zone-center mode Γ_4^- with isotropy subgroup *P*4*mm* is the origin of spontaneous polarization along the c-axis. The zone-boundary mode M_2^+ with isotropy subgroup *P*4*/mbm* leads to the octahedral tilt pattern $a^o a^o c^+$.

Tab. 11.14 shows how these distortion modes alter upon chemical ordering. Upon '111'-ordering only the dimensions of the displacement vectors the two modes are increased according to the Wyckoff splitting, that the occupied sites experience. Upon '001'-ordering not only the chemically induced Γ_1^+-mode appears, but also an additional tilt-mode M_3^+, which induces anti-phase rotations about the same axis as the in-phase tilt resulting from M_2^+.

Table 11.14: Comparison of the symmetry-adapted distortion modes in the simple and chemically ordered *P*4*bm*-like structures.

Distortion Type	*P*4*bm*	*P*4$_2$*nm*	*P*4*bm*
polar	Γ_4^- $(0,0,a)$ 4	Γ_4^- $(0,0,a)$ 6	Γ_3^- (a) 6
	*P*4*mm*	*I*4*mm*	*P*4*mm*
in-phase tilt	M_2^+ $(0,0,a)$ 1	X_2^+ $(0,a,0)$ 2	M_2^+ (a) 1
	*P*4*/mbm*	*P*4$_2$*/mnm*	*P*4*/mbm*
chemically induced			Γ_1^+ (a) 2
			*P*4*/mmm*
anti-phase tilt			M_4^- (a) 1
			*P*4*/nbm*

For both chemical orders the polar and the tilt mode were highly competitive resulting in a small volume range, where both distortions can coexist. It can be assumed that this finding is independent of the chemical order and is also true for the simple perovskite $P4bm$-structure. Still, differences in the ferroic properties can arise from coexistence of other distortion modes and the possibility of different ways of coupling between polar and the tilt modes, which will be investigated more thoroughly in the following chapter.

11.3.5 Domain Structure

In the introductory part we explained, which conclusions can be drawn from the transformation indices about the type and number of domain states in the distorted phases. The *translationengleiche* index $[i_t]$ indicates the number of twin domains (orientational twins) and the *klassengleiche* index $[i_k]$ is identical to the number of antiphase domains (translational twins), the product of both indices gives the total number of domain states.

In Tab. 11.15 the transformation indices are given with respect to the undistorted simple perovskite $Pm\bar{3}m$ structure for the '111'-ordered structures. Upon chemical '111'-ordering that leads to F-centring two antiphase domains can develop, they are schematically illustrated in Fig. 11.20 (a). Given are also the origin shifts that lead to identical antiphase domains. The additional introduction of polarization and octahedral tilts increases the number of possible domain states substantially as can be seen from Tab. 11.15.

Table 11.15: Indices of group-subgroup relations for '111'-ordered structures.

Space group $\mathcal{H}$	Point group $\mathcal{P}_\mathcal{H}$	Order $\lvert\mathcal{P}_\mathcal{H}\rvert$	Formula units Z	Index $[i_t]$	Index $[i_k]$	Index $[i]$
$Pm\bar{3}m$	$m\bar{3}m$	48	1	1	1	1
$Fm\bar{3}m$	$m\bar{3}m$	48	2	1	2	2
$R3$	3	3	2	16	2	32
$Pmn2_1$	$mm2$	4	4	12	4	48
$P4_2nm$	$4mm$	8	4	6	4	24
$P4_2/mnm$	$4/mmm$	16	4	3	4	12
$I4mm$	$4mm$	8	2	6	2	12

A '111'-ordered single crystal, which undergoes the phase transition $Pm\bar{3}m \rightarrow R3$ can develop 32 different domains. There are eight possible orientations for the tilts (all $\langle 111\rangle$-directions), each allowing for two directions of the spontaneous polarization (parallel and antiparallel to the tilt axis), in total resulting in 16 twin domains, which can have each of them a corresponding antiphase domain originating from the two possibilities of the chemical order. The antiphase domains developing due to the anti-phase tilts, however, are equivalent to those originating from chemical order, as can be seen in Fig. 11.20 (b).

The 12 twin domains in the $Pmn2_1$ structure originate from six possible orientations (half of the $\langle 110\rangle$-directions) for the anti-phase tilt multiplied by two for the two possible orientations of the additional in-phase tilt. In addition to the antiphase domains, which have different chemical

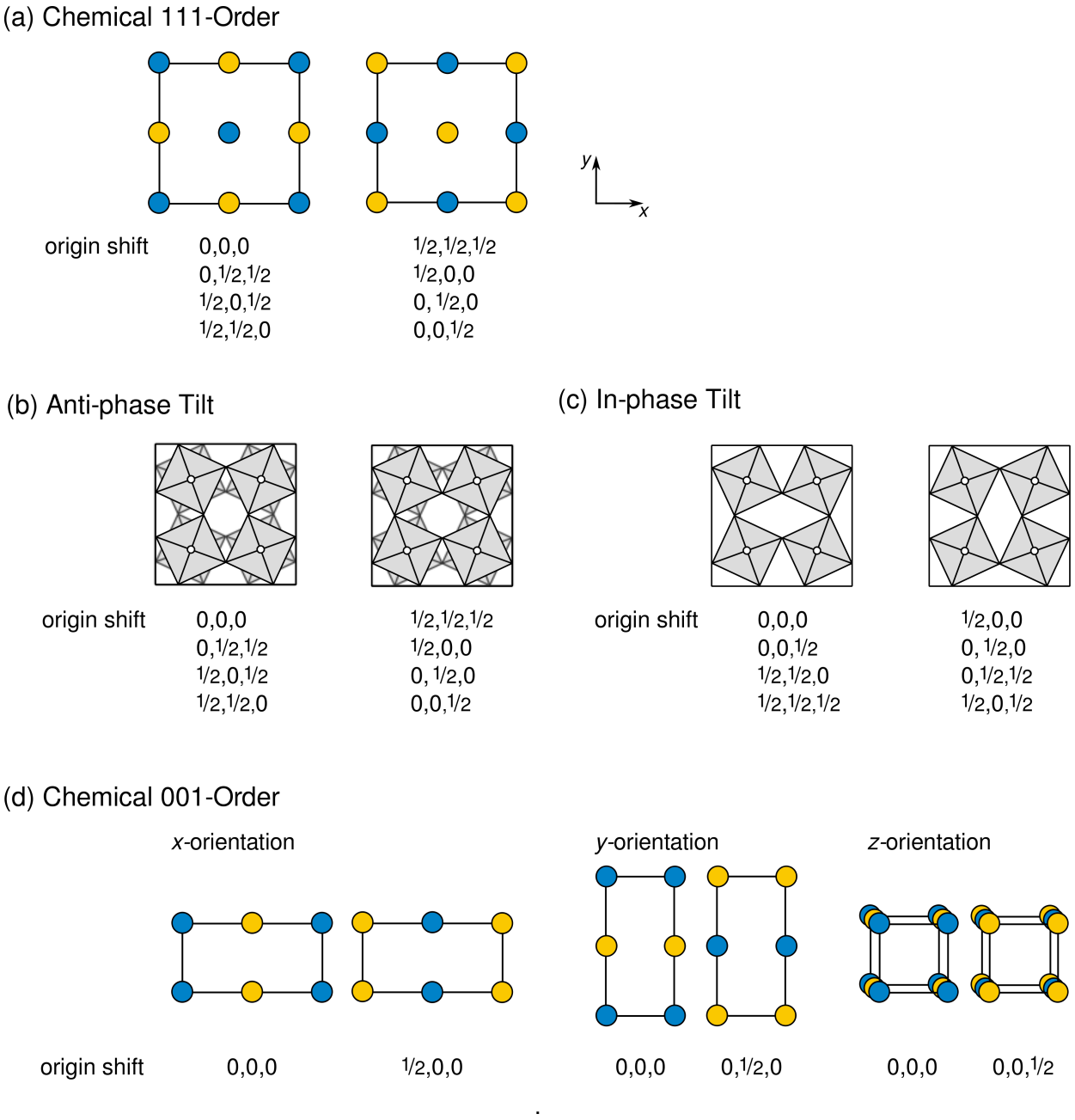

Figure 11.20: Antiphase and twin domains resulting from (a) chemical '111'-order, (b) anti-phase tilt $a^o a^o c^-$ and (c) in-phase tilt $a^o a^o c^+$, and from (d) chemical '001'-order. Different colors indicate different atom types. In the first three cases only antiphase domains develop, in (d) also twin domains characterized by the orientation of the Na/Bi-layers can be distinguished.

order, there are additional antiphase domains due to the in-phase tilts, schematically shown in Fig. 11.20 (c).

In the $P4_2nm$ phase, we can have three orientations for the in-phase tilt ([100], [010] and [001]) with two possible directions (parallel and antiparalell) for the spontaneous polarization each. In the tilt-only $P4_2/mnm$ structure three different twin domains with four antiphase domains each can de-

velop. In the polar-only *I*4*mm* six orientations of the polar vector are possible (all $\langle 100 \rangle$-directions) giving six twin domains, multiplied by two for the two possibilities of antiphase domains for the chemical ordering.

In Tab. 11.16 the respective results for the '001'-ordered structures are summarized. On chemical ordering in the *P*4*/mmm* structure already three different twins with two corresponding antiphase domains are possible, as presented in Fig. 11.20 (d). The twins arise from different orientations of the layers relative to the axes a, b, c of the cubic parent structure.
In the *Pc* phase, we can find 24 possible twin orientations, three originate from the chemical ordering, which have to be multiplied by eight for the orientation of the tilt axis. This is different from the '111'-ordered case, where for every tilt orientation two polarization directions were equivalent. Due to the additional in-phase tilt $a^o a^o c^+$ the two polarization directions $[111]$ and $[\bar{1}\bar{1}\bar{1}]$ become different. Leaving for every tilt orientation in the *Pc* structure only one explicit polar vector. Due to the additional presence of tilts four antiphase domains are possible, giving us in total not less than 96 possible domain configurations, three times more than in the *R*3 structure.
The remaining phases result in the same numbers of domain configurations as in the '111'-ordered phases, because the space groups of all corresponding structures belong to the same point groups and contain the same number of formula units. Thus, this is leading to exactly the same transformation indices and therefore to the same numbers and types of domains.

Table 11.16: Indices of group-subgroup relations for '001'-ordered structures.

Space group $\mathcal{H}$	Point group $\mathcal{P}_\mathcal{H}$	Order $\lvert\mathcal{P}_\mathcal{H}\rvert$	Formula units Z	Index $[i_t]$	Index $[i_k]$	Index $[i]$
Pm$\bar{3}$*m*	*m*$\bar{3}$*m*	48	1	1	1	1
*P*4*/mmm*	4*/mmm*	16	2	3	2	6
Pc	*m*	2	4	24	4	96
Pmc2_1	*mm*2	4	4	12	4	48
*P*4*bm*	4*mm*	8	4	6	4	24
*P*4*/mbm*	4*/mmm*	16	4	3	4	12
*P*4*mm*	4*mm*	8	2	6	2	12

11.4 Summary

In this chapter we saw how powerful group theoretical tools are in simplifying crystal structures and how they can help to understand the evolution of different distortion modes and their resulting atomic displacements with volume. Any kind of structure, irrespective of its origin (resulting from calculations, Rietveld refinement or night visions), can be characterized in the framework of symmetry-adapted distortion modes, which allows to unambiguously attribute atomic displacement to specific distortion modes.

We could see how the number and complexity of the distortion modes increase with the introduction of chemical order. Here is a short summary of what chemical ordering can initiate:

1. Introduction of chemically induced secondary distortion modes.
2. Introduction of additional secondary modes, which are allowed by symmetry, these can be Jahn-Teller distortions, additional tilt modes or shear deformations of the octahedra.
3. Splitting of polar and tilt modes.
4. Transforming antipolar modes into polar modes.
5. Increasing the number of possible domain states.

From these results it should be clear that the crystal structure on the local scale resulting from chemical (dis)order can show substantial deviations from the average crystal structure as determined by diffraction experiments. Namely, in the $R3c$ structure leads chemical (dis)order to local monoclinic or even triclinic symmetry (cf. App. C).

We learned which distortion modes are responsible for the development of several crystal structures, that can be found in the phase diagram of NBT. In all these structures in-phase and antiphase tilts and (anti)polar distortion modes play major roles, while all other distortion modes are of minor relevance. In the following chapter we want to investigate the interplay between the structure-determining order parameters. From the above observations it should be sufficient to include the tilt and (anti)polar modes in that study, only.

12 Coupling of Order Parameters

After we identified the dominating distortion modes in the previous chapter, we are now able to investigate the coupling relations between their order parameters and to distinguish primary from secondary distortion modes. Polynomial invariants of the distortion mode irreps provide the basis of the Landau potentials employed in this chapter. We will discuss the possibilities of improper and triggered ferroelectricity, and we will discover that not only the local structure and the pressure of phase transition are changed upon chemical ordering but also the ferroic properties.

In the previous chapter we identified the different tilt and (anti-)polar modes as the main actors in the play of phase stabilities. In this chapter we are essentially interested in the direct interactions between polar, antipolar, in-phase and anti-phase tilt modes in the fully optimized structures, thus any kind of explicit interactions of these order parameters with spontaneous strain components is left out. The possibility of indirect coupling via common strain components though is implicitly included.
The full Landau potentials will be developed for all six phases discussed in the previous chapter. The specific single mode and coupling coefficients were determined only for four phases. The two phases $Pmn2_1$ and Pc, in which more than three dominating order parameters exist, were omitted, because calculation times would have exceeded several weeks.
All Landau coefficients obtained via the fitting procedures can be found in App. F.

12.1 Chemical '111'-Order: *Fm*$\bar{3}$*m* Parent Structure

12.1.1 *R*3-Structures

In the *R3* structure we found two primary distortion modes Γ_4^- and Γ_5^- leading to spontaneous polarization along the hexagonal c_h-axis and to anti-phase tilts about the same axis. Only the coexistence of both distortion modes leads to space group *R3*.
In the following the interaction between these two distortion modes is studied at the equilibrium volume $V_0 = 56.62$ Å^3/f.u. in the hexagonal unit cell. We can expand the energy[1] in terms of the respective mode amplitudes (order parameters) P for the polar mode Γ_5^- and θ for the anti-phase tilt mode Γ_4^- leading to the single mode Landau potentials $E(P)$ and $E(\theta)$.

$$E(P) = a_{20}P^2 + b_{40}P^4 + c_{60}P^6 \tag{12.1}$$

$$E(\theta) = a_{02}\theta^2 + b_{04}\theta^4 + c_{06}\theta^6 \tag{12.2}$$

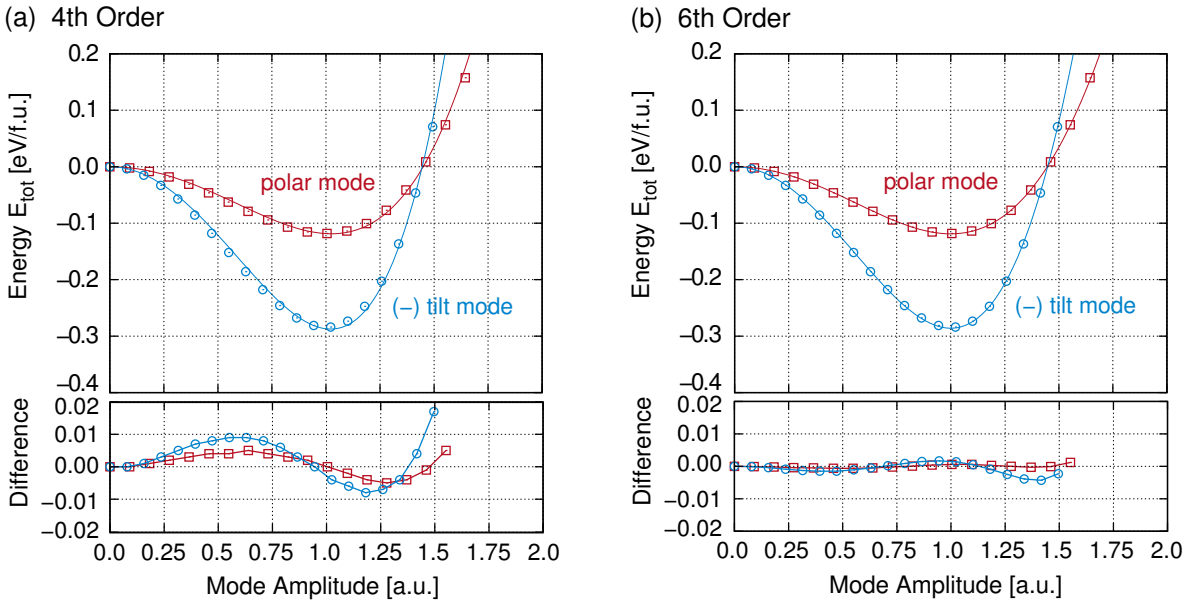

Figure 12.1: Single modes in the *R3*-structure at $V_0 = 56.62$ Å^3/f.u., mode amplitudes are normalized with respect to the values $|P_0^{\mathrm{sm}}| = 0.49$ and $|\theta_0^{\mathrm{sm}}| = 0.90$ corresponding to the minimum of energy. Calculated energies were fitted to the expansion up to (a) 4th order and (b) 6th order.

In Fig. 12.1 the energies, calculated under systematic change of only one of the order parameters, while the second one was kept equal to zero, were fitted to expansions Eq. 12.1 and Eq. 12.2 up to (a) 4th order and (b) 6th order. In both (a) and (b), the mode amplitudes are normalized with respect to the absolute mode amplitudes at the energy minima as obtained in the 6th order expansion in (b). These absolute amplitudes of the single modes are $|P_0^{\mathrm{sm}}| = 0.49$ for the polar mode and $|\theta_0^{\mathrm{sm}}| = 0.90$ for the anti-phase tilt mode.

[1] For $T = 0$ K, the free energy F becomes equal to the energy E.

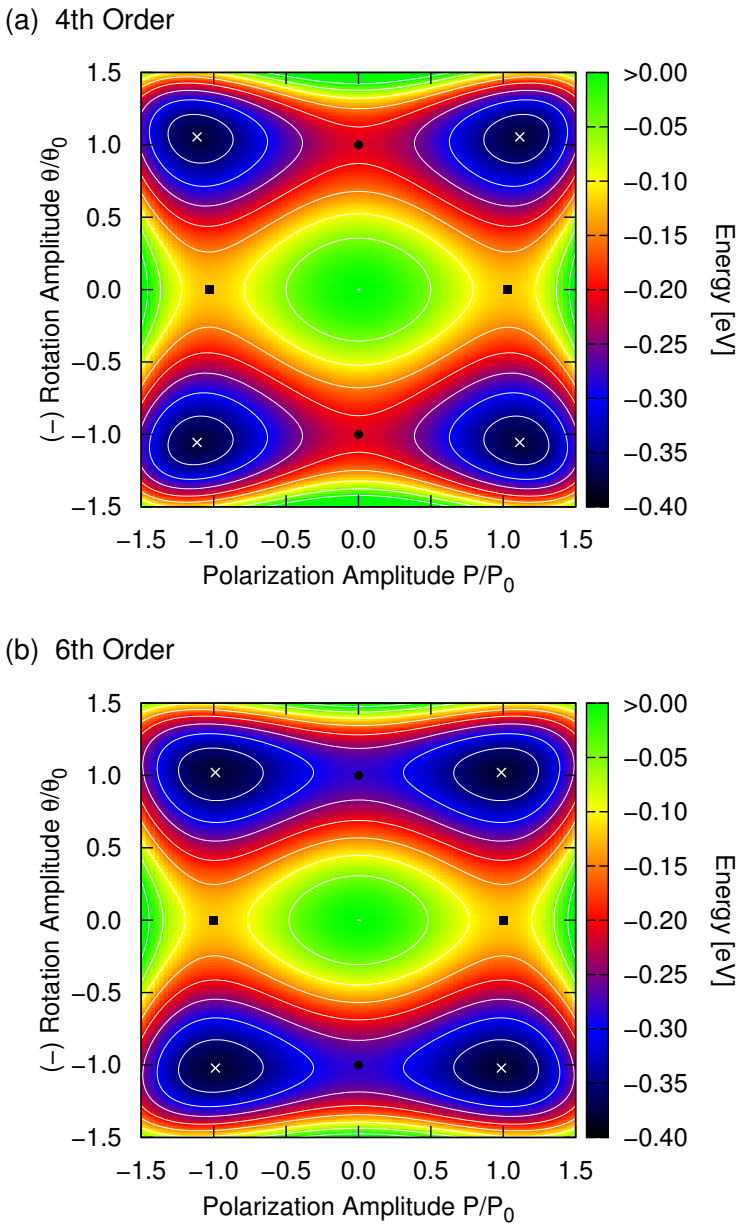

Figure 12.2: Energy E_{tot} depending on the amplitudes of the polar and anti-phase tilt modes. Energies were fitted to the Landau potential up to (a) 4th order and (b) 6th order. Amplitudes are normalized with respect to the single mode values of the 6th order potential ($|P_0^{\text{sm}}| = 0.49$ and $|\theta_0^{\text{sm}}| = 0.90$). Global energy minima are marked with white cross and energy barriers with black circle (zero polarization) and black square (zero tilt). The distance between the isolines is 0.05 eV.

Below the energies, we also give the differences between the Landau potential energies and the calculated data. While the 6th order expansion reproduces the calculated data perfectly over the whole amplitude range, the 4th order expansion gives rather approximate correspondence to the calculated energies with deviations up to 0.01 eV. Moreover, the positions of the minima are shifted to higher amplitudes $|P_0^{4\text{th}}| = 0.51$ and $|\theta_0^{4\text{th}}| = 0.92$.
Overall, the minimum energy of the anti-phase tilt distortion is with 0.286 eV/f.u. about 2.5 times lower than the 0.119 eV/f.u. of the polar distortion. The system is much more prone to tilt distortion than to polar distortion at the given volume.

However, we are interested in the coexistence of both distortion modes. The complete Landau potential E_{tot} is a sum of the single mode energies and additional interaction terms $E(P, \theta)$ resulting from the coupling of the two modes, where the Landau expansion reads as

$$E_{\text{tot}} = E(P) + E(\theta) + E(P, \theta), \tag{12.3}$$

with

$$E(P, \theta) = b_{22}P^2\theta^2 + c_{24}P^2\theta^4 + c_{42}P^4\theta^2. \tag{12.4}$$

We obtain three common coupling terms. The biquadratic $b_{22}P^2\theta^2$ is the lowest order coupling term. The remaining two are of 6th order and are both quadratic-quartic, $c_{24}P^2\theta^4$ and $c_{42}P^4\theta^2$. As shown in the introductory part, the coexistence of both distortions can lead to an increase or decrease in energy and alter the amplitudes of the two modes with respect to their single mode values, depending on the signs and magnitudes of the coefficients b_{22}, c_{24} and c_{42}.

In Fig. 12.2 (a) and (b) the fit (according to Eq. 12.3) of energies E_{tot} depending on the amplitudes of the polar and anti-phase tilt modes are given, truncated after the 4th order terms or taken also the 6th order terms into account, respectively. At the origin we find the high-symmetry structure with energy $E(0, 0) = 0$, which only exhibits the lattice strain of the optimized equilibrium structure. Moving from this position in the horizontal direction and keeping $\theta = 0$ we follow the polarization-only curves, moving in vertical direction keeping $P = 0$ we follow the tilt-only curves. At any other positions we impose coexistence of polarization and anti-phase tilt. In the figures the positions of the global energy minima are marked by white cross, also marked are the tilt-switching barriers at $\theta = 0$ (black square) and the polarization-switching barriers at $P = 0$ (black circle).

Both diagrams in Fig. 12.2 (a) and (b) resemble energy profiles of the "pointy sunglasses" type. This shape results from the fact that the rotation mode is about 2.5 times stronger than the polar mode. Moreover, we can state from this shape, that some of the coupling coefficients become negative.

Yet, both energy profiles exhibit some substantial differences concerning the most important information such as the positions and energies of the global minima and the heights of the switching barriers.
In (a) the global energy minimum is at $E(1.11, 1.00) = -0.375$ eV/f.u. and the switching barriers are at $E(1.03, 0) = -0.120$ eV/f.u. for tilt-switching and at $E(0, 1.0) = -0.213$ eV/f.u. for polarization-switching, while in (b) the global energy minimum is

at $E(0.99, 1.02) = -0.379$ eV/f.u. and the switching barriers are at $E(1.0, 0.0) = -0.120$ eV/f.u. for tilt-switching and $E(0.0, 1.0) = -0.280$ eV/f.u. for polarization-switching. The differences between the global energy minima and between the tilt-switching barriers in the two different energy expansions are within the accuracy limit of the ab-initio calculations, but the absolute energy of the polarization-switching barrier in (a) is underestimated by about 25% as compared to the higher order expansion in (b), resulting in an overestimation of the polarization-switching barrier with respect to the global energy minimum of 60%. Because the lower order expansion is incapable of reproducing this basic information of the energy surface, we will employ the more accurate energy expansions up to 6th order in the following, even though it complicates the fitting procedure in those cases, where we are dealing with more than two order parameters and thus more than three coupling terms have to be considered. The absolute amplitudes $|P_0| = 0.48$ and $|\theta_0| = 0.92$ are in good agreement with the values $|P_0^*| = 0.54$ and $|\theta_0^*| = 0.85$ in the fully optimized structure with the same cell parameters at $V = 56.62$. As these values are also very close to the single mode amplitudes $|P_0^{\mathrm{sm}}| = 0.49$ and $|\theta_0^{\mathrm{sm}}| = 0.90$ we can conclude that coupling between tilt and polarization in the *R*3 structure at this specific volume is very weak.

The values of the fitting parameters for the sixth order expansion are given in Tab. 12.1 for the normalized distortion modes. We can see that the sixth order single mode coefficients c_{60} and c_{06} both are very small. The coupling coefficients are very small as well, b_{22} is positive, while c_{24} and c_{42} are both negative, leading to a seemingly decoupled energy profile.

Table 12.1: Coefficients of Landau-type energy expansions.

Coefficient	Value	Abs. Standard Error	Rel. Standard Error
a_{20}	-0.2470	0.0020	0.81
b_{40}	0.1361	0.0023	1.67
c_{60}	-0.0086	0.0006	7.50
a_{02}	-0.5574	0.0039	0.70
b_{04}	0.2951	0.0042	1.44
c_{06}	-0.0180	0.0014	7.75
b_{22}	0.0544	0.0055	10.18
c_{24}	-0.0185	0.0025	13.58
c_{42}	-0.0150	0.0022	14.64

12.1.2 *Pmn*2_1-Structures

The *Pmn*2_1 structure is more complex than the *R*3 structure, where interactions between the two primary modes are dominating and interactions with secondary modes are negligible. In the *Pmn*2_1 structure we assigned the in-phase and anti-phase tilt modes X_2^+ and Γ_5^- as dominating modes, but also the antipolar X_5^- mode and the polar Γ_4^- mode exhibit considerable amplitudes. Thus, we have to include all interactions between these four distortion modes. The full Landau potential becomes the sum of all the single mode energies and the pair, triple and quadruple interactions of the amplitudes P of the polar mode, ϕ of the in-phase tilt mode, θ of the anti-phase tilt mode and P_{anti} of the antipolar mode,

$$\begin{aligned} E_{\text{tot}} &= E(P) + E(\phi) + E(\theta) + E(P_{\text{anti}}) \\ &\quad + E(P,\phi) + E(P,\theta) + E(P,P_{\text{anti}}) + E(\phi,\theta) + E(\phi,P_{\text{anti}}) + E(\theta,P_{\text{anti}}) \\ &\quad + E(P,\phi,\theta) + E(P,\phi,P_{\text{anti}}) + E(P,\theta,P_{\text{anti}}) + E(\phi,\theta,P_{\text{anti}}) \\ &\quad + E(P,\phi,\theta,P_{\text{anti}}), \end{aligned}$$

with the single mode energies

$$\begin{aligned} E(P) &= a_{2000}P^2 + b_{4000}P^4 + c_{6000}P^6, \\ E(\phi) &= a_{0200}\phi^2 + b_{0400}\phi^4 + c_{0600}\phi^6, \\ E(\theta) &= a_{0020}\theta^2 + b_{0040}\theta^4 + c_{0060}\theta^6, \\ E(P_{\text{anti}}) &= a_{0002}P_{\text{anti}}^2 + b_{0004}P_{\text{anti}}^4 + c_{0006}P_{\text{anti}}^6, \end{aligned}$$

and the pairwise interaction energies $E(P,\phi)$, $E(P,\theta)$, $E(P,P_{\text{anti}})$, $E(\phi,\theta)$, $E(\phi,P_{\text{anti}})$, and $E(\theta,P_{\text{anti}})$, which all contain the common pairwise terms with coefficients of the type b_{22}, c_{24} and c_{42} only, except for $E(P,\theta)$.
As both distortions Γ_4^- and Γ_5^- possess the same isotropy subgroup, additional coupling terms containing odd powers of the order parameters are allowed by symmetry:

$$\begin{aligned} E(P,\theta) &= b_{1030}P\theta^3 + b_{3010}P^3\theta + b_{2020}P^2\theta^2 + \\ &\quad + c_{1050}P\theta^5 + c_{5010}P^5\theta + c_{2040}P^2\theta^4 + c_{4020}P^4\theta^2 + c_{3030}P^3\theta^3. \end{aligned}$$

The four triple interaction energies all contain the common triquadratic term with coefficients of the type $c_{222}Q_1^2Q_2^2Q_3^2$, but they also contain additional lower order terms:

$$\begin{aligned}
E(P,\phi,\theta) &= b_{1210}P\phi^2\theta + c_{2220}P^2\phi^2\theta^2 \\
&\quad + c_{3210}P^3\phi^2\theta + c_{1230}P\phi^2\theta^3 + c_{1410}P\phi^4\theta, \\
E(P,\phi,P_{\text{anti}}) &= d_{1101}P\phi\,P_{\text{anti}} + e_{3101}P^3\phi\,P_{\text{anti}} + e_{1301}P\phi^3P_{\text{anti}} + \\
&\quad + e_{1103}P\phi\,P_{\text{anti}}^3 + c_{2202}P^2\phi^2P_{\text{anti}}^2, \\
E(P,\theta,P_{\text{anti}}) &= b_{1012}P\theta\,P_{\text{anti}}^2 + c_{2022}P^2\theta^2P_{\text{anti}}^2 \\
&\quad + c_{3012}P^3\theta\,P_{\text{anti}}^2 + c_{1032}P\theta^3\,P_{\text{anti}}^2 + c_{1014}P\theta\,P_{\text{anti}}^4, \\
E(\phi,\theta,P_{\text{anti}}) &= d_{0111}\phi\,\theta\,P_{\text{anti}} + e_{0311}\phi^3\theta\,P_{\text{anti}} + e_{0131}\phi\,\theta^3P_{\text{anti}} + \\
&\quad + e_{0113}\phi\,\theta\,P_{\text{anti}}^3 + c_{0222}\phi^2\theta^2P_{\text{anti}}^2.
\end{aligned}$$

Moreover, three quadruply coupled terms exist:

$$E(P,\phi,\theta,P_{\text{anti}}) = e_{1121}P\phi\,\theta^2P_{\text{anti}} + e_{2111}P^2\phi\,\theta\,P_{\text{anti}} + c_{1212}P\phi^2\theta\,P_{\text{anti}}^2.$$

A closer look at the triple and quadruple coupling terms reveals an analogy between the Γ-modes on the one hand and the X-modes on the other hand. The triple coupling terms in $E(P,\theta,P_{\text{anti}})$ combining the modes Γ_4^-, Γ_5^- and X_2^+ are identical to those in $E(P,\phi,\theta)$ combining Γ_4^-, Γ_5^- and X_5^-. Similarly, the coupling terms in $E(P,\phi,P_{\text{anti}})$ describing interaction between X_2^+, X_5^- and Γ_4^- are identical to those in $E(\phi,\theta,P_{\text{anti}})$ giving coupling between X_2^+, X_5^- and Γ_5^-. The same analogy is reflected in the quadruple coupling terms.
The interaction energies $E(P,\phi,P_{\text{anti}})$ and $E(\phi,\theta,P_{\text{anti}})$ have trilinear coupled terms as their lowest order terms, which are typical for improper ferroic behaviour. Thus, the antipolar mode can be induced or enhanced by improper coupling to the two tilt-modes. While the polar mode can be induced or enhanced by higher order coupling terms only, like the bilinear-quadratic $b_{1210}P\phi^2\theta$. Cross-talking between the polar and anti-polar modes via the triple interactions $E(P,\phi,P_{\text{anti}})$ and $E(P,\theta,P_{\text{anti}})$ might lead to unexpected feedback phenomena and means that it is not sufficient to determine only the triple contributions which couple two primary to one secondary order parameter but all four interactions.

12.1.3 $P4_2nm$-Structures

For the $P4_2nm$ structure we found three different stable phases depending on the volume. For volumes $V < 54.1$ Å^3/f.u. an in-phase tilted $P4_2/mnm$ phase is stable and for volumes $V > 57.4$ Å^3/f.u. a polar $I4mm$ phase is favored. Only for intermediate volumes 54.1 Å^3/f.u.$< V < 57.4$ Å^3/f.u. polar and in-phase tilt distortions can coexist in the $P4_2nm$ phase. Accordingly, we chose three different volumes to be investigated, each in the stability range of another phase.
First, we want to discuss the single modes. All energies were fitted to Landau potentials expanded up to 6th order in the order parameters P of the polar mode Γ_4^- and ϕ of the in-phase tilt mode X_2^+:

$$E(P) = a_{20}P^2 + b_{40}P^4 + c_{60}P^6, \quad (12.5)$$

$$E(\phi) = a_{02}\phi^2 + b_{04}\phi^4 + c_{06}\phi^6. \quad (12.6)$$

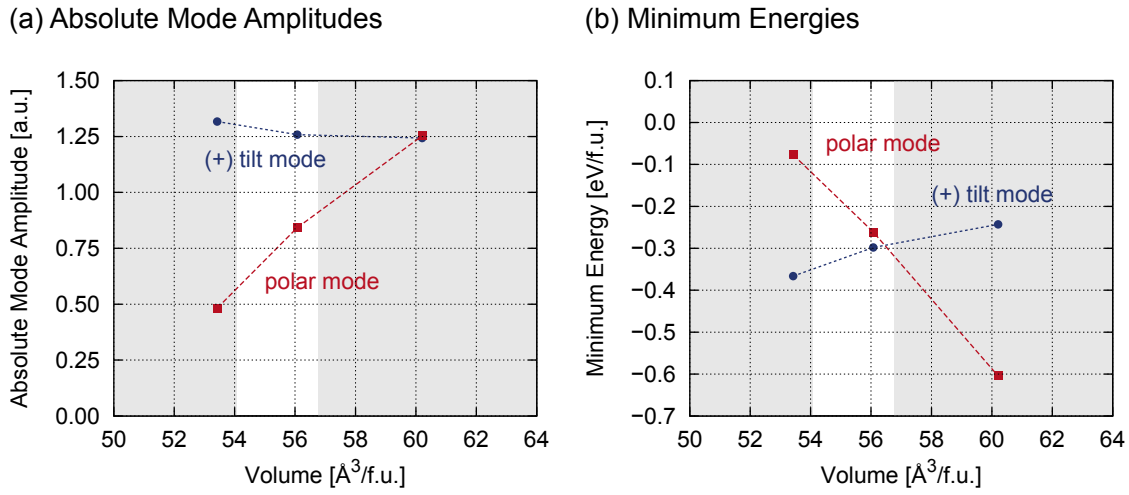

Figure 12.3: Absolute amplitudes of the single modes (a) and the respective minimum energies (b) as a function of volume. The lines are guides for the eyes. The stability ranges of the three different phases $P4_2/mnm$, $P4_2nm$ and $I4mm$ are indicated by different background colours.

In Fig. 12.3 (a) and (b) the absolute mode amplitudes and minimum energies, respectively, of the two single modes are given as a function of the unit cell volume. Both absolute mode amplitudes and energy minima depend nearly linearly on the volume. Both single modes are soft modes in the investigated volume range. The polar mode becomes softer with increasing volume, the minimum energy adopts larger values and the absolute mode amplitudes increase. The tilt mode shows the opposite effect, it becomes less soft with increasing volume. The minimum energy adopts smaller values and the absolute amplitude decreases with increasing volume. Overall, the sensitivity of the tilt mode on the volume is much smaller than that of the polar mode.

As both modes stay soft in the whole investigated volume range, the observed absence of polarization at small and of in-phase tilt at large volumes can not be explained by the absent mode being a hard mode at the respective volume. Only the competition between polar and tilt mode can explain their alternative absence at small and large volumes and the narrow volume range of coexistence.

The full Landau potential for the coexistence of polarization P and in-phase tilt ϕ besides the single mode energies contains only the so-called common pairwise coupling terms

$$E_{\text{tot}} = E(P) + E(\phi) + E(P, \phi) \tag{12.7}$$

with

$$E(P, \phi) = b_{22}P^2\phi^2 + c_{24}P^2\phi^4 + c_{42}P^4\phi^2 \tag{12.8}$$

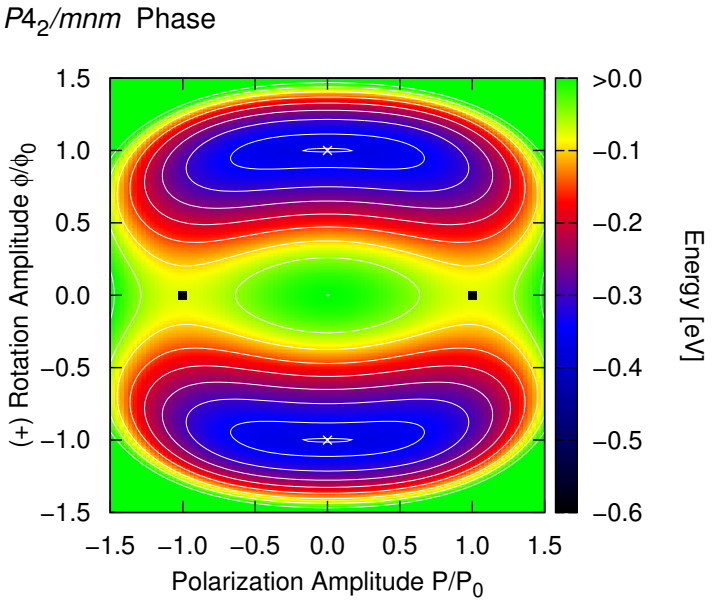

Figure 12.4: Energy E_{tot} as a function of the amplitudes of the polar and in-phase tilt modes within the *P*4_2*/mnm* phase at volume $V = 53.42$ Å^3/f.u. The amplitudes are normalized with respect to their single mode values $|P_0| = 0.48$ and $|\phi_0| = 1.30$. Isolines are given for every 0.05 eV. Energy minima are marked with white cross and energy barriers with black square (zero tilt).

In Fig. 12.4 and 12.6 the energies E_{tot} are given for the three different volumes. At the small volume $V = 53.42$ Å^3/f.u. we find a "kidney"-shaped energy profile, that is characteristic of a nearly 2:1 ratio of the single mode coefficients a_{02} and a_{20} and a biquadratic coupling term b_{22} equal to the smaller a_{20}. Moreover, c_{24} and c_{42} should be close to zero. Two global energy minima exist, which are located at zero-polarization $E_0(0.0, \pm 1.0) = -0.367$ eV and a tilt-switching barrier can be found at $P = 1.0$ with a height of $\Delta E = 0.291$ eV with respect to the global energy minima. Therefore the ground state structure is tilted with zero spontaneous polarization, although small amplitudes of spontaneous polarization might be induceable by an electric field due the very flat energy landscape in the vicinity of the global minima. Increasing polarization does not reduce

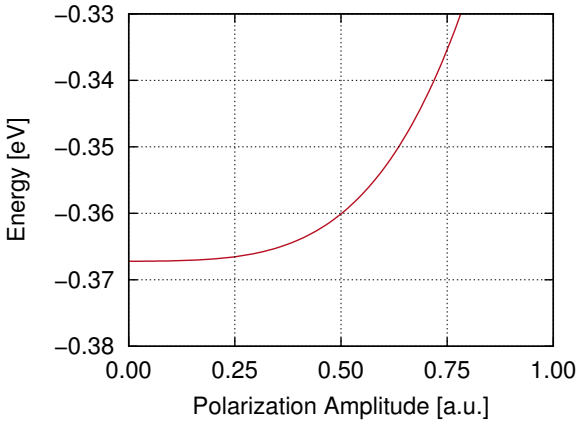

Figure 12.5: Energy E_{tot} as a function of the polar mode at fixed tilt amplitude $|\phi_0| = 1.0$ and volume $V = 53.42$ Å^3/f.u.

the tilt. Although both order parameter compete with each other, small amplitudes of spontaneous polarization about the optimum tilt amplitudes could be tolerated. In Fig. 12.5 the energies of the polar mode at fixed tilt amplitude $|\phi_0| = 1.0$ are shown.

At the intermediate volume $V = 56.07$ Å^3/f.u. we find a completely different energy profile $E(P, \phi)$, which possesses similarity with both the "goggles" and the "donut" shape with four rather flat global minima. From the shape of the energy profile we can already conclude that the single mode parameters a_{02} and a_{20} are both in the same range as the biquadratic coupling coefficient b_{22}. At large rotation amplitudes the donut is U-shaped, thus c_{24} should be still close to zero, but the V-shape at large polarization amplitudes indicates that c_{42} has increased as compared to the small volume. The global energy minima are located at $E_0(\pm 0.54, \pm 0.87) = -0.313$ eV. We find two different very small barriers at zero-polarization with height $\Delta E = 0.018$ eV and at zero-tilt with height $\Delta E = 0.055$ eV. Both barriers are in the order of magnitude of $k_{\text{B}}T$ in the temperature range, where the *P4bm* phase is reported to be stable (250-540°C). Thus the energy barriers for switching of polarization and/or tilt are easy to overcome and all combinations of spontaneous polarization and in-phase tilt corresponding to the minimal energy path at the bottom of the donut should be observable. Both order parameters are, however, highly competitive, any enhancement of one order parameter is achieved at the expense of the other one. Moreover, the "donut" shape is only characteristic for this specific intermediate volume, at smaller and larger volumes the energy profile changes quite fast towards tilt-only and polarization-only ground states. Thus, ferroic properties should vary strongly with volume in the $P4_2nm$ phase.

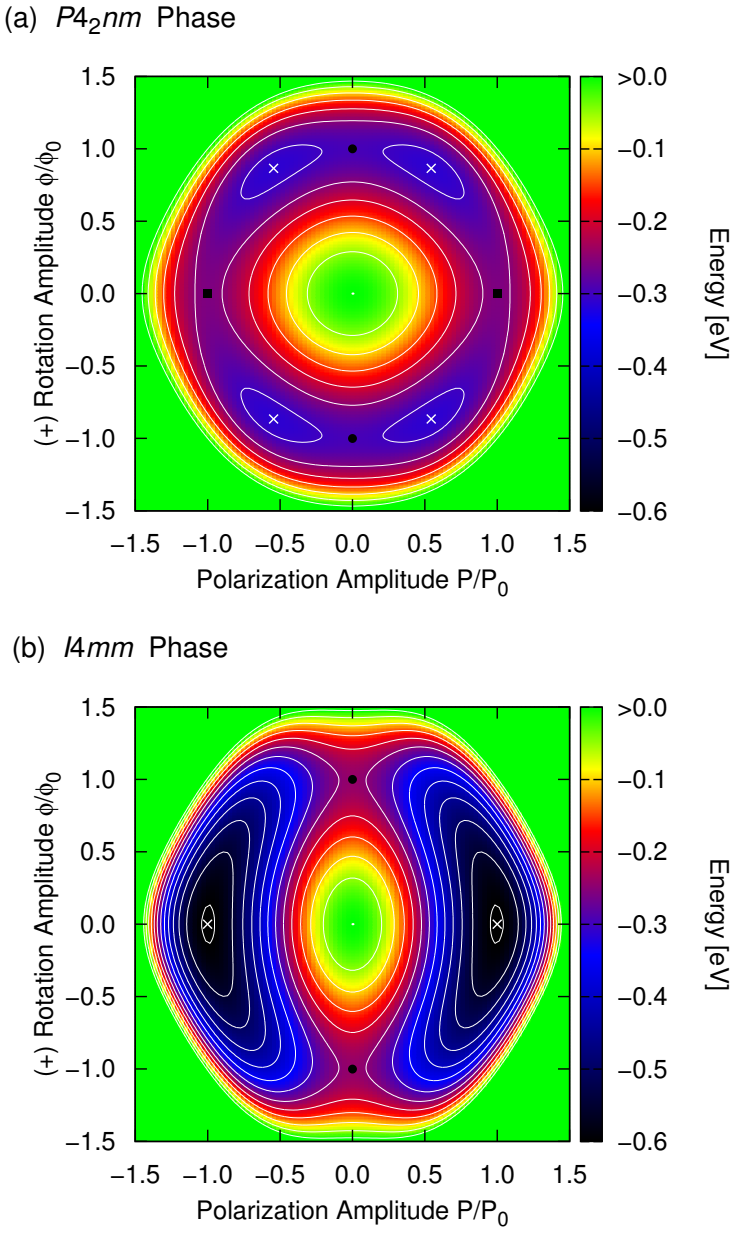

Figure 12.6: Energy E_{tot} as a function of the amplitudes of the polar and in-phase tilt modes (a) within the *P*4_2*nm* phase at volume $V = 56.07$ Å^3/f.u. and (b) within the *I*4*mm* phase at volume $V = 60.21$ Å^3/f.u. Amplitudes are normalized with respect to their respective single mode values, which are (a) $|P_0| = 0.84$ and $|\phi_0| = 1.26$ and (b) $|P_0| = 1.25$ and $|\phi_0| = 1.24$. Isolines are given for every 0.05 eV. Energy minima are marked with white cross and energy barriers with black circle (zero polarization) and black square (zero tilt).

For the large volume $V = 60.21$ Å^3/f.u. the energy profile is "V"-shaped with two global minima at the polar zero-tilt positions. Which means that the single mode parameters a_{02} and a_{20} have now roughly the ratio 1:2 with $b_{22} \approx a_{02}$. The strong "V"-shape at large polarization amplitudes indicates a large quadratic-quartic coupling term $c_{42} \approx a_{02}$. The global energy minimum can be found at $E_0(1.0, 0) = -0.605$ eV/f.u. and the polarization-switching barrier at $\theta = 1.0$ has a height of $\Delta E = 0.362$ eV/f.u. The ground state structure exhibits spontaneous polarization only, but no tilt. Any introduction of tilt reduces the amplitude of spontaneous polarization.

From the shapes of the energy profiles we could draw already qualitative conclusions concerning the ratios of certain Landau coefficients, but let us now have a quantitative look at them and their changes on increasing volume. In Fig. 12.7 (a)-(c) the Landau coefficients are given in dependence on the unit cell volume.

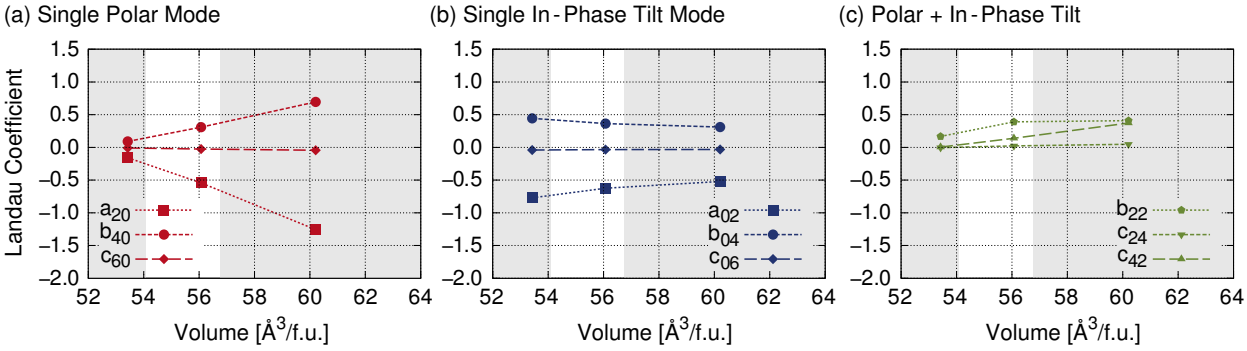

Figure 12.7: Landau coefficients as a function of volume of (a) the polar single-mode, (b) the in-phase tilt single-mode and (c) the coupling between tilt and in-phase tilt. The stability ranges of the three different phases *P*4$_2$*/mnm*, *P*4$_2$*nm* and *I*4*mm* are indicated by different background colours. Lines are guides for the eyes.

The coefficients a_{20}, b_{40} and c_{60} of the polar single-mode shown in (a) depend linearly on the volume and reflect the tendency of enhanced softening of the polar mode with increasing volume. The variation in coefficients a_{02}, b_{04} and c_{06} of the in-phase tilt single-mode with volume given in (b) overall is smaller than that of the polar mode, but the coefficients decrease nearly linearly with volume, which reflects the decreasing softness of the tilt mode with increasing volume. Both sixth order coefficients c_{60} and c_{06} adopt values close to zero. The ratio a_{20}/a_{02} changes from 0.21 (≤ 0.5) for the small volume, to 0.87 (≈ 1) for the intermediate volume and finally to 2.41 (≥ 2) for the large volume, explaining the shape evolution from "kidneys" to "donut" and finally to "kidneys" rotated by 90°. More interesting is the evolution of the coupling coefficients b_{22}, c_{24} and c_{42}. The two sixth order coupling terms c_{24} and c_{42} depend linearly on the volume. At the small volume both coefficients are close to zero, at larger volumes c_{42} is always one order of magnitude larger than c_{24}. Important for the shape of the energy profiles are again the ratios like $-b_{22}/a_{\text{min}}$ and $-c_{42}/a_{20}$ or $-c_{24}/a_{02}$. The ratio $-b_{22}/a_{\text{min}}$ changes from 1.05 for the small volume to 0.72 for the intermediate volume and 0.79 at the large volume, thus it stays always close to 1, which explains the "kidney" shapes at small and large volumes and the nearly "donut" shape at intermediate volume. The ratio $-c_{42}/a_{20}$ is 0.03 for the small volume (≈ 0) but increases to

0.26 at the intermediate volume and stays then almost constant with a value of 0.30 at the large volume. This explains the very similar "V"-shape at large polarization amplitudes for intermediate and large volume.
All three coupling coefficients adopt positive values in the whole volume range, thus the polar and tilt mode are always highly competitive distortion modes. This strong competition is the origin of the tilted-only and polar-only ground states at small and large volumes, respectively, despite the fact that both distortion modes are soft in the whole volume range.

12.2 Chemical '001'-Order: *P*4/*mmm* Parent Structure

12.2.1 *Pc*-Structures

The most complex coupling interactions can probably be observed in the *Pc* structures, where in total five different polar and tilt modes coexist. As *Pc* is a subgroup of *Pmn*2_1 and *P*4*bm*, the most important triple interactions will be discussed in the context of these supergroup phases.
The full Landau potential is expanded in the order parameters P_z of the out-of-plane polar mode Γ_3^-, P_{xy} of the in-plane polar mode Γ_5^-, ϕ_z of the in-phase tilt about the z-axis associated with M_2^+, θ_z of the anti-phase tilt mode about the same axis associated with M_4^- and θ_{xy} of the anti-phase tilt mode about the axes x and y of the pseudocubic unit cell associated with M_4^-:

$$E_{\text{tot}} = E(P_z) + E(P_{xy}) + E(\phi_z) + E(\theta_z) + E(\theta_{xy}) + \dots ,$$

with the single mode energies

$$\begin{aligned} E(P_z) &= a_{20000}P_z^2 + b_{40000}P_z^4 + c_{60000}P_z^6, \\ E(P_{xy}) &= a_{02000}P_{xy}^2 + b_{04000}P_{xy}^4 + c_{06000}P_{xy}^6, \\ E(\phi_z) &= a_{00200}\phi_z^2 + b_{00400}\phi_z^4 + c_{00600}\phi_z^6, \\ E(\theta_z) &= a_{00020}\theta_z^2 + b_{00040}\theta_z^4 + c_{00060}\theta_z^6, \\ E(\theta_{xy}) &= a_{00002}\theta_{xy}^2 + b_{00004}\theta_{xy}^4 + c_{00006}\theta_{xy}^6. \end{aligned}$$

All pairwise interactions contain only the common pairwise coupling terms of the type $b_{22}Q_1^2Q_2^2$, $c_{24}Q_1^2Q_2^4$ and $c_{42}Q_1^4Q_2^2$, they are not repeated here. We want to focus on the triple and quadruple coupling contributions to the total energy. Up to 6th order there exists no term that couples all five modes together.
The common triquadratic term of the type $c_{222}Q_1^2Q_2^2Q_3^2$ exists for all combinations of triple couplings. Only the interaction energies $E(P_z, \phi_z, \theta_z)$ and $E(P_{xy}, \phi_z, \theta_{xy})$ contain additional trilinear and bilinear-cubic terms:

$$\begin{aligned} E(P_z, \phi_z, \theta_z) &= d_{10110}P_z\phi_z\theta_z + e_{30110}P^3\phi_z\theta_z + e_{10310}P\phi_z^3\theta_z + \\ &\quad + e_{10130}P\phi_z\theta_z^3 + c_{20220}P^2\phi_z^2\theta_z^2, \\ E(P_{xy}, \phi_z, \theta_{xy}) &= d_{01101}P_{xy}\phi_z\theta_{xy} + e_{03101}P_{xy}^3\phi_z\theta_{xy} \\ &\quad + e_{01301}P_{xy}\phi_z^3\theta_{xy} + e_{01103}P_{xy}\phi_z\theta_{xy}^3 + c_{02202}P_z^2P_{xy}^2\theta_{xy}^2. \end{aligned}$$

Thus, the in-phase tilt ϕ_z can be induced or enhanced by improper coupling to a polar and an anti-phase tilt mode about the same axis. The occurrence of the same in-phase tilt mode coupled to anti-phase tilt and polarization along the same axes is very interesting, as these two sets of triple couplings are structure determining in the two supergroups *Pmc*2_1 and *P*4*bm*. $E(P_{xy}, \phi_z, \theta_{xy})$ describes in the *Pmc*2_1 the interaction between the dominating distortion modes, and $E(P_z, \phi_z, \theta_z)$

represents the coupling between the three possible distortion modes in the *P4bm* structure. However, the displacement vectors especially of the polar mode are not identical in the different phases, especially the displacement vectors of the P_{xy} mode in the *Pmc*2_1 phase is different from those in the *Pc* phase. With the displacement vectors also the coupling coefficients change.
There exist five possibilities to couple four of the five order parameters with each other. Four of them contain one trilinear-quadratic term only. These terms contain the in-phase tilt mode linearly and the polar or anti-phase tilt mode, whose counterpart is missing, appears quadratically. The coupling between the two polar and two anti-phase tilt modes is different. It contains a quadrilinear term and the four possible trilinear-cubic terms:

$$\begin{aligned}
E(P_z, P_{xy}, \phi_z, \theta_z) &= e_{12110} P_z P_{xy}^2 \phi_z \, \theta_z, \\
E(P_z, P_{xy}, \phi_z, \theta_{xy}) &= e_{21101} P_z^2 P_{xy} \phi_z \, \theta_{xy}, \\
E(P_z, \phi_z, \theta_z, \theta_{xy}) &= e_{10112} P_z \phi_z \, \theta_z \, \theta_{xy}^2, \\
E(P_{xy}, \phi_z, \theta_z, \theta_{xy}) &= e_{01121} P_{xy} \phi_z \, \theta_z^2 \theta_{xy}, \\
E(P_z, P_{xy}, \theta_z, \theta_{xy}) &= b_{11011} P_z P_{xy} \theta_z \, \theta_{xy} + c_{31011} P_z^3 P_{xy} \theta_z \, \theta_{xy} \\
&\quad + c_{13011} P_z P_{xy}^3 \theta_z \, \theta_{xy} + c_{11031} P_z P_{xy} \theta_z^3 \theta_{xy} + c_{11013} P_z P_{xy} \theta_z \, \theta_{xy}^3.
\end{aligned}$$

12.2.2 *Pmc*2_1-Structures

In the *Pmc*2_1 structures three distortion modes were identified as dominating, the polar mode Γ_5^-, the anti-phase tilt mode M_5^- and the in-phase tilt mode M_2^+. These are in the following described by the order parameters P, θ and ϕ, respectively. The full Landau potential has the form

$$E_{\text{tot}} = E(P) + E(\phi) + E(\theta) + E(P,\phi) + E(P,\theta) + E(\phi,\theta) + E(P,\phi,\theta), \tag{12.9}$$

with the single mode terms

$$E(P) = a_{200}P^2 + b_{400}P^4 + c_{600}P^6, \tag{12.10}$$
$$E(\phi) = a_{020}\phi^2 + b_{040}\phi^4 + c_{060}\phi^6, \tag{12.11}$$
$$E(\theta) = a_{002}\theta^2 + b_{004}\theta^4 + c_{006}\theta^6, \tag{12.12}$$

the pairwise coupling terms

$$E(P,\phi) = b_{220}P^2\phi^2 + c_{240}P^2\phi^4 + c_{420}P^4\phi^2, \tag{12.13}$$
$$E(P,\theta) = b_{202}P^2\theta^2 + c_{204}P^2\theta^4 + c_{402}P^4\theta^2, \tag{12.14}$$
$$E(\phi,\theta) = b_{022}\phi^2\theta^2 + c_{024}\phi^2\theta^4 + c_{042}\phi^4\theta^2, \tag{12.15}$$

and the five triply coupled terms

$$E(P,\phi,\theta) = d_{111}P\phi\,\theta + e_{311}P^3\phi\,\theta + e_{131}P\phi^3\theta + e_{113}P\phi\,\theta^3 + c_{222}P^2\phi^2\theta^2. \tag{12.16}$$

There exist four non-common odd-order triple coupling terms, the lowest of them is the trilinear term $d_{111}P\phi\,\theta$. These terms bear some special meaning, as they indicate the possibility of improper ferroelectricity. Let us recall the conditions, that have to be fulfilled for improper ferroelectricity: P should be a hard (or weakly soft) mode, while ϕ and θ must be soft and able to coexist.

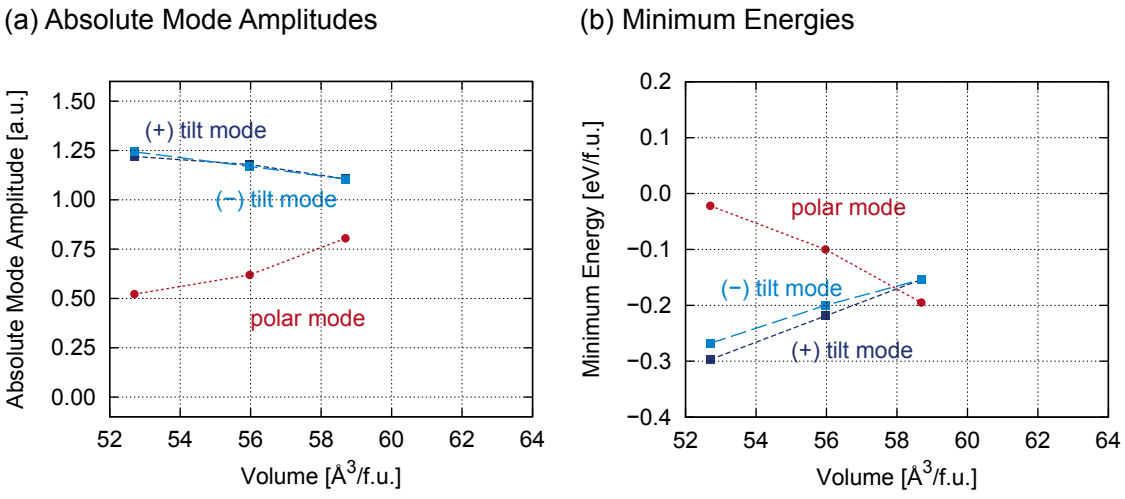

Figure 12.8: Absolute amplitudes P_0^{sm}, ϕ_0^{sm} and θ_0^{sm} of the single modes (a) and the respective energy minima (b) as a function of volume. The lines are guides for the eyes only.

Let us check first the softness of the single modes depending on the unit cell volume. Absolute mode amplitudes and minimum energies are shown in Fig. 12.8 (a) and (b), respectively. The polar mode indeed is only weakly soft at the smallest volume, but it becomes softer with increasing volume. Despite its weakness the absolute amplitude of the polar mode is quite large already at the small volume. Both tilt modes are soft in the whole volume range. The in-phase tilt mode shows similar absolute mode amplitudes, but it leads to lower energies. Thus, the in-phase tilt mode is slightly more stable than the anti-phase tilt mode. The weakest mode is the one associated with polarization, though all three distortions possess similar stabilities at the large volume.

Next we want to investigate the pairwise and triple coupling interactions at the different volumes. We will start with the small volume of $V = 52.70$ Å^3/f.u. At this volume the polar mode is a very weakly soft mode. This fact is also reflected in the 2D energy surfaces shown in Fig. 12.9. The two cuts with polarization as variable have the characteristic kidney-shape, indicating that competitive pairwise interactions between tilts and polarization lead to suppression of the polar mode. The $E(\phi, \theta)$ plane shows a goggles-shaped energy surface, typical for two modes not too different in their softness and a coupling coefficient b_{022} smaller than $-a_{002}$ of the less soft anti-phase tilt mode. The planes of pairwise coexistence of the three order parameters do not give us any hint about the asymmetries induced by the odd order terms in E_{tot}.
However, chances are good to find improper ferroelectricity, as not only the single polar mode is weakly soft but also the two tilt modes are able to coexist.
Indeed, in Fig. 12.10, where the 3D energy surfaces for different isovalues are presented, we find a global energy minimum at

$$E_{\text{min}}(0.86 \cdot P_0^{\text{sm}}, 0.84 \cdot \phi_0^{\text{sm}}, 0.80 \cdot \theta_0^{\text{sm}}) = -0.391\,\text{eV},$$

which corresponds to the four equivalent domain states:

$$\begin{aligned}(+P_0, +\phi_0, +\theta_0),\\ (-P_0, -\phi_0, +\theta_0),\\ (-P_0, +\phi_0, -\theta_0),\\ (+P_0, -\phi_0, -\theta_0).\end{aligned}$$

The absolute values of the three order parameters are

$$\begin{aligned}|P_0| &= 0.45,\\ |\phi_0| &= 1.02,\\ |\theta_0| &= 0.99.\end{aligned}$$

The global minima can be seen in (a). Two different barriers for switching between these domain states can be discerned. The smaller barrier is found for simultaneous switching of polarization and anti-phase tilt at $E = -0.297$ eV ($\Delta E = 0.094$ eV) in (b) and a slightly higher barrier for simultaneous switching of polarization together with the direction of the in-phase tilt at $E = -0.267$ eV ($\Delta E = 0.124$ meV) presented in (c).

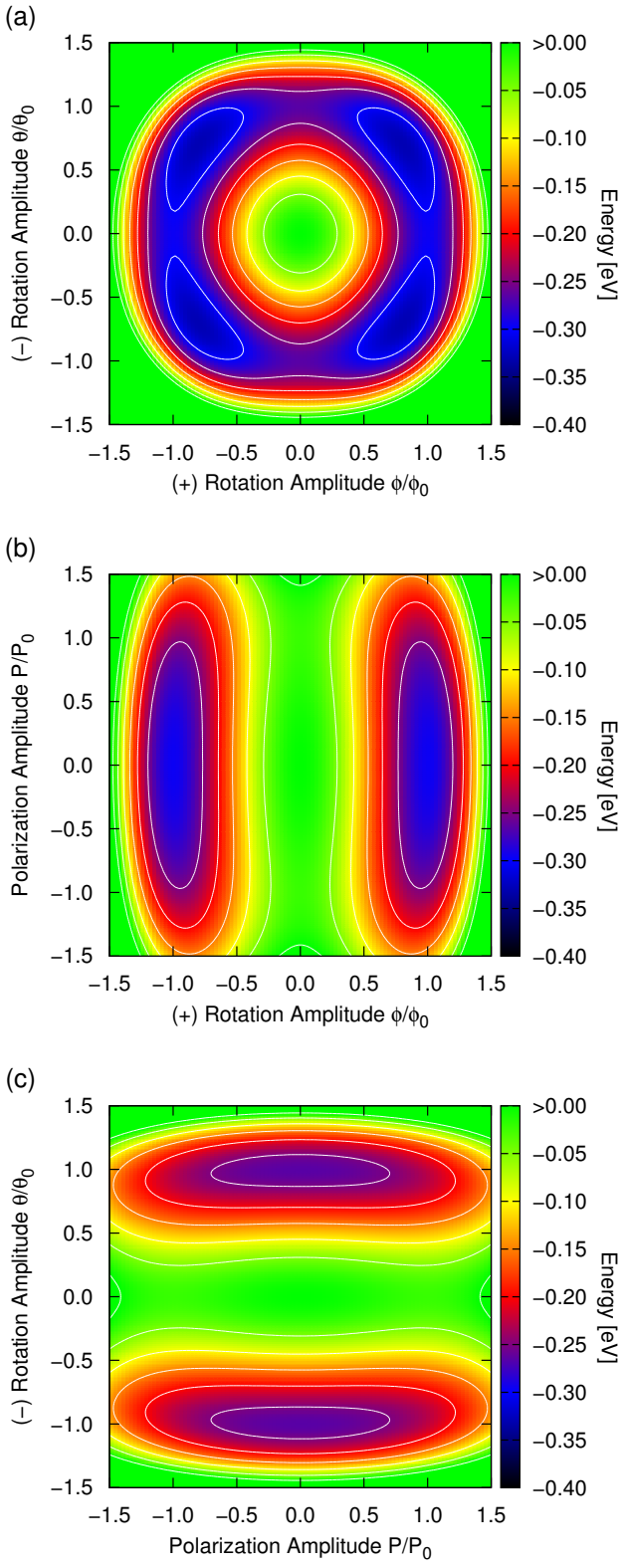

Figure 12.9: 2D energy profiles $E(\theta, \phi)$, $E(\phi, P)$ and $E(P, \theta)$ for the *Pmc*2_1 structure at $V = 52.70$ Å^3/f.u. Amplitudes are normalized with respect to their respective single mode values, which are $|P_0^{\mathrm{sm}}| = 0.52$ and $|\phi_0^{\mathrm{sm}}| = 1.22$ and $|\theta_0^{\mathrm{sm}}| = 1.24$. Isolines are given for every 0.05 eV.

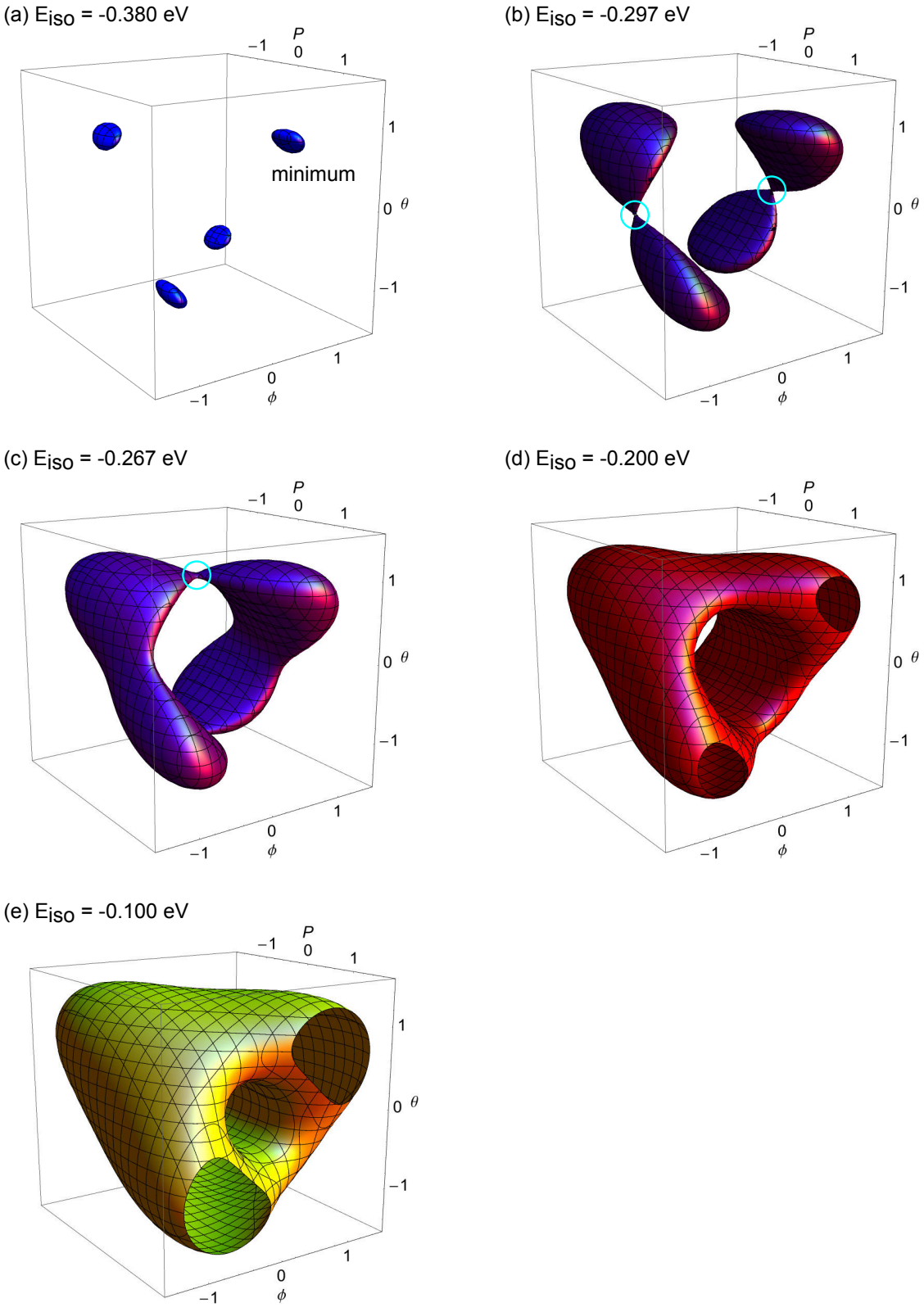

Figure 12.10: 3D energy surfaces $E(P, \phi, \theta)$ for different isovalues in the *Pmc*2_1 structure at $V = 52.70$ Å^3/f.u. Amplitudes are normalized with respect to their respective single mode values, which are $|P_0^{\mathrm{sm}}| = 0.52$ and $|\phi_0^{\mathrm{sm}}| = 1.22$ and $|\theta_0^{\mathrm{sm}}| = 1.24$. The colours of the isosurfaces are adapted to the colour scheme in Fig. 12.9.

As the isosurfaces of higher energies in (d) and (e) show, a minimum energy path to switch simultaneously in-phase and anti-phase tilts at constant polarization does not exist. Polarisation has always to change together with a tilt mode. The anti-phase tilt is the easiest to change. This is a typical behaviour for an improper ferroelectric, although we do not observe an enhancement of the amplitude of the polarization mode with respect to the single mode value. But we have to recall that polarization cannot pairwise coexist with any of the tilt modes. Only coexistence of all three modes leads to a gain in energy that favours their simultaneous presence, indicating that the triple improper coupling terms must be stronger than the pairwise competitive terms. Thus triple coupling interactions are dominating in the *Pmc*2_1 structure at $V = 52.70$ Å^3/f.u.

Let us now focus on the intermediate volume, which is the equilibrium volume of this phase ($V_0 = 55.97$ Å^3/f.u.), and where the polar mode becomes considerably soft. The energy diagrams resulting from pairwise coexistence of the order parameters are shown in Fig. 12.11. Compared to the smaller volume we find significant changes. The two tilt modes still exhibit a goggles-shaped energy surface, indicating weakly competitive behaviour. But now also the polarization-tilt interactions result in goggles-shaped energy surfaces, showing that the increased softness of the polar mode is stronger now than the competition between tilts and polarization.

In Fig. 12.12 the 3D energy surfaces resulting from the full Landau potential $E(P, \phi, \theta)$ for five different isovalues are given. There are four equivalent minima at

$$E_{\text{min}}(0.77 \cdot P_0^{\text{sm}}, 0.81 \cdot \phi_0^{\text{sm}}, 0.80 \cdot \theta_0^{\text{sm}}) = -0.311\,\text{eV}$$

The global minima are shown in (a). The absolute values of the three order parameters are

$$\begin{aligned} |P_0| &= 0.48, \\ |\phi_0| &= 0.95, \\ |\theta_0| &= 0.94. \end{aligned}$$

As for the smaller volume two sets of energy barriers can be found, they are marked in (b) and (c). Due to the goggles-shaped energy surfaces in the $E(P, \phi, 0)$ and $E(P, 0, \theta)$ planes, there are double as many equivalent paths as before. The smaller barrier is found at $E = -0.227$ eV ($\Delta E = 0.084$ meV) for simultaneous switching of polarization and anti-phase tilt shown in (b). The larger barrier is developed for the simultaneous switching of polarization and in-phase tilt at $E = -0.210$ eV ($\Delta E = 0.101$ eV) marked in (c). The more closed shapes of the isosurfaces in (d) and (e) are a result of the overall flatter energy landscape as compared to the smaller volume.

In comparison with the smaller volume the major change at this intermediate volume are the possible pairwise coexistences of all three distortion modes. The pairwise couplings are still weakly competitive, indicating that dominating triple improper interactions are responsible for the characteristic shape of the 3D energy surface with its four global minima.

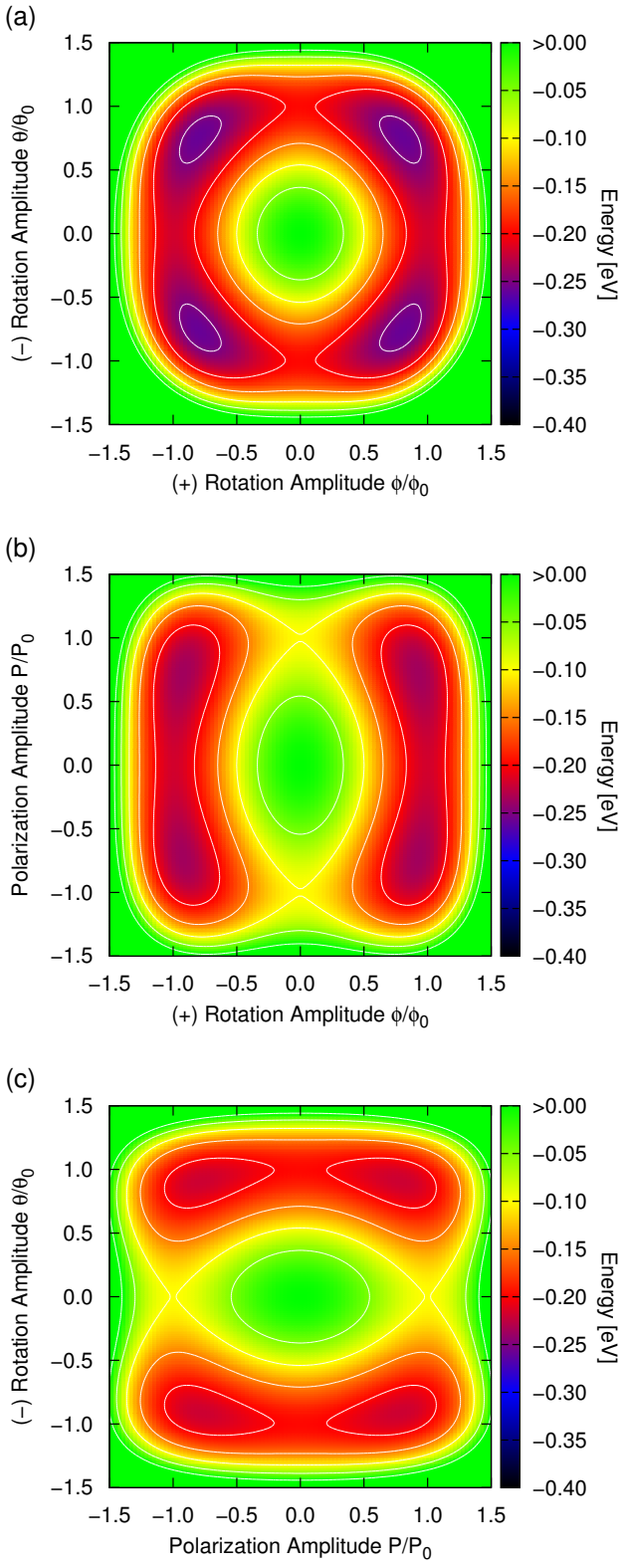

Figure 12.11: 2D energy profiles $E(\theta, \phi)$, $E(\phi, P)$ and $E(P, \theta)$ for the *Pmc*2_1 structure at $V_0 = 55.97$ Å^3/f.u. Amplitudes are normalized with respect to their respective single mode values, which are $|P_0^{\mathrm{sm}}| = 0.62$ and $|\phi_0^{\mathrm{sm}}| = 1.18$ and $|\theta_0^{\mathrm{sm}}| = 1.17$. Isolines are given for every 0.05 eV.

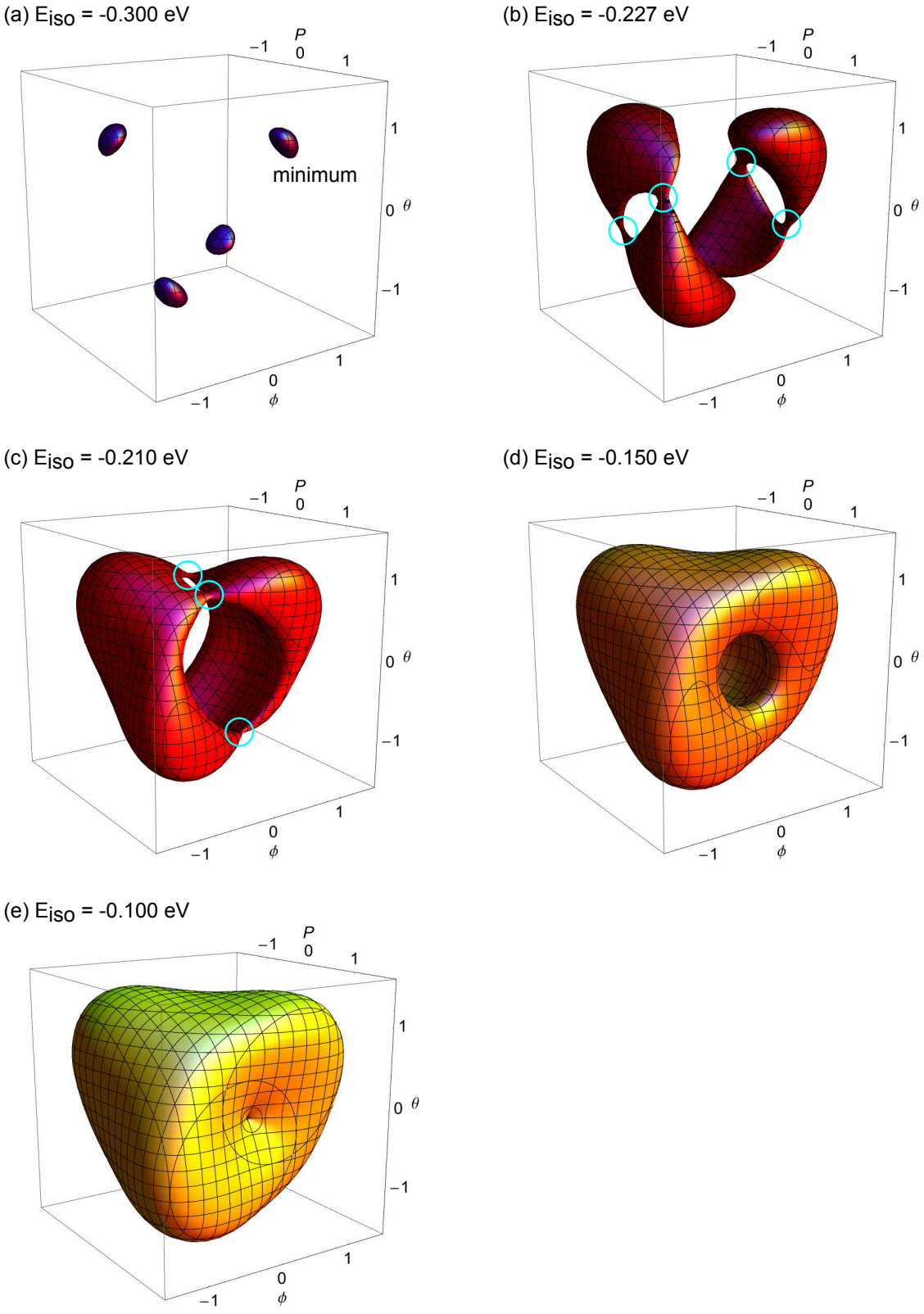

Figure 12.12: 3D energy surfaces $E(P, \phi, \theta)$ for different isovalues in the *Pmc*2_1 structure at $V_0 = 55.97$ Å^3/f.u. Amplitudes are normalized with respect to their respective single mode values, which are $|P_0^{\mathrm{sm}}| = 0.62$ and $|\phi_0^{\mathrm{sm}}| = 1.18$ and $|\theta_0^{\mathrm{sm}}| = 1.17$. The colours of the isosurfaces are adapted to the colour scheme in Fig. 12.11.

The situation changes significantly at the larger volume of $V = 58.69$ Å^3/f.u. In Fig. 12.13 the 2D energy surfaces are presented for the pairwise order parameter interactions. We can see that the energy profile of in-phase and anti-phase tilt modes changed to perfect square-shaped with a slight tendency to donut-shape arising from competitive interactions at equal single mode minimum energies. The energy profiles for the coexistence of polarization and any of the tilt modes have goggles-shape. Still the positions of the minima are shifted to values slightly smaller than the single mode amplitudes. This indicates that the competition between polarization and the tilt modes is becoming weaker with increasing volume.

The shapes of the 3D energy surfaces are presented in Fig. 12.14. We still find a set of four equivalent energy minima in (a) positioned at

$$E_{\text{min}}(0.89 \cdot P_0^{\text{sm}}, 0.72 \cdot \phi_0^{\text{sm}}, 0.77 \cdot \theta_0^{\text{sm}}) = -0.294\,\text{eV}$$

The absolute mode amplitudes become

$$\begin{aligned} |P_0| &= 0.72, \\ |\phi_0| &= 0.80, \\ |\theta_0| &= 0.85. \end{aligned}$$

The remaining isosurfaces indicate major changes in the mode interactions. At $E = -0.260$ eV shown in (b) a second set of four local minima can be found just 0.034 eV above the global minima. In (c) and (d) the different marked energy barriers correspond to the energy of polarization direction reversal in this structure. The lowest barriers visible at $E = -0.256$ eV are exhibited for simultaneously changing the two tilts at constant polarization. The barriers marked in orange and turquoise are not degenerate, the latter ones are higher by 2 meV. The isosurface has the shape of two deformed rings, one for $+P$ and the other one for $-P$. The second type of barriers we can see at $E = -0.201$ eV in-between the two rings. As a consequence, if we want to change polarization along a minimum energy path as shown here, there has always the second minimum to be passed by changing first both tilts and afterwards the direction of polarization. This is fundamentally different from the two volumes discussed before. Moreover, the isosurface of $E = -0.100$ eV approaches cube-shape, a perfect cube is expected for a normal ferroelectric, where tilts and polarization are equally strong and do not interact with each other. This material is not improper ferroelectric any more, with its $4 + 4$ minima it resembles more a proper ferroelectric.

Thus, in the *Pmc*2_1-structures we can observe a transition from improper to proper ferroelectric behaviour induced by volume change. The chemically ordered regions in NBT as well as the high-pressure phase should in fact be improper ferroelectric, not antiferroelectric.

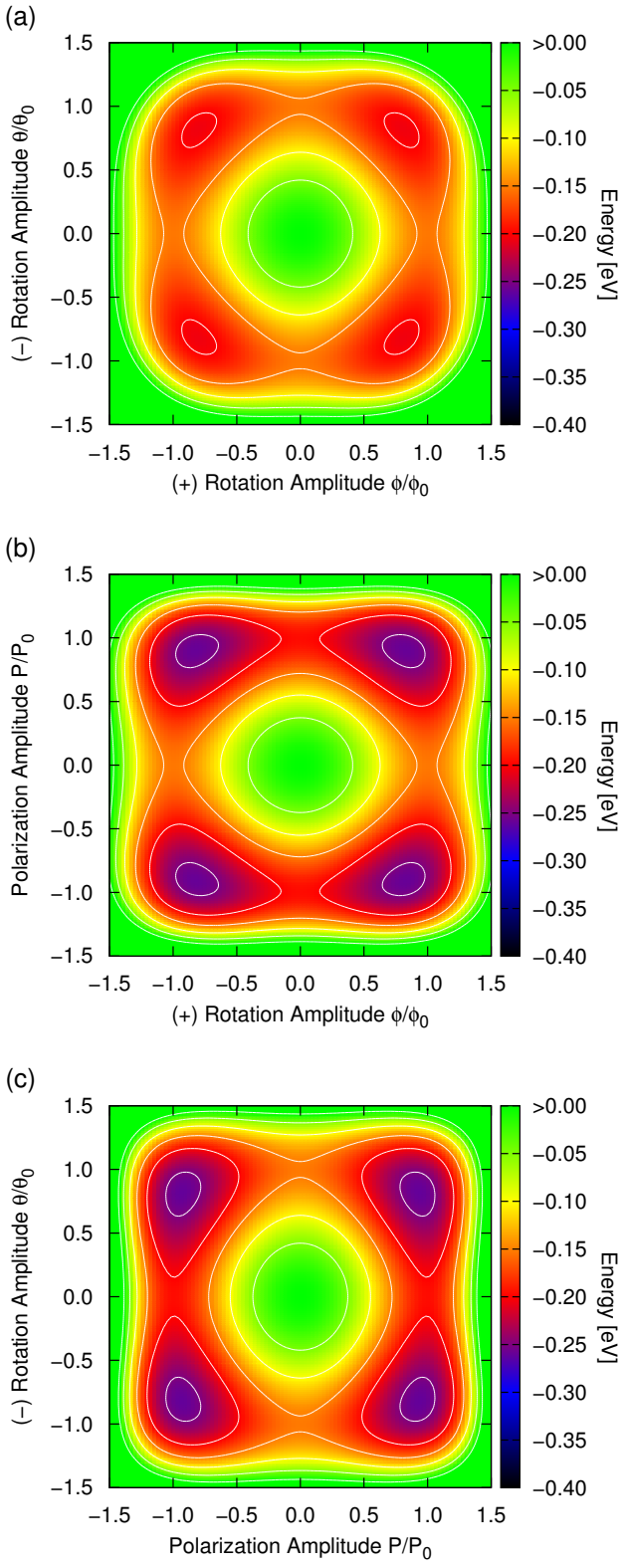

Figure 12.13: 2D energy profiles $E(\theta, \phi)$, $E(\phi, P)$ and $E(P, \theta)$ for the *Pmc*2_1 structure at $V = 58.69$ Å^3/f.u. Amplitudes are normalized with respect to their respective single mode values, which are $|P_0^{\mathrm{sm}}| = 0.81$ and $|\phi_0^{\mathrm{sm}}| = 1.11$ and $|\theta_0^{\mathrm{sm}}| = 1.11$. Isolines are given for every 0.05 eV.

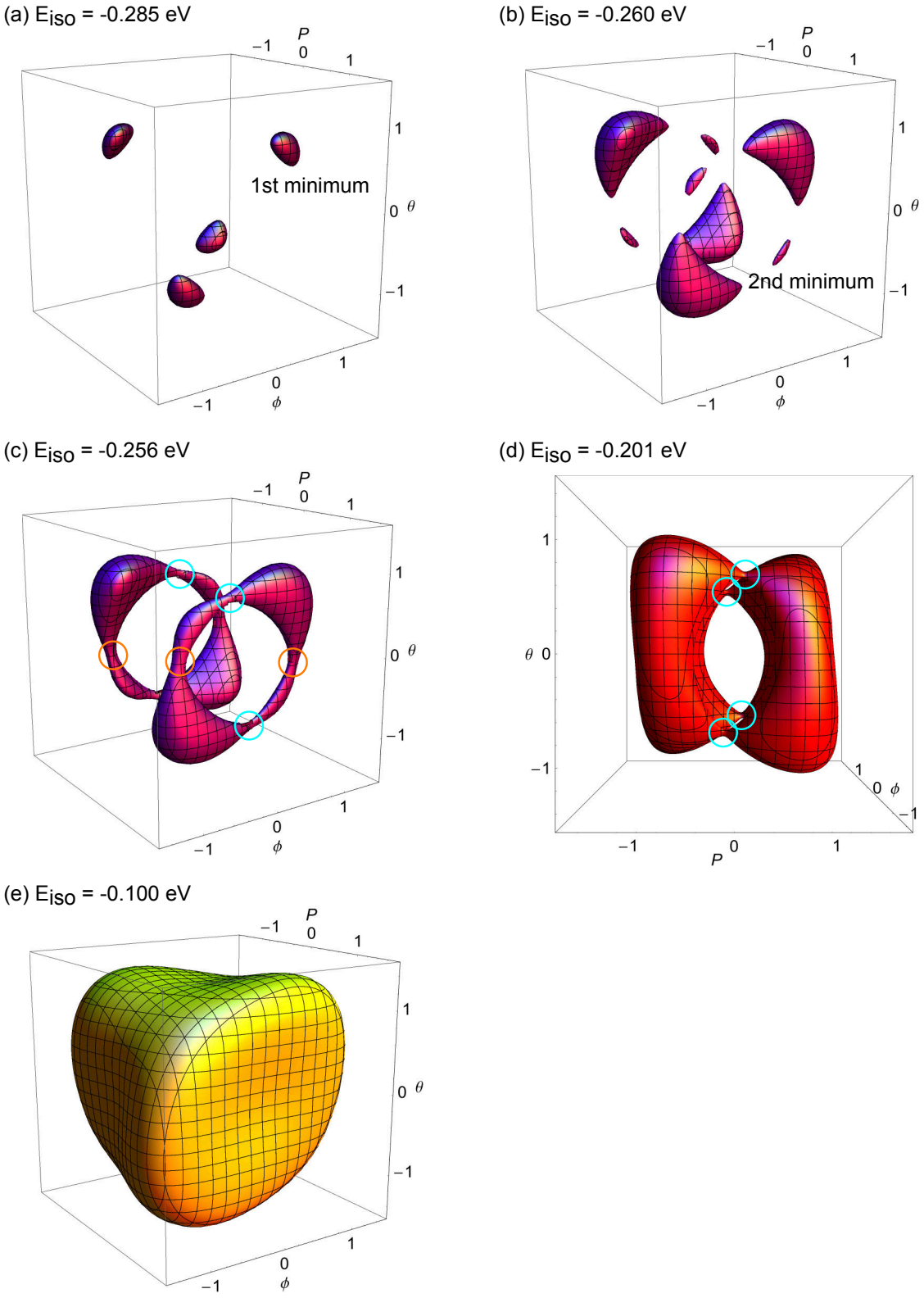

Figure 12.14: 3D energy surfaces $E(P, \phi, \theta)$ for different isovalues in the *Pmc*2_1 structure at $V = 58.69$ Å^3/f.u. Amplitudes are normalized with respect to their respective single mode values, which are $|P_0^{\mathrm{sm}}| = 0.81$ and $|\phi_0^{\mathrm{sm}}| = 1.11$ and $|\theta_0^{\mathrm{sm}}| = 1.11$. The colours of the isosurfaces are adapted to the colour scheme in Fig. 12.13.

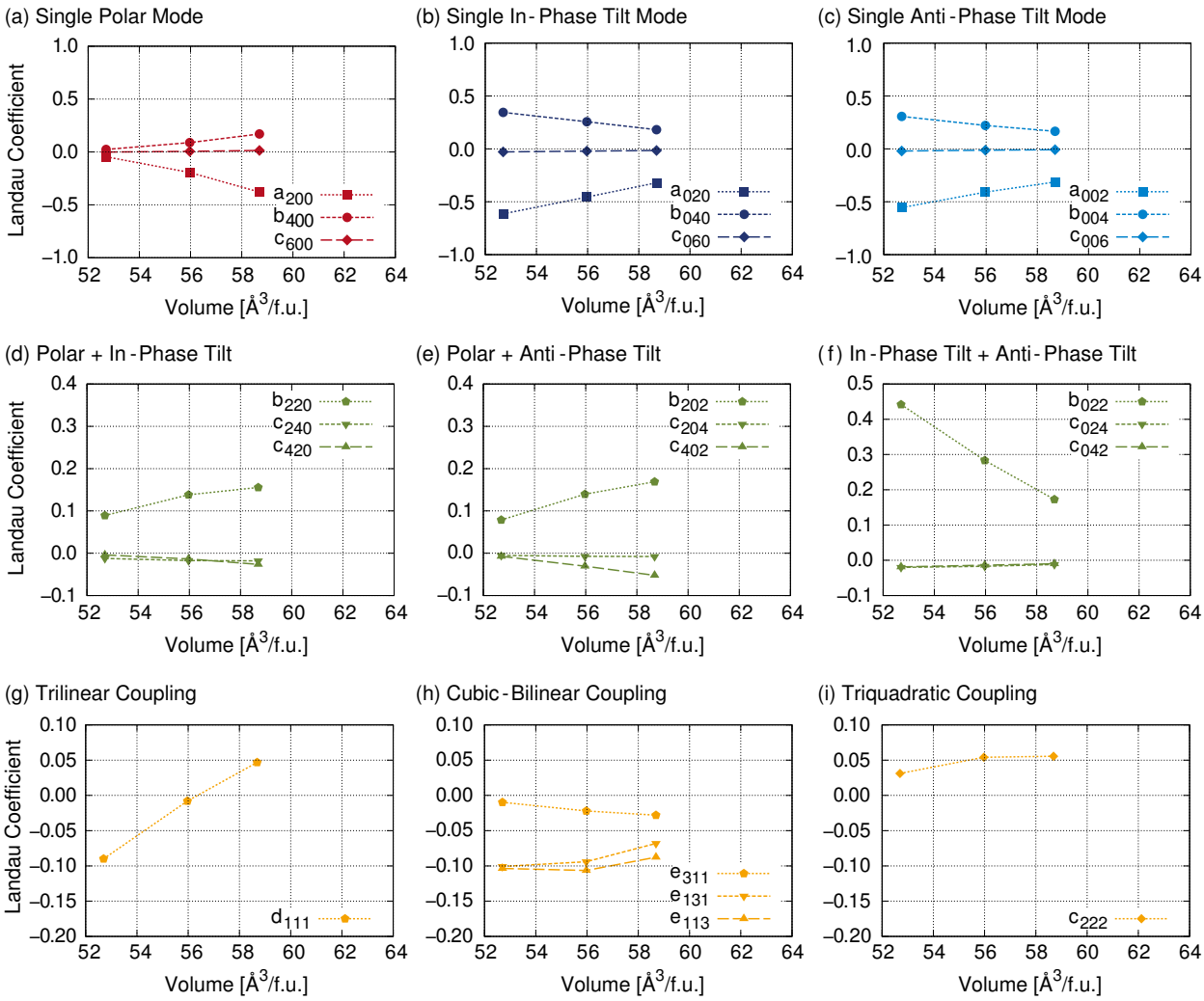

Figure 12.15: Landau coefficients obtained for the *Pmc*2_1-structures at different volumes. In the top row Landau coefficients of the single modes are given, followed by pairwise coupling coefficients in the middle row. In the bottom row coefficients of triple coupling terms can be found.

Let us finally discuss the Landau coefficients, presented in Fig. 12.15. In the top row coefficients of the single modes are given, in the middle row coupling coefficients of the pairwise and in the bottom row those of the triple interactions. Again the general trends of increased softness with increasing volume of polar modes in (a) and decreased softness of tilt modes in (b) and (c) are confirmed. The in-phase tilt mode in (b) is a little bit more stable than the anti-phase tilt mode in (c). All three pairwise coupling coefficients shown in (d)-(f) are positive. Those of polar-tilt interactions increase with increasing volume in (d) and (e), those of tilt-tilt interaction in (f) decrease. Negative sixth order coefficients diminish the competition slightly. At the smallest volume the coupling coefficients b_{220} and b_{202} are larger than $-a_{200}$ leading to the suppression of the tilt mode in presence of any of the tilt modes. Moreover, with increasing volume all ratios of the type $a_2 : b_{22}$ are increasing indicating that the pairwise competitions between all modes become weaker at larger volumes. The trilinear coupling coefficient given in (g) is negative at the small volume, almost zero at the intermediate volume and positive at the large volume. The

bilinear-quadratic coupling coefficients in (h) are always negative, while the triquadratic coupling term in (i) is always positive and almost independent of the volume. This means, that the trilinear term favors at the small volume the domain state $(+P_0, +\phi_0, +\theta_0)$ and its equivalents, while at large volumes it favors the domain state $(-P_0, -\phi_0, -\theta_0)$ and its equivalents, the fifth order terms all favour these domain states, while the sixth order term punishes equally any coexistence of the three order parameter. This is exactly, what we observed. At the small and intermediate volumes four energy minima corresponding to the domain states:

$$(+P_0, +\phi_0, +\theta_0),$$
$$(-P_0, -\phi_0, +\theta_0),$$
$$(-P_0, +\phi_0, -\theta_0),$$
$$(+P_0, -\phi_0, -\theta_0),$$

were found, while at the large volume a second set of minima arises, which corresponds to the domain states:

$$(-P_0, -\phi_0, -\theta_0),$$
$$(+P_0, +\phi_0, -\theta_0),$$
$$(+P_0, -\phi_0, +\theta_0),$$
$$(-P_0, +\phi_0, +\theta_0).$$

Moreover, the trilinear coupling originating from the fifth order terms is reduced at the large volume. All these changes together lead to an energy landscape of the large volume, which differs completely from those resulting at smaller volumes.

At the equilibrium volume of the *Pmc*2_1-phase we find an improper-proper hybrid state. This is a literal hybrid state with properties intermediate between improper and proper ferroelectric, not to be confused with the hybrid improper ferroelectric term introduced by Benedek and Fennie.[206]

12.2.3 *P*4*bm*-Structures

For the *P*4*bm* structure we found three different phases to be stable depending on the volume. At volumes $V < 57.5$ Å^3/f.u. an in-phase tilted *P*4*/mbm* phase is stable and at volumes $V > 62.3$ Å^3/f.u. a polar *P*4*mm* phase is favored. Only at intermediate volumes 57.5 Å^3/f.u.$< V < 62.3$ Å^3/f.u. polar and in-phase tilt distortions can coexist in the *P*4*bm* phase, which also exhibits anti-phase tilts. Accordingly, we chose three different volumes to be investigated, each in the stability range of another phase.
The Landau potential of the *P*4*bm*-structure depending on the polar mode Γ_3^-, the in-phase tilt mode M_2^+ and anti-phase tilt mode M_4^-, which are in the following described by the order parameters P, ϕ and θ, respectively, has essentially the same form as the Landau potential of the *Pmc*2_1-structure,

$$E_{\text{tot}} = E(P) + E(\phi) + E(\theta) + E(P,\phi) + E(P,\theta) + E(\phi,\theta) + E(P,\phi,\theta), \tag{12.17}$$

with the single mode terms

$$\begin{aligned} E(P) &= a_{200}P^2 + b_{400}P^4 + c_{600}P^6, & (12.18)\\ E(\phi) &= a_{020}\phi^2 + b_{040}\phi^4 + c_{060}\phi^6, & (12.19)\\ E(\theta) &= a_{002}\theta^2 + b_{004}\theta^4 + c_{006}\theta^6, & (12.20) \end{aligned}$$

the pairwise coupling terms

$$\begin{aligned} E(P,\phi) &= b_{220}P^2\phi^2 + c_{240}P^2\phi^4 + c_{420}P^4\phi^2, & (12.21)\\ E(P,\theta) &= b_{202}P^2\theta^2 + c_{204}P^2\theta^4 + c_{402}P^4\theta^2, & (12.22)\\ E(\phi,\theta) &= b_{022}\phi^2\theta^2 + c_{024}\phi^2\theta^4 + c_{042}\phi^4\theta^2, & (12.23) \end{aligned}$$

and the triply coupled terms

$$E(P,\phi,\theta) = d_{111}P\phi\,\theta + e_{311}P^3\phi\,\theta + e_{131}P\phi^3\theta + e_{113}P\phi\,\theta^3 + c_{222}P^2\phi^2\theta^2. \tag{12.24}$$

The odd-order triple coupling terms $d_{111}P\phi\,\theta$, $e_{311}P^3\phi\,\theta$ and $e_{131}P\phi^3\theta$, $e_{113}P\phi\,\theta^3$ offer again the possibility of improper ferroelectricity.
Let us investigate first the single modes in the three different phases. The absolute distortion amplitudes and the minimum energies of the single modes are given in Fig. 12.16. The polar mode is only weakly soft at the small (*P*4*/mbm* phase) and intermediate volume (*P*4*bm phase*), but leads to large energy gain at the large volume (*P*4*mm phase*). Whereas the two tilt modes lead to similar energies, with the anti-phase tilt being slightly favored over the in-phase tilt. The tilts are favored at the small volume and show a decrease of their amplitudes and minimum energies at the intermediate volume, but they hardly change from the intermediate to large volume, as the volume increase mainly results from elongation of the c-axis. At the intermediate volume all three modes have similar minimum energies, at the large volume polarization is strongly favored.

Next, we want to investigate the pairwise and triple interactions of the three distortion modes at the different volumes in more detail.

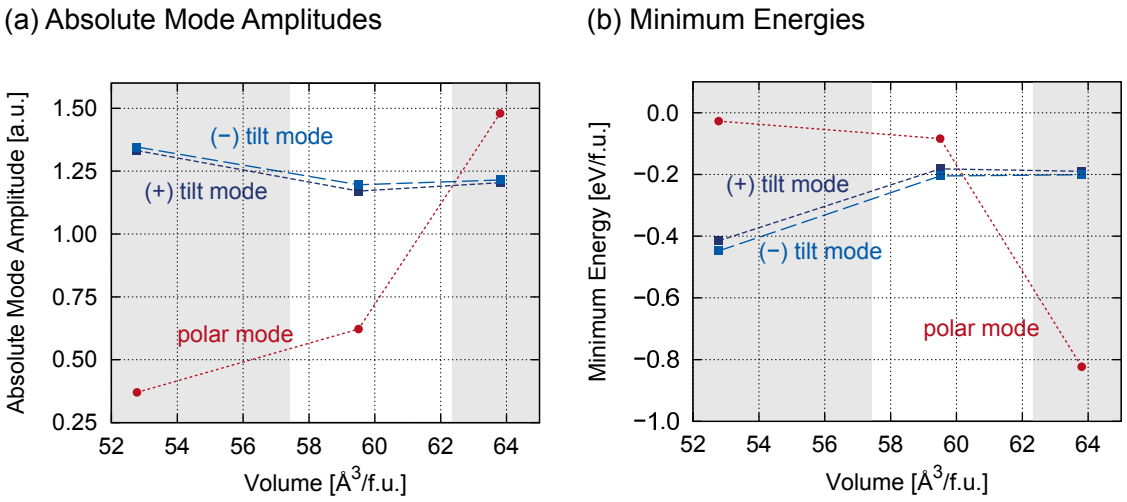

Figure 12.16: Absolute mode amplitudes and minimum energies of the polar, in-phase and anti-phase tilt modes present in the *P4bm*-structure as they change with unit cell volume. The background colours indicate the ranges of phase stabilities of phases *P4/mbm*, *P4bm* and *P4mm* obtained from the symmetry mode analysis in the previous chapter.

In Fig. 12.17 the three different energy surfaces $E(\theta, \phi)$ in (a), $E(P, \phi)$ in (b) and $E(\theta, P)$ in (c) are given for the small volume of $V = 52.78$ Å^3/f.u., where we found a *P4/mbm* phase to be favored. In this structure the polar and any of the tilt modes exclude each other, as can be seen in (b) and (c), in both cases we find the kidney-shaped energy surface, which implies that the less soft polar mode is completely suppressed by the competitive coupling to the softer tilt mode. But (a) indicates that also the competition between the two tilt modes is so strong, that they cannot coexist, although they are both extremely soft. The diamond-shaped energy surface results. Thus, we know already that $b_{022} > -a_{020}, -a_{002}$. In Fig. 12.18 the 3D energy surfaces resulting from the full Landau potential $E(P, \phi, \theta)$ for five different isovalues are given. The first (absolute) energy minima can be found at

$$E_{\text{min}}(0, 0, \theta_0^{\text{sm}}) = -0.447\,\text{eV},$$

corresponding to the two equivalent domain states,

$$(0, 0, +\theta_0),$$
$$(0, 0, -\theta_0),$$

as shown in (a). The absolute mode amplitudes become:

$$|P_0| = 0.00,\ |\phi_0| = 0.00,\ |\theta_0| = 1.35.$$

In (b) a second set of energy minima is shown, they are local minima at

$$E_{\text{min}}(0, \pm\phi_0^{\text{sm}}, 0) = -0.400\,\text{eV},$$

corresponding to the two equivalent domain states

$$(0, +\phi_0, 0),$$
$$(0, -\phi_0, 0).$$

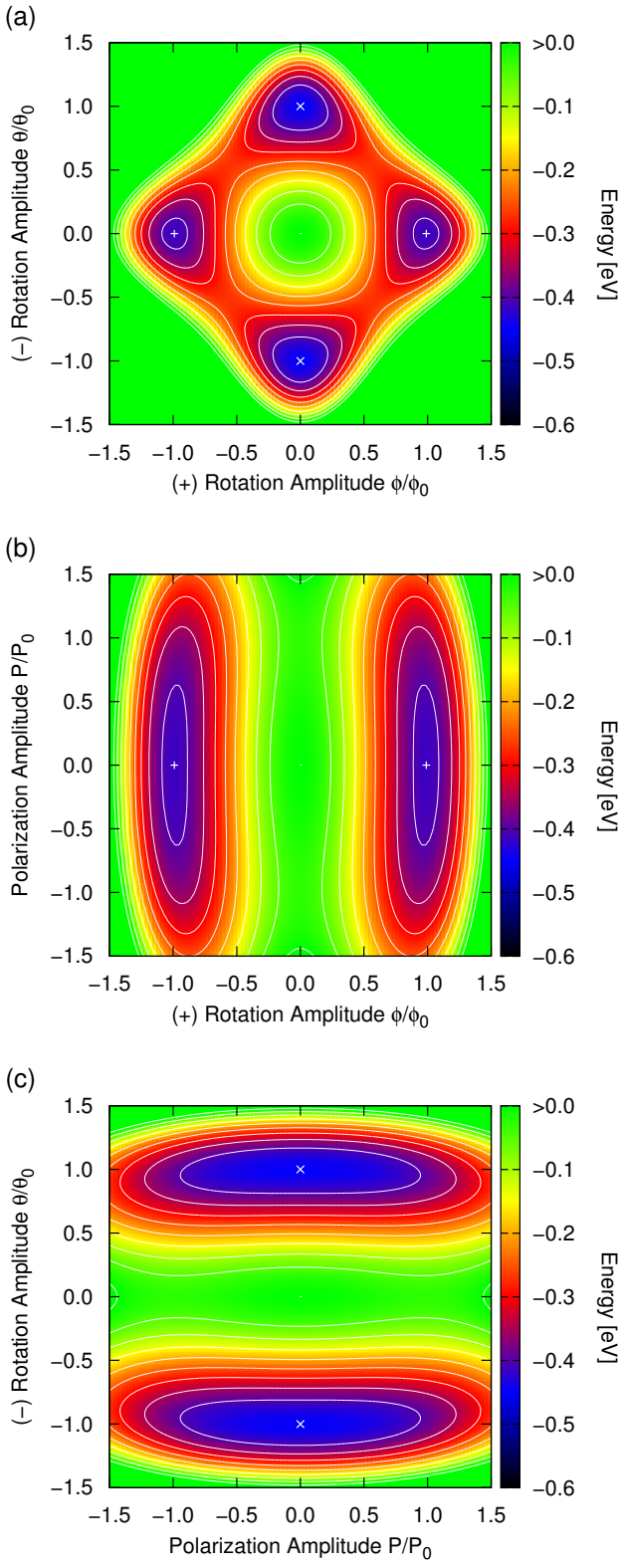

Figure 12.17: 2D energy profiles $E(\theta, \phi)$, $E(P, \phi)$ and $E(\theta, P)$ for the *P*4*bm* structure at $V = 52.78$ Å^3/f.u. Amplitudes are normalized with respect to their respective single mode values, which are $|P_0^{\mathrm{sm}}| = 0.37$ and $|\phi_0^{\mathrm{sm}}| = 1.33$ and $|\theta_0^{\mathrm{sm}}| = 1.35$. Isolines are given for every 0.05 eV.

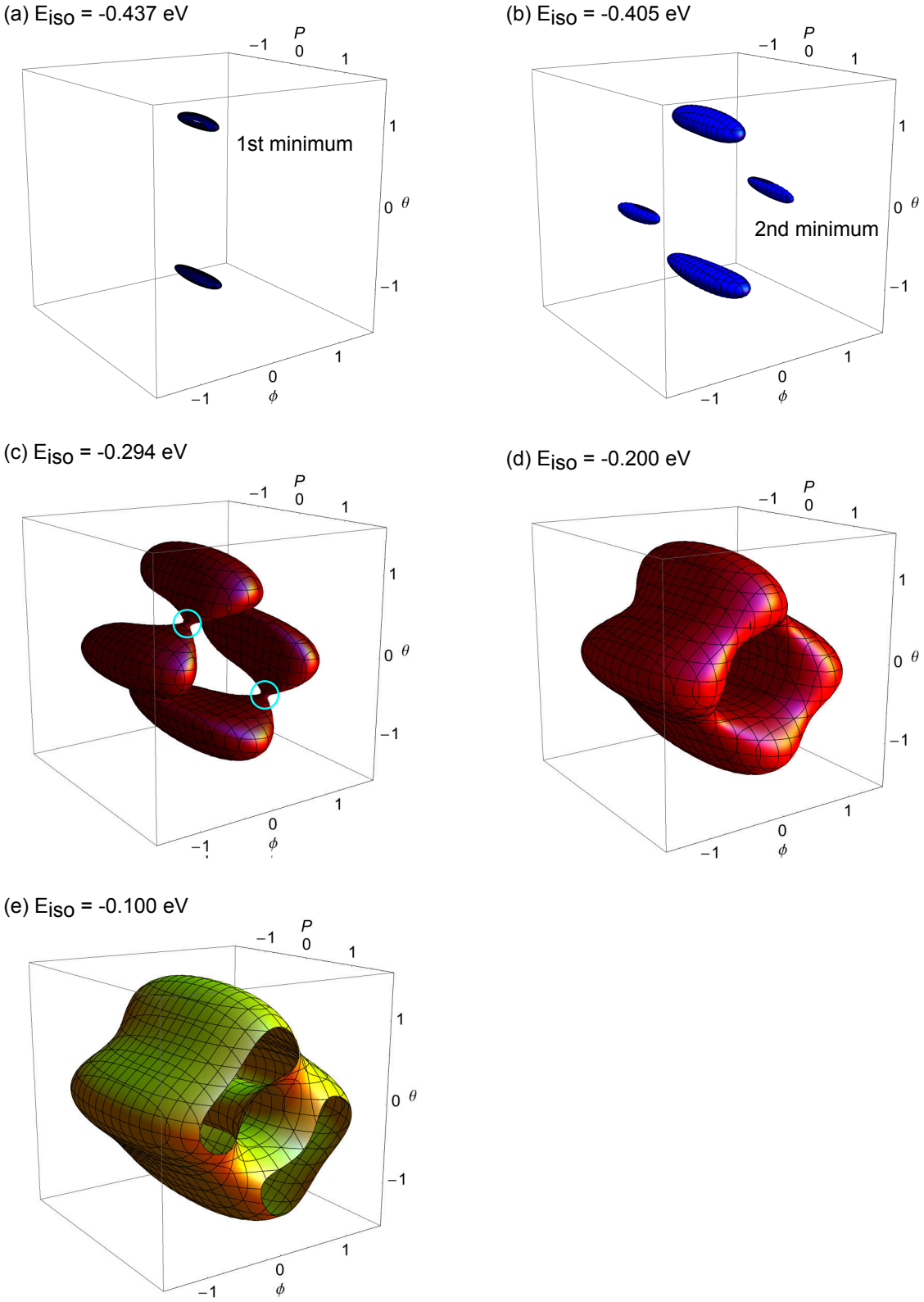

Figure 12.18: 3D energy surfaces $E(P, \phi, \theta)$ for different isovalues in the *P4bm* structure at $V = 52.78$ Å^3/f.u. Amplitudes are normalized with respect to their respective single mode values, which are $|P_0^{\mathrm{sm}}| = 0.37$ and $|\phi_0^{\mathrm{sm}}| = 1.33$ and $|\theta_0^{\mathrm{sm}}| = 1.35$. The colours of the isosurfaces are adapted to the colour scheme in Fig. 12.17.

The overall isosurface has the shape of four worms, two of them bigger than the other two. Although the absolute minimum is located at the single mode amplitudes of the anti-phase tilt mode, there exist additional local minima at the single mode amplitudes of the in-phase tilt as well. As for the $P4_2nm$-structure the energy landscape is very flat towards non-zero values of polarization, so that polarization might be not spontaneous but (reversibly) inducable by application of an electric field. In (c) the energy barriers between the absolute and local minima are shown, they are positioned at $E(0, \pm\phi_0^{\text{sm}}, \pm\theta_0^{\text{sm}}) = -0.294$ eV. An energy of 0.154 eV has to be overcome to change from in-phase to anti-phase tilt. Overall, the Landau potential is dominated by the strong competition of all three distortion modes. Therefore no improper behaviour can be found at this volume. Only tilted structures can be expected, which might be prone to induced polarization.

Let us turn to the intermediate volume of $V = 52.78$ Å^3/f.u., where the $P4bm$ phase was found. The pairwise energy surfaces are presented in Fig. 12.19 (a)-(c). There are substantial changes as compared to the small volume. Now the polar mode is able to coexist with both tilt modes. Instead of the kidney-shapes resulting at the small volume, we find goggles-shaped energy surfaces with energy minima at non-zero amplitudes of both distortion modes. There is still some competition, so that the minima are shifted to amplitudes lower than the single mode values, but tilt and polarization can coexist. In contrast to the two tilt modes, which are still too competitive to coexist on their own.
This situation is changed completely if we come to the 3D energy surface resulting from the full Landau potential $E(P, \phi, \theta)$ shown in Fig. 12.20 for various isovalues. All energy surfaces have a rather complex shape. The first (absolute) minima are shown in (a), they are positioned at

$$E_{\text{min}}(-0.75 \cdot P_0^{\text{sm}}, -0.15 \cdot \phi_0^{\text{sm}}, -0.91 \cdot \theta_0^{\text{sm}}) = -0.232\,\text{eV},$$

which correspond to the four different domain states

$$\begin{aligned}
&(-P_0, -\phi_0, -\theta_0),\\
&(+P_0, +\phi_0, -\theta_0),\\
&(+P_0, -\phi_0, +\theta_0),\\
&(-P_0, +\phi_0, +\theta_0).
\end{aligned}$$

The absolute mode amplitudes become:

$$|P_0| = -0.47,\ |\phi_0| = -0.18,\ |\theta_0| = -1.09.$$

At $E = -0.215$ a second set of local minima arises, given in (b), where the amplitudes for ϕ and θ are roughly inverted. Both minima differ by 17 meV only, and they are separated by a small energy barrier at $E = -0.207$ eV ($\Delta E = 0.025$ eV), presented in (c). The barrier for switching of the polarization together with the anti-phase tilt from $E_{\text{min}}(-P_0, -\phi_0, -\theta_0)$ to $E_{\text{min}}(+P_0, +\phi_0, -\theta_0)$ is given in (d), it is at $E = -0.204$ ($\Delta E = 0.028$ eV). Two more types of energy barriers can be found at $E = -0.182$ eV ($\Delta E = 0.050$ eV) and $E = -0.128$ eV ($\Delta E = 0.104$ eV), presented in (e) and (f), respectively.

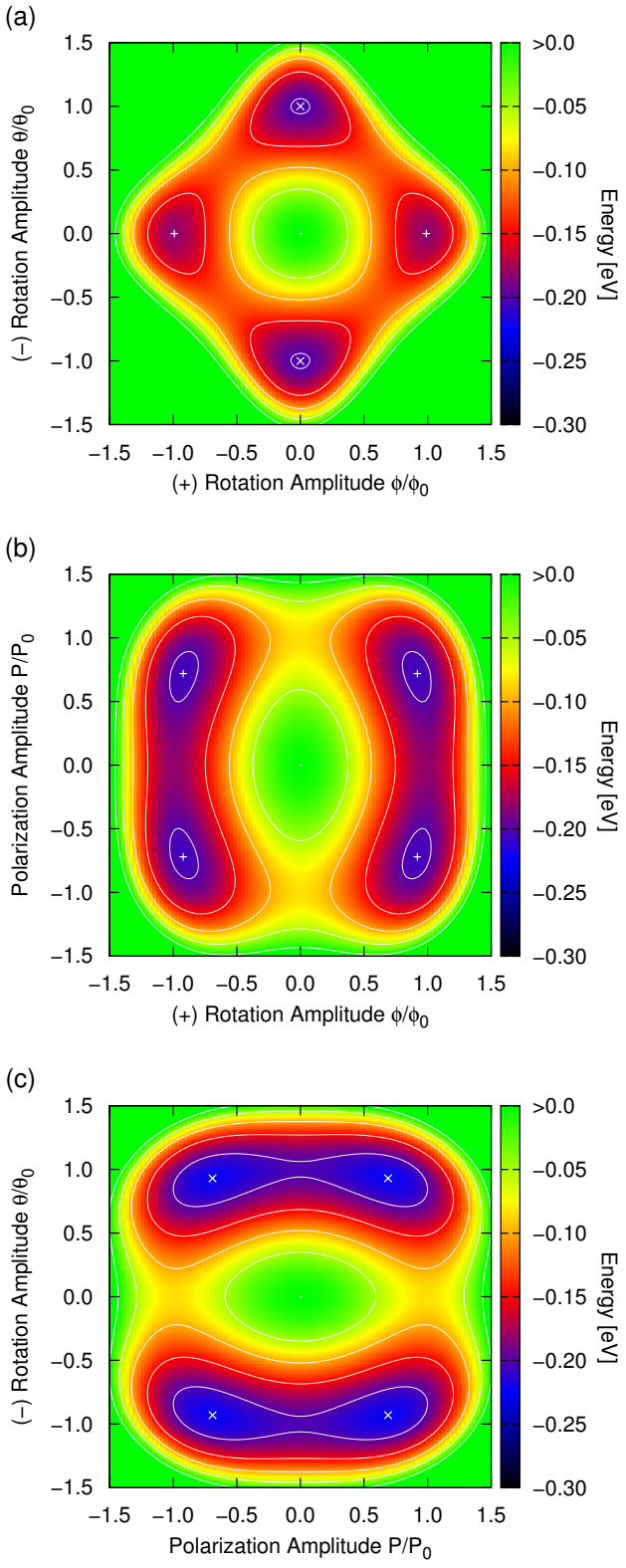

Figure 12.19: 2D energy profiles $E(\theta, \phi)$, $E(P, \phi)$ and $E(\theta, P)$ for the *P4bm* structure at $V = 59.51$ Å^3/f.u. Amplitudes are normalized with respect to their respective single mode values, which are $|P_0^{\mathrm{sm}}| = 0.62$ and $|\phi_0^{\mathrm{sm}}| = 1.17$ and $|\theta_0^{\mathrm{sm}}| = 1.20$. Isolines are given for every 0.05 eV.

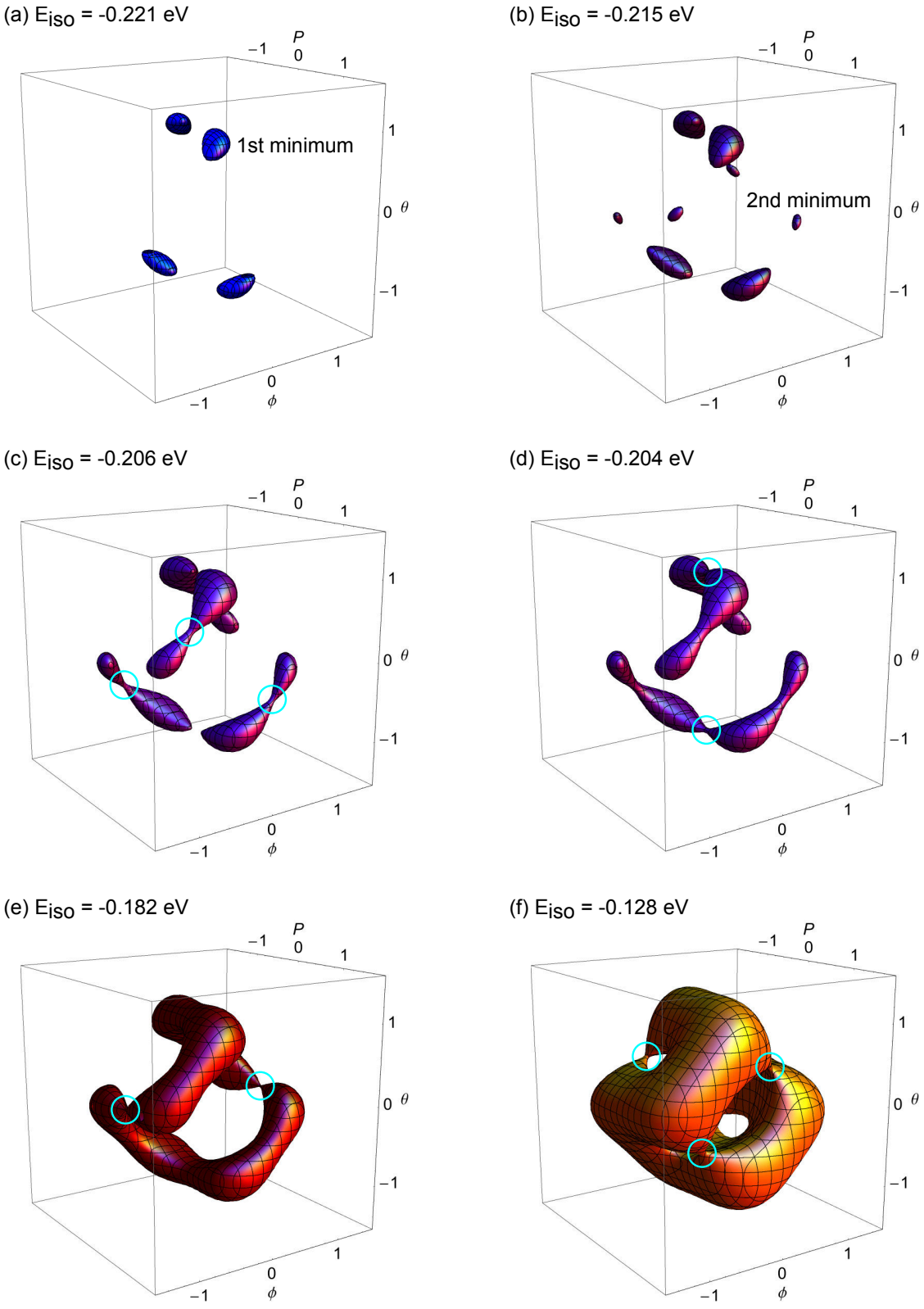

Figure 12.20: 3D energy surfaces $E(P, \phi, \theta)$ for different isovalues in the *P*4*bm* structure at $V = 59.51$ Å^3/f.u. Amplitudes are normalized with respect to their respective single mode values, which are $|P_0^{\mathrm{sm}}| = 0.62$ and $|\phi_0^{\mathrm{sm}}| = 1.17$ and $|\theta_0^{\mathrm{sm}}| = 1.20$. The colours of the isosurfaces are adapted to the colour scheme in Fig. 12.19.

The donut-shaped energy surface of the $P4_2nm$-structure thus has a 3D analogue in the $P4bm$-structure. Polarisation, in-phase tilt and anti-phase tilt coexist and can be easily changed along a closed minimum energy path with the highest barrier amounting 0.050 eV. Although the two tilts cannot coexist on their own and are highly competitive at $P = 0$, they can be brought together by improper coupling to the equally soft polar mode.

Finally, let us describe the findings for the large volume. The pairwise energy surfaces are presented in Fig. 12.21 (a)-(c). Again, substantial changes in the polarization-tilt interactions as compared to the small and intermediate volumes can be observed. The two tilt modes become weaker, but they are still as competitive as before. The polar-tilt interactions are now dominated by the immensely soft polar mode. Additionally, there must be strong competition between the polar and tilt modes, as the single tilts become suppressed in the presence of polarization. Kidney-shaped energy profiles result with a pronounced V-shape in the direction of polarization, indicating that we have large c_{420} and c_{402}. It seems that the ground state is a purely polar structure corresponding to space group $P4mm$.
This picture changes completely, if all three distortions are considered together. In Fig. 12.22 3D energy surfaces resulting from the full Landau potential $E(P, \phi, \theta)$ for several isovalues are shown. The absolute minima are positioned at

$$E_{\text{min}}(-0.95 \cdot P_0^{\text{sm}}, -0.50 \cdot \phi_0^{\text{sm}}, -0.49 \cdot \theta_0^{\text{sm}}) = -0.945\,\text{eV}.$$

They can be seen in (a). The absolute mode amplitudes become

$$|P_0| = -1.41,\ |\phi_0| = -0.60,\ |\theta_0| = -0.60.$$

The lowest energy barrier is associated with a simultaneous change of the tilts at constant polarization at $E = -0.809$ eV ($\Delta E = 0.136$ eV) and is given in (b). This barrier is still small compared to the huge barrier at $E(0, 0, \pm\theta_0^{\text{sm}}) = -0.200$ eV ($\Delta E = 0.745$ eV) shown in (c) to switch the polarization at constant θ, or the second barrier for polarization switching at constant ϕ at $E(0, \pm\phi_0^{\text{sm}}, 0) = -0.189$ eV ($\Delta E = 0.756$ eV), presented in (d). The isosurface for $E = -0.100$ eV has the shape of two facing pillows, one rotated by 90°, reflecting the dominance of the polarization, while at the same time improper interactions are active favouring the simultaneous presence of the two tilt modes.

To summarize, the shapes of the energy surfaces depend strongly on the volume. As in the $Pmc2_1$ structures we find improper coupling interactions to play an important role, especially in the intermediate and large volume range. The strongest impact of the improper coupling terms is the development of four absolute minima at positions with non-zero values of all three order parameters. Yet, the polarization switching properties are completely different from those in the orthorhombic structure, where the improper coupling enabled the presence of polarization. In the $P4bm$ structures it is rather the concurrent tilts that are induced. The odd-order triple coupling terms must be enormous to overcome the strong competition between the two tilts. In contrast to the symmetry mode analysis of structurally optimized structures, we find rather different phases to be most stable. At small volumes an anti-phase tilted *P4/nbm* phase is stable, while at intermediate and large volumes a $P4bm$ phase is favored with the anti-phase tilt being stronger than the in-phase tilt at intermediate volumes and the polarization dominating at large volumes.

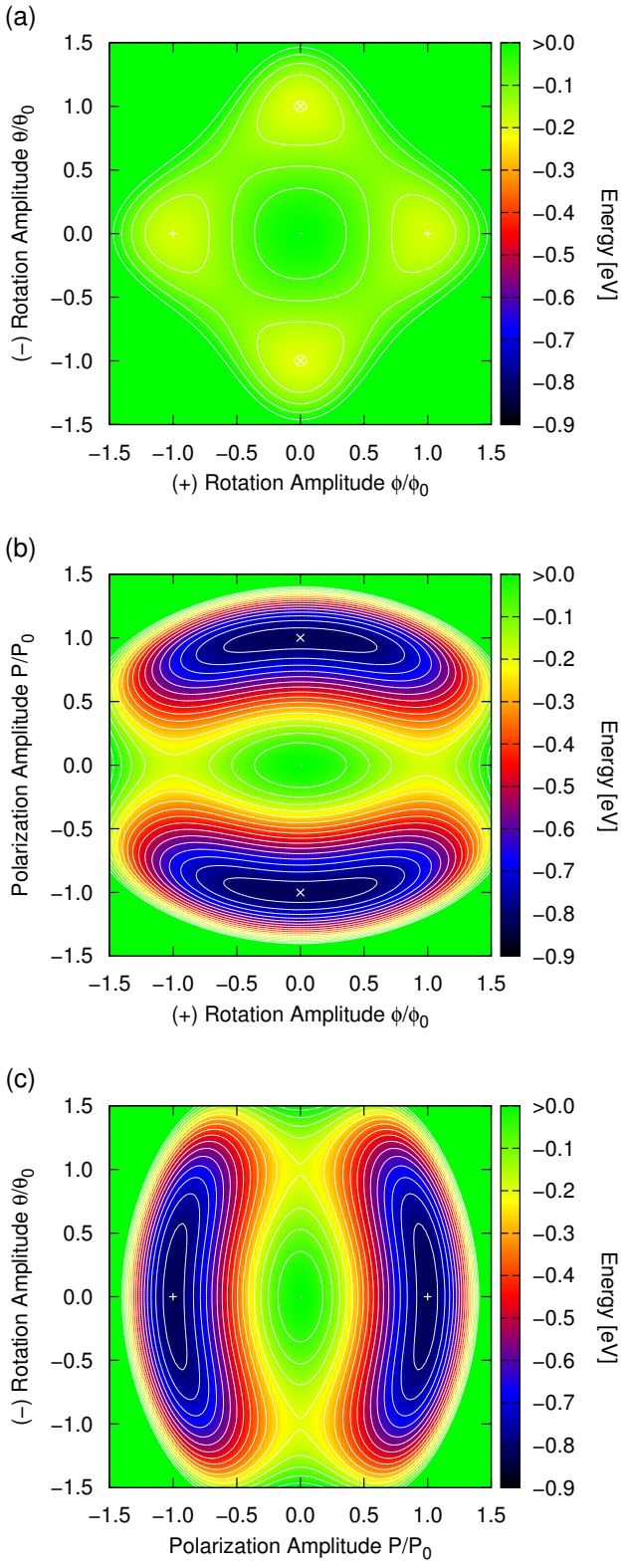

Figure 12.21: 2D energy profiles $E(\theta, \phi)$, $E(P, \phi)$ and $E(\theta, P)$ for the *P*4*bm* structure at $V = 63.81$ Å^3/f.u. Amplitudes are normalized with respect to their respective single mode values, which are $|P_0^{\mathrm{sm}}| = 1.48$ and $|\phi_0^{\mathrm{sm}}| = 1.20$ and $|\theta_0^{\mathrm{sm}}| = 1.22$. Isolines are given for every 0.05 eV.

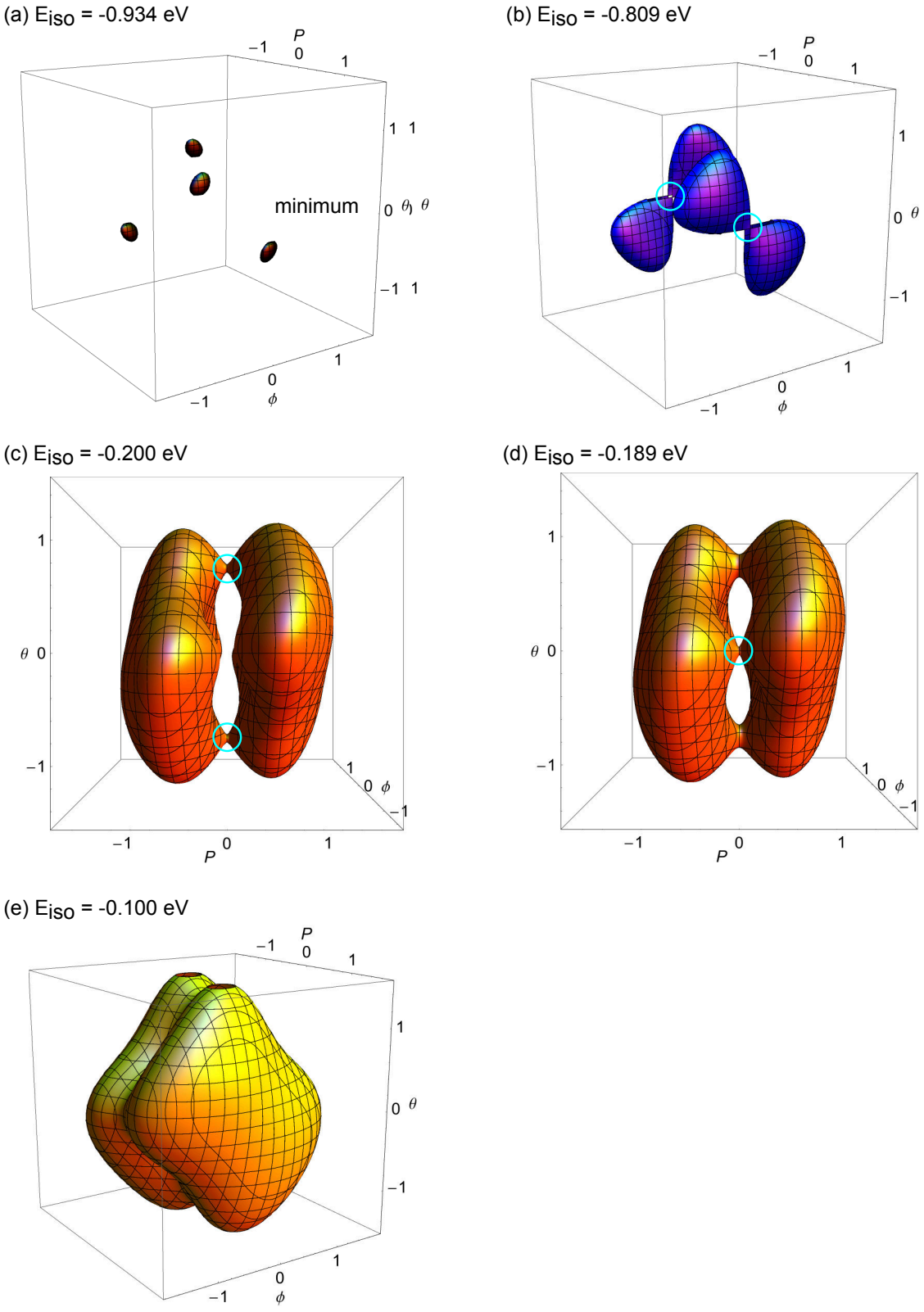

Figure 12.22: 3D energy surfaces $E(P, \phi, \theta)$ for different isovalues in the *P4bm* structure at $V = 63.81$ Å^3/f.u. Amplitudes are normalized with respect to their respective single mode values, which are $|P_0^{\mathrm{sm}}| = 1.48$ and $|\phi_0^{\mathrm{sm}}| = 1.20$ and $|\theta_0^{\mathrm{sm}}| = 1.22$.The colours of the isosurfaces are adapted to the colour scheme in Fig. 12.21.

Finally, we want to discuss the coupling terms. They are given in Fig. 12.23. In the first row the single mode coefficients are given, in the second row the pairwise coupling coefficients and in the third row the coupling coefficients describing triple interactions. At all volumes is $b_{022} > -2a_{020}, -2a_{002}$, explaining the strong competition between the two tilt modes, which cannot be compensated by the small negative c_{024} and c_{042}. At the small and intermediate volume all other pairwise coupling terms adopt very small values only. The trilinear coupling coefficient is extremely large with about 0.2, which is the double of the largest coefficient found in the $Pmc2_1$ structure. The main difference in the 3D energy surfaces arise from the differences in the improper coupling coefficients, especially d_{111} and e_{311}. At the large volume all triple coupling coefficients become very large, allowing for the stability of the much weaker tilt modes in the presence of the strongly dominating polar mode.

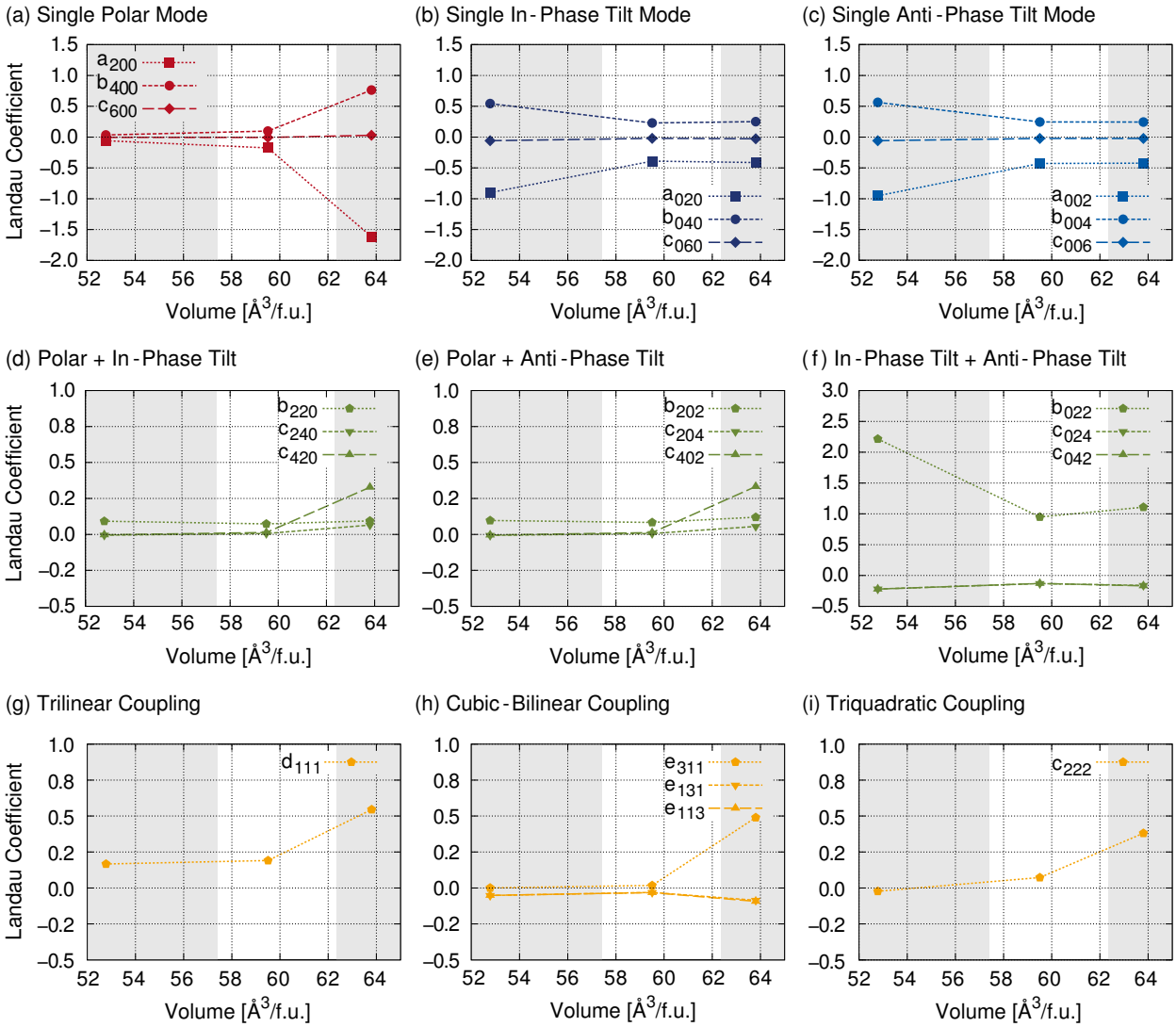

Figure 12.23: Landau coefficients obtained for the *P*4*bm*-structures at different volumes. The background colours indicate the ranges of phase stabilities of phases *P*4/*mbm*, *P*4*bm* and *P*4*mm* obtained from the symmetry mode analysis in the previous chapter.

These calculations essentially show something new, namely that the in-phase tilt and polarization dominated *P4bm* structure is actually not the ground state within this space group, the anti-phase tilted polar alternative leads to lower energies. Moreover, at the large volume a purely polar structure was expected, but in fact all three distortion modes should coexist. The 3D energy surfaces, however, show also how easy it is to "fall" into the in-phase tilted polar local minimum during a structure optimization driven by minimization of the forces. If first the tilts are reduced to zero due to their strong competition, there is no way to escape from the saddle point of the polarization-only state.

This example demonstrates how decisive the choice of the initial structural parameters can be, as within the same space group under consideration of the same distortions (but different amplitudes) different structures can be obtained all of them representing a (local) minimum in the 3D energy surface.

The structure optimizations of the *P4bm* structure were repeated with three different initial structures including always modes with equal amplitudes $E(P_0, \phi_0, \theta_0)$, $(P_0, \phi_0, 0)$, $(P_0, 0, \theta_0)$ and $(0, \phi_0, \theta_0)$, but also $(P_0, 0, 0)$, $E(0, \phi_0, 0)$ and $E(0, 0, \theta_0)$ were included. The results are shown in Fig. 12.24. We obtain four sets of different curves, depending on the imposed modes as the dominating distortions. At smaller volumes, the non-polar structures *P4/nbm*, *P4/mbm* and *P4bm*(+/-) are favored and undergo at different volumes continuous phase transitions to the polar structures *P4bm*(P/-), *P4bm*(P/+) and *P4bm*(P/+/-), respectively. At volumes larger than 62 Å^3/f.u. the purely polar structure was found to be more stable. Although there was an initial structure with equal amplitudes of all three distortion modes included, the high volume ground state indicated by the Landau expansion was not found by the structure optimization algorithm.

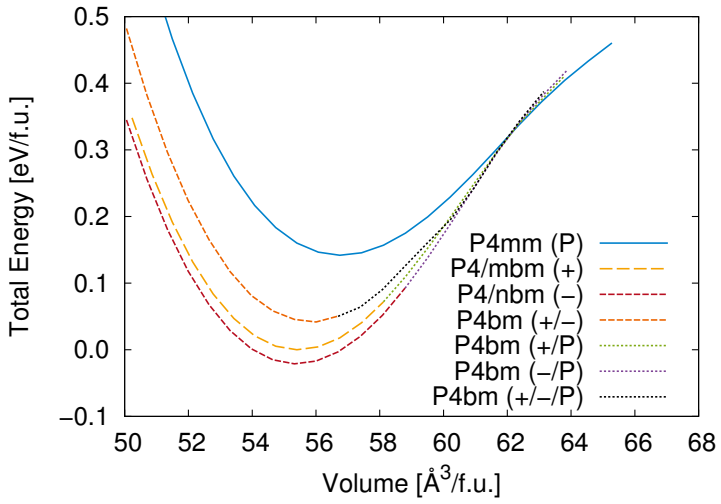

Figure 12.24: $E(V)$ curves for structures of the *(*P4/mmm) $\rightarrow$ *P4bm* group-subgroup family. Depending on the initial structure used for the structural optimization different "ground states" are reached. Symbols in parentheses indicate the dominating distortion modes: "P" for polarization, "$+$" for in-phase tilt and "$-$" for anti-phase tilt.

12.3 Comparison with Optimized Structures

We want to compare the results of the Landau potentials with those of the symmetry analyses of optimized structures. In Fig. 12.25 all results are summarized. For the $R3$, $P4_2nm$ and $Pmc2_1$ structures the agreement between both data sets are quite satisfying. The underestimation of the amplitudes of the anti-phase tilt mode in the $Pmc2_1$ structures is probably a result of the neglected Γ_1^+ mode, which would affect the atomic distances relevant for the energy development of the anti-phase tilt mode. As discussed above, the $P4bm$ structures are completely out of line, when it comes to the tilt modes. The amplitude of the polar mode though, corresponds well to the values obtained in the optimized structures, which might be a coincidence.

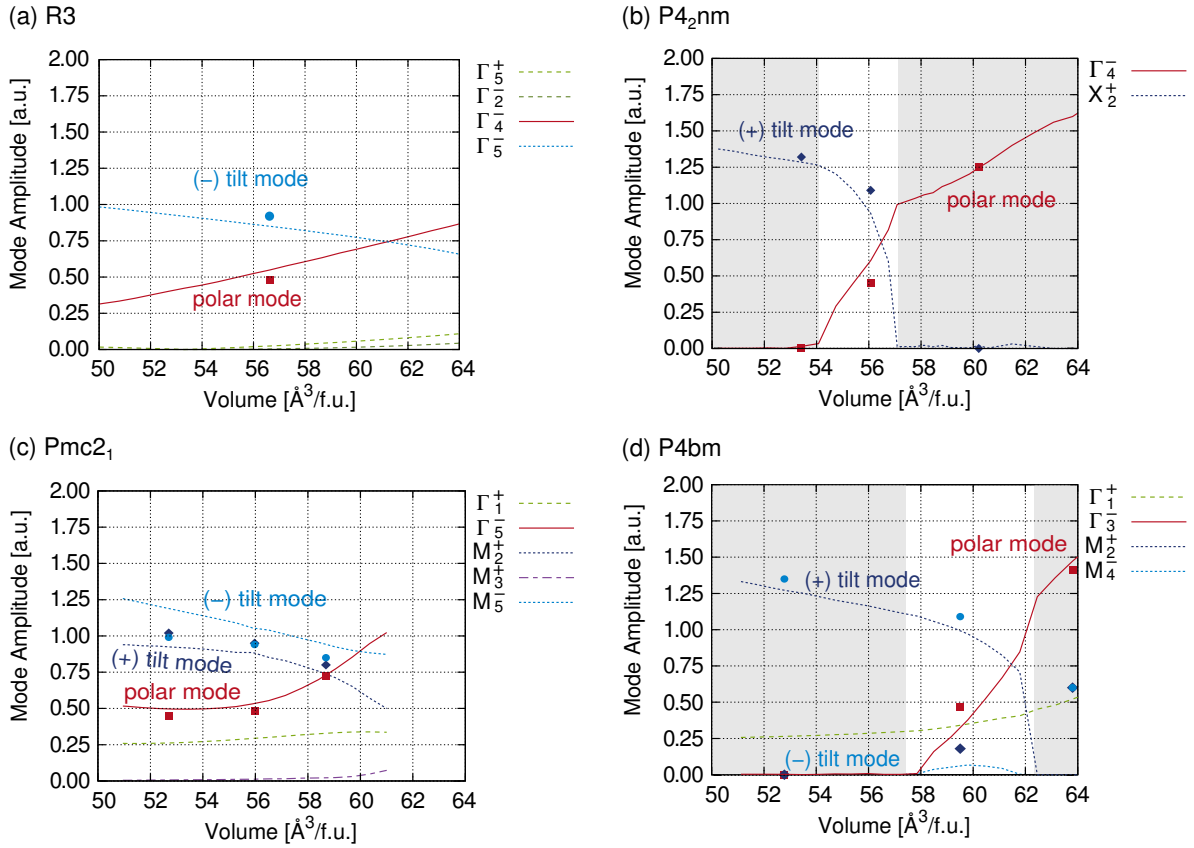

Figure 12.25: Comparison between the mode amplitudes determined in the optimized structures in Ch. 11 and those resulting from fitting to Landau potentials in the phases (a) $R3$, (b) $P4_2nm$, (c) $Pmc2_1$ and (d) $P4bm$.

12.4 Summary

In this chapter we employed Landau potentials deduced from invariants of the irreps of the dominating distortion modes discovered in the previous chapter. All distortion modes were found to be soft in the investigated phases and volume ranges. In that sense all tilt and polar instabilities are associated with primary distortion modes. A distinction can only be made between dominating and weak distortion modes.
In all structures we always found both competition and cooperation between different order parameters. In contrast to $BiFeO_3$, where triggered ferroelectricity in the $R3c$ structure was reported,[212] polarization and anti-phase tilts in the $R3$ structure of NBT do not enhance each other.
In the $P4_2nm$-structure also two modes have to be taken into account, a polar and an in-phase tilt mode. Interactions between these two modes are exclusively competitive. Only in a very narrow volume range both distortions can coexist, at smaller volumes only tilt exists and at larger volumes only polarization. The intermediate phase has an almost donut-shaped energy surface, indicating that tilt and polarization can be easily transformed into each other.
Improper coupling terms are indifferent to ferroelectricity or any physical meaning of the order parameters. Clear limits between proper and improper ferroelectricity are not always obvious. Crucial for the discrimination between improper and proper ferroelectricity is not only the existence of odd-order coupling terms, but also the pairwise mode interactions have to be taken into account. In the $Pmc2_1$-structures we observed a transition from improper to proper ferroelectricity with increasing volume. This is possible because the two tilt modes can coexist in the absence of polarization, while the single polar mode is only weakly soft at the smallest investigated volume and becomes stronger with increasing volume. In contrast, the $P4bm$ structures, despite their very large improper coupling coefficients, should not show any improper ferroelectricity, but have to be considered as proper ferroelectrics. Improper coupling induces tilts not polarization in these structures. A comparison between $P4_2nm$ and $P4bm$ structures shows, that chemical order does not change the physical properties completely. At small volumes tilts are favored, and at large volumes polarization. At the intermediate volumes in both cases we found very flat energy surfaces, which allow for a “free” variation of all order parameters.
The results of the last two chapters are briefly summarized in Fig. 12.26 for both chemical orders '111' and '001' and their effect on the primary distortion modes and their coupling interactions.

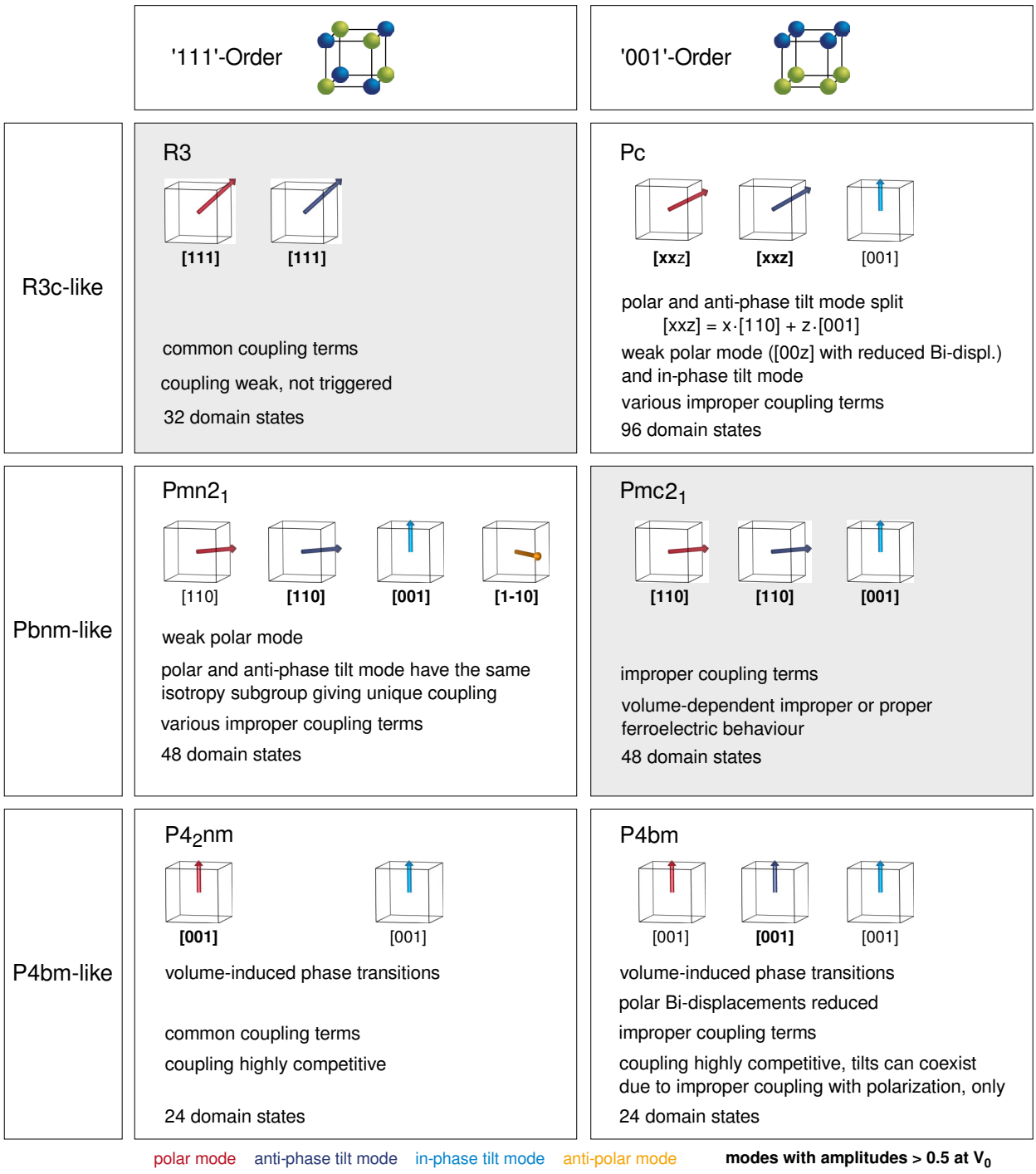

Figure 12.26: Effect of chemical order on the distortion modes (schematically shown are their vectors and directions) and ferroic properties in the phases of NBT. Please note, that for '111'-order the *R*3*c*-like phase is energetically most stable at $p = 0$ GPa, while for '001'-order it is the *Pbnm*-like phase (marked in grey).

13 NBT-Based Solid Solutions

One goal in developing new lead-free ferroelectrics is the prediction of morphotropic phase boundaries in arbitrary solid solutions. As response properties are enhanced in the vicinity of these compositional regions of structural ambiguity, the wish for reliable prediction tools is comprehensible, yet to date a reliable technique is still missing. In the following a new method is introduced based on the concept of flat energy surfaces and the prediction of pressure-induced phase transitions in NBT-based solid solutions. Four different A-site alloyed systems were tested, namely $(NBT)_{(1-x)}$-$(CaTiO_3)_x$, $(NBT)_{(1-x)}$-$(BaTiO_3)_x$, $(NBT)_{(1-x)}$-$(Li_{1/2}Bi_{1/2}TiO_3)_x$ and $(NBT)_{(1-x)}$-$(K_{1/2}Bi_{1/2}TiO_3)_x$. The successes and limitations of this new technique will be discussed. Finally, the concept of chemical pressure is introduced and chemical pressure is compared with hydrostatic pressure in NBT-based solid solutions.

13.1 Pressure-Induced Phase Transitions

In order to study the influence of chemical substitution on the pressure-induced phase transitions found in pure NBT we performed total energy calculations of four different NBT-based solid solutions. These are the earth alkali metal-substituted solid solutions $(NBT)_{(1-x)}$-$(CaTiO_3)_x$ and $(NBT)_{(1-x)}$-$(BaTiO_3)_x$ discussed in Sec. 13.1.1 and the alkali metal substituted solid solutions $(NBT)_{(1-x)}$-$(Li_{1/2}Bi_{1/2}TiO_3)_x$ and $(NBT)_{(1-x)}$-$(K_{1/2}Bi_{1/2}TiO_3)_x$ discussed in Sec. 13.1.2. Finally, we discuss in Sec. 13.2 how chemical substitution influences the $a^-a^-a^-$ anti-phase tilt soft-mode.

We used small supercells of sizes $2 \times 2 \times 2$ or $2 \times 2 \times 4$ the perovskite unit cell to model the different contents of the non-NBT end member $x = 0.00, 0.125, 0.25, 0.50, 0.75, 1.00$. The A-site configurations of the alkali earth metal-substituted solid solutions $(Na_{1/2}Bi_{1/2}TiO_3)_{(1-x)}$-$(M TiO_3)_x$ (M=Ca, Ba) are given in Fig. 13.1, those of the alkali metal-substituted solid solutions $(Na_{1/2}Bi_{1/2}TiO_3)_{(1-x)}$-$(M_{1/2}Bi_{1/2}TiO_3)_x$ (M=Li, K) are shown in Fig. 13.2. Configurations obtained from consecutive substitution of Na/Bi-atoms in '111' ordered NBT were chosen.

13.1.1 Earth Alkali Metal Substituted Solid Solutions

Pure '111' ordered NBT is stable in the $R3c$-structure, while the two other earth alkali end members $CaTiO_3$ and $BaTiO_3$ adopt *Pbnm* and *P4mm* structures, respectively. Depending on the non-NBT end member a phase transition from $R3c$ to *Pbnm* ($CaTiO_3$) or to *P4mm* ($BaTiO_3$) is induced upon alloying. In Fig. 13.3 we can see how the pressures of these two phase transitions depend on the compositions of the solid solutions. In both solid solutions the transition pressures depend linearly on the concentration x of the non-NBT end member.

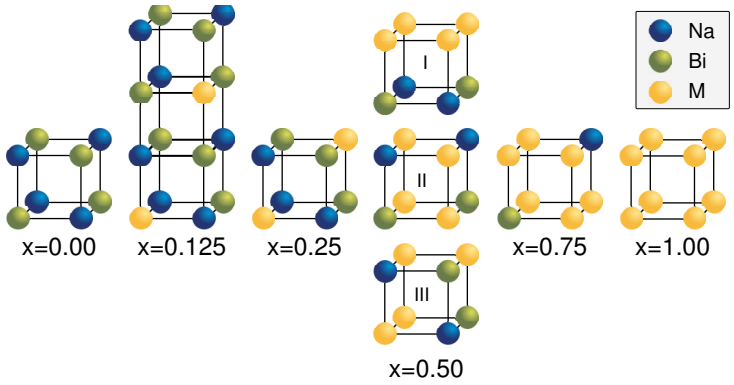

Figure 13.1: A-site configurations of alkali earth metal-substituted solid solutions $(Na_{1/2}Bi_{1/2}TiO_3)_{(1-x)}$-$(MTiO_3)_x$ (M=Ca,Ba)

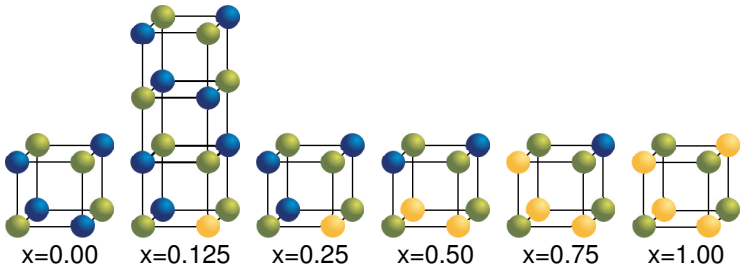

Figure 13.2: A-site configurations of alkali metal-substituted solid solutions $(Na_{1/2}Bi_{1/2}TiO_3)_{(1-x)}$-$(M_{1/2}Bi_{1/2}TiO_3)_x$ (M=Li,K)

The composition at which the transition pressure equals zero indicates the 0 Kelvin morphotropic phase boundary. In $(NBT)_{(1-x)}$-$(CaTiO_3)_x$ this composition is found at $x = 0.15$. For $x < 0.15$ the *R*3*c*-structure is stable at ambient pressure and a phase transition to *Pbnm* can be induced by the application of hydrostatic pressure. For $x > 0.15$ the *Pbnm*-structure is most stable at ambient pressure. Only under tensile conditions the *R*3*c*-structure could be stabilized. The results are in very good agreement with the experimental findings by Ranjan *et al.*,[138] who found for $0.05 < x < 0.15$ a coexistence region of *R*3*c*- and *Pbnm*-phases.

In the solid solution $(NBT)_{(1-x)}$-$(BaTiO_3)_x$ the composition at which the phase transition from *R*3*c* to *P*4*mm* is shifted to ambient pressure is around $x = 0.35$. We performed calculations for x=0.00, 0.125, 0.25, 0.50, 0.75 and 1.00, but transition pressures are given only for the first three compositions. The reason is that at $x = 0.50$ the tilted *R*3*c*-structure is only stable at pressures above 23 GPa, which is out of range of the figure. Thus, the phase boundary between *R*3*c* and *P*4*mm* has to turn into the nearly vertical line marked as tilt instability limit (how this limit line was determined will be explained in Sec. 13.2). The morphotropic composition of $x = 0.35$ is about three times larger than the values found in literature of $0.06 < x < 0.11$.[141–143] Moreover, we did not find the rhombohedral untilted $R3m$-structure to be most stable at any composition, this structure always lead to higher energies than the structures *R*3*c* and *P*4*mm*. On the other hand, our results are well consistent with a previous study on ferroelectricity in $(NBT)_{(1-x)}$-$(BaTiO_3)_x$,

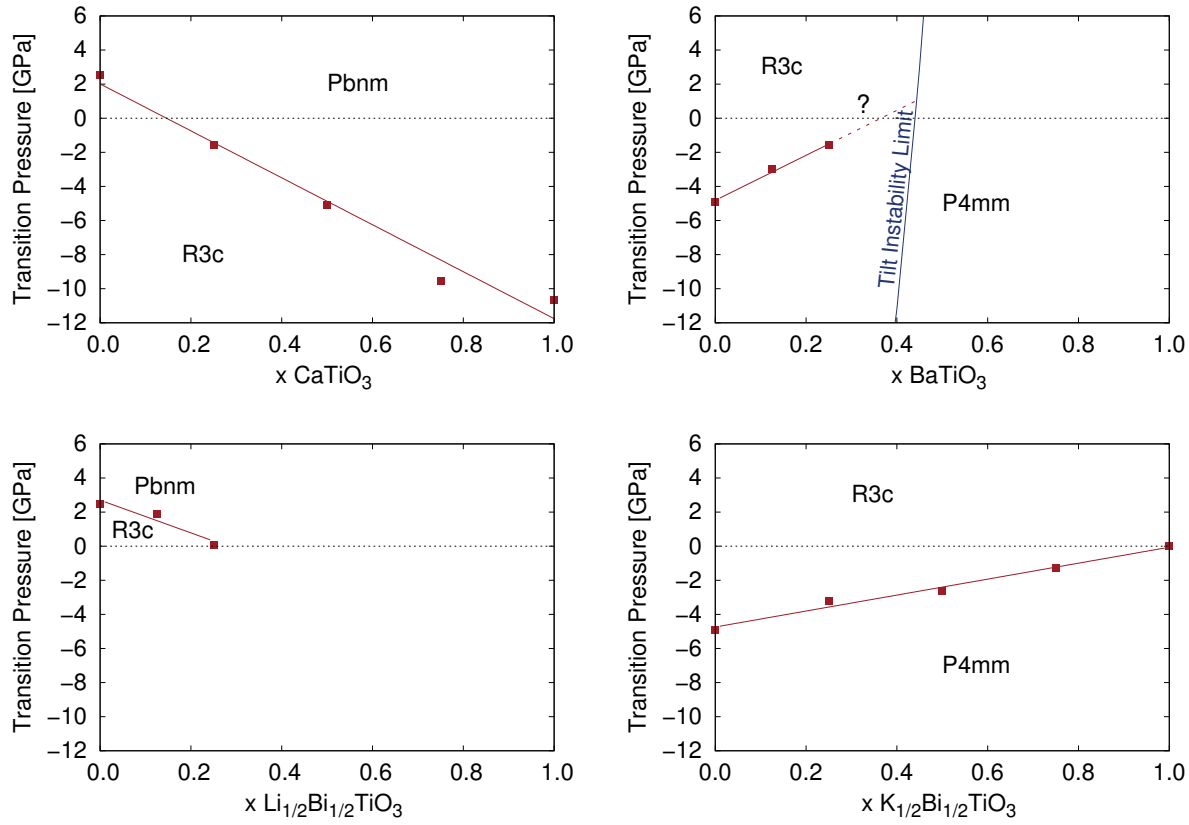

Figure 13.3: Phase diagrams of $(NBT)_{(1-x)}$-$(CaTiO_3)_x$ (top left), $(NBT)_{(1-x)}$-$(BaTiO_3)_x$ (top right), $(NBT)_{(1-x)}$-$(Li_{1/2}Bi_{1/2}TiO_3)_x$ (bottom left) and $(NBT)_{(1-x)}$-$(K_{1/2}Bi_{1/2}TiO_3)_x$ (bottom right). Shown are transition pressures for phase transformations *R3c* $\rightleftharpoons$ *Pbnm* ($CaTiO_3$, $Li_{1/2}Bi_{1/2}TiO_3$) and *R3c* $\rightleftharpoons$ *P4mm* ($BaTiO_3$, $K_{1/2}Bi_{1/2}TiO_3$).

where the transition from A-site activity to B-site ferroelectricity was found in the region $0.19 < x < 0.40$.[47] Ghita *et al.* postulated that morphotropic phase boundaries are formed in solid solutions where a crossover from A-site to B-site ferroelectricity occurs.[46]

13.1.2 Alkali Metal Substituted Solid Solutions

Similarly to the aforementioned earth alkali-substituted solid solutions in the alkali metal-substituted solid solutions phase transitions from *R3c* to *P4mm* or *Pbnm* can be induced upon chemical substitution. The two phase diagrams of the solid solutions $(NBT)_{(1-x)}$-$(Li_{1/2}Bi_{1/2}TiO_3)_x$ and $(NBT)_{(1-x)}$-$(K_{1/2}Bi_{1/2}TiO_3)_x$ are presented in Fig. 13.3, too.

In the solid solution $(NBT)_{(1-x)}$-$(Li_{1/2}Bi_{1/2}TiO_3)_x$ we find a linear dependence of the transition pressure for $0.00 < x < 0.25$. For $x > 0.25$ anomalously large ferroelectric displacements of the Li^+ cations were found, which shows that the very small Li^+ cations fit poorly in the large AO_{12} cuboctahedrons and probably a different post-perovskite crystal structure would be

preferred. Experiments revealed a solution limit of $Li_{0.5}Bi_{0.5}TiO_3$ in NBT at $x = 0.24$, which supports our results.

In the solid solution with the larger alkali metal cation $(NBT)_{(1-x)}$-$(K_{1/2}Bi_{1/2}TiO_3)_x$ our calculations do not give the correct structure for the end member $K_{1/2}Bi_{1/2}TiO_3$, as both structures *P*4*mm* and *R*3*c* are degenerate, they give the same energy. Hence, the composition at which the phase transition is shifted to ambient pressure is at $x = 1.00$, which is far off the values of $0.16 \geq x \geq 0.20$ reported in literature for polycrystalline materials.[128,148] Moreover, although the K^+ cation according to its Shannon radius is much larger than the Ba^{2+} cation, the complete substitution of Na^+ cations by K^+ is not sufficient to inhibit octahedral tilting, the *R*3*c*-structure remains stable over the whole composition range. Additionally, as in $(NBT)_{(1-x)}$-$(BaTiO_3)_x$, we did not find an $R3m$ structure to be favoured at any composition.

13.2 Substitutional Effects on Tilt Instabilities

We calculated energies depending on the tilt angle in the $R\bar{3}c$-like structures ($a^-a^-a^-$ tilt system, excluding polarization along [111]-direction, which further reduces the symmetry to *R*3*c*) for the two solid solutions $(NBT)_{(1-x)}$-$(BaTiO_3)_x$ and $(NBT)_{(1-x)}$-$(CaTiO_3)_x$ under variation of volume/pressure and composition. For that purpose the atom positions were kept fixed except those of the oxygen atoms, which were moved along the eigenvector of the $a^-a^-a^-$ tilt soft-mode. We expand the total energy of the unit cell in a power series of the order parameter δ, which is the oxygen displacement in units relative to the cell lattice parameter

$$E = E_0 + \frac{a}{2}\,\delta^2 + \frac{b}{4}\,\delta^4, \tag{13.1}$$

where E_0 is the energy of the ideal perovskite structure. If $a < 0$ this equation describes a double-well potential and the distorted structure is stable. If $a > 0$ it describes a parabola and the high-symmetry structure is stable. The fourth order term dominates at large δ and describes the repulsive forces. The minimum position δ_0 can be easily determined from

$$\left.\frac{dE}{d\delta}\right|_{\delta_0} = 0, \;\; \left.\frac{d^2E}{d\delta^2}\right|_{\delta_0} > 0 \tag{13.2}$$

It can be found at

$$\delta_0 = \pm\sqrt{-\frac{a}{b}} \tag{13.3}$$

The order parameter δ is related to the tilt angle ω by the following equation

$$\tan\omega = \frac{\delta/a_0}{d/a_0} \tag{13.4}$$

with the denominator $d/a_0 = 0.25$. δ/a_0 was varied in the range $0.00 < \delta/a_0 < 0.07$, which is equivalent to tilt angles up to $\omega = 15.64°$. The volume range (and thus the pressure range) was chosen as $42.875 < V < 71.473$ in Å^3/f.u., which corresponds to pressures from -30 (-20) GPa up to 160 (90) GPa depending on the composition.

In a previous study the influence of $BaTiO_3$-substitution on the ferroelectric activities on the two cation sites A and B in the solid solution $(NBT)_{(1-x)}$-$(BaTiO_3)_x$ was discussed.[47] Now we want to investigate how chemical substitution influences the anti-phase tilt soft-mode. As found in Sec. 13.1.1 can high concentrations of Ba^{2+} inhibit octahedral tilting.

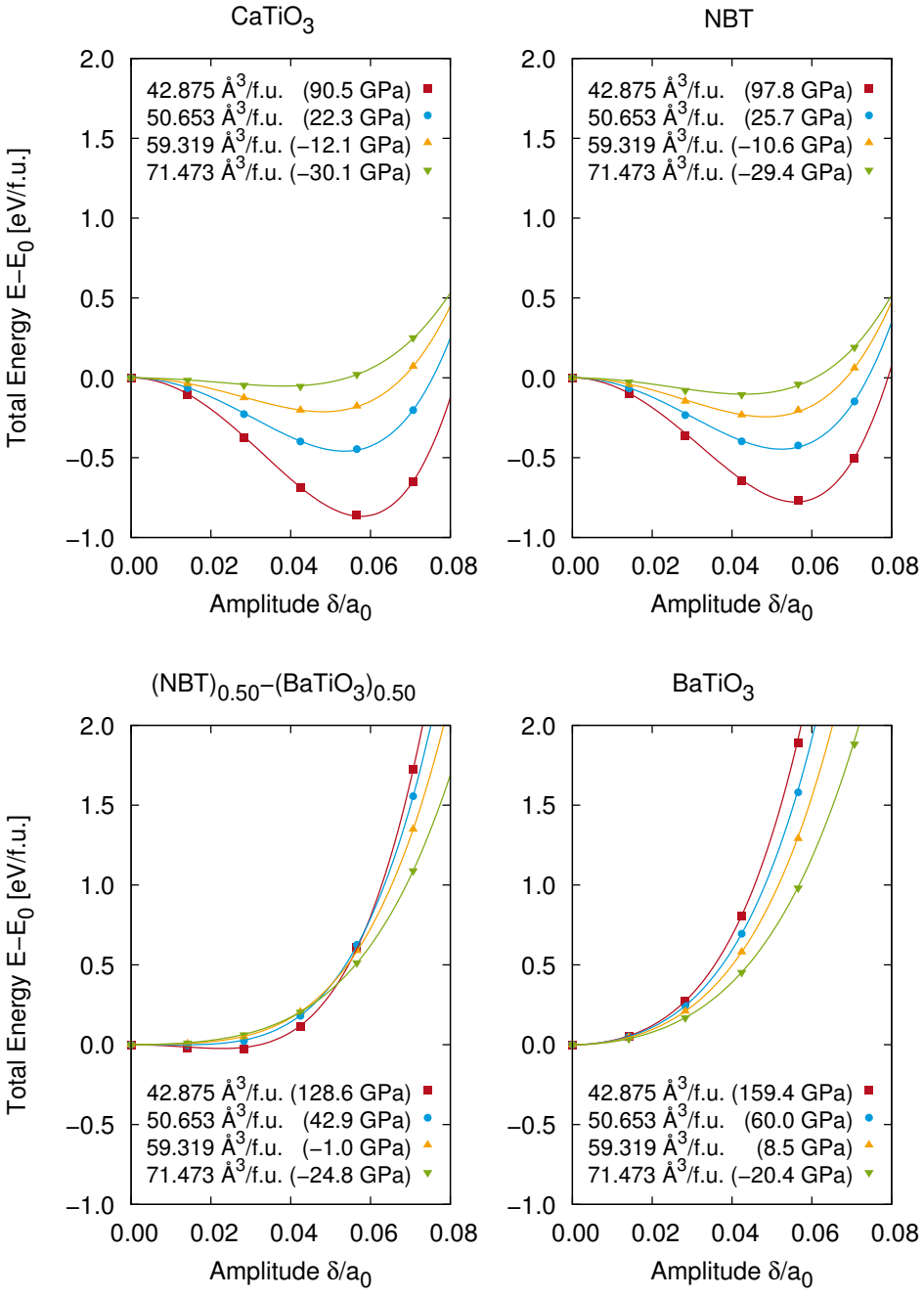

Figure 13.4: Total energies of tilted structures in $CaTiO_3$, NBT, $(NBT)_{0.50}$-$(BaTiO_3)_{0.50}$ and $BaTiO_3$. The energies were fitted to Eq. 13.1.

In Fig. 13.4 it is shown exemplary how the total energies evolve with increasing tilt amplitude δ/a_0 at different volumes in the four compounds $CaTiO_3$, NBT, $(NBT)_{0.50}$-$(BaTiO_3)_{0.50}$ and $BaTiO_3$.

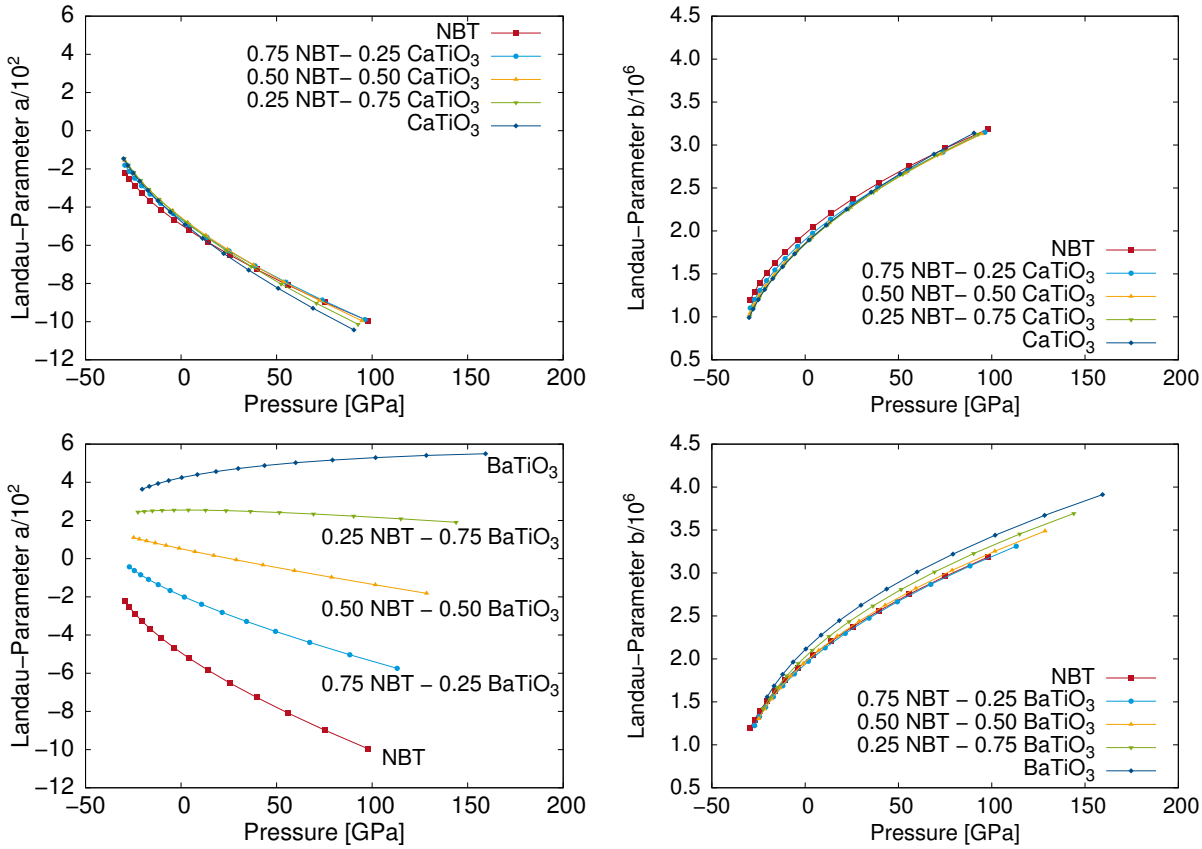

Figure 13.5: Tilt instabilities in $(NBT)_{(1-x)}$-$(CaTiO_3)_x$ and $(NBT)_{(1-x)}$-$(BaTiO_3)_x$

In $CaTiO_3$ and NBT at all volumes a minimum between tilt amplitudes of 0.05 and 0.06 is found. Therefore at all pressures the tilt-mode is soft. $BaTiO_3$ in contrast cannot be tilted at any volume, not even at very high pressures. The energy minimum is always at the high-symmetry structure. This is consistent with phonon calculations of $BaTiO_3$, which do not reveal any R-point instability, which corresponds to anti-phase tilts.[250] In $(NBT)_{0.50}$-$(BaTiO_3)_{0.50}$ both tilted and non-tilted structures can be found to be stable. At sufficiently large pressures tilts with small amplitudes can be induced, but at ambient pressure they are absent. This finding was already discussed in Sec. 13.1.1. There it was found that the tilted $R3c$-structure can only be stabilized at pressures above 23 GPa. In the following we want to investigate the softness of this tilt-mode and how it depends on pressure and composition more thoroughly.

The total energies were fitted to the fourth order Landau-potential from Eq. 13.1. In Fig. 13.5 the Landau-parameters a and b for the two solid solutions $(NBT)_{(1-x)}$-$(CaTiO_3)_x$ and $(NBT)_{(1-x)}$-$(BaTiO_3)_x$ are given as they depend on pressure and composition. In $(NBT)_{(1-x)}$-$(CaTiO_3)_x$ Landau coefficient a is lower than zero at any composition, which means that all compounds are prone to octahedral tilting. We find only little variation with composition, but large variation with pressure. The higher the pressure the lower is a. Similarly, we find for the second Landau coefficient b only low variation with composition, but high variation with pressure. In this case b increases upon increasing pressure. At high pressures repulsion is increased at large displacements, but at the same time attraction is increased at small displacements. Thus the application of pressure leads

to a steeper double-well potential in the vicinity of $\delta/a_0 = 0$, but not to a large change of optimum tilt angle when changing composition from pure NBT to pure $CaTiO_3$, as can be seen in Fig. 13.4. The parameters a and b unambiguously determine the optimum tilt angle, which can be calculated using Eq. 13.4. In Fig. 13.6 we show how the optimum tilt angles vary with pressure and composition. For $(NBT)_{(1-x)}$-$(CaTiO_3)_x$ we find only small variations with composition, between pure NBT and $CaTiO_3$ $\Delta\omega = 0.14°$at $P = 0$ GPa. At high pressures $CaTiO_3$ possesses the largest tilt angle, while at negative pressures pure NBT has the largest tilt angle. Overall, the variation between $0 \leq P \leq 90$ GPa is $\Delta\omega = 1.55°$ in $CaTiO_3$ and $\Delta\omega = 1.25°$ in pure NBT.

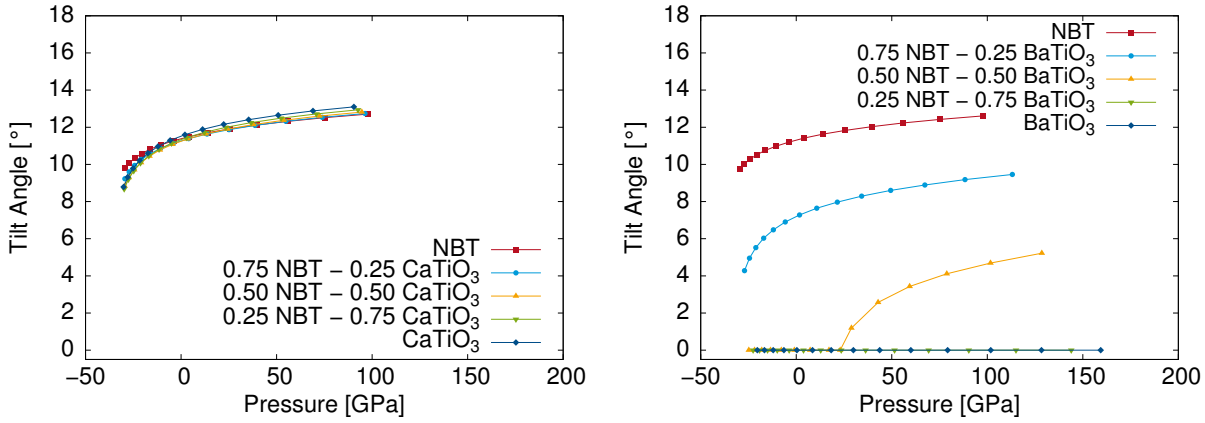

Figure 13.6: Evolution of tilt angles depending on pressure and composition in $(NBT)_{(1-x)}$-$(CaTiO_3)_x$ (top) and $(NBT)_{(1-x)}$-$(BaTiO_3)_x$ (bottom)

In $(NBT)_{(1-x)}$-$(BaTiO_3)_x$ the situation is completely different. Landau coefficient b again mainly depends on pressure but not significantly on composition, although repulsion becomes slightly stronger with $BaTiO_3$-content for $x > 0.50$. But the tilt inhibition effect is more reflected in Landau coefficient a, which depends strongly on pressure and composition, a even changes sign for $BaTiO_3$-concentration of 50%. At the higher $BaTiO_3$-contents $x = 0.75, 1.00$ it stays positive over the whole pressure range, while for the lower $BaTiO_3$-contents $x = 0.00, 0.25$ always $a < 0$. In Fig. 13.6 we can see how the strong variation of a leads to a strong variation of tilt angles. Tilt angles depend much stronger on the $BaTiO_3$-content than on the pressure. Increasing the $BaTiO_3$-content leads to a drastic decrease of the tilt angle at a given pressure.
Tilts can only be stable if $a < 0$. In order to find the tilt instability limit in composition-pressure space for $(NBT)_{(1-x)}$-$(BaTiO_3)_x$, we fitted the Landau-parameters $a(x, P)$ to a third order polynomial of the form

$$\begin{aligned} a(x,P) = a_0 &+ c_{10}x + c_{20}x^2 + c_{30}x^3 \\ &+ c_{01}p + c_{02}p^2 + c_{03}p^3 \\ &+ c_{11}xp + c_{12}xp^2 + c_{21}x^2p \end{aligned} \tag{13.5}$$

with the composition x and the pressure p. In Fig. 13.7 the obtained values of a are projected on the (x, p)-plane. Octahedral tilts can be induced at high enough pressures (say 60 GPa) in compounds with $BaTiO_3$-contents up to $x = 0.53$. The zero-value contour is marked as a red dashed line, it indicates the tilt instability limit, which is included in the phase diagram in Fig. 13.3. At lower

x the tilt-mode is soft and at higher x it is hard. For zero pressure the highest possible $BaTiO_3$-fraction where the tilt mode is still soft is $x = 0.44$.

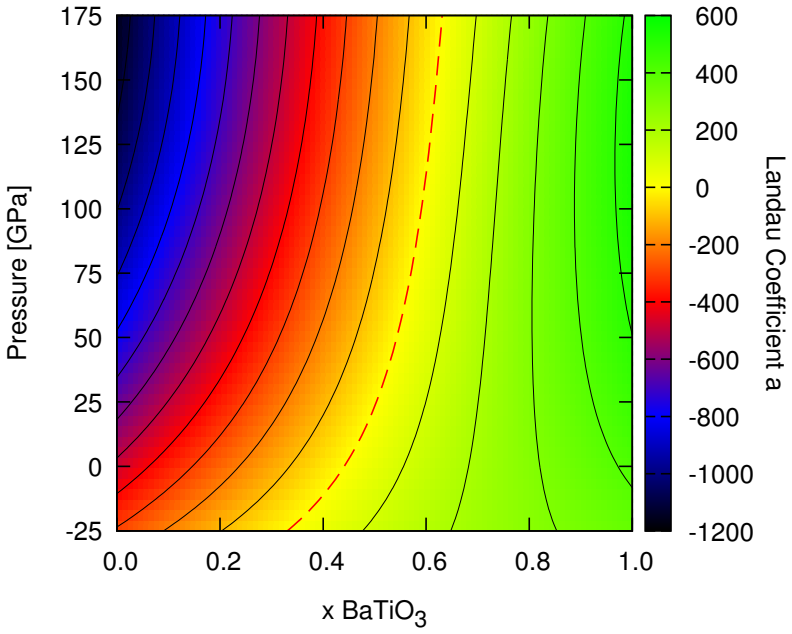

Figure 13.7: Landau coefficient a as a function of composition and pressure in $(NBT)_{(1-x)}$-$(BaTiO_3)_x$. The contour lines are separated by $\Delta a = 100$. The zero-value contour is marked as a red dashed line, it indicates the tilt instability limit within this solid solution.

13.3 The Concept of Chemical Pressure

From fitting of $E(V)$-curves with the Birch-Murnaghan equation of state pressures can be obtained for all volumes and compositions in the relaxed cubic perovskite structures. Comparison of pressures under variation of composition at a given volume gives a measure of the chemical pressure relative to the pure NBT-compound induced by substitution. These pressures were found to depend only on the volume but not on the composition, which means that the $p(V)$-curves for $x = 0.25, 0.50, 0.75, 1$ are equidistant for a given volume, e.g. addition of 25% $BaTiO_3$ induces the same additional pressure in pure NBT and in $(NBT)_{0.50}$-$(BaTiO_3)_{0.50}$. In Fig. 13.8 pressures are given with respect to the pressures of pure NBT as they vary with unit cell volume and composition in the four solid solutions we investigated. These pressures can be regarded as chemical pressures, as they result from chemical substitution at constant volume. Besides these chemical pressures also the equilibrium volumes are marked in the figure for all compositions.

In this way, chemical pressure is defined from the perspective of the crystal and not from the perspective of the spectator.

$$p_{\text{ext}} = -p_{\text{chem}} \tag{13.6}$$

Thus, negative chemical pressures do not imply tensile conditions, but conditions that induce a decrease of volume instead. Positive chemical pressure refers to a force directed outwards leading to an increase of volume.

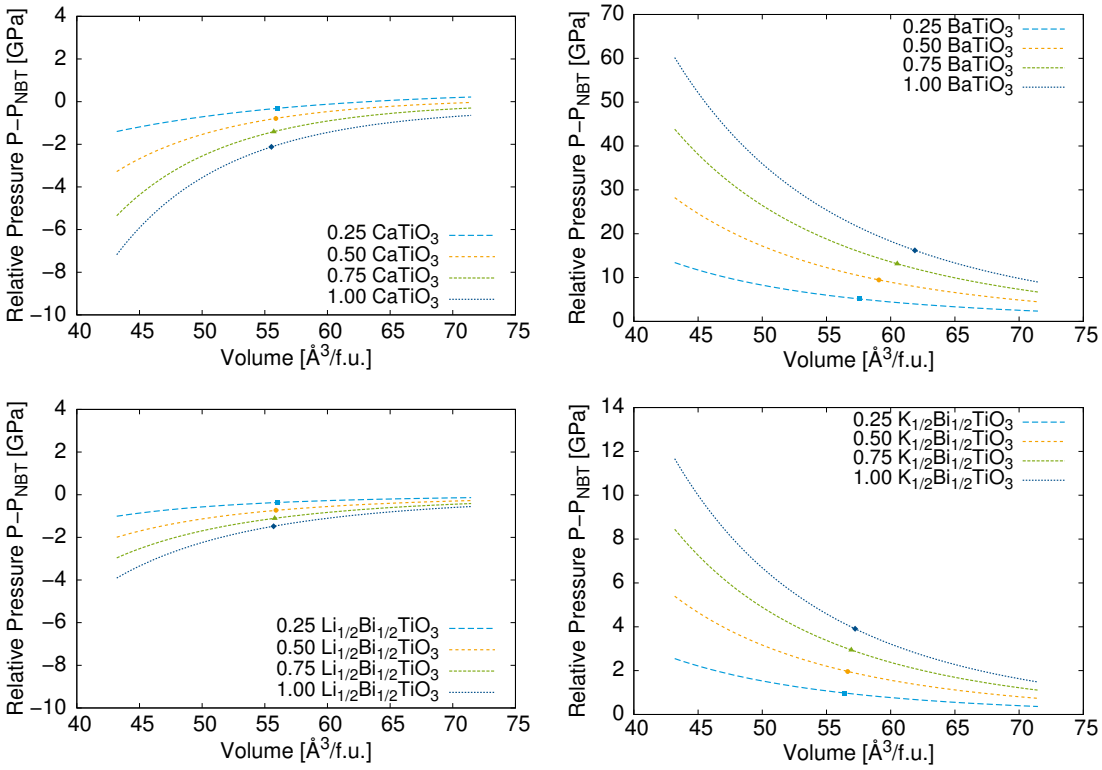

Figure 13.8: Chemical pressures induced by non-NBT end member relative to pure NBT in solid solutions (NBT)$_{(1-x)}$-(CaTiO$_3$)$_x$ (top left), (NBT)$_{(1-x)}$-(BaTiO$_3$)$_x$ (top right), (NBT)$_{(1-x)}$-(Li$_{1/2}$Bi$_{1/2}$TiO$_3$)$_x$ (bottom left) and (NBT)$_{(1-x)}$-(K$_{1/2}$Bi$_{1/2}$TiO$_3$)$_x$ (bottom right). Equilibrium volumes are marked. Please mind different scales of pressure.

The small cations Ca^{2+} and Li^+ give negative chemical pressures. The values in the $CaTiO_3$-substituted compounds are about double as high as those in the $Li_{1/2}Bi_{1/2}TiO_3$-substituted ones. Although Li^+ is much smaller than Ca^{2+} we should not forget that in the first case only Na^+ is exchanged, while in the second case also Bi^{3+} is substituted. The effect of Li^+-substitution should be less pronounced, as half of the A-sites is still occupied by the larger Bi^{3+}.

The large cations Ba^{2+} and K^+ induce positive chemical pressure relative to pure NBT. The pressures induced in the $BaTiO_3$-substituted compounds are five times larger than those induced in the $K_{1/2}Bi_{1/2}TiO_3$-substituted ones. Substitution by $BaTiO_3$ increases also the equilibrium volume much stronger than the substitution by $K_{1/2}Bi_{1/2}TiO_3$. This is probably the reason why we cannot see the phase transition $R3c \rightleftharpoons P4mm$ in the solid solution (NBT)$_{(1-x)}$-(K$_{1/2}$Bi$_{1/2}$TiO$_3$)$_x$ at lower x-values. The compressibility of K^+ compared to Ba^{2+} is higher. Potassium has the valence electron configuration $4s^1$, while barium has $6s^2$. According to that has the barium cation two more complete electron shells and also possesses d-electrons resulting in a much higher electron density than in the potassium cation. This explains the higher resistance of Ba^{2+} to compression. Moreover, only half the cations is substituted in (NBT)$_{(1-x)}$-(K$_{1/2}$Bi$_{1/2}$TiO$_3$)$_x$.

In Fig. 13.9 the induced chemical pressures at the equilibrium volumes of the solid solutions for $x = 0, 0.25, 0.5, 0.75, 1$ and the pressures of phase transitions determined in Sec. 13.1 are com-

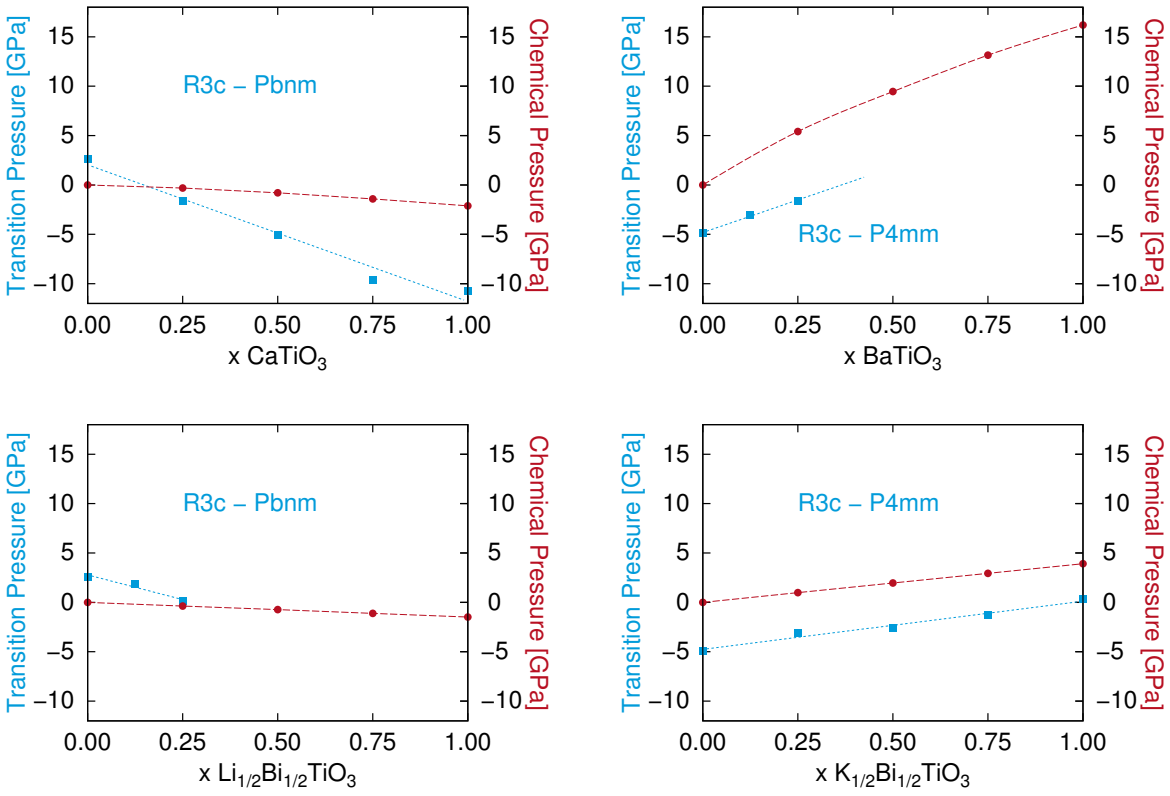

Figure 13.9: Comparison of pressures of phase transitions from Fig. 13.3 and chemical pressures at equilibrium volumes taken from Fig. 13.8 for $(NBT)_{(1-x)}$-$(CaTiO_3)_x$ (top left), $(NBT)_{(1-x)}$-$(BaTiO_3)_x$ (top right), $(NBT)_{(1-x)}$-$(Li_{1/2}Bi_{1/2}TiO_3)_x$ (bottom left) and $(NBT)_{(1-x)}$-$(K_{1/2}Bi_{1/2}TiO_3)_x$ (bottom right).

pared. Interestingly, the chemical pressures induced by the large cations Ba^{2+} and K^+ exhibit a strong correlation with the pressures of phase transition. The phase transitions do not only occur, where the phase transition is shifted to zero pressure, but also where the chemical pressure induced by substitution amounts to 5 GPa, thus compensates for the hydrostatic pressure of -5 GPa necessary to induce the $R3c \rightleftharpoons P4mm$ phase transition in pure NBT. It seems that pressure is the driving force of this phase transition, irrespective of its origin, whether hydrostatic or chemical. Trujillo *et al.* [55] determined experimentally a chemical pressure of 2.5 GPa at $BaTiO_3$-content of 11%, which is in very good agreement with our values.

For the solid solutions with the smaller cations Ca^{2+} and Li^+ a similar correlation between the two different types of pressure does not exist. The chemically induced pressures at the equilibrium volumes of the solid solutions are much lower than the pressure shift the phase transition $R3c \rightleftharpoons Pbnm$ experiences. Maybe the method works only for reference states of smaller volume, that is only for larger cations inducing positive chemical pressures in a material of smaller equilibrium volume.

13.4 Successes and Limitations of the Method

A-site substitution of Bi^{3+}/Na^{+} or just of Na^{+} by smaller or larger cations can shift the phase transition pressures of pure NBT to ambient conditions. This works well for both phase transitions found in NBT, i.e. *R*3*c* $\rightleftharpoons$ *P*4*mm* under tensile and *R*3*c* $\rightleftharpoons$ *Pbnm* under compressive conditions. The first phase transition can be shifted to ambient pressure by substitution with larger cations such as Ba^{2+} or K^{+}, and the latter by substitution with smaller cations like Ca^{2+} or Li^{+}. Best agreement with experimental phase diagrams at elevated temperatures (like room temperature and above) is found for the two solid solutions with smaller cations. Compositions at the predicted morphotropic phase boundaries are $(NBT)_{0.85}$-$(CaTiO_3)_{0.15}$ and $(NBT)_{0.75}$-$(Li_{1/2}Bi_{1/2}TiO_3)_{0.25}$, the latter composition marks simultaneously the solid solution limit.
Accordance between experimental phase diagrams and our predicted compositions at the morphotropic phase boundaries in the solid solutions with larger substituting cations is much weaker. We find the compositions at which *R*3*c* and *P*4*mm*-structures are equal in enthalpy to be at $(NBT)_{0.65}$-$(BaTiO_3)_{0.35}$ and for pure $K_{0.5}Bi_{0.5}TiO_3$, which overestimate the fraction of non-NBT end member between three and four times compared to experimental values. This discrepancy can be caused by several facts. First, it is well-known that the local density approximation overestimates bonding, which leads to underestimation of lattice constants and bond lengths and also to overestimation of bulk moduli. This could indeed affect the relative stability of tilted structures towards non-tilted structures, as octahedral tilting leads to a reduction of A-O distances (better bonding) and smaller lattice parameters. Thus, the exchange correlation functional could be one reason for the apparent overestimation of stability of *R*3*c* towards *P*4*mm*-structures. One could try to achieve better results with more sophisticated functionals like PBEsol or hybrid functionals, which are expected to be more reliable in prediction of lattice parameters, but the latter are also much more demanding in terms of computational time. Moreover, we believe that the main reason is not the "primitive" but very efficient exchange correlation functional we used, but the 0 Kelvin limit of this type of calculations.
In a first-principles study by Frantti *et al.*[251] on $PbTiO_3$ it was shown how strongly phonon contributions can influence the pressure of the phase transition *R*3*c* $\rightleftharpoons$ *P*4*mm*. The authors performed phonon calculations of $PbTiO_3$ under pressure in the two structures *R*3*c* and *P*4*mm* and were thus able to study the phase stability as a function of pressure and temperature. They found that phonon contributions to energy and entropy favour *P*4*mm* at elevated temperatures, whereas the pV-term favours the octahedral tilting in *R*3*c*. At elevated temperatures the phase transition pressure from *P*4*mm* to *R*3*c* is shifted towards higher pressures. At 280 K for example the transition pressure is shifted by 2 GPa. Although we did not perform any phonon calculations on our large supercells, it is reasonable to assume that the same holds for our perovskite solid solutions, which show the same lattice instabilities as $PbTiO_3$. A pressure-shift of 2 GPa would reduce our 0 GPa MPB-compositions to 60% of the above reported values.

13.5 Summary

We developed a method based on *ab-initio* supercell calculations which enables us to predict 0 Kelvin morphotropic phase boundaries in A-site mixed NBT-based solid solutions. We could show that this method works for at least two different types of phase transitions, namely $R3c \rightleftharpoons Pbnm$ in $CaTiO_3$ and $Li_{1/2}Bi_{1/2}TiO_3$, which is accompanied by a change of tilt system from $a^-a^-a^-$ to $a^-a^-c^+$ and loss of polarization, and $R3c \rightleftharpoons P4mm$ in $BaTiO_3$ and $K_{1/2}Bi_{1/2}TiO_3$, which is characterized by loss of octahedral tilting and change of polarization direction. The discrepancies between the experimental phase diagrams at room temperature and the predicted ones in the solid solutions with larger substituting cations we attribute to temperature effects.
Moreover, we could show how chemical substitution affects the $a^-a^-a^-$ tilt soft-mode. Substitution by Ca^{2+} has almost no effect on the tilt angle. Similarly, pressure has only minor influence on the size of the tilt angle. Much stronger is the effect of Ba^{2+} substitution. In pure $BaTiO_3$ this tilt-mode is completely suppressed. Without application of pressure the highest possible $BaTiO_3$-fraction where tilts are still soft we found to be at $x = 0.44$.
Finally, we found a way to quantify chemical pressures in NBT-based solid solutions. For end members having larger A-cations than Na^+ and Bi^{3+} chemical pressures correlate perfectly well with the shift experienced by phase transition pressures upon chemical substitution. Chemical pressures induced by smaller A-cation are much smaller than the shifts of transition pressures, for them does not exist such a correlation.

Part IV

Conclusions and Future Work

14 Answers to 13 Specific Questions

1. **Is there any type of chemical order preferred in NBT?**
   Yes, there is a preference for structures with non-stoichiometric layers of Bi and Na in the {001}-planes. Especially, alternating layers of Bi and Na are more stable than any other chemical configuration. In contrast to B-site mixed perovskites, A-site mixed perovskites do not prefer rock-salt order. Rock-salt order is even the least stable chemical configuration of Bi/Na atoms.

2. **What are the driving forces for ordering?**
   The driving force for oxygen displacements and thus stabilization of the layered structures lies in the enhanced charge transfer between Bi and O and enhanced orbital interactions, namely Bi $6sp$-O$2p$ hybridization also known as lone-pair effect.

3. **Can ordering occur under synthesis conditions?**
   Although there is a clear preferred chemically ordered state, the free energy difference to an estimated disordered state is so small, that long-range ordered structures are unlikely to form at elevated temperatures, where ceramics are sintered. However, the preference for non-stoichiometric layers should prevail even in a long-range disordered state, thus we believe that short-range order should be able to develop.

4. **Is it possible to enhance chemical ordering at elevated temperatures?**
   Two different possibilities to enhance chemical ordering in NBT and related compounds where investigated. These are volume change (e.g. by application of pressure) in pure NBT and substitution of Na by other monovalent cations leading to compounds MBT with M=Li, Na, Ag, K, Rb, Tl and Cs. Only the extremely toxic thallium induced significant shifts in the relative stabilities of the different chemical configurations, which should be large enough to allow for ordering at temperatures as high as 1000 K. This finding is probably due to the additional lone-pair effect of the Tl^+ cation with electron configuration $6s^2$.

5. **How does chemical order affect the average and local crystal structure?**
   Different chemical configurations prefer different ground state structures. While more stable configurations with stronger stoichiometric imbalances prefer a *Pbnm*-like structure, the less stable configurations prefer the *R*3*c*-like structure. Thus, the local structure directly affects also the average structure, because *Pbnm* and *R*3*c* are significantly different concerning off-center displacements and octahedral tilting, as in *Pbnm* additional in-phase tilts exist. These in-phase tilts were discussed to be responsible for the change of the average symmetry from *R*3*c* to *Cc*.[103]

6. **Which phases are stable under hydrostatic pressure?**
   In total three different crystal structure types are found in the pressure range between -15 and +25 GPa. Depending on the chemical configuration and the mechanical boundary conditions the phases and transition pressures vary. All configurations adopt under sufficiently high

tensile conditions (p<0 GPa) a polar $P4mm$-like structure. At pressures above +3 GPa the *Pbnm*-like structures are most stable. Only in the intermediate pressure range $R3c$-like and *Pbnm*-like structures coexist. The $P4bm$-like structures do not appear as a ground state, their energies are too high.

7. **Can in-phase tilts be stable in an anti-phase tilted matrix?**
   Yes, in-phase tilts can be stabilized in an anti-phase tilted matrix. In-phase tilted areas can be as small as two or three unit cells (10-15 Å).

8. **How do chemical order and volume affect the different lattice instabilities polarization, octahedral tilting and chemically induced distortions?**
   The lower the symmetry of the chemical order the larger is the number of distortion modes induced in the complexer perovskite structures exhibiting polarization and octahedral tilting. This leads not only to secondary distortion modes, but also to splitting of the polar and tilt modes.
   Polar and tilt modes are oppositely affected by volume changes. Tilts dominate at small volumes/high pressures, while polarization is stronger at large volumes/negative pressures. Chemically induced distortion modes become significant at large volumes, only.

9. **How strongly are the different lattice instabilities coupled to each other?**
   This question cannot be answered in general. The energy surfaces resulting from interactions between different distortion modes result from a fine balance between single mode stabilities and the different types of order parameter coupling. Coupling depends on many factors, first the structure and its symmetry, which determines the possible coupling terms. The values of the coupling coefficients are constrained by the bonding properties in the material studied and can exhibit strong variation with volume. Most of the pairwise mode interactions investigated in this work were found to be competitive, while odd-order coupling always leads to cooperative interactions.

10. **What are the ferroic properties of the phases $R3c$, *Pbnm* and $P4bm$?**
    The rock-salt ordered $R3$ structure is typically ferroelectric. Polarization and anti-phase tilt are not very strongly coupled to each other at the equilibrium volume, thus no triggered ferroelectricity as it was found in $BiFeO_3$ is present. Yet, weak coupling does not mean that polarization and tilt can be changed independently from each other, they are still restricted by symmetry.
    The ferroic properties of the layered $Pmc2_1$-structure depend strongly on the volume. The Landau potential of this structure offers the possibility of improper coupling between polarization and in-phase and anti-phase tilt modes. At small volumes the material indeed shows typical improper characteristics, while at large volumes rather proper ferroelectric behaviour can be expected.
    The ferroic properties of the layered $P4bm$-structures are somehow surprising, as they demonstrate that in contrast to the experimentally observed in-phase tilt, from the bare energetic point of view the by symmetry also allowed anti-phase tilt should be preferred. Both tilts, however, compete so strongly that they exclude each other pairwise. Only the additional

presence of polarization can bring them together. The interaction between polarization and the tilts though depends on volume. It can be strongly competitive, leading to complete suppression of any other distortion mode than the anti-phase tilt at small volumes. Only at larger volumes all distortions are able to coexist. At intermediate volumes an anti-phase tilt dominated structure results, at larger volumes polarization is the strongest mode. Again this 001-ordered structure offers the possibility of improper coupling between polarization and the two tilt modes, but the material has to be considered rather proper ferroelectric, as competitive interactions between the modes are dominating.
The situation in the 111-ordered $P4_2nm$ structures is a bit simpler, as this space group only allows for polarization and in-phase tilt. Both distortion modes are so competitive, that they can only coexist in a narrow intermediate volume range. At smaller volumes only tilts exist and at larger volumes polarization prevails.

11. **Is it possible to predict morphotropic phase boundaries in NBT-based solid solutions based on determination of pressure-induced phase transformations?**
In the presented approach, it is assumed that at the morphotropic phase boundary the average crystal structure undergoes a macroscopic phase transformation. All investigated material systems $(NBT)_{(1-x)}$-$(CaTiO_3)_x$, $(NBT)_{(1-x)}$-$(BaTiO_3)_x$, $(NBT)_{(1-x)}$-$(Li_{1/2}Bi_{1/2}TiO_3)_x$ and $(NBT)_{(1-x)}$-$(K_{1/2}Bi_{1/2}TiO_3)_x$ exhibited the expected phase transitions, but only partly at the compositions as they are reported in literature at room temperature. Taken into account the simplicity of the fast-and-easy supercell approach introduced in this work the results are absolutely satisfactory.

12. **What are the limitations of such a technique?**
There are two major limitations of this technique. The first one is the restriction to 0 Kelvin, which is probably the origin of the large discrepancies between prediction and experiment in case of the material systems exhibiting the phase transition $R3c \rightleftharpoons P4mm$.
The second limitation is the supercell approach itself, since it is questionable if more complex material systems such as $(NBT)_{(1-x-y)}$-$(BaTiO_3)_x$-$((K,Na)NbO_3)_y$ etc., where also the B-site is mixed can be covered that easily. Moreover, a big drawback is, that only phase transitions between structures included in the structure search can be identified, whereas in many cases these structures are unknown.

13. **Can alloying be understood as an analogue to hydrostatic pressure, is chemical pressure something real and quantifiable?**
We developed a technique, to assign chemical pressures to substitution levels. For NBT-based solid solutions where the second end member has larger A-cations than Na^+ and Bi^{3+} we found that the chemical pressures induced at the predicted morphotropic phase boundaries correlate perfectly well with the hydrostatic pressures inducing the same phase transformations.

15 Discussion

This work demonstrates that *ab-initio* calculations are a very versatile tool for investigating systematically material properties that are hard to access via experiments, like driving forces for phase transformations and local structure motifs in chemically mixed perovskites, as well as coupling between different order parameters.

We used supercell calculations to investigate the local structure induced by different types of chemical order and their relative phase stabilities. It was found not only that in $Na_{1/2}Bi_{1/2}TiO_3$ short-range order manifested in Na/Bi separation into layers in $\{001\}$-planes is preferred ('001'-order), but also that these chemically ordered regions induce additional in-phase tilts leading to local *Pmc*2_1 symmetry. Even very small contents of *Pmc*2_1 phase should be stable in a matrix of average *R*3*c*-symmetry. This type of tilt disorder was reported frequently in literature, but its origin was completely unidentified. A possible reason is that chemically ordered regions must be large enough and should not contain too many occupational defects to be detectable by diffraction techniques. We find though, that already small deviations from stoichiometry in the $\{001\}$-planes induce the additional in-phase tilts. No perfect '001'-order is necessary, which anyway from an electrostatic point of view is problematic, as it is the source of local electric fields similar to those in a multilayer plate capacitor.

Under tensile conditions purely polar *P*4*mm*-like structures with large c/a-ratios were found, similar to the super tetragonal perovskite phases under tensile hydrostatic pressure found by Tinte[252] and Moriwake[253] and to the *Cm* phase formed in $BiFeO_3$ thin films if subjected to epitaxial compressive strain.[254,255] [1]

For the study of local structures and relative phase stabilities supercell calculations are ideal, although there is no possibility to access a truly disordered state. Very large unit cells would be necessary to map rather disordered configurations, as periodic boundary conditions render any supercell the smallest unit of a periodically repeated structure motif i.e. a special type of order. This problem is generally avoided by using the virtual crystal approximation (VCA), where the random distribution of atoms on the mixed crystallographic site is approximated by an "intermediate" atom incorporated in the primitive unit cell. This method was successfully applied to solid solutions and compounds, but it is questionable that it would work for $Na_{1/2}Bi_{1/2}TiO_3$, as the cations on the mixed site possess not only different charges, but are also chemically completely different. VCA works the better the more similar the two elements are, which have to be mixed. Only one attempt of modelling the solid solution $(Na_{1/2}Bi_{1/2}TiO_3)_{(1-x)}$-$(BaTiO_3)_x$ by the VCA method can be found in literature[257] which gave rather dubious results.

[1] The epitaxial misfit strain, resulting from the inequality of the lattice parameters of the free standing film a_0 and of the substrate b, $u_m = \frac{b-a_0}{b}$ is defined with respect to the lattice parameter b of the substrate.[256] Compressive epitaxial strain ($b < a_0$) gives $u_m < 0$ and tensile epitaxial strain ($b > a_0$) gives $u_m > 0$.

Moreover, $Na_{1/2}Bi_{1/2}TiO_3$ is a challenging model system to study the interactions between various order parameters, that do not only affect the average crystal structure described by polarization, tilts and spontaneous strain, but also their interplay with chemical order/disorder. Group theoretical tools were applied to characterize and quantify the induced distortion modes in the stable phases of $Na_{1/2}Bi_{1/2}TiO_3$. By constructing Landau potentials for the dominating distortion modes associated with polarization and octahedral tilts, we were able to study the interactions between tilts and polarization in a large variety of structures. The coefficients of the Landau potentials not only vary from phase to phase, but also depend crucially on the chemical configuration and volume or pressure. It was found that the chemically ordered regions with $Pmc2_1$ in fact should be rather improper ferroelectric than antiferroelectric. The same might be true for the high-pressure *Pbnm*-phase. Chemical disorder breaks the inversion symmetry and allows for local polar order. Measurements of polarization under pressure are difficult to realize, but measurements of Second Harmonic Generation (SHG) should be accomplishable.

Finally, we developed a very simple technique for the prediction of composition-induced phase transitions on the basis of pressure-induced phase transitions, which in principle can be used to predict morphotropic phase boundaries in solid solutions. Shortcomings of the technique are the limited supercell size, which restricts us to pseudo-binary solid solutions, the trivial fact, that crystal structures, which were not included in the search cannot be found, and the limitation of standard DFT calculations to 0 Kelvin.

All approaches are completely transferable to other mixed perovskite compounds and solid solutions. We hope that our results stimulate further theoretical and experimental studies of $Na_{1/2}Bi_{1/2}TiO_3$ and other relaxor materials.
There are still plenty of open questions concerning the response properties of the chemically ordered configurations and the origin of the relaxor behaviour in $Na_{1/2}Bi_{1/2}TiO_3$. In the last section we want to give an overview of open questions and suitable computational techniques to obtain their answers.

16 Outlook

This work dealt with the basic questions concerning the relaxor ferroelectric NBT. We treated the questions of chemical ordering tendency and phase stabilities under variation of pressure and composition in NBT-based solid solutions. Moreover, we investigated the different stable phases in terms of symmetry and order parameter coupling.

There exist still plenty of open questions about this complex material to be answered in the future. We want to divide the problems into two groups, the first group concerns properties accessible by *ab-initio* calculations and the second group treats high-temperature large-length-scale properties, which are only accessible by development of an effective Hamiltonian, which can be used either for Monte Carlo or Molecular Dynamics simulations.

Ab-initio Calculations

Linear-response DFT calculations make physical properties of piezoelectric materials accessible by *ab-initio* calculations, such as polarization, phase stability in an applied electric field or electromechanical response coefficients.[258–262]
Another field are defect calculations in large supercells, which can give insights into the intrinsic stability of a material towards point defect formation and non-stoichiometries under certain experimental conditions, but also into the stability of extrinsic point defects resulting from doping and their tendency to form defect dipoles.[263–266]
Typical questions, that can be answered by these techniques are:

- What is the origin of the field-induced phase transition $Cc \rightarrow R3c$ observed in pure NBT?
- Can intrinsic electromechanical coupling explain the high strains in NBT-based solid solutions?
- How does doping relate to the effect of alloying?
- What are the dominating intrinsic point defects in NBT and do they preferentially accumulate in the ordered or in the disordered regions?
- How does the incorporation of larger A-cations like Ba^{2+} change the nanostructure of NBT?

Effective Hamiltonian

An effective Hamiltonian can be used in combination with both Monte Carlo[267–269] or Molecular Dynamics[87,89,270] simulations to either access thermodynamic and/or kinetic properties of a material.
Typical questions, that can be answered by such approaches are:

- Can chemically ordered nanoregions really develop under synthesis conditions and how perfect is the order?
- Which phase transitions evolve with temperature?
- What stabilizes the *P*4*bm* phase at high temperatures?
- What is the origin of the relaxor behaviour?
- Which relaxor model describes NBT better, bulky polar nanoregions in a nonpolar matrix or polar nanodomains separated by domain walls with different response properties?
- Are chemically ordered and polar nanoregions spatially correlated?

The results of our study of order parameter coupling, however, showed how difficult the development of a suitable Hamiltonian for this very complex material will be. NBT is a material, that exhibits not only different tilt and polar distortions accompanied by spontaneous strains, but also chemical order/disorder, which influences strongly the relative phase stabilities and local displacive disorder. The nanostructure and physical properties are the result of interactions of all these different order parameters. A vital example for the difficulties one can meet, is the structure optimization of the 001-ordered *P*4*bm* structure, resulting from the interaction of three different order parameters. We found several different structures by relaxation, which all fulfil the condition of representing a minimum of residual forces acting on the atoms, yet the amplitudes of the order parameters show strong variations. In fact, the structural optimization, an absolute standard method employed in DFT calculations, was not reliable to give the lowest energy structure within given symmetry constraints in this case. Different starting configurations lead to different local minima in configuration space, which is a very non-satisfying situation. This might be a general problem in the structural optimization of materials with several lattice instabilities.

Part V

Appendix

A Convergence Tests for DFT Calculations

The convergence of total energies and forces with respect to the cutoff energy and the k-point mesh were tested prior to performing calculations. The results are shown here.
Moreover, the Bader analysis requires a convergence test of the Bader charges with respect to the FFT-mesh.

DFT-Calculations

Cutoff Energy

The cutoff energy `ENCUT` determines the number of plane waves used and has thus direct influence on the quality of the wave functions and thus on the accuracy of the total energies and forces. Fig. A.1 shows total energies of '001' and '111' ordered cubic NBT diminished by the values obtained at a cutoff of 1000 eV. At 600 eV, the absolute energies are converged up to 3 meV/atom in both structures. The convergence of absolute energies is only important if structures containing different elements are compared with each other. Within this work we only compare different structures containing the same elements, thus convergence of the energy difference is decisive. The convergence of the energy difference between '001' and '111' order is one order of magnitude better than that of the absolute values. For the total energies we can assume that the accuracy is better than 0.1 meV/atom for energy cutoffs higher than 450 eV ($8\times8\times8$ Monkhorst-Pack mesh).

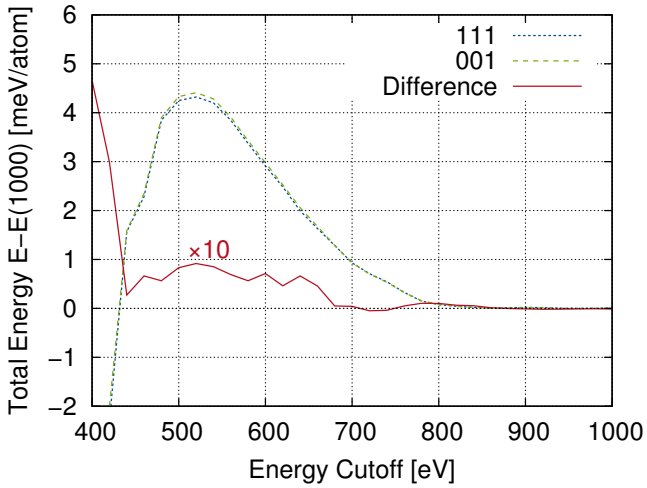

Figure A.1: Convergence of the absolute energies and energy differences with the cutoff energy for '001' and '111' ordered NBT. ($8 \times 8 \times 8$ Monkhorst-Pack mesh)

The effect of the energy cutoff on the forces was tested in '001' ordered NBT, where the Bi atom was displaced by 0.01 Å along the z-axis. The displacement causes forces acting on all atoms in the unit cell, monitored was the force on the Bi atom only. The development of the force with increasing cutoff energy is presented in Fig. A.2. There cannot be seen any obvious trend, the force is oscillating with an amplitude of about 0.1 meV/Å. Any cutoff energy higher than 450 eV is as good as another.

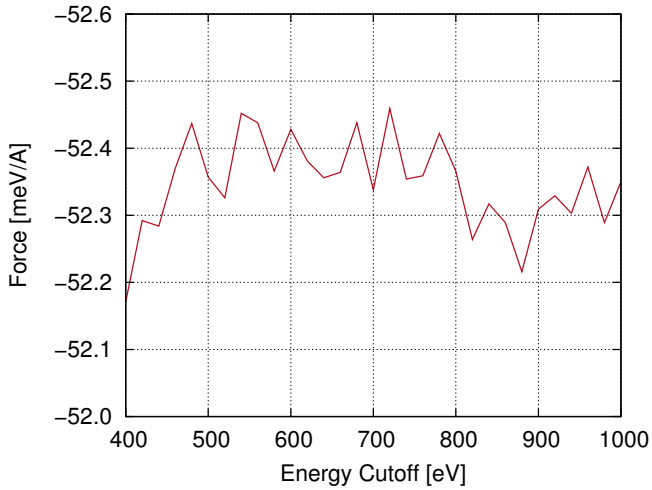

Figure A.2: Convergence of the force with the cutoff energy for the Bi atom in '001' ordered NBT displaced by 0.01 Å from its ideal position along the z-axis. ($8 \times 8 \times 8$ Monkhorst-Pack mesh)

However, we chose an energy cutoff of 600 eV, which is a good compromise between high accuracy and not too high computation time costs.

k-Point Mesh

The other quantity to be tested for convergence is the *k*-point mesh used for the reciprocal space integration. VASP can generate automatically two different types of *k*-point meshes, Monkhorst-Pack and Γ-centred Monkhorst-Pack. For odd numbers of *k*-points both meshes are identical. Another variable is the number of *k*-points or the density of the mesh. In Fig. A.3 the total energies are shown and how they change with the type and density of the *k*-point mesh. For meshes equivalent to more than $8 \times 8 \times 8$ *k*-points in the 5-atom perovskite unit cell, there is almost no difference between the two types. As NBT is not metallic, also the mesh density is not crucial. An $8 \times 8 \times 8$ mesh is sufficient for an accuracy better than 0.1 meV/atom.

How about the forces? The forces are shown in Fig. A.4, they vary within 0.4 meV/Å for the Monkhorst-Pack mesh and 0.15 meV/Å for the Γ-centred mesh, though no convergence can be observed with increasing numbers of *k*-points. Thus, the *k*-point meshes have little impact on the accuracy of the calculations, as long as a sufficient number of points is chosen. Another important factor, however, is the rate, at which electronic convergence is achieved. It was found,

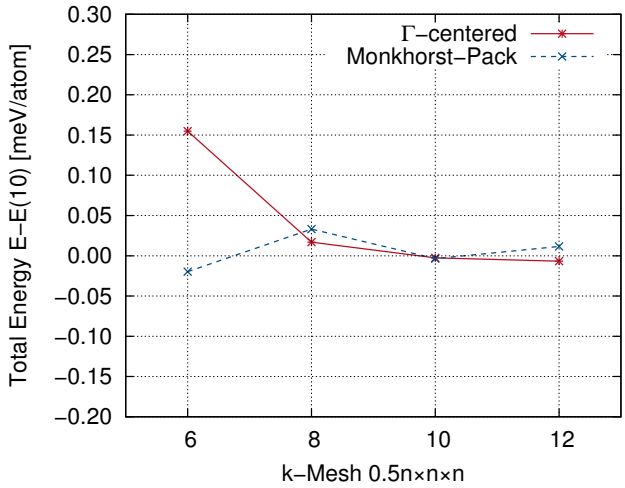

Figure A.3: Convergence of the absolute energies with respect to the *k*-point mesh for '001' ordered NBT. (ENCUT=800 eV)

that the tetragonal $P4mm$-like structures exhibit convergence problems, if not calculated with the Monkhorst-Pack mesh, while calculations of hexagonal structures show better performance with Γ-centred meshes.

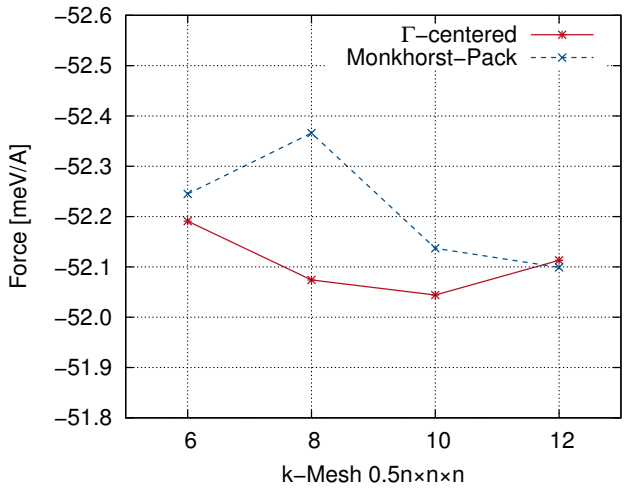

Figure A.4: Convergence of the force with respect to the *k*-point mesh for the Bi atom in '001' ordered NBT displaced by 0.01 Å from its ideal position along the z-axis. (ENCUT=800 eV)

Bader Analysis

For the Bader analysis the convergence of the Bader charges with the FFT-mesh has to be tested. The FFT-mesh is adapted in VASP by setting the parameters `NGXF`, `NGYF` and `NGZF`. In Fig. A.5 the convergence of the absolute charges relative to the value of the chosen mesh of $300 \times 300 \times 300$ points in '001' and '111' ordered NBT are shown. The accuracy limit for the absolute charges is about $0.01e$. We are primarily interested in charge differences between different chemical configurations and not in absolute charges, so it is more important to compare these Bader charge differences. In Fig. A.6 Bader charge differences between atoms in '001' and '111' ordered NBT are shown. The accuracy limit improves to $0.005e$ for a mesh of $300 \times 300 \times 300$.

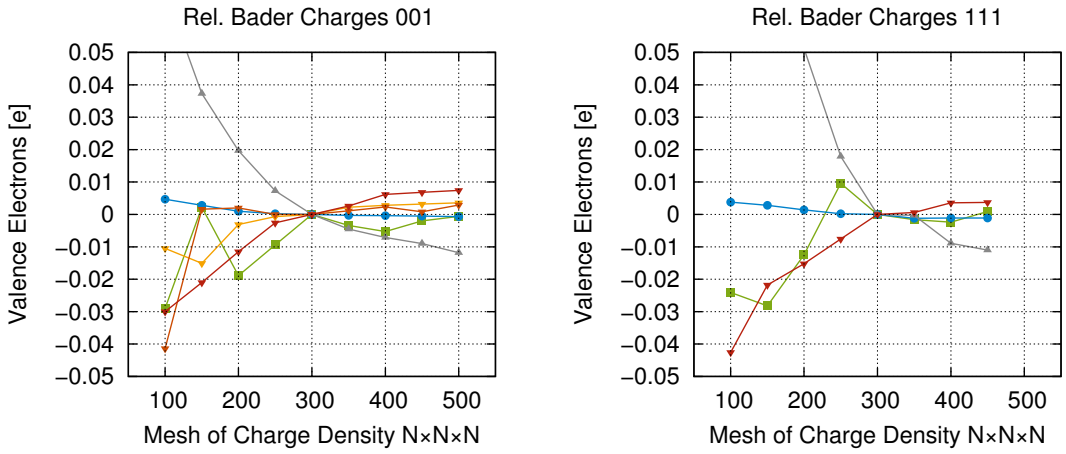

Figure A.5: Convergence of the absolute Bader charges with respect to the FFT-mesh in '001' and '111' ordered NBT. Colours correspond to the different atom types: Bi (green), Na (blue), Ti (grey) and O (yellow/orange/red).

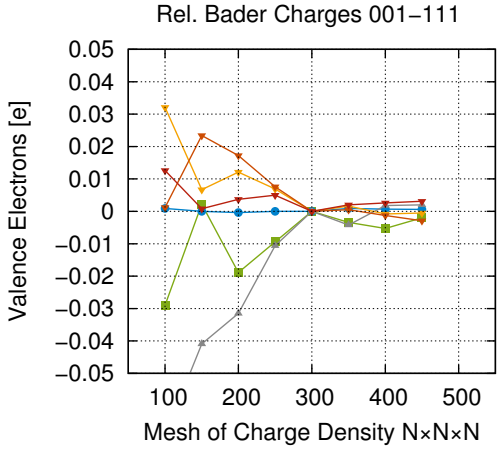

Figure A.6: Convergence of the Bader charges between atoms of the same elements in '001' and '111' ordered NBT. Given are differences in the numbers of valence electrons with respect to the FFT-mesh.

B Symmetry Adapted Distortion Modes in Chemically Ordered MBT

Atomic displacements associated with the chemically induced distortion modes in the chemically ordered structures of MBT with M=Li, Na, Ag, K, Rb, Tl and Cs are given in Fig. B.1.

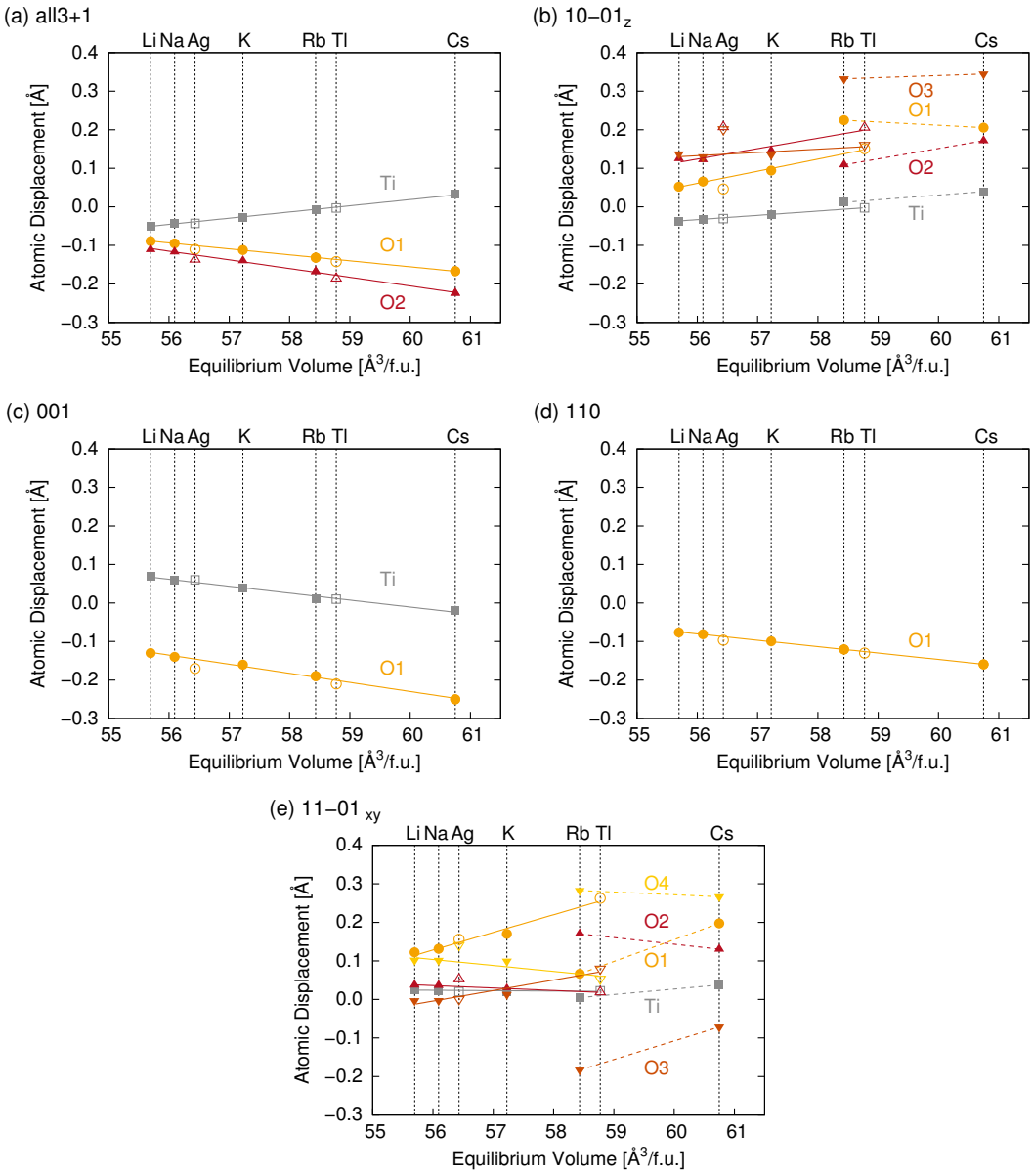

Figure B.1: Atomic displacements associated with the chemically induced distortion modes in compounds MBT with M=Li, Na, Ag, K, Rb, Tl and Cs.

C Equation of State

All energies were fitted to the 3rd order Birch-Murnaghan Equation of State given in Eq. 6.11. In the following tables, the fit-parameters E_0, V_0, B_0 and B_0' of all structures are given as optimized in the strain-free and stress-free regime.

Strain-free Structure Optimization

Table C.1: 111-order

Structure	Symbol	Space group	E_0 [eV]	V_0 [Å^3/f.u.]	B_0 [GPa]	B_0'
*R*3*c*-like	$x_+^- y_+^- z_+^-$	*R*3	-41.251	56.313	144.3	6.52
R$\bar{3}$*c*-like	$x_o^- y_o^- z_o^-$	*R*32	-41.164	55.291	193.8	4.23
Pbnm-like	$x_-^- y_-^- z_o^+$	*Pmn*2_1	-41.235	55.222	155.7	8.19
P4_2*/nmc*-like	$x_o^+ y_o^+ z_-^-$	*P*$\bar{4}$*m*2	-41.183	55.265	184.0	4.95
Im$\bar{3}$-like	$x_o^+ y_o^+ z_o^+$	*Pm*$\bar{3}$	-41.102	55.287	196.4	4.17
*P*4*mm*-like	$x_o^o y_o^o z_+^o$	*I*4*mm*	-41.113	58.026	142.8	5.93
*R*3*m*-like	$x_+^o y_+^o z_+^o$	*R*3*m*	-41.104	57.942	142.3	6.37
Pm$\bar{3}$*m*-like	$x_o^o y_o^o z_o^o$	*Fm*$\bar{3}$*m*	-40.842	56.084	205.4	4.38

Table C.2: 110-order

Structure	Symbol	Space group	E_0 [eV]	V_0 [Å^3/f.u.]	B_0 [GPa]	B'
*R*3*c*-like	$x_+^- y_+^- z_+^-$	*Pc*	-41.271	56.584	142.9	6.81
R$\bar{3}$*c*-like	$x_o^- y_o^- z_o^-$	*P*2*/c*	-41.211	55.472	193.6	4.40
Pbnm-like	$x_-^- y_-^- z_o^+$(1)	*P*2_1*/m*	-41.248	55.315	185.0	4.67
Pbnm-like	$x_-^- y_-^- z_o^+$(2)	*P*2_1*/m*	-41.220	55.366	183.4	5.06
P4_2*/nmc*-like	$x_o^+ y_o^+ z_-^-$(1)	*P*4_2*/nmc*	-41.203	55.126	172.4	6.52
P4_2*/nmc*-like	$x_o^+ y_o^+ z_-^-$(2)	*P*4_2*/nmc*	-41.164	55.882	197.5	4.04
P4_2*/nmc*-like	$x_o^+ y_o^+ z_-^-$(3)	*Pmnm*	-41.208	55.512	183.9	5.32
Im$\bar{3}$-like	$x_o^+ y_o^+ z_o^+$(1)	*Immm*	-41.188	55.371	184.3	4.76
Im$\bar{3}$-like	$x_o^+ y_o^+ z_o^+$(2)	*Immm*	-41.188	55.372	184.4	4.73
*P*4*mm*-like	$x_o^o y_o^o z_+^o$(1)	*P*4*mm*	-41.131	58.037	143.9	5.99
*P*4*mm*-like	$x_o^o y_o^o z_+^o$(2)	*Amm*2	-41.202	58.035	147.4	5.94
*R*3*m*-like	$x_+^o y_+^o z_+^o$	*Pm*	-41.158	58.052	141.0	6.26
Pm$\bar{3}$*m*-like	$x_o^o y_o^o z_o^o$	*P*4*/mmm*	-40.945	56.427	202.7	4.32

Table C.3: $11-01$-order

Structure	Symbol	Space group	E_0 [eV]	V_0 [Å^3/f.u.]	B_0 [GPa]	B'
*R*3*c*-like	$x_+^- y_+^- z_+^-$	*P*1	-41.275	56.418	146.3	7.18
R$\bar{3}$*c*-like	$x_o^- y_o^- z_o^-$	*C*2	-41.196	55.457	187.8	5.19
Pbnm-like	$x_-^- y_-^- z_o^+$(1)	*Pm*	-41.259	55.518	157.5	6.75
Pbnm-like	$x_-^- y_-^- z_o^+$(2)	*Pm*	-41.258	55.384	172.2	5.45
*P*4*mm*-like	$x_o^o y_o^o z_+^o$(1)	*Pmm*2	-41.166	58.008	145.3	5.95
*P*4*mm*-like	$x_o^o y_o^o z_+^o$(2)	*Pmm*2	-41.166	58.009	145.3	5.95
*R*3*m*-like	$x_+^o y_+^o z_+^o$	*Cm*	-41.149	57.964	149.0	5.23
Pm$\bar{3}$*m*-like	$x_o^o y_o^o z_o^o$	*P*4/*mmm*	-40.949	56.355	201.8	4.42

Table C.4: $10-01$-order

Structure	Symbol	Space group	E_0 [eV]	V_0 [Å^3/f.u.]	B_0 [GPa]	B'
*R*3*c*-like	$x_+^- y_+^- z_+^-$	*Cc*	-41.286	56.402	143.3	6.91
R$\bar{3}$*c*-like	$x_o^- y_o^- z_o^-$	*Cc*	-41.241	55.845	158.0	6.99
Pbnm-like	$x_-^- y_-^- z_o^+$(1)	*Pm*	- 41.274	55.559	156.8	7.01
Pbnm-like	$x_-^- y_-^- z_o^+$(2)	*Pm*	-41.305	56.087	133.7	7.36
*P*4$_2$*/nmc*-like	$x_o^+ y_o^+ z_-^-$(1)	*P*4$_2$*mc*	-41.247	55.383	186.8	3.89
*P*4$_2$*/nmc*-like	$x_o^+ y_o^+ z_-^-$(2)	*Pmm*2	-41.252	55.082	212.0	2.65
*P*4$_2$*/nmc*-like	$x_o^+ y_o^+ z_-^-$(3)	*Pmm*2	-41.227	55.545	194.2	4.83
Im$\bar{3}$-like	$x_o^+ y_o^+ z_o^+$(1)	*Pmmm*	-41.212	55.572	184.1	3.64
Im$\bar{3}$-like	$x_o^+ y_o^+ z_o^+$(2)	*Pmmm*	-41.212	55.547	183.8	4.05
Im$\bar{3}$-like	$x_o^+ y_o^+ z_o^+$(3)	*Pmmm*	-41.212	55.575	186.2	4.01
*P*4*mm*-like	$x_o^o y_o^o z_+^o$(1)	*P*4$_2$*mc*	-41.213	58.026	148.6	5.65
*P*4*mm*-like	$x_o^o y_o^o z_+^o$(2)	*Pmm*2	-41.139	57.682	151.0	6.13
*R*3*m*-like	$x_+^o y_+^o z_+^o$	*Cc*	-41.161	57.910	152.2	4.81
Pm$\bar{3}$*m*-like	$x_o^o y_o^o z_o^o$	*P*4$_2$*/mmc*	-41.001	56.408	201.6	4.42

Table C.5: all$3+1$-order

Structure	Symbol	Space group	E_0 [eV]	V_0 [Å^3/f.u.]	B_0 [GPa]	B'
*R*3*c*-like	$x_+^- y_+^- z_+^-$	*R*3	-41.291	56.182	141.6	7.46
R$\bar{3}$*c*-like	$x_o^- y_o^- z_o^-$	*R*32	-41.251	55.403	191.2	4.40
Pbnm-like	$x_-^- y_-^- z_o^+$	*Pm*	-41.302	55.398	164.2	6.01
*P*4$_2$*/nmc*-like	$x_o^+ y_o^+ z_-^-$	*P*$\bar{4}$*m*2	-41.234	55.340	189.7	5.04
*P*4$_2$*/nmc*-like	$x_o^+ y_o^+ z_-^-$	*Pmm*2	-41.268	55.415	168.8	7.15
Im$\bar{3}$-like	$x_o^+ y_o^+ z_o^+$(1)	*Pm*$\bar{3}$	-41.235	55.568	191.3	4.00
Im$\bar{3}$-like	$x_o^+ y_o^+ z_o^+$(2)	*Pmmm*	-41.178	55.468	195.0	4.44
*P*4*mm*-like	$x_o^o y_o^o z_+^o$	*P*4*mm*	-41.137	57.659	150.2	6.11
*R*3*m*-like	$x_+^o y_+^o z_+^o$	*R*3*m*	-41.155	57.801	146.1	6.41
Pm$\bar{3}$*m*-like	$x_o^o y_o^o z_o^o$	*Pm*$\bar{3}$*m*	-40.998	56.303	202.4	4.45

Table C.6: 001-order

Structure	Symbol	Space group	E_0 [eV]	V_0 [Å^3/f.u.]	B_0 [GPa]	B'
*R*3*c*-like	$x_+^- y_+^- z_+^-$	*Pc*	-41.312	56.209	143.7	6.75
R$\bar{3}$*c*-like	$x_o^- y_o^- z_o^-$	*P*2/*c*	-41.276	55.450	184.2	5.28
Pbnm-like	$x_-^- y_-^- z_o^+$(1)	*Pmc*2_1	-41.343	55.736	144.2	7.24
Pbnm-like	$x_-^- y_-^- z_o^+$(2)	*P*2_1/*m*	-41.318	55.405	166.3	5.81
P4_2/*nmc*-like	$x_o^+ y_o^+ z_-^-$(1)	*P*$\bar{4}$*m*2	-41.286	55.731	171.1	4.80
P4_2/*nmc*-like	$x_o^+ y_o^+ z_-^-$(2)	*Pmm*2	-41.279	55.343	183.0	5.13
Im$\bar{3}$-like	$x_o^+ y_o^+ z_o^+$	*Pmmm*	-41.221	55.618	190.3	4.09
*P*4*mm*-like	$x_o^o y_o^o z_+^o$(1)	*P*4*mm*	-41.046	56.647	173.5	6.53
*P*4*mm*-like	$x_o^o y_o^o z_+^o$(2)	*Pmm*2	-41.220	57.954	147.4	5.94
*R*3*m*-like	$x_+^o y_+^o z_+^o$	*Cm*	-41.204	57.735	154.3	5.84
Pm$\bar{3}$*m*-like	$x_o^o y_o^o z_o^o$	*P*4/*mmm*	-41.040	56.390	203.0	4.34

Stress-free Structure Optimization

Table C.7: 111-order

Structure	Symbol	Space group	E_0 [eV]	V_0 [Å^3/f.u.]	B_0 [GPa]	B_0'
*R*3*c*-like	$x_+^- y_+^- z_+^-$	*R*3	-41.254	56.465	135.1	6.56
Pbnm-like	$x_-^- y_-^- z_o^+$	*Pmn*2$_1$	-41.243	55.329	154.0	7.59
*P*4*bm*-like	$x_o^o y_o^o z_+^+$	*P*4$_2$*nm*	-41.114	55.754	126.2	10.35
*P*4*mm*-like	$x_o^o y_o^o z_+^o$	*I*4*mm*	-41.148	58.524	124.7	6.50
*R*3*m*-like	$x_+^o y_+^o z_+^o$	*R*3*m*	-41.112	58.103	134.1	6.97
Pm$\bar{3}$*m*-like	$x_o^o y_o^o z_o^o$	*Fm*$\bar{3}$*m*	-40.841	56.083	205.2	4.39

Table C.8: 001-order

Structure	Symbol	Space group	E_0 [eV]	V_0 [Å^3/f.u.]	B_0 [GPa]	B'
*R*3*c*-like	$x_+^- y_+^- z_+^-$	*Pc*	-41.316	56.351	135.4	6.71
Pbnm-like	$x_-^- y_-^- z_o^+$(1)	*Pmc*2$_1$	-41.349	55.792	139.5	7.88
Pbnm-like	$x_-^- y_-^- z_o^+$(2)	*P*2$_1$/*m*	-41.325	55.427	170.4	5.03
*P*4*bm*-like	$x_o^o y_o^o z_+^+$(1)	*P*4*bm*	-41.195	55.441	192.3	4.17
*P*4*bm*-like	$x_o^o y_o^o z_+^+$(2)	*Pmm*2	-41.228	55.494	187.5	4.04
*P*4*mm*-like	$x_o^o y_o^o z_+^o$(1)	*P*4*mm*	-41.053	56.763	166.4	6.56
*P*4*mm*-like	$x_o^o y_o^o z_+^o$(2)	*Pmm*2	-41.249	58.429	127.0	6.91
*R*3*m*-like	$x_+^o y_+^o z_+^o$	*Cm*	-41.215	57.984	139.7	7.40
Pm$\bar{3}$*m*-like	$x_o^o y_o^o z_o^o$	*P*4/*mmm*	-41.039	56.388	202.5	4.41

D Structural Parameters

In the following the crystallographic data of the optimized equilibrium structures of the *Pm*$\bar{3}$*m*-like, *R*3*c*-like, *Pbnm*-like and *P*4*mm*/*P*4*bm*-like phases are given.

Fm$\bar{3}$*m* Subgroup

Fm$\bar{3}$*m*

Crystallographic data in the cubic setting

a_c (Å)	5.40296
b_c (Å)	5.40296
c_c (Å)	13.39703
α (°)	90
β (°)	90
γ (°)	90
V (Å^3)	338.691
Z	8

Fractional coordinates

Atom	Wyckoff	x	y	z
Bi	4a	0.00000	0.00000	0.00000
Na	4b	0.50000	0.50000	0.50000
Ti	8c	0.25000	0.25000	0.25000
O	24d	0.00000	0.25000	0.25000

*R*3

Crystallographic data in the hexagonal setting

a_{h} (Å)	5.40296
b_{h} (Å)	5.40296
c_{h} (Å)	13.39703
α (°)	90
β (°)	90
γ (°)	120
V (Å^3)	338.691
Z	6

Fractional coordinates

Atom	Wyckoff	x	y	z
Bi	$1a$	0.00000	0.00000	0.03325
Na	$1a$	0.00000	0.00000	-0.47480
Ti1	$1a$	0.00000	0.00000	0.26565
Ti2	$1a$	0.00000	0.00000	-0.23676
O1	$3b$	-0.43368	-0.43664	0.00085
O2	$3b$	-0.22494	0.09632	0.16270

Pmn2_1

Crystallographic data

a_o (Å)	7.57758
b_o (Å)	5.45578
c_o (Å)	5.35335
α (°)	90
β (°)	90
γ (°)	90
V (Å^3)	221.317
Z	4

Fractional coordinates

Atom	Wyckoff	x	y	z
Bi	$2a$	0.00000	-0.19863	-0.01829
Na	$2a$	0.00000	0.27832	-0.49776
Ti	$4b$	-0.25229	-0.25932	0.49044
O1.1	$4b$	-0.29055	-0.03158	0.22360
O1.2	$4b$	-0.20783	-0.45809	-0.20521
O2	$2a$	0.00000	-0.26892	0.42257
O3	$2a$	0.00000	0.23516	0.07584

I4mm

Crystallographic data

a_t (Å)	5.38331
b_t (Å)	5.38331
c_t (Å)	8.11430
α (°)	90
β (°)	90
γ (°)	90
V (Å^3)	235.153
Z	4

Fractional coordinates

Atom	Wyckoff	x	y	z
Bi	$2a$	0.00000	0.00000	0.07285
Na	$2a$	0.00000	0.00000	-0.44447
Ti	$4b$	0.00000	0.50000	-0.21878
O1	$8c$	-0.24284	-0.24284	0.23684
O2	$4b$	0.00000	0.50000	0.49840

*P*4/*mmm* Subgroup

*P*4/*mmm*

Crystallographic Data

a_t (Å)	3.83467
b_t (Å)	3.83467
c_t (Å)	7.66933
α (°)	90
β (°)	90
γ (°)	90
V (Å^3)	112.775
Z	2

Fractional coordinates

Atom	Wyckoff	x	y	z
Bi	$1a$	0.00000	0.00000	0.00000
Na	$1b$	0.00000	0.00000	0.50000
Ti	$2h$	0.50000	0.50000	0.25693
O1	$4i$	0.00000	0.50000	0.76802
O2	$1c$	0.50000	0.50000	0.00000
O3	$1d$	0.50000	0.50000	0.50000

Pc

Crystallographic data

a_{m} (Å)	7.68270
b_{m} (Å)	5.40094
c_{m} (Å)	5.44361
α (°)	90
β (°)	90.677
γ (°)	90
V (Å^3)	225.861
Z	4

Fractional coordinates

Atom	Wyckoff	x	y	z
Bi	$2a$	0.01504	-0.25440	-0.06569
Na	$2a$	-0.47066	-0.25209	-0.04760
Ti1	$2a$	0.27352	0.24452	-0.01874
Ti2	$2a$	-0.25334	0.24575	-0.03674
O1.1	$2a$	0.27665	-0.04613	-0.20258
O1.2	$2a$	0.20784	-0.47474	0.22887
O1.3	$2a$	-0.27424	0.01289	-0.27663
O1.4	$2a$	-0.20550	0.48629	0.25220
O2	$2a$	0.00454	0.18214	0.01766
O3	$2a$	-0.49587	0.31757	-0.00675

Pmc2_1

Crystallographic data

a_o (Å)	7.70955
b_o (Å)	5.34132
c_o (Å)	5.41943
α (°)	90
β (°)	90
γ (°)	90
V (Å^3)	223.168
Z	4

Fractional coordinates

Atom	Wyckoff	x	y	z
Bi	$2a$	0.00000	0.24473	-0.05438
Na	$2b$	0.50000	0.24584	0.00861
Ti	$4c$	-0.26348	-0.25652	-0.01175
O1.1	$4c$	0.00000	-0.32278	0.02559
O1.2	$4c$	0.50000	-0.18718	-0.01318
O2	$2a$	-0.27379	0.45107	-0.19635
O3	$2b$	-0.20650	0.03479	0.22478

$P2_1/m$

Crystallographic data

a_m (Å)	7.69367
b_m (Å)	7.60100
c_m (Å)	7.58324
α (°)	90
β (°)	89.129
γ (°)	90
V (Å^3)	443.413
Z	8

Fractional coordinates

Atom	Wyckoff	x	y	z
Bi1	$2e$	0.02421	0.25000	0.02590
Bi2	$2e$	0.03006	0.25000	-0.48561
Na1	$2e$	-0.48737	0.25000	0.01301
Na2	$2e$	-0.49034	0.25000	-0.48020
Ti1	$4f$	0.26425	-0.49683	0.25087
Ti2	$4f$	0.26368	-0.49464	-0.25100
O1.1	$4f$	0.27828	0.45395	0.49921
O1.2	$4f$	-0.20294	0.47176	0.00016
O1.3	$4f$	0.00130	-0.46032	-0.28934
O1.4	$4f$	-0.49973	-0.46241	0.21262
O2.1	$2e$	0.29076	0.25000	0.27868
O2.2	$2e$	0.27040	0.25000	0.20253
O3.1	$2e$	-0.21821	0.25000	-0.29068
O3.2	$2e$	0.19999	0.25000	-0.22105

P4mm

Crystallographic data

a_t (Å)	3.81792
b_t (Å)	3.81792
c_t (Å)	7.78823
α (°)	90
β (°)	90
γ (°)	90
V (Å^3)	113.525
Z	2

Fractional coordinates

Atom	Wyckoff	x	y	z
Bi	$1a$	0.00000	0.00000	-0.02571
Na	$1a$	0.00000	0.00000	0.44328
Ti	$1b$	0.50000	0.50000	-0.27828
Ti	$1b$	0.50000	0.50000	0.23655
O1.1	$2c$	0.50000	0.00000	-0.23182
O1.2	$2c$	0.50000	0.00000	0.23335
O2	$1b$	0.50000	0.50000	-0.00735
O3	$1b$	0.50000	0.50000	0.49346

*Pmm*2

Crystallographic data

a_o (Å)	3.79200
b_o (Å)	7.70400
c_o (Å)	4.00012
α (°)	90
β (°)	90
γ (°)	90
V (Å^3)	116.858
Z	2

Fractional coordinates

Atom	Wyckoff	x	y	z
Bi	$1a$	0.00000	0.00000	0.13032
Na	$1b$	0.00000	0.50000	0.10508
Ti	$2h$	0.50000	0.26124	-0.44242
O1.1	$2g$	0.00000	0.23086	0.48013
O1.2	$2h$	0.50000	0.24536	0.00112
O2	$1c$	0.50000	0.00000	0.45511
O3	$1d$	0.50000	0.50000	-0.49817

E Unit Cell Transformations

Transformation of the Basis Vectors and the Atomic Coordinates

When studying crystal structures in terms of symmetry-adapted distortion modes it is necessary to express crystal structures in non-conventional settings. The transformation from one unit cell setting to another one can be described by matrices. Details can be found for example in the *International Tables of Crystallography Vol. A*.[224] The crystal structure itself stays at rest, while the basis vectors of the unit cell and the atomic coordinates are changed. The transformation of the basis vectors of the initial unit cell $(\mathbf{a}, \mathbf{b}, \mathbf{c})$ into those of the new cell setting $(\mathbf{a}', \mathbf{b}', \mathbf{c}')$ is represented by the transformation $(\boldsymbol{P}, \boldsymbol{p})$. It consists of the linear part $\boldsymbol{P}$, which indicates a change of the orientation and/or length of the basis vectors and is described by a (3×3)-matrix, and a shift of origin $\boldsymbol{p}$, described by a (3×1) column matrix. The transformation $(\mathbf{a}, \mathbf{b}, \mathbf{c}) \rightarrow (\mathbf{a}', \mathbf{b}', \mathbf{c}')$ is then given by

$$(\mathbf{a}', \mathbf{b}', \mathbf{c}') = (\mathbf{a}, \mathbf{b}, \mathbf{c})\boldsymbol{P} + \boldsymbol{p} \tag{E.1}$$

The transformation of the atomic coordinates is achieved by applying the inverse matrices of $\boldsymbol{P}$ and $\boldsymbol{p}$ on the coordinates in the initial setting. They are

$$\boldsymbol{Q} = \boldsymbol{P}^{-1} \tag{E.2}$$

and

$$\boldsymbol{q} = -\boldsymbol{P}^{-1}\boldsymbol{p} \tag{E.3}$$

The transformation $x, y, z \rightarrow x', y', z'$ is given by $(\boldsymbol{Q}, \boldsymbol{q})$

$$\begin{pmatrix} x' \\ y' \\ z' \end{pmatrix} = \boldsymbol{Q} \begin{pmatrix} x \\ y \\ z \end{pmatrix} + \boldsymbol{q} \tag{E.4}$$

The volume of the initial unit cell V and the volume of the new unit cell V' obey the following relationship

$$V' = \det \boldsymbol{P} V \tag{E.5}$$

In the following the transformations $(\boldsymbol{P}, \boldsymbol{p})$ and $(\boldsymbol{Q}, \boldsymbol{q})$ are reproduced, which were applied in this work. They were all obtained with the aid of STRUCTURE RELATIONS, available on the *Bilbao Crystallographic Server*.[226,227]

Transformation Matrices

$Fm\bar{3}m \rightarrow R3$

$$\boldsymbol{P} = \begin{pmatrix} -1/2 & 0 & 1 \\ 0 & -1/2 & -1 \\ 1/2 & -1/2 & 1 \end{pmatrix}, \boldsymbol{p} = \begin{pmatrix} 0 \\ 0 \\ 0 \end{pmatrix} \tag{E.6}$$

$$\boldsymbol{Q} = \begin{pmatrix} -4/3 & -2/3 & 2/3 \\ -2/3 & -4/3 & -2/3 \\ 1/3 & -1/3 & 1/3 \end{pmatrix}, \boldsymbol{q} = \begin{pmatrix} 0 \\ 0 \\ 0 \end{pmatrix} \tag{E.7}$$

$Fm\bar{3}m \rightarrow Pmn2_1$

$$\boldsymbol{P} = \begin{pmatrix} 0 & 1/2 & 1/2 \\ 0 & -1/2 & 1/2 \\ 1 & 0 & 0 \end{pmatrix}, \boldsymbol{p} = \begin{pmatrix} -1/8 \\ -3/8 \\ 1/2 \end{pmatrix} \tag{E.8}$$

$$\boldsymbol{Q} = \begin{pmatrix} 0 & 0 & 1 \\ 1 & -1 & 0 \\ 1 & 1 & 0 \end{pmatrix}, \boldsymbol{q} = \begin{pmatrix} -1/2 \\ -1/4 \\ 1/2 \end{pmatrix} \tag{E.9}$$

$Fm\bar{3}m \rightarrow P4_2nm$

$$\boldsymbol{P} = \begin{pmatrix} 1/2 & 1/2 & 0 \\ -1/2 & 1/2 & 0 \\ 0 & 0 & 1 \end{pmatrix}, \boldsymbol{p} = \begin{pmatrix} 0 \\ 0 \\ 0 \end{pmatrix} \tag{E.10}$$

$$\boldsymbol{Q} = \begin{pmatrix} 1 & -1 & 0 \\ 1 & 1 & 0 \\ 0 & 0 & 1 \end{pmatrix}, \boldsymbol{q} = \begin{pmatrix} 0 \\ 0 \\ 0 \end{pmatrix} \tag{E.11}$$

$P4/mmm \rightarrow Pc$

$$\boldsymbol{P} = \begin{pmatrix} 0 & 1 & -1 \\ 0 & 1 & 1 \\ 1 & 0 & 0 \end{pmatrix}, \boldsymbol{p} = \begin{pmatrix} 1/4 \\ 1/4 \\ 0 \end{pmatrix} \tag{E.12}$$

$$\boldsymbol{Q} = \begin{pmatrix} 0 & 0 & 1 \\ 1/2 & 1/2 & 0 \\ -1/2 & 1/2 & 0 \end{pmatrix}, \boldsymbol{q} = \begin{pmatrix} 0 \\ -1/4 \\ 0 \end{pmatrix} \tag{E.13}$$

$P4/mmm \rightarrow Pmc2_1$

$$\boldsymbol{P} = \begin{pmatrix} 0 & 1 & 1 \\ 0 & -1 & 1 \\ 1 & 0 & 0 \end{pmatrix}, \boldsymbol{p} = \begin{pmatrix} 3/4 \\ 1/4 \\ 0 \end{pmatrix} \tag{E.14}$$

$$\boldsymbol{Q} = \begin{pmatrix} 0 & 0 & 1 \\ 1/2 & -1/2 & 0 \\ 1/2 & 1/2 & 0 \end{pmatrix}, \boldsymbol{q} = \begin{pmatrix} 0 \\ -1/4 \\ -1/2 \end{pmatrix} \tag{E.15}$$

$P4/mmm \rightarrow P4bm$

$$\boldsymbol{P} = \begin{pmatrix} 1 & 1 & 0 \\ -1 & 1 & 0 \\ 0 & 0 & 1 \end{pmatrix}, \boldsymbol{p} = \begin{pmatrix} 1/2 \\ 1/2 \\ 0 \end{pmatrix} \tag{E.16}$$

$$\boldsymbol{Q} = \begin{pmatrix} 1/2 & -1/2 & 0 \\ 1/2 & 1/2 & 0 \\ 0 & 0 & 1 \end{pmatrix}, \boldsymbol{q} = \begin{pmatrix} 0 \\ -1/2 \\ 0 \end{pmatrix} \tag{E.17}$$

$Pm\bar{3}m \rightarrow R3c$

$$\boldsymbol{P} = \begin{pmatrix} 0 & 1 & 2 \\ -1 & 0 & 2 \\ 1 & -1 & 2 \end{pmatrix}, \boldsymbol{p} = \begin{pmatrix} 0 \\ 0 \\ 0 \end{pmatrix} \tag{E.18}$$

$$\boldsymbol{Q} = \begin{pmatrix} 1/3 & -2/3 & 1/3 \\ 2/3 & -1/3 & -1/3 \\ 1/6 & 1/6 & 1/6 \end{pmatrix}, \boldsymbol{q} = \begin{pmatrix} 0 \\ 0 \\ 0 \end{pmatrix} \tag{E.19}$$

$Pm\bar{3}m \rightarrow Pbnm$

$$\boldsymbol{P} = \begin{pmatrix} 0 & 2 & 0 \\ 1 & 0 & 1 \\ 1 & 0 & -1 \end{pmatrix}, \boldsymbol{p} = \begin{pmatrix} 1/2 \\ 1/2 \\ 1/2 \end{pmatrix} \tag{E.20}$$

$$\boldsymbol{Q} = \begin{pmatrix} 0 & 1/2 & 1/2 \\ 1/2 & 0 & 0 \\ 0 & 1/2 & -1/2 \end{pmatrix}, \boldsymbol{q} = \begin{pmatrix} -1/2 \\ -1/4 \\ 0 \end{pmatrix} \tag{E.21}$$

$Pm\bar{3}m \rightarrow P4bm$

$$\boldsymbol{P} = \begin{pmatrix} 1 & -1 & 0 \\ 1 & 1 & 0 \\ 0 & 0 & 1 \end{pmatrix}, \boldsymbol{p} = \begin{pmatrix} 1/2 \\ 1/2 \\ 0 \end{pmatrix} \tag{E.22}$$

$$\boldsymbol{Q} = \begin{pmatrix} 1/2 & 1/2 & 0 \\ -1/2 & 1/2 & 0 \\ 0 & 0 & 1 \end{pmatrix}, \boldsymbol{q} = \begin{pmatrix} -1/2 \\ 0 \\ 0 \end{pmatrix} \tag{E.23}$$

F Landau Coefficients

In the following the Landau coefficients obtained from fitting the Landau potentials of the different phases on DFT energies are given. The values were obtained for mode amplitudes normalized with respect to the single mode values. Only energies below 0.1 eV were included in the fit.

*R*3-Structures

Table F.1: Coefficients of Landau-type energy expansions for single modes.

Coefficient	Value	Abs. Standard Error	Rel. Standard Error
a_{20}	-0.2259	0.0026	1.15
b_{40}	0.1075	0.0014	1.27
a_{02}	-0.5506	0.0052	0.95
b_{04}	0.2636	0.0030	1.14
a_{20}	-0.2468	0.0008	0.31
b_{40}	0.1372	0.0010	0.73
c_{60}	-0.0092	0.0003	3.31
a_{20}	-0.5950	0.0022	0.38
b_{40}	0.3321	0.0031	0.95
c_{60}	-0.0231	0.0010	4.51

Table F.2: Coefficients of Landau-type energy expansions. Comparison of 2-4 potential and 2-4-6 potential.

Coefficient	Value	Abs. Standard Error	Rel. Standard Error
a_{20}	-0.2265	0.0057	2.52
b_{40}	0.1068	0.0028	2.59
a_{02}	-0.4218	0.0112	2.66
b_{04}	0.2086	0.0055	2.62
b_{22}	-0.0346	0.0070	20.22
a_{20}	-0.2470	0.0020	0.81
b_{40}	0.1361	0.0023	1.67
c_{60}	-0.0086	0.0006	7.50
a_{02}	-0.5574	0.0039	0.70
b_{04}	0.2951	0.0042	1.44
c_{06}	-0.0180	0.0014	7.75
b_{22}	0.0544	0.0055	10.18
c_{24}	-0.0185	0.0025	13.58
c_{42}	-0.0150	0.0022	14.64

$P4_2nm$ Structures

Table F.3: Coefficients of Landau-type energy expansions. $V = 53.42$ Å^3/f.u.

Coefficient	Value	Abs. Standard Error	Rel. Standard Error %
a_{20}	-0.1593	0.0012	0.75
b_{40}	0.0915	0.0015	1.62
c_{60}	-0.0083	0.0005	5.53
a_{02}	-0.7705	0.0008	0.10
b_{04}	0.4430	0.0011	0.24
c_{06}	-0.0397	0.0003	0.84
b_{22}	0.1672	0.0017	1.02
c_{24}	-0.0030	0.0007	24.47
c_{42}	0.0052	0.0007	13.03

Table F.4: Coefficients of Landau-type energy expansions. $V = 56.07$ Å^3/f.u.

Coefficient	Value	Abs. Standard Error	Rel. Standard Error
a_{20}	-0.5428	0.0013	0.25
b_{40}	0.3091	0.0022	0.70
c_{60}	-0.0247	0.0008	3.19
a_{02}	-0.6241	0.0012	0.19
b_{04}	0.3637	0.0017	0.47
c_{06}	-0.0343	0.0006	1.69
b_{22}	0.3907	0.0029	0.75
c_{24}	0.0227	0.0016	7.08
c_{42}	0.1394	0.0020	1.41

Table F.5: Coefficients of Landau-type energy expansions. $V = 60.21$ Å^3/f.u.

Coefficient	Value	Abs. Standard Error	Rel. Standard Error
a_{20}	-1.2556	0.0058	0.46
b_{40}	0.6951	0.0095	1.36
c_{60}	-0.0440	0.0037	8.46
a_{02}	-0.5207	0.0043	0.83
b_{04}	0.3108	0.0057	1.83
c_{06}	-0.0329	0.0018	5.59
b_{22}	0.4086	0.0122	2.99
c_{24}	0.0484	0.0054	11.25
c_{42}	0.3724	0.0076	2.04

Pmc2_1 Structures

Table F.6: Coefficients of Landau-type energy expansions. $V = 52.695$ Å^3/f.u.

Coefficient	Value	Abs. Standard Error	Rel. Standard Error
a_{200}	-0.0459	0.0005	-1.10
b_{400}	0.0242	0.0006	2.61
c_{600}	-0.0006	0.0002	-32.61
a_{020}	-0.6137	0.0006	-0.09
b_{040}	0.3449	0.0007	0.21
c_{060}	-0.0283	0.0003	-0.90
a_{002}	-0.5556	0.0006	-0.10
b_{004}	0.3073	0.0007	0.23
c_{006}	-0.0196	0.0002	-1.24
b_{220}	0.0892	0.0005	0.61
c_{240}	-0.0122	0.0002	-1.84
c_{420}	-0.0039	0.0002	-5.58
b_{202}	0.0786	0.0005	0.65
c_{204}	-0.0052	0.0002	-4.14
c_{402}	-0.0074	0.0002	-2.67
b_{022}	0.4418	0.0010	0.22
c_{024}	-0.0202	0.0004	-2.19
c_{042}	-0.0187	0.0004	-2.34
d_{111}	-0.0899	0.0007	-0.79
e_{311}	-0.0098	0.0003	-2.73
e_{131}	-0.1008	0.0004	-0.43
e_{113}	-0.1036	0.0004	-0.41
c_{222}	0.0311	0.0004	1.41

Table F.7: Coefficients of Landau-type energy expansions. $V = 55.973$ Å^3/f.u.

Coefficient	Value	Abs. Standard Error	Rel. Standard Error
a_{200}	-0.1944	0.0004	-0.19
b_{400}	0.0896	0.0005	0.53
c_{600}	0.0050	0.0002	3.34
a_{020}	-0.4547	0.0004	-0.09
b_{040}	0.2566	0.0006	0.22
c_{060}	-0.0205	0.0002	-0.93
a_{002}	-0.4083	0.0004	-0.10
b_{004}	0.2206	0.0005	0.24
c_{006}	-0.0119	0.0002	-1.55
b_{220}	0.1376	0.0005	0.34
c_{240}	-0.0167	0.0002	-1.12
c_{420}	-0.0139	0.0002	-1.31
b_{202}	0.1388	0.0004	0.30
c_{204}	-0.0065	0.0002	-2.78
c_{402}	-0.0308	0.0002	-0.58
b_{022}	0.2830	0.0007	0.25
c_{024}	-0.0167	0.0003	-1.93
c_{042}	-0.0138	0.0003	-2.16
d_{111}	-0.0078	0.0005	-6.69
e_{311}	-0.0226	0.0002	-1.02
e_{131}	-0.0938	0.0003	-0.34
e_{113}	-0.1065	0.0003	-0.28
c_{222}	0.0538	0.0004	0.66

Table F.8: Coefficients of Landau-type energy expansions. $V = 58.693$ Å^3/f.u.

Coefficient	Value	Abs. Standard Error	Rel. Standard Error
a_{200}	-0.3791	0.0004	-0.11
b_{400}	0.1698	0.0005	0.30
c_{600}	0.0144	0.0002	1.11
a_{020}	-0.3172	0.0005	-0.15
b_{040}	0.1789	0.0006	0.31
c_{060}	-0.0147	0.0002	-1.20
a_{002}	-0.3134	0.0004	-0.14
b_{004}	0.1663	0.0005	0.32
c_{006}	-0.0073	0.0002	-2.47
b_{220}	0.1529	0.0006	0.38
c_{240}	-0.0171	0.0002	-1.23
c_{420}	-0.0260	0.0002	-0.86
b_{202}	0.1705	0.0005	0.28
c_{204}	-0.0080	0.0002	-2.36
c_{402}	-0.0531	0.0002	-0.34
b_{022}	0.1710	0.0006	0.37
c_{024}	-0.0114	0.0002	-2.18
c_{042}	-0.0093	0.0003	-2.75
d_{111}	0.0436	0.0005	1.22
e_{311}	-0.0256	0.0002	-0.92
e_{131}	-0.0670	0.0003	-0.38
e_{113}	-0.0880	0.0003	-0.32
c_{222}	0.0552	0.0003	0.61

*P*4*bm* Structure

Table F.9: Coefficients of Landau-type energy expansions. $V = 52.778$ Å^3/f.u.

Coefficient	Value	Abs. Standard Error	Rel. Standard Error
a_{200}	-0.0582	0.0002	0.36
b_{400}	0.0350	0.0004	1.04
c_{600}	-0.0033	0.0001	4.32
a_{020}	-0.8996	0.0067	0.75
b_{040}	0.5429	0.0115	2.13
c_{060}	-0.0581	0.0046	7.93
a_{002}	-0.9526	0.0069	0.72
b_{004}	0.5633	0.0118	2.09
c_{006}	-0.0587	0.0047	8.02
b_{220}	0.0914	0.0013	1.41
c_{240}	-0.0054	0.0006	11.59
c_{420}	-0.0033	0.0006	19.03
b_{202}	0.0970	0.0013	1.37
c_{204}	-0.0064	0.0006	10.05
c_{402}	-0.0042	0.0006	15.59
b_{022}	2.2156	0.0164	0.74
c_{024}	-0.2182	0.0125	5.72
c_{042}	-0.2203	0.0128	5.81
d_{111}	0.1663	0.0018	1.09
e_{311}	0.0006	0.0008	122.50
e_{131}	-0.0521	0.0014	2.67
e_{113}	-0.0516	0.0013	2.59
c_{222}	-0.0232	0.0009	4.09

Table F.10: Coefficients of Landau-type energy expansions. $V = 59.505$ Å^3/f.u.

Coefficient	Value	Abs. Standard Error	Rel. Standard Error
a_{200}	-0.1755	0.0005	0.29
b_{400}	0.0979	0.0009	0.89
c_{600}	-0.0061	0.0003	5.72
a_{020}	-0.3898	0.0035	0.89
b_{040}	0.2288	0.0047	2.05
c_{060}	-0.0212	0.0015	7.03
a_{002}	-0.4277	0.0037	0.85
b_{004}	0.2450	0.0050	2.03
c_{006}	-0.0220	0.0016	7.16
b_{220}	0.0735	0.0011	1.48
c_{240}	0.0065	0.0005	7.57
c_{420}	0.0135	0.0005	3.62
b_{202}	0.0835	0.0011	1.37
c_{204}	0.0061	0.0005	8.42
c_{402}	0.0123	0.0005	4.14
b_{022}	0.9497	0.0055	0.58
c_{024}	-0.1308	0.0042	3.19
c_{042}	-0.1297	0.0042	3.21
d_{111}	0.1910	0.0010	0.52
e_{311}	0.0173	0.0004	2.59
e_{131}	-0.0311	0.0007	2.14
e_{113}	-0.0323	0.0007	2.04
c_{222}	0.0726	0.0006	0.76

Table F.11: Coefficients of Landau-type energy expansions. $V = 63.805$ Å^3/f.u.

Coefficient	Value	Abs. Standard Error	Rel. Standard Error
a_{200}	-1.6164	0.0090	0.56
b_{400}	0.7631	0.0154	2.02
c_{600}	0.0302	0.0062	20.45
a_{020}	-0.4136	0.0028	0.67
b_{040}	0.2515	0.0047	1.88
c_{060}	-0.0278	0.0019	6.81
a_{002}	-0.4233	0.0037	0.88
b_{004}	0.2434	0.0051	2.09
c_{006}	-0.0214	0.0016	7.55
b_{220}	0.0940	0.0073	7.80
c_{240}	0.0645	0.0032	4.92
c_{420}	0.3279	0.0047	1.42
b_{202}	0.1192	0.0086	7.20
c_{204}	0.0552	0.0032	5.73
c_{402}	0.3328	0.0055	1.66
b_{022}	1.1086	0.0067	0.60
c_{024}	-0.1612	0.0050	3.13
c_{042}	-0.1671	0.0051	3.07
d_{111}	0.5450	0.0055	1.01
e_{311}	0.4892	0.0034	0.70
e_{131}	-0.0857	0.0034	3.93
e_{113}	-0.0929	0.0032	3.40
c_{222}	0.3805	0.0039	1.02

Bibliography

[1] G. H. Brundtland, Our Common Future, UN Documents, 1987, http://www.un-documents.net/our-common-future.pdf.

[2] LOEWE-Zentrum AdRIA (Adaptronik - Research, Innovation Application), http://www.loewe-adria.de.

[3] H. Janocha, Editor, *Adaptronics and Smart Structures - Basics, Materials, Design and Applications* (Springer Berlin Heidelberg, 2007).

[4] Piezoelectric Ceramic, Polymer and Ceramic/Polymer Composite Devices - Types, Materials, Applications, New Developments, Industry Structure and Global Markets, 2008, http://marketpublishers.com/members/innoresearch/info.html.

[5] B. Jaffe, W. R. Cook, and H. Jaffe, *Piezoelectric Ceramics* (Academic Press Ltd., 1971).

[6] J. Rödel *et al.*, Journal of the American Ceramic Society **92**, 1153 (2009).

[7] W. Maier, K. Stöwe, and S. Sieg, Angewandte Chemie (Int. Ed.) **46**, 6016 (2007).

[8] G. Hautier *et al.*, Chemistry of Materials **23**, 3495 (2011).

[9] R. Armiento, B. Kozinsky, M. Fornari, and G. Ceder, Physical Review B **84**, 014103 (2011).

[10] J. W. Bennett, K. M. Rabe, Journal of Solid State Chemistry **195**, 21 (2012).

[11] R. Resta, Modelling and Simulation in Materials Science and Engineering **11**, R69 (2003).

[12] K. M. Rabe and P. Ghosez, *Physics of Ferroelectrics: A Modern Perspective* (Springer-Verlag Berlin, 2007), Chapter: First-Principles Studies of Ferroelectric Oxides, pp. 117–174.

[13] S. B. Vakhrushev *et al.*, Ferroelectrics **63**, 153 (1985).

[14] G. O. Jones and P. A. Thomas, Acta Crystallographica Section B **58**, 168 (2002).

[15] C. S. Tu, I. G. Siny, and V. H. Schmidt, Physical Review B **49**, 11550 (1994).

[16] Y. Hiruma, H. Nagata, and T. Takenaka, Journal of Applied Physics **105**, 084112 (2009).

[17] Official Journal of the European Union **L197**, 38 (2012).

[18] Official Journal of the European Union **L174**, 88 (2011).

[19] A. Walsh, D. J. Payne, R. G. Egdell, and G. W. Watson, Chemical Society Reviews **40**, 4455 (2011).

[20] D. J. Payne *et al.*, Physical Review Letters **96**, 157403 (2006).

[21] A. Walsh *et al.*, Physical Review B **73**, 235104 (2006).

[22] L. A. Olsen, J. Lopez-Solano, A. Garcia, T. Balic-Zunic, and E. Makovicky, Journal of Solid State Chemistry **183**, 2133 (2010).

[23] Chemical Safety Information from Intergovernmental Organizations, http://www.inchem.org/.

[24] IARC Monographs on the Evaluation of Carcinogenic Risks to Humans - Inorganic and Organic Lead Compounds (Volume 87), 2006, http://www.inchem.org/documents/iarc/vol87/volume87.pdf.

[25] DFG, Editor, *MAK- und BAT-Werte-Liste 2012: Maximale Arbeitsplatzkonzentrationen und Biologische Arbeitsstofftoleranzwerte. Mitteilung 48* (Wiley-VCH Verlag GmbH & Co. KGaA, 2012), Chap. 2. Stoffliste, pp. 18–148.

[26] H. Suzuki and Y. Matano, *Organobismuth Chemistry* (Elsevier Sci. Ltd., 2001).

[27] B. D. Fahlmann, *Materials Chemistry* (Springer, 2011).

[28] M. T. Dove, American Mineralogist **82**, 213 (1997).

[29] M. T. Dove, *Structure and Dynamics: An Atomic View of Materials* (Oxford University Press, 2003).

[30] R. E. Cohen, Nature **358**, 136 (1992).

[31] B. Noheda *et al.*, Applied Physics Letters **74**, 2059 (1999).

[32] A. M. Glazer, P. A. Thomas, K. Z. Baba-Kishi, G. K. H. Pang, and C. W. Tai, Physical Review B **70**, 184123 (2004).

[33] K. A. Schönau *et al.*, Physical Review B **75**, 184117 (2007).

[34] G. A. Rossetti, W. Zhang, and A. G. Khachaturyan, Applied Physics Letters **88**, 072912 (2006).

[35] J. B. Clark, J. W. Hastie, L. H. E. Kihlborg, R. Metselaar, and M. M. Thackeray, Pure and Applied Chemistry **66**, 577 (1994).

[36] H. X. Fu and R. E. Cohen, Nature **403**, 281 (2000).

[37] M. Budimir, D. Damjanovic, and N. Setter, Physical Review B **73**, 174106 (2006).

[38] D. Damjanovic, Journal of the American Ceramic Society **88**, 2663 (2005).

[39] G. A. Rossetti and A. G. Khachaturyan, Applied Physics Letters **91**, 072909 (2007).

[40] G. A. Rossetti, A. G. Khachaturyan, G. Akcay, and Y. Ni, Journal of Applied Physics **103**, 114113 (2008).

[41] D. Damjanovic, Applied Physics Letters **97**, 062906 (2010).

[42] R. E. Eitel *et al.*, Japanese Journal of Applied Physics **40**, 5999 (2001).

[43] M. R. Suchomel and P. K. Davies, Journal of Applied Physics **96**, 4405 (2004).

[44] I. Grinberg, M. R. Suchomel, P. K. Davies, and A. M. Rappe, Journal of Applied Physics **98**, 094111 (2005).

[45] P. M. Woodward, Acta Crystallographica Section B **53**, 44 (1997).

[46] M. Ghita, M. Fornari, D. J. Singh, and S. V. Halilov, Physical Review B **72**, 054114 (2005).

[47] S. Hayn, M. Gröting, and K. Albe., to be published.

[48] G. A. Samara, T. Sakudo, and K. Yoshimitsu, Physical Review Letters **35**, 1767 (1975).

[49] I. A. Kornev and L. Bellaiche, Phase Transitions **80**, 385 (2007).

[50] R. J. Angel, J. Zhao, and N. L. Ross, Physical Review Letters **95**, 025503 (2005).

[51] Z. G. Wu and R. E. Cohen, Physical Review Letters **95**, 037601 (2005).

[52] I. A. Kornev *et al.*, Physical Review Letters **95**, 196804 (2005).

[53] P. Ganesh and R. E. Cohen, Journal of Physics: Condensed Matter **21**, 064225 (2009).

[54] M. Ahart *et al.*, Nature **451**, 545 (2008).

[55] S. Trujillo *et al.*, Journal of Physics: Condensed Matter **17**, 6587 (2005).

[56] S.-E. Park and T. R. Shrout, Journal of Applied Physics **82**, 1804 (1997).

[57] A. Safari and E. K. Akdoğan, Editors, *Piezoelectric and Acoustic Materials for Transducer Applications* (Springer, 2008).

[58] L. E. Cross, Ferroelectrics **76**, 241 (1987).

[59] A. A. Bokov and Z. G. Ye, Journal of Materials Science **41**, 31 (2006).

[60] G. A. Samara, Journal of Physics: Condensed Matter **15**, R367 (2003).

[61] N. Setter and L. E. Cross, Journal of Applied Physics **51**, 4356 (1980).

[62] E. Dagotto, New Journal of Physics **7**, 67 (2005).

[63] E. Dagotto, Science **309**, 257 (2005).

[64] Z. Kutnjak, J. Petzelt, and R. Blinc, Nature **441**, 956 (2006).

[65] J. Dec, W. Kleemann, and T. Łukasiewicz, Phase Transitions **79**, 505 (2006).

[66] V. V. Shvartsman and D. C. Lupascu, Journal of the American Ceramic Society **95**, 1 (2012).

[67] G. O. Jones and P. A. Thomas, Acta Crystallographica Section B **56**, 426 (2000).

[68] A. Simon, J. Ravez, and M. Maglione, Journal of Physics: Condensed Matter **16**, 963 (2004).

[69] C. Laulhé *et al.*, Physical Review B **74**, 014106 (2006).

[70] C. Laulhé, F. Hippert, R. Bellissent, A. Simon, and G. J. Cuello, Physical Review B **79**, 064104 (2009).

[71] C. Laulhé, A. Pasturel, F. Hippert, and J. Kreisel, Physical Review B **82**, 132102 (2010).

[72] A. R. Akbarzadeh, S. Prosandeev, E. J. Walter, A. Al-Barakaty, and L. Bellaiche, Physical Review Letters **108**, 257601 (2012).

[73] G. Burns and F. H. Dacol, Physical Review B **28**, 2527 (1983).

[74] D. Viehland, J. F. Li, S. J. Jang, L. E. Cross, and M. Wuttig, Physical Review B **46**, 8013 (1992).

[75] H. Arndt and G. Schmidt, Ferroelectrics **79**, 149 (1988).

[76] Y. Moriya, H. Kawaji, T. Tojo, and T. Atake, Physical Review Letters **90**, 205901 (2003).

[77] N. de Mathan *et al.*, Journal of Physics: Condensed Matter **3**, 8159 (1991).

[78] A. Bosak, D. Chernyshov, S. Vakhrushev, and M. Krisch, Acta Crystallographica Section A **68**, 117 (2012).

[79] E. Dul'kin, M. Roth, P. E. Janolin, and B. Dkhil, Physical Review B **73**, 012102 (2006).

[80] M. Yoshida, S. Mori, N. Yamamoto, Y. Uesu, and J. M. Kiat, Ferroelectrics **217**, 327 (1998).

[81] J. Toulouse, Ferroelectrics **369**, 203 (2008).

[82] B. Dkhil *et al.*, Physical Review B **80**, 064103 (2009).

[83] A. E. Glazounov and A. K. Tagantsev, Applied Physics Letters **73**, 856 (1998).

[84] R. Pirc and R. Blinc, Physical Review B **76**, 020101 (2007).

[85] G. Y. Xu, P. M. Gehring, and G. Shirane, Physical Review B **72**, 214106 (2005).

[86] G. A. Samara and E. L. Venturini, Phase Transitions **79**, 21 (2006).

[87] S. Tinte, B. P. Burton, E. Cockayne, and U. V. Waghmare, Physical Review Letters **97**, 137601 (2006).

[88] W. Qu, X. Zhao, and X. Tan, Journal of Applied Physics **102**, 084101 (2007).

[89] B. P. Burton, E. Cockayne, and U. V. Waghmare, Physical Review B **72**, 064113 (2005).

[90] R. A. Cowley, S. N. Gvasaliya, S. G. Lushnikov, B. Roessli, and G. M. Rotaru, Advances in Physics **60**, 229 (2011).

[91] V. Westphal, W. Kleemann, and M. D. Glinchuk, Physical Review Letters **68**, 847 (1992).

[92] R. Pirc and R. Blinc, Physical Review B **60**, 13470 (1999).

[93] Y. Imry, Journal of Physics C: Solid State Physics **8**, 567 (1975).

[94] V. V. Shvartsman, W. Kleemann, T. Łukasiewicz, and J. Dec, Physical Review B **77**, 054105 (2008).

[95] N. Novak, R. Pirc, M. Wencka, and Z. Kutnjak, Physical Review Letters **109**, 037601 (2012).

[96] P. K. Davies, H. Wu, A. Y. Borisevich, I. E. Molodetsky, and L. Farber, Annual Review of Materials Research **38**, 369 (2008).

[97] M. C. Knapp and P. M. Woodward, Journal of Solid State Chemistry **179**, 1076 (2006).

[98] G. King and P. M. Woodward, Journal of Materials Chemistry **20**, 5785 (2010).

[99] W. Jo, T. Granzow, E. Aulbach, J. Rödel, and D. Damjanovic, Journal of Applied Physics **105**, 094102 (2009).

[100] W. Jo *et al.*, Journal of Electroceramics **29**, 71 (2012).

[101] V. A. Isupov, Ferroelectrics **315**, 123 (2005).

[102] G. A. Smolenskii, V. A. Isupov, A. I. Agranovskaya, and N. N. Krainik, Fizika Tverdogo Tela **2**, 2982 (1960).

[103] I. Levin and I. M. Reaney, Advanced Functional Materials **22**, 3445 (2012).

[104] B. N. Rao and R. Ranjan, Physical Review B **86**, 134103 (2012).

[105] E. Aksel *et al.*, Physical Review B **85**, 024121 (2012).

[106] J. E. Daniels, W. Jo, J. Rödel, D. Rytz, and W. Donner, Applied Physics Letters **98**, 252904 (2011).

[107] A. O'Brien, D. I. Woodward, K. Sardar, R. I. Walton, and P. A. Thomas, Applied Physics Letters **101**, 142902 (2012).

[108] A. M. Glazer, Acta Crystallographica Section B **28**, 3384 (1972).

[109] V. Dorcet, G. Trolliard, and P. Boullay, Chemistry of Materials **20**, 5061 (2008).

[110] G. Trolliard and V. Dorcet, Chemistry of Materials **20**, 5074 (2008).

[111] S. Gorfman *et al.*, Journal of Applied Crystallography **45**, 444 (2012).

[112] S. Gorfman and P. A. Thomas, Journal of Applied Crystallography **43**, 1409 (2010).

[113] P. A. Thomas *et al.*, Zeitschrift für Kristallographie **220**, 717 (2005).

[114] E. Aksel *et al.*, Applied Physics Letters **98**, 152901 (2011).

[115] T. Egami, Annual Review of Materials Research **37**, 297 (2007).

[116] R. Comès, M. Lambert, and A. Guinier, Acta Crystallographica Section A **26**, 244 (1970).

[117] S. Gomez-Salces *et al.*, Physical Review B **85**, 144109 (2012).

[118] I. P. Aleksandrova, Y. N. Ivanov, A. A. Sukhovskii, and S. B. Vakhrushev, Physics of the Solid State **48**, 1120 (2006).

[119] I. P. Aleksandrova, A. A. Sukhovskii, Y. N. Ivanov, Y. E. Yablonskaya, and S. B. Vakhrushev, Physics of the Solid State **50**, 496 (2008).

[120] I. P. Aleksandrova, A. A. Sukhovsky, Y. N. Ivanov, Y. E. Yablonskaya, and S. B. Vakhrushev, Ferroelectrics **378**, 16 (2009).

[121] J. Kreisel *et al.*, Journal of Physics: Condensed Matter **12**, 3267 (2000).

[122] J. Kreisel, A. M. Glazer, P. Bouvier, and G. Lucazeau, Physical Review B **63**, 174106 (2001).

[123] E. Aksel, E. Erdem, P. Jakes, J. L. Jones, and R.-A. Eichel, Applied Physics Letters **97**, 012903 (2010).

[124] E. Aksel *et al.*, Journal of the American Ceramic Society **94**, 1363 (2011).

[125] Y. P. Guo, M. Y. Gu, H. S. Luo, Y. Liu, and R. L. Withers, Physical Review B **83**, 054118 (2011).

[126] J. Kreisel *et al.*, Physical Review B **68**, 014113 (2003).

[127] P. A. Thomas, S. Trujillo, M. Boudard, S. Gorfman, and J. Kreisel, Solid State Sciences **12**, 311 (2010).

[128] I. Jeong *et al.*, Zeitschrift für Kristallographie **226**, 150 (2011).

[129] V. A. Shuvaeva *et al.*, Physical Review B **71**, 174114 (2005).

[130] J. E. Daniels, W. Jo, J. Rödel, and J. L. Jones, Applied Physics Letters **95**, 032904 (2009).

[131] Y. P. Guo, Y. Liu, R. L. Withers, F. Brink, and H. Chen, Chemistry of Materials **23**, 219 (2011).

[132] D. S. Keeble *et al.*, Advanced Functional Materials **23**, 185 (2013).

[133] S. E. Park, S. J. Chung, I. T. Kim, and K. S. Hong, Journal of the American Ceramic Society **77**, 2641 (1994).

[134] J. Petzelt *et al.*, Journal of Physics: Condensed Matter **16**, 2719 (2004).

[135] B. P. Burton and E. Cockayne, Ferroelectrics **270**, 1359 (2002).

[136] J. Kreisel *et al.*, Ferroelectrics **302**, 293 (2004).

[137] R. Ranjan *et al.*, Applied Physics Letters **95**, 042904 (2009).

[138] R. Ranjan *et al.*, Journal of Physics: Condensed Matter **22**, 075901 (2010).

[139] S. Sasaki, C. T. Prewitt, J. D. Bass, and W. A. Schulze, Acta Crystallographica Section C **43**, 1668 (1987).

[140] Y. Watanabe, Y. Hiruma, H. Nagata, and T. Takenaka, Ceramics International **34**, 761 (2008).

[141] B. Wylie-van Eerd, D. Damjanovic, N. Klein, N. Setter, and J. Trodahl, Physical Review B **82**, 104112 (2010).

[142] C. Ma and X. Tan, Solid State Communications **150**, 1497 (2010).

[143] W. Jo *et al.*, Journal of Applied Physics **109**, 014110 (2011).

[144] W. Jo and J. Rödel, Applied Physics Letters **99**, 042901 (2011).

[145] C. Ma, H. Guo, S. P. Beckman, and X. Tan, Physical Review Letters **109**, 107602 (2012).

[146] Y. Hiruma, K. Yoshii, H. Nagata, and T. Takenaka, Journal of Applied Physics **103**, 084121 (2008).

[147] G. O. Jones, J. Kreisel, and P. A. Thomas, Powder Diffraction **17**, 301 (2002).

[148] A. Sasaki, T. Chiba, Y. Mamiya, and E. Otsuki, Japanese Journal of Applied Physics **38**, 5564 (1999).

[149] Y. Hiruma, H. Nagata, and T. Takenaka, Journal of Applied Physics **104**, 124106 (2008).

[150] A. J. Royles *et al.*, Applied Physics Letters **97**, 132909 (2010).

[151] B. Holm, Physical Review Letters **83**, 788 (1999).

[152] E. Runge and E. K. U. Gross, Physical Review Letters **52**, 997 (1984).

[153] R. E. Martin, *Electronic Structure - Basic Theory and Practical Methods* (Cambridge University Press, 2004).

[154] M. Born and R. Oppenheimer, Annalen der Physik **389**, 457 (1927).

[155] P. Hohenberg and W. Kohn, Physical Review **136**, B 864 (1964).

[156] W. Kohn and L. J. Sham, Physical Review **140**, A 1133 (1965).

[157] J. P. Perdew, R. G. Parr, M. Levy, and J. L. Balduz, Physical Review Letters **49**, 1691 (1982).

[158] J. Heyd, G. E. Scuseria, and M. Ernzerhof, Journal of Chemical Physics **118**, 8207 (2003).

[159] J. Heyd, G. E. Scuseria, and M. Ernzerhof, Journal of Chemical Physics **124**, 219906 (2006).

[160] A. D. Becke, Journal of Chemical Physics **98**, 5648 (1993).

[161] C. T. Lee, W. T. Yang, and R. G. Parr, Physical Review B **37**, 785 (1988).

[162] D. M. Ceperley and B. J. Alder, Physical Review Letters **45**, 566 (1980).

[163] J. P. Perdew, K. Burke, and M. Ernzerhof, Physical Review Letters **77**, 3865 (1996).

[164] J. P. Perdew, Y. Wang, Physical Review B **45**, 13244 (1992).

[165] D. Vanderbilt, Physical Review B **41**, 7892 (1990).

[166] G. Kresse and D. Joubert, Physical Review B **59**, 1758 (1999).

[167] P. E. Blöchl, Physical Review B **50**, 17953 (1994).

[168] E. Wimmer, H. Krakauer, M. Weinert, and A. J. Freeman, Physical Review B **24**, 864 (1981).

[169] M. Weinert, E. Wimmer, and A. J. Freeman, Physical Review B **26**, 4571 (1982).

[170] Gaussian, http://www.gaussian.com/.

[171] Siesta, http://icmab.cat/leem/siesta/.

[172] J. M. Soler *et al.*, Journal of Physics: Condensed Matter **14**, 2745 (2002).

[173] G. Kresse and J. Hafner, Physical Review B **47**, 558 (1993).

[174] G. Kresse and J. Hafner, Physical Review B **49**, 14251 (1994).

[175] G. Kresse and J. Furthmüller, Computational Materials Science **6**, 15 (1996).

[176] G. Kresse and J. Furthmüller, Physical Review B **54**, 11169 (1996).

[177] Abinit, http://www.abinit.org/.

[178] X. Gonze *et al.*, Computational Materials Science **25**, 478 (2002).

[179] X. Gonze *et al.*, Zeitschrift für Kristallographie **220**, 558 (2005).

[180] Quantum-Espresso, http://www.quantum-espresso.org/.

[181] Fleur, http://www.flapw.de/.

[182] H. J. Monkhorst and J. D. Pack, Physical Review B **13**, 5188 (1976).

[183] R. P. Feynman, Physical Review **56**, 340 (1939).

[184] K. Momma and F. Izumi, Journal of Applied Crystallography **44**, 1272 (2011).

[185] F. Birch, Physical Review **71**, 809 (1947).

[186] G. Henkelman, A. Arnaldsson, and H. Jonsson, Computational Materials Science **36**, 354 (2006).

[187] E. Sanville, S. D. Kenny, R. Smith, and G. Henkelman, Journal of Computational Chemistry **28**, 899 (2007).

[188] W. Tang, E. Sanville, and G. Henkelman, Journal of Physics: Condensed Matter **21**, 084204 (2009).

[189] H. T. Stokes, E. H. Kisi, D. M. Hatch, and C. J. Howard, Acta Crystallographica Section B **58**, 934 (2002).

[190] J. C. Toledano and P. Toledano, *The Landau Theory of Phase Transitions* (World Scientific, 1987).

[191] A. F. Devonshire, Philosophical Magazine **40**, 1040 (1949).

[192] A. F. Devonshire, Philosophical Magazine **42**, 1065 (1951).

[193] M. Lines and A. Glass, *Principles and Applications of Ferroelectrics and Related Materials* (Clarendon Press, Oxford, UK, 1977).

[194] R. Cowley, Advances in Physics **29**, 1 (1980).

[195] P. Chandra and P. B. Littlewood, *Physics of Ferroelectrics: A Modern Perspective* (Springer-Verlag, 2007), Chapter: A Landau Primer for Ferroelectrics, pp. 69–115.

[196] M. A. Carpenter, *The Stability of Minerals* (Kluwer Academics Publishers, 1992), Chapter: Thermodynamics of Phase Transitions in Minerals: A Macroscopic Approach, pp. 172–215.

[197] H. T. Stokes, D. M. Hatch, and B. J. Campbell, Isotropy, 2007, http://stokes.byu.edu/iso/isotropy.html/.

[198] A. I. M. Rae, M. T. Dove, Journal of Physics C: Solid State Physics **16**, 3233 (1983).

[199] A. P. Levanyuk and D. G. Sannikov, Soviet Physics - Uspekhi **17**, 199 (1974).

[200] J. Holakovsky, Physica Status Solidi B **56**, 615 (1973).

[201] J. D. Axe, B. Dorner, and G. Shirane, Physical Review Letters **26**, 519 (1971).

[202] B. Dorner, J. D. Axe, and G. Shirane, Physical Review B **6**, 1950 (1972).

[203] V. Dvorak, Physica Status Solidi B **46**, 763 (1971).

[204] E. Bousquet *et al.*, Nature **452**, 732 (2008).

[205] C. J. Fennie and K. M. Rabe, Physical Review B **72**, 100103 (2005).

[206] N. A. Benedek and C. J. Fennie, Physical Review Letters **106**, 107204 (2011).

[207] T. Fukushima, A. Stroppa, S. Picozzi, and J. M. Perez-Mato, Physical Chemistry Chemical Physics **13**, 12186 (2011).

[208] J. M. Rondinelli and C. J. Fennie, Advanced Materials **24**, 1961 (2012).

[209] N. Sai, C. J. Fennie, and A. A. Demkov, Physical Review Letters **102**, 107601 (2009).

[210] M. Stengel, C. J. Fennie, and P. Ghosez, Physical Review B **86**, 094112 (2012).

[211] M. Stengel, D. Vanderbilt, and N. A. Spaldin, Nature Materials **8**, 392 (2009).

[212] I. A. Kornev and L. Bellaiche, Physical Review B **79**, 100105 (2009).

[213] J. M. Perez-Mato *et al.*, Physical Review B **77**, 184104 (2008).

[214] R. E. Newnham, *Properties of Materials - Anisotropy, Symmetry, Structure* (Oxford University Press, 2005).

[215] A. F. Devonshire, Advances in Physics **3**, 85 (1954).

[216] W. Ma, Physica Status Solidi B **245**, 761 (2008).

[217] P. V. Yudin, A. K. Tagantsev, E. A. Eliseev, A. N. Morozovska, and N. Setter, Physical Review B **86**, 134102 (2012).

[218] E. Salje and V. Devarajan, Phase Transitions **6**, 235 (1986).

[219] N. A. Pertsev and E. K. H. Salje, Physical Review B **61**, 902 (2000).

[220] J. M. Perez-Mato, D. Orobengoa, and M. I. Aroyo, Acta Crystallographica Section A **66**, 558 (2010).

[221] H. Bärnighausen, MATCH, Communication in Mathematical Chemistry **9**, 139 (1980).

[222] U. Müller, Zeitschrift für Anorganische und Allgemeine Chemie **630**, 1519 (2004).

[223] H. Wondratschek and U. Müller, Editors, *International Tables for Crystallography, Volume A1, Symmetry Relations between Space Groups* (Springer, 2004).

[224] T. Hahn, Editor, *International Tables for Crystallography, Volume A, Space Group Symmetry* (Springer, 2005).

[225] A. P. B. Cracknell, B. L. Davies, S. C. Miller, and W. F. Love, *Kronecker Product Tables, Vol. I, General Introduction and Tables of Irreducible Representations of Space Groups* (Plenum, New York, 1979).

[226] M. I. Aroyo *et al.*, Zeitschrift für Kristallographie **221**, 15 (2006).

[227] M. I. Aroyo, A. Kirov, C. Capillas, J. M. Perez-Mato, and H. Wondratschek, Acta Crystallographica Section A **62**, 115 (2006).

[228] M. I. Aroyo *et al.*, Bulgarian Chemical Communications **43**, 183 (2011).

[229] L. Vasylechko *et al.*, Journal of Solid State Chemistry **180**, 1277 (2007).

[230] C. Capillas *et al.*, Journal of Applied Crystallography **36**, 953 (2003).

[231] I. Etxebarria, J. M. Perez-Mato, and P. Boullay, Ferroelectrics **401**, 17 (2010).

[232] D. Orobengoa, C. Capillas, M. I. Aroyo, and J. M. Perez-Mato, Journal of Applied Crystallography **42**, 820 (2009).

[233] P. M. Woodward, Acta Crystallographica Section B **53**, 32 (1997).

[234] K. A. Müller, E. Brun, B. Derighetti, J. E. Drumheller, and F. Waldner, Physics Letters **9**, 223 (1964).

[235] K. A. Müller, W. Berlinge, and F. Waldner, Physical Review Letters **21**, 814 (1968).

[236] S. Geller, The Journal of Chemical Physics **24**, 1236 (1956).

[237] K. Leinenweber and J. Parise, Journal of Solid State Chemistry **114**, 277 (1995).

[238] V. Propach, Zeitschrift für Anorganische und Allgemeine Chemie **435**, 161 (1977).

[239] M. A. Carpenter and C. J. Howard, Acta Crystallographica Section B **65**, 134 (2009).

[240] R. D. Shannon, Acta Crystallographica Section A **32**, 751 (1976).

[241] M. Bousquet *et al.*, Journal of Applied Physics **107**, 104107 (2010).

[242] J. H. Park *et al.*, Chemistry of Materials **11**, 177 (1999).

[243] V. Goldschmidt, Naturwissenschaften **14**, 477 (1926).

[244] R. D. Shannon and C. T. Prewitt, Acta Crystallographica Section B **25**, 925 (1969).

[245] C. A. Randall and A. S. Bhalla, Japanese Journal of Applied Physics **29**, 327 (1990).

[246] B. P. Burton and E. Cockayne, Fundamental Physics of Ferroelectrics 2001, AIP Conference Proceedings **582**, 82 (2001).

[247] M. Gröting, S. Hayn, and K. Albe, Journal of Solid State Chemistry **184**, 2041 (2011).

[248] I. M. Reaney, D. I. Woodward, and C. A. Randall, Journal of the American Ceramic Society **94**, 2242 (2011).

[249] R. Beanland, Acta Crystallographica Section A **67**, 191 (2011).

[250] P. Ghosez, X. Gonze, and J. P. Michenaud, Ferroelectrics **206**, 205 (1998).

[251] J. Frantti *et al.*, Journal of Physical Chemistry B **113**, 7967 (2009).

[252] S. Tinte, K. M. Rabe, and D. Vanderbilt, Physical Review B **68**, 144105 (2003).

[253] H. Moriwake, Y. Koyama, K. Matsunaga, T. Hirayama, and I. Tanaka, Journal of Physics: Condensed Matter **20**, 345207 (2008).

[254] H. Béa *et al.*, Physical Review Letters **102**, 217603 (2009).

[255] B. Dupé *et al.*, Physical Review B **81**, 144128 (2010).

[256] N. A. Pertsev, A. G. Zembilgotov, and A. K. Tagantsev, Physical Review Letters **80**, 1988 (1998).

[257] Y. Deng *et al.*, Applied Physics A - Materials Science & Processing **104**, 1085 (2011).

[258] R. Yu and H. Krakauer, Physical Review B **49**, 4467 (1994).

[259] X. Gonze and C. Lee, Physical Review B **55**, 10355 (1997).

[260] S. Baroni, S. de Gironcoli, A. dal Corso, and P. Giannozzi, Reviews of Modern Physics **73**, 515 (2001).

[261] I. Souza, J. Iñiguez, and D. Vanderbilt, Physical Review Letters **89**, 117602 (2002).

[262] D. R. Hamann, X. F. Wu, K. M. Rabe, and D. Vanderbilt, Physical Review B **71**, 035117 (2005).

[263] P. Erhart and K. Albe, Journal of Applied Physics **102**, 084111 (2007).

[264] P. Erhart and K. Albe, Journal of Applied Physics **104**, 044315 (2008).

[265] P. Erhart, R.-A. Eichel, P. Träskelin, and K. Albe, Physical Review B **76**, 174116 (2007).

[266] R.-A. Eichel *et al.*, Physical Review Letters **100**, 095504 (2008).

[267] L. Bellaiche and D. Vanderbilt, Physical Review B **61**, 7877 (2000).

[268] L. Bellaiche, A. Garcia, and D. Vanderbilt, Physical Review B **64**, 060103 (2001).

[269] L. Bellaiche, A. Garcia, and D. Vanderbilt, Ferroelectrics **266**, 41 (2002).

[270] B. P. Burton, E. Cockayne, S. Tinte, and U. V. Waghmare, Physical Review B **77**, 144114 (2008).

Copyright Notice

Results of this thesis were published already in articles of scientific journals:

- Ch. 9 "Chemical A-site Order" is partly reprinted from article:

  M. Gröting, S. Hayn, K. Albe, *Chemical order and local structure of the lead-free relaxor ferroelectric* $Na_{1/2}Bi_{1/2}TiO_3$, Journal of Solid State Chemistry **184**, 2041-2046 (2011).

- Ch. 10 "Ground State Structures" is partly reprinted from article:

  M. Gröting, I. Kornev, B. Dkhil, K. Albe, *Pressure-induced phase transitions and structure of chemically ordered nanoregions in the lead-free relaxor ferroelectric* $Na_{1/2}Bi_{1/2}TiO_3$, Physical Review B **86**, 134118 (2012).

Erklärung

Hiermit versichere ich an Eides statt, dass ich die vorliegende Arbeit selbstständig und nur unter Verwendung der angegebenen Hilfsmittel angefertigt habe. Von mir wurde weder an der Technischen Universität Darmstadt noch an einer anderen Hochschule ein Promotionsversuch unternommen.

Darmstadt, 5. März 2013

Melanie Gröting

Curriculum Vitae

Personal Data

Name	Melanie Gröting
Birth	19. September 1979 in Frankfurt am Main, Germany
Nationality	German
Address	Wöllstädter Str. 7 60385 Frankfurt

University Education

05/2013	Defense of PhD Thesis
10/2008-04/2013	**PhD Thesis**: *"Ab-initio Calculations of the Relaxor Ferroelectric $Na_{1/2}Bi_{1/2}TiO_3$ and its Solid Solutions"* Materials Modeling Division (Prof. K. Albe) Materials Science, Technical University Darmstadt, Darmstadt, Germany
03/2006-06/2007	**Graduate School of Chemistry and Biology** Ruhr-University Bochum, Bochum, Germany
08/2004-01/2006	**Studies: Chinese Language** Beijing Foreign Studies University, Beijing, P. R. China
07/2004	**Diplom-Ingenieurin Chemie** Diploma Thesis: *"Optische Anregung in Fluorid-Wirtsgittern für Zweiphotonen-Leuchtstofflampen"* Theoretical Chemistry of Solids Division (Prof. P. C. Schmidt) Chemistry, Technical University Darmstadt, Darmstadt, Germany
10/1999-07/2004	**Studies: Chemistry** Technical University Darmstadt, Darmstadt, Germany

Work Experience

04/2008-today	**Research Associate** (Wissenschaftliche Mitarbeiterin) Materials Modeling Division (Prof. K. Albe) Materials Science, Technical University Darmstadt, Darmstadt, Germany
11/2010-02/2011	**Visiting Scientist** Laboratoire Structure, Propriétés, Modélisation des Solides (Prof. Igor Kornev and Dr. Brahim Dkhil) École Centrale Paris, Châtenay-Malabry, France
03/2006-06/2007	**Research Associate** (Wissenschaftliche Mitarbeiterin) Reaction Technology Degussa GmbH, Marl, Germany
08/2005-01/2006	**Assistant to Senior Project Manager** Chemical Engineering Degussa (China) Co., Ltd., Beijing, P.R. China

School Education

07/1999	**Graduation from Secondary School**
08/1990-07/1999	**Secondary School**: Heinrich-von-Gagern Gymnasium Frankfurt am Main, Germany

Scholarships, Honours and Awards

11/2010-02/2011	3-Months Scholarship of the German Academic Exchange Service (DAAD) for École Centrale Paris, France.
04/2007	Poster Award at European Conference on Combinatorial Catalysis Research and High-Throughput Technologies, 22.-25.04.2007, Bari, Italy.
08/2004-01/2006	14-Months Scholarship of the German Academic Exchange Service (DAAD) *"Language and Practical Experience in China"* (Sprache und Praxis in der VR China)
02/2002	Award of the Dr.-Anton Keller Foundation, Technical University Darmstadt, Darmstadt, Germany.

Frankfurt am Main, 4. März 2013

Publications

Peer-Reviewed Articles

- **M. Gröting**, I. Kornev, B. Dkhil, K. Albe, *Pressure-induced phase transitions and structure of chemically ordered nanoregions in the lead-free relaxor ferroelectric* $Na_{1/2}Bi_{1/2}TiO_3$, Physical Review B **86**, 134118 (2012).
- **M. Gröting**, S. Hayn, K. Albe, *Chemical order and local structure of the lead-free relaxor ferroelectric* $Na_{1/2}Bi_{1/2}TiO_3$, Journal of Solid State Chemistry **184**, 2041-2046 (2011).
- J. Kling, S. Hayn, L. Schmitt, **M. Gröting**, H.-J. Kleebe, K. Albe, *A-site occupancy in the lead-free* $(Bi_{1/2}Na_{1/2}TiO_3)_{0.94}$*-*$(BaTiO_3)_{0.06}$ *piezoceramic: Combining first-principles study and TEM*, Journal of Applied Physics **107**, 114113 (2010).
- S. Laubach, S. Laubach, P. C. Schmidt, **M. Gröting**, K. Albe, W. Jaegermann, W. Wolf, *Structure, electronic structure and defect formation energies of* $Li_xCo_{1-y}Ni_yO_2$ *as a function of* x *(*$0 < x < 1$*) and* y *(*$y = 0,\ 0.5,\ 1$*)*, Zeitschrift für Physikalische Chemie **223**, 1327-1340 (2009).
- M. Stephan, M. Zachau, **M. Gröting**, O. Karplak, V. Eyert, K. C. Mishra, P. C. Schmidt, *A theoretical investigation of* $4f \rightarrow 5d$ *transition of trivalent rare earth ions in fluorides and complex oxides*, Journal of Luminescence **114**, 255-266 (2005).

Oral Presentations at International Conferences

- **M. Gröting**, I. Kornev, B. Dkhil, K. Albe, *Lead-free relaxor ferroelectric* $Na_{1/2}Bi_{1/2}TiO_3$*: On the stability and ferroic properties of chemically ordered nanoregions*, International Symposium on Integrated Functionalities, 18.-21.06.2012, Hong Kong, P.R. China.
- **M. Gröting**, S. Hayn, I. Kornev, B. Dkhil, K. Albe, *Comparison of hydrostatic and chemical pressure in lead-free* $Bi_{0.5}Na_{0.5}TiO_3$*-based materials studied by first-principles methods*, DPG Frühjahrstagung Sektion Kondensierte Materie, 25.-30.03.2012, Berlin, Germany.
- **M. Gröting**, S. Hayn, I. Kornev, B. Dkhil, K. Albe, *Ferroelectric Instabilities in Lead-Free* $Na_{0.5}Bi_{0.5}TiO_3$*-Based Ferroelectric Materials Studied by First-Principles Methods*, MRS Fall Meeting, 28.11.-02.12.2011, Boston (MA), USA.
- **M. Gröting**, I. Kornev, B. Dkhil, K. Albe, *First-Principles Study of the Lead-Free Perovskite* $Na_{1/2}Bi_{1/2}TiO_3$*: Relative Phase Stabilities and Local Structure*, 12th European Meeting on Ferroelectricity, 26.06.-02.07.2011, Bordeaux, France.
- **M. Gröting**, S. Hayn, K. Albe, *Ordering in the A-site mixed perovskite* $Bi_{0.5}Na_{0.5}TiO_3$, DPG Frühjahrstagung Sektion Kondensierte Materie, 21.-26.03.2010, Regensburg, Germany.

- **M. Gröting**, K. Albe, *Investigation of point defects in the cathode material $LiCoO_2$: first-principles calculations*, DPG Frühjahrstagung Sektion Kondensierte Materie, 21.-26.03.2010, Regensburg, Germany.
- S. Laubach, St. Laubach, P. C. Schmidt, **M. Gröting**, K. Albe, D. Ensling, S. Schmid, W. Jaegermann, K. Nikolowski, H. Ehrenberg, *Changes in the crystal and electronic structure of $Li(Co,Ni)O_2$ upon Li-deintercalation*, Bunsentagung, 21.-23.05.2009, Köln, Germany.
- S. Hayn, **M. Gröting**, K. Albe, *Lead-free ferroelectric solid solutions from first-principles calculations*, DPG Frühjahrstagung Sektion Kondensierte Materie, 22.-27.03.2009, Dresden, Germany.

Poster Presentations at International Conferences

- **M. Gröting**, I. Kornev, B. Dkhil, K. Albe, *Lead-free relaxor ferroelectric $Na_{1/2}Bi_{1/2}TiO_3$: On the stability and ferroic properties of chemically ordered nanoregions*, International Workshop on Relaxor Ferroelectrics, 07.-11.10.2012, Edesheim (Pfalz), Germany.
- **M. Gröting**, M. Diehm, K. Albe, *Thermodynamic stability and degradation mechanisms of the cathode material $LiCoO_2$*, MSE Congress, 25.-27.09.2012, Darmstadt, Germany.
- **M. Gröting**, I. Kornev, B. Dkhil, K. Albe, *Local structure and ferroic properties of the lead- free relaxor ferroelectric $Na_{1/2}Bi_{1/2}TiO_3$*, MSE Congress, 25.-27.09.2012, Darmstadt, Germany.
- **M. Gröting**, I. Kornev, B. Dkhil, K. Albe, *First-principles study of the lead-free perovskite $Na_{1/2}Bi_{1/2}TiO_3$: Relative phase stabilities and local structure*, Workshop on the Fundamental Physics of Ferroelectrics and Related Materials, 30.01.-02.02.2011, Gaithersburg (MD), USA.
- **M. Gröting**, K. Albe, *Influence of A-site ordering on oxygen displacement and relative stability: First-principles study of the lead-free perovskite $Bi_{0.5}Na_{0.5}TiO_3$*, 19th International Symposium on the Applications of Ferroelectrics and 10th European Conference on the Applications of Polar Dielectrics, 9.-12.08.2010, Edinburgh, Great Britain.
- **M. Gröting**, D. Ensling, W. Jaegermann, P. C. Schmidt, K. Albe, *Investigation of point defects in the cathode material Li_xCoO_2 - first-principles calculations*, DPG Frühjahrstagung der Sektion Kondensierte Materie, 22.-27.03.2009, Dresden, Germany.
- **M. Gröting**, H. W. Zanthoff, J. Sauer, D. Maschmeyer, *High-Throughput Kinetic Screening in Catalytic Process Development*, European Conference on Combinatorial Catalysis Research and High-Throughput Technologies, 22.-25.04.2007, Bari, Italy.
- **M. Gröting**, E. Löffler, H. W. Zanthoff, D. Maschmeyer, *Eigenschaften saurer Katalysatoren für die Spaltung von Ethern*, 40. Jahrestreffen Deutscher Katalytiker, 14.-16.03.2007, Weimar, Germany.